A N N U A L R E P O R T

2020

and list of publications

Bayerisches Forschungsinstitut
für Experimentelle Geochemie und Geophysik
Universität Bayreuth

Bayerisches Geoinstitut
Universität Bayreuth
95440 Bayreuth
Germany

Telephone: +49-(0)921-55-3700
Telefax: +49-(0)921-55-3769
e-mail: bayerisches.geoinstitut@uni-bayreuth.de
www: https://www.bgi.uni-bayreuth.de

Editorial compilation by: Florian Heidelbach and Petra Buchert
Section editors: Andreas Audétat, Tiziana Boffa Ballaran, Audrey Bouvier,
Leonid Dubrovinsky, Dan Frost, Florian Heidelbach, Gregor Golabek,
Tomoo Katsura, Hans Keppler, Catherine McCammon,
Nobuyoshi Miyajima, Dave Rubie, Gerd Steinle-Neumann, Tony Withers

Staff and guests of the Bayerisches Geoinstitut in **September 2020**:

Die Mitarbeiter und Gäste des Bayerischen Geoinstituts im **September 2020:**

first row, from left (1. Reihe, v. links) Laura Czekay, Kirill Vlasov, Rong Huang, Catherine McCammon, Caterina Melai, Ulrike Trenz, Dorothea Wiesner, Danielle Silva Souza, Sergey Ovsyannikov

second row, from left (2. Reihe, v. links) Greta Rustioni, Dan Frost, Gerald Bauer, Janina Potzel, Petra Buchert, Iuliia Koemets, Alena Krupp, Alena Aslandukova, Saiana Khandarkhaeva, Eun Jeong Kim

third row, from left (3. Reihe, v. links) Alexander Kurnosov, Dominic Langhammer, Liang Yuan, Hongzhan Fei, Kassidy Nikole Yatso, Niccolò Satta, Giacomo Criniti, Marija Putak Juriček, Andrey Aslandukov, Jing Fang, Rizaldi Putra

back rows, from left (hintere Reihen, v. links) Florian Trybel, Tomoo Katsura, Florian Heidelbach, Jie Yao, Alexander Rother, Longjian Xie, Anna Dinius, Lianjie Man, Timofey Fedotenko, Filippe Ferreira, Gerd Steinle-Neumann, Nobuyoshi Mijayima, Takayuki Ishii, Raphael Njul, Leonid Dubrovinsky, Jonathan Dolinschi, Hans Keppler, Danilo Di Genova, Keisuke Nishida, Adrien Néri, Tristan Pausch, Detlef Krauße, Tony Withers, Dominique Laniel, Stefan Übelhack, Audrey Bouvier, Thomas Meier, Dmitry Bondar

Absent (Es fehlten) Sumith Abeykoon, Andreas Audétat, Tiziana Boffa Ballaran, Laura Cialdella, Serena, Dominijanni, Lisa Eberhard, Heinz Fischer, Michaela Flanigan, Gregor Golabek, Sven Linhardt, Ning Ma, Enrico Marzotto, Edna Obengo, Esther Posner, Anke Potzel, Narangoo Purevjav, Dave Rubie, Romina Scharfenberg, Hubert Schulze, Victoria Szlachta, Marcel Thielmann, Biao Wang

Contents

Foreword

While the year 2020 started more or less normal, after a few months everything at the institute was overshadowed by the corona pandemic. In March, three of our Ph.D. students had to abruptely terminate their stay at Tohoku University and returned to Bayreuth. While normally we have more than fifty external groups of scientists visiting our institute during one year, this number dropped to almost zero. Seminars were only possible online and the public had to be excluded from Ph.D. defenses. However, our laboratories always remained in full operation and the scientific productivity at the institute was not reduced. A careful observer may note that the number of pages of this annual report is slightly less than in previous years – but this is simply because the joint contributions with many external visitors to the institute are missing. Thanks to the prudence and sense of duty of our scientific and technical staff, we managed the situation with only limited restrictions and so far, with zero infections. The institute group photo was taken as usual, just with enlarged distances. The most serious effect of the corona pandemic on the institute was probably that we had to cancel both our summer barbeque and the Christmas party, as well as numerous receptions and joint coffee breaks in the foyer.

Like always, the current annual report contains a number of scientific highlights. The distribution of carbon on the early Earth is very important, as it largely determines the habitability of the planetary surface. Usually, it is assumed that during core formation, most of the carbon is concentrated in the iron metal phase and a strongly carbon-depleted mantle is left behind. In a contribution on page 35 ff, Dave Rubie and colleagues demonstrate that this may not necessarily be so. Experiments in laser-heated diamond cells show that carbon becomes less siderophile at very high pressures. More importantly, the details of accretion and of the dynamics in the early solar system need to be taken into account to construct a realistic picture of how Earth may have formed. The accretion model described here suggests that many planetesimals colliding with the growing Earth may have come from the outer part of the solar system, where conditions were so oxidized that no iron metal was present and therefore, during the impact of these planetesimals, all carbon was added to the mantle.

During the early stages of Earth's history, the mantle may have been completely molten. Unfortunately, many properties of such peridotitic melts are rather poorly known. One reason for this is that so far, it was impossible to rapidly quench a peridotite melt to a glass at high pressure. Glasses are "frozen in" silicate melts that may be conveniently investigated at ambient conditions in order to study their structure and properties. On page 139 ff, Dmitry Bondar and colleagues describe a new rapid-quench device for the multianvil apparatus, which may reach cooling rates of more than 7000 °C per second. With this device, it was for the first time possible to produce glasses by rapid cooling of a peridotite melt at high pressure. It is expected that the further investigation of these samples will yield completely new insights into the structure and properties of peridotite melts.

A very positive development in the year 2020 was that despite the problems caused by the corona pandemic, the construction of the new laboratories for cosmochemistry at BGI progressed quickly. The entire external construction of the new part of the building is essentially finished. The current annual report already contains some contributions *e.g.*, on cosmochemical studies of meteorites (pages 24 ff, 26 ff) and we expect that these activities will greatly expand once the new laboratories are fully in operation.

On the behalf of my colleagues, I would like to thank the *Free State of Bavaria* as represented by the *Bavarian State Ministry of Science, Research and Art*, as well as the *Advisory Board for High-Pressure Research in Geoscience* of the *Bavarian Academy of Sciences* for their continuing support and strong commitment to the Bayerisches Geoinstitut. I would further like to thank the *President and Leadership of the University of Bayreuth* for their high regard of our institute. We also gratefully acknowledge generous support from external funding agencies, in particular the *Alexander von Humboldt Foundation*, the *European Union*, the *German Science Foundation,* and the *Federal Ministry of Education and Research*, which continue to contribute greatly to the further development and success of the Geoinstitut.

Bayreuth, March 2021 Hans Keppler

Vorwort

Das Jahr 2020 begann normal, aber nach wenigen Monaten hat die Corona-Pandemie alle Ereignisse am Institut überschattet. Drei unserer Doktoranden mussten im März ihren Aufenthalt an der Tohoku-Universität in Japan abbrechen und nach Bayreuth zurückkehren. Normalerweise besuchen mehr als fünfzig Gruppen von externen Wissenschaftlern jedes Jahr unser Institut. In 2020 ging diese Zahl fast auf Null zurück. Seminare waren nur im Online-Format möglich und die Öffentlichkeit musste bei Promotionsprüfungen ausgeschlossen werden. Alle unsere Labore blieben jedoch ohne Unterbrechung in vollem Betrieb und die wissenschaftliche Produktivität des Instituts war unvermindert. Ein sorgfältiger Leser wird vielleicht feststellen, dass dieser Jahresbericht geringfügig kürzer ist als in den vorangegangenen Jahren. Dies liegt jedoch primär daran, dass die Beiträge von externen Nutzern unserer Hochdruckeinrichtungen fehlen. Dank der Umsicht und dem Verantwortungsbewusstsein unserer wissenschaftlichen und technischen Mitarbeiter konnten wir die Situation mit relativ wenigen Einschränkungen unter Kontrolle halten, bisher ohne eine einzige Infektion am Institut. Das Gruppenfoto der Mitarbeiter wurde aufgenommen wie immer, nur die Abstände haben sich etwas vergrößert. Die schwerwiegendste Auswirkung der Corona-Pandemie auf das Institut war vermutlich, dass wir unser Grillfest im Sommer und die Weihnachtsfeier ausfallen lassen mussten, ebenso wie viele kleine Empfänge und gemeinsame Kaffeepausen im Foyer.

Wie immer enthält dieser Jahresbericht einige herausragende wissenschaftliche Ergebnisse. Die Verteilung von Kohlenstoff auf der frühen Erde bestimmt zu einem guten Teil, ob die Oberfläche unseres Planeten bewohnbar war. In der Regel wird angenommen, dass bei der Bildung des Erdkerns der größte Teil des Kohlenstoffs in der Eisen-Metallschmelze gelöst wird und nur ein kleiner Teil im Erdmantel zurückbleibt. In einem Beitrag auf Seite 35 ff demonstrieren Dave Rubie und Kollegen, dass dies nicht notwendigerweise der Fall ist. Experimente in Laser-geheizten Diamantstempelzellen zeigen, dass Kohlenstoff mit steigendem Druck weniger siderophil wird. Vor allem muss man aber die Details der Akkretion und der Dynamik im frühen Sonnensystem berücksichtigen, um ein realistisches Bild der Entstehung der Erde zu erhalten. Viele der Planetesimale, die mit der wachsenden Erde kollidiert sind, kamen wahrscheinlich aus dem äußeren Teil des Sonnensystems. Dort waren die Bedingungen so oxidiert, dass kein metallisches Eisen mehr vorhanden war. Beim Einschlag dieser Planetesimale auf der Erde wurde daher der gesamte Kohlenstoff dem Mantel hinzugefügt.

In der frühesten Erdgeschichte war der Mantel wahrscheinlich vollständig aufgeschmolzen. Leider sind viele Eigenschaften der entsprechenden Peridotit-Schmelzen nicht bekannt. Ein Grund hierfür ist, dass es bisher unmöglich war, unter hohem Druck eine Peridotitschmelze zu einem Glas abzuschrecken. Gläser sind "eingefrorene" Silikatschmelzen, die man bequem bei Normalbedingungen untersuchen kann, um ihre Struktur und verschiedene Eigenschaften zu

bestimmen. Auf Seite 139 ff beschreiben Dmitry Bondar und Kollegen eine neue Apparatur zum schnellen Abschrecken von Multi-Anvil-Experimenten, mit der Abkühlgeschwindigkeiten bis über 7000 °C pro Sekunde erreicht werden können. Mit dieser Technik war es erstmals möglich, Peridotit-Gläser im Labor zu erzeugen. Man kann davon ausgehen, dass die weitere Untersuchung dieser Proben völlig neue Erkenntnisse über die Struktur und Eigenschaften von Peridotit-Schmelzen liefern wird.

Eine sehr positive Entwicklung im Jahr 2020 war, dass trotz der Corona-Pandemie der Bau der neuen Laborräume für Kosmochemie am BGI schnelle Fortschritte gemacht hat. Die gesamte externe Konstruktion der entsprechenden Gebäudeteile ist im wesentlichen abgeschlossen. Im vorliegenen Jahresbericht finden sich bereits Beiträge über kosmochemische Untersuchungen an Meteoriten (z. B. Seite 24 ff, 26 ff) und wir gehen davon aus, dass sich diese Aktivitäten enorm verstärken werden, sobald die neuen Labore in vollem Betrieb sind.

Meine Kollegen und ich möchten dem *Freistaat Bayern*, vertreten durch das *Bayerische Staatsministerium für Wissenschaft, Forschung und Kunst*, und dem *Beirat für Geowissenschaftliche Hochdruckforschung der Bayerischen Akademie der Wissenschaften* unseren Dank für ihre fortwährende Unterstützung des Bayerischen Geoinstituts aussprechen. Darüber hinaus möchten wir dem Präsidenten und der Hochschulleitung der Universität Bayreuth ausdrücklich für ihre zuverlässige und kontinuierliche Unterstützung unseres Instituts danken. Wir sind auch für die großzügige Förderung durch externe Geldgeber dankbar, insbesondere der *Alexander-von-Humboldt-Stiftung*, der *Europäischen Union* und der *Deutschen Forschungsgemeinschaft*, die ebenfalls wesentlich zur Entwicklung und zum Erfolg des Bayerischen Geoinstituts beigetragen haben.

Bayreuth, im März 2021 Hans Keppler

1. Advisory Board and Directorship

1.1 Advisory Board

The *Beirat für Geowissenschaftliche Hochdruckforschung der Bayerischen Akademie der Wissenschaften* advises on the organisation and scientific activities of the institute. Members of this board are:

Prof. Dr. Gerhard BREY	Institut für Geowissenschaften der Johann Wolfgang Goethe-Universität, Frankfurt am Main
Prof. Dr. Ulrich CHRISTENSEN	Max-Planck-Institut für Sonnensystemforschung, Göttingen
Prof. Dr. Rudolf GROSS (Vice Chairman)	Walther-Meißner-Institut für Tieftemperatur-forschung (WMI), Garching
Prof. Dr. Rüdiger KNIEP *until March 2020*	Emeritus, Max-Planck-Institut für Chemische Physik fester Stoffe, Dresden
Prof. Dr. Herbert PALME	Emeritus, Institut für Mineralogie und Geochemie der Universität zu Köln – Senckenberg Forschungsinstitut und Naturmuseum Frankfurt/M.
Prof. Dr. Markus RIEDERER (Chairman)	Julius-von-Sachs-Institut für Biowissenschaften, Würzburg
Prof. Dr. Ekhard SALJE, FRS, FRSA	Department of Earth Sciences, University of Cambridge
Prof. Dr. Christine THOMAS	Institut für Geophysik der Westfälischen Wilhelms-Universität Münster

1.2 Leadership

Prof. Dr. Hans KEPPLER (Director)
Prof. Dr. Dan FROST (Deputy Director)
Prof. Dr. Tomoo KATSURA

2. Staff, Funding and Facilities

2.1 Staff

At the end of 2020 the following staff positions existed in the Institute:

- Scientific staff: **15**
- Technical staff: **14**
- Administrative staff: **2**
- Administrative officer: **1**

During 2020, 37 scientific and 1 coordinator positions (360 months) were funded by grants raised externally by staff members of the institute. In addition, 4 long-term scientific positions (44,5 months) were funded by the resources of the BGI Visiting Scientists' Programme (see Sect. 8) which also supported short-term visits for discussing future projects or presenting research results (see Sect. 5). 10 student assistants (62 months) were funded by externally raised grants. 5 scientists and 1 master student (57.5 months) were supported by personal grants or stipends.

2.2 Funding

In 2020, the following financial resources were available from the Free State of Bavaria:

- Visiting Scientists' Programme: 328.000 €
- Consumables: 535.000 €
- Investment funding: 60.000 €

The total amount of national/international external funding *("Drittmittel"*) used for ongoing research projects in 2020 was 3.100.000 € (Positions: 1.855.000 €; equipment, consumables and travel grants: 1.245.000 €).

	positions	**equipment, consumables, travel grants**	**total**
• AvH	0 €	4.000 €	4.000 €
• BMBF	152.000 €	198.000 €	350.000 €
• DFG	1.492.000 €	887.000 €	2.379.000 €
• EU	169.000 €	156.000 €	325.000 €
• Others	42.000 €	0 €	42.000 €
	1.855.000 €	**1.245.000 €**	**3.100.000 €**

(AvH = Alexander von Humboldt Foundation; BMBF = Federal Ministry of Education and Research; DFG = German Science Foundation; EU = European Union; Others: DAAD, Chinese Science Council, Japanese Society for the Promotion of Science, Swiss National Science Foundation)

In the following list only the BGI components of the funding are listed in cases where joint projects involved other research institutions. Principal investigators and the duration of the grants are listed in brackets. Total project funding refers to the funding over the entire duration of this project.

Funding institution	Project, Funding	Total Project Funding
BMBF	05K19WCA (H. Keppler – 7/19-6/22) "Aufbau einer Hochdruckpresse vom Multi-Anvil-Typ an der Forschungs-Neutronenquelle FRM II in Garching" Total funding:	579.116 €
BMBF	05K16WC2 (T. Katsura – 7/16-6/21) "Erweiterung der Druckbereiche der In-Situ-Röntgen-beobachtung mit der Großvolumen-Hochdruckapparatur an der PETRA-III-Extension des Deutschen Elektronen-Synchrotrons DESY" Positions E 12-E 15: 349.727 € Consumables and travel funding: 421.540 € Equipment: 43.000 € Overhead: 162.857 €	977.124 €
Carnegie Institution	Carnegie Institution of Washington (H. Keppler, T. Katsura – 11/20-11/21) "Densities of hydrous silicate melts at high pressure"	83.850 €
DFG	DU 393/9-2 (L.S. Dubrovinsky – 1/18-12/20) 'Chemische Reaktionen zwischen Karbonaten und pyrolitischem Erdmantel und Entstehung ultratiefer Diamanten', "Structures, properties and reactions of carbonates at high temperatures and pressures" Positions: E 13 (67 %), 36 months 132.800 € Consumables: 32.250 € Overhead: 36.300 €	201.350 €
DFG	DU 393/13-1 (L.S. Dubrovinsky – 4/17-3/20) "Mantel formende Materialien von Super Erden bei Statischen Drücken von über 500 GPa und hohen Temperaturen" Positions: E 13, 36 months 209.400 € student assistant 8.000 € Consumables: 27.750 € Overhead: 53.900 €	299.050 €
DFG	FR 1555/11-1 (D.J. Frost – 3/16-2/23) Gottfried Wilhelm Leibniz-Preis 2016	2.500.000 €

DFG	GRK 2156/1 (D.J. Frost, et al. – 4/16-10/20) Internationales Graduiertenkolleg "Deep Earth Volatile Cycles"	3.257.358 €
DFG	IS 350/1-1 (T. Ishii – 4/19-12/20) "Hochdruck-Temperatur-Phasenbeziehungen der basaltischen Kruste unter Bedingungen des unteren Mantels: Auswirkungen auf die chemische Heterogenität im unteren Mantel" Position: E 13, 18 months: 107.800 € Consumables and travel funding: 24.000 € Overhead: 29.000 €	160.800 €
DFG	KA 3434/3-2 (T. Katsura – 7/18-6/21) "Dislocation recovery experiment of hydrous olivine as a function of water content and crystallographic orientation" Positions: E 13, 12 months 69.300 € E 13 (75 %), 12 months 48.100 € student assistant 5.000 € Consumables: 20.000 € Overhead: 31.300 €	173.700 €
DFG	KA 3434/11-1 (T. Katsura – 12/18-11/21) "Determining the water dissociation constant from the relationship between water solubility in ringwoodite and oxygen fugacity" Positions: E 13, 24 months 141.700 € Consumables: 23.500 € Overhead: 36.300 €	201.500 €
DFG	KA 3434/12-1 (T. Katsura – 10/18-12/21) "Determination of water partition coefficients between upper mantle minerals and melts as a function of pressure, temperature, and CO_2 content using a rapid quench cell in multi-anvil experiments" Positions: E 13, 24 months 142.700 € Consumables: 40.000 € Overhead: 40.200 €	222.900 €
DFG	KE 501/11-2 (H. Keppler – 2018-2020) "Electrical conductivity and dissociation of fluids in crust and mantle" Total funding:	209.600 €
DFG	KE 501/13-2 (H. Keppler – 2019-2020) "Nitrogen in the deep mantle" Total funding:	136.200 €
DFG	KE 501/16-1 (H. Keppler – 2020-2023) "Cassiterite solubility, tin partitioning, and the origin of porphyry tin deposits" Total funding:	242.288 €

DFG	KU 3447/1-1 (A. Kurnosov – 10/18-9/21) "Einkristall-Elastizität von Mars-Mineralen und ein flexibles CO_2 Laserheizsystem" Position: E 13, 36 months 217.700 € Consumables and travel funding: 15.250 € Overhead: 51.200 €		284.150 €
DFG	MA 4534/5-1 (H. Marquardt – 6/17-5/20) "Experimentelle Untersuchung von planetaren Eis-Verbindungen bei hohen Drücken mittels dynamisch-betriebener Diamantstempelzellen" Position: E 13 (75 %), 36 months: 145.700 € Consumables: 27.750 € Overhead: 38.200 €		211.650 €
DFG	MC 3/20-2 (C.A. McCammon – 1/18-12/22) DFG FOR 2125 (CarboPaT) "Elastic properties of carbonates at high pressure and high temperature" Position: E 13 (67 %), 36 months: 132.800 € Equipment, consumables and travel funding: 27.750 € Overhead: 35.300 €		195.850 €
DFG	MC 3/21-1 (C.A. McCammon – 6/17-5/21) "Fe Spinübergang im Erdmantel: Einblicke durch Röntgen-Raman-Streuung und Röntgenabsorptionsspektroskopie" Position: student assistant (Bachelor) 9.482 € Equipment, consumables and travel funding: 6.000 € Overhead: 3.400 €		18.882 €
DFG	ME 5206/3-1 (T. Meier – 6/19-5/22) "Wasserstoffbrückenbindungen unter extremen Bedingungen: Kernquanteneffekte und Symmetrisierung der Wasserstoff-brückenbindung untersucht mit ^{1}H-NMR in Diamantstempel-zellen" Position: E 13, 36 months: 221.500 € Consumables and travel funding: 29.250 € Overhead: 55.200 €		305.950 €
DFG	MI 1721/3-1 (N. Miyajima – 9/19-8/22) "Al, Si-Interdiffusion in Bridgmanit und die Viskosität des unteren Mantels" Position: E 13 (75 %), 36 months: 157.000 € student assistant 7.500 € Consumables and travel funding: 29.500 € Overhead: 41.000 €		227.500 €

DFG	OV 110/3-1 (S.V. Ovsyannikov – 9/18-8/20) "High-pressure synthesis and properties of novel simple oxides with unusual stoichiometries" Position: E 13, 24 months 141.600 € Consumables and travel funding: 30.250 € Overhead: 37.800 €	209.650 €
DFG	OV 110/3-2 (S.V. Ovsyannikov – 12/20-11/22) "High-pressure synthesis and properties of novel simple oxides with unusual stoichiometries" Position: E 13, 24 months 151.600 € Consumables and travel funding: 39.550 € Overhead: 42.100 €	233.250 €
DFG	STE 1105/13-1 (G. Steinle-Neumann – 8/17-7/20) "Thermodynamic properties of silicate solids and liquids and iron to the TPa range from *ab initio* calculations" Positions: E 13 (75%), 36 months 145.700 € student assistant 15.000 € Consumables: 7.750 € Overhead: 37.100 €	205.550 €
DFG	STE 1105/13-2 (G. Steinle-Neumann – 7/20-6/23) "Thermodynamic properties of silicate solids and liquids and iron to the TPa range from *ab initio* calculations" Positions: E 13 (75%), 36 months 158.600 € student assistant 7.000 € Consumables: 8.250 € Overhead: 38.200 €	212.050 €
DFG	TH 2076/7-1 (M. Thielmann – 6/21-5/24) "Quantifizierung des Oberflächensignals durch Lithosphärenablösung in den Alpen" Positions: personnel funds 244.700 € Consumables: 17.050 € Overhead: 57.600 €	319.350 €
EU	European Research Council (ERC) Advanced Grant No. 787 527 (T. Katsura – 10/18-9/23) "Chemistry and transport properties of bridgmanite controlling lower-mantle dynamics" ("UltraLVP") Positions (post docs): 860.144 € Travel funding: 187.380 € Equipment: 49.250 € Consumables: 997.722 € In-kind contributions: 24.000 € Overhead: 523.624 €	2.642.120 €

EU	Europlanet 2024 Research Infrastructure, award 20-EPN-050 (A. Bouvier) "26-Aluminium-26-Magnesium systematics of chondrules and clasts in unequilibrated ordinary chondrites"	8.000 €

2.3 Laboratory and office facilities

The institute occupies an area of

ca. 1350 m^2	laboratory space
ca. 480 m^2	infrastructural areas (machine shops, computer facilities, seminar room, library)
ca. 460 m^2	office space

in a building which was completed in 1994.

2.4 Experimental and analytical equipment

The following major equipment is available at the Bayerisches Geoinstitut:

I. High-pressure apparatus
- 15 MN/1500 tonne Kawai-type multianvil high-pressure apparatus (40 GPa, 2000 K)
- 6 x 8 MN/6x800 tonne independently acting-anvil press (25 GPa, 3000 K)
- 50 MN/5000 tonne multianvil press (25 GPa, 3000 K)
- 12 MN/1200 tonne multianvil press (25 GPa, 3000 K)
- 10 MN/1000 tonne multianvil press (25 GPa, 3000 K)
- 5 MN/500 tonne multianvil press (20 GPa, 3000 K)
- 5 MN/500 tonne press with a deformation DIA apparatus
- 5 piston-cylinder presses (4 GPa, 2100 K)
- Cold-seal vessels (700 MPa, 1100 K, H_2O), TZM vessels (300 MPa, 1400 K, Ar), rapid-quench cold-seal vessels (400 MPa, 1200 K, H_2O)
- Internally-heated autoclave (1 GPa, 1600 K)
- High-pressure gas loading apparatus for DAC

II. Structural and chemical analysis
- 1 X-ray powder micro-diffractometer
- 1 X-ray powder diffractometer with furnace and cryostat
- 2 automated single-crystal X-ray diffractometers
- High-brilliance X-ray system
- Single crystal X-ray diffraction with super-bright source
- 1 Mössbauer spectrometer (1.5 - 1300 K)
- 3 Mössbauer microspectrometers
- 2 FTIR spectrometers with IR microscope

FEG transmission electron microscope (TEM), 200 kV analytical, with EDS
FEG scanning TEM, 80-200 kV analytical, with 4-SDDs EDS and post-column energy filter (EFTEM/EELS)
FEG scanning electron microscope (SEM) with BSE detector, EDS, EBSD and CL
Dual beam device, focused ion beam (FIB) and FEG SEM. In situ easy-lift manipulator, STEM, EDS and EBSD detectors, and beam deceleration option
3 Micro-Raman spectrometers with ultraviolet and visible lasers
Tandem-multipass Fabry-Perot interferometer for Brillouin scattering spectroscopy
JEOL JXA-8200 electron microprobe; fully-automated with 14 crystals, 5 spectrometer configuration, EDX, capability for light elements
193 nm Excimer Laser-Ablation ICP-MS
Water content determination by Karl-Fischer titration
GC/MS-MS for organic analyses
Confocal 3D surface measurement system
1.4 Tesla sweepable ESR magnet
Solid state 300 MHz NMR spectrometer

III. *In situ* determination of properties

Diamond anvil cells for powder and single crystal X-ray diffraction, Mössbauer, IR, Raman, optical spectroscopy, NMR specroscopy, electrical resistivity measurements over 200 GPa
Facility for in situ hydrothermal studies in DAC
Externally heated DACs for in situ studies at pressures to 100 GPa and 1200 K
1-atm furnaces to 1950 K, gas mixing to 1600 K, zirconia fO_2 probes
1-atm high-temperature creep apparatus
Gigahertz ultrasonic interferometer with interface to resistance-heated diamond-anvil cells
Freezing-heating stage for fluid inclusion studies
Impedance/gain-phase analyser for electrical conductivity studies
Apparatus for in situ measurements of thermal diffusivity at high P and T
Laser-heating facility for DAC
Portable pulsed laser heating system for DAC

The Geoinstitut maintains a well equipped machine shop, an electronic workshop and sample preparation laboratories. It has access to supercomputing resources at the University and Leibniz computer centres.

3. Forschungsprojekte

3.1 Struktur und Dynamik der Erde und Planeten

Sowohl astronomische Beobachtungen als auch geochemische Daten zeigen, dass die Entstehung von Planeten kurz nach der Geburt eines Sterns einsetzt. Die Kondensation im Sonnensystem begann vor ≈ 4,57 Milliarden Jahren mit der Entstehung der Calcium-Aluminium-reichen Einschlüsse (CAI). Diese CAIs definieren daher den Beginn der Chronologie der Planetenentstehung. Untersuchungen an Meteoriten zeigen, dass viele Planetesimale, die Bausteine der Planeten, in kurzer Zeit entstanden und kurz danach Kern, Mantel und Kruste ausgebildet haben. Dies geschah noch vor dem Ende der Entstehungsphase von Chondrulen und Chondriten. Die frühe Differentiation wurde durch den Zerfall des kurzlebigen radioaktiven Isotops ^{26}Al (Halbwertszeit ~ 0,7 Millionen Jahre) angetrieben. Massenunabhängige Isotopen-Anomalien in Meteoriten haben gezeigt, dass im frühen Sonnensystem eine fundamentale Dichotomie in der protoplanetaren Scheibe existierte. Nicht-kohlige (NC) und kohlige (CC) Meteoriten-Ursprungskörper entstanden in zwei separaten Reservoiren, welche jeweils den inneren und den äußeren Teil der Scheibe repräsentierten. Die NC Meteoriten-Ursprungskörper scheinen dabei früher entstanden zu sein (< 0.5-3 Millionen Jahre nach Entstehung des Sonnensystems) und wurden stärker durch thermische Metamorphose überprägt als die kohligen Chondriten (~ 2 bis 4 Millionen Jahre), welche häufig durch flüssiges Wasser verändert wurden. Für die terrestrischen Planeten zeigen Modelle, die auf Studien der kurzlebigen Hf-W und Fe-Ni Isotopen-Systeme beruhen, dass Mars innerhalb von 5 Millionen Jahren nach der CAI-Entstehung 90 % seiner finalen Masse erreicht hat. Dagegen hatte die Erde eine längere Akkretionsgeschichte, die bis zu 100 Millionen Jahre dauerte. Etwa 10 % der Masse wurden durch einen großen Einschlag beigetragen, der zur Bildung des Mondes führte. Nach dem Ende der Kernbildung folgte für mehrere hundert Millionen Jahre die Phase der späten Akkretion, die weitere ≈ 0.5 % der Erdmasse lieferte. Das Material, dass nach der Kernbildung ankam, war für die Erde eine wichtige Quelle siderophiler und flüchtiger Elemente.

Der erste Beitrag beschreibt einen gekoppelten numerischen Ansatz, bei dem ein Model für die Entstehung der protoplanetaren Scheibe mit einem thermischen Modell von Planetesimalen verbunden wird, um die frühe Entwicklung der Körper im Sonnensystem zu beschreiben. Die Resultate zeigen, dass die Migration der Eislinie, wo die Temperaturen in der protoplanetaren Scheibe niedrig genug sind um die Entstehung von festem Wassereis zu ermöglichen, zwei separate Episoden der Planetesimal-Entstehung verursacht. Diese Episoden sind zeitlich und räumlich voneinander getrennt. Die beiden getrennten Reservoire im inneren und äußeren Sonnensystem entwickeln sich unterschiedlich wegen verschiedenen ursprünglichen Mengen an ^{26}Al. Die Resultate stimmen überein mit der Entstehungschronologie von NC- und CC-Meteoriten, dem Wassergehalt und den Massenunterschieden zwischen innerem und äußerem Sonnensystem.

Meteoriten von differenzierten Ursprungskörpern sind unter den kohligen Chondriten relativ selten verglichen mit NC Meteoriten. Der Übergang zwischen primitiven und differenzierten Körpern wird unter CC-Meteoriten auch nicht beobachtet. Die Studie von Ma und Kollegen beschreibt eine neue Gruppe von primitiven Achondriten, den Tafassiten, die aus dem kohligen Chondriten-Reservoir stammen. Die Entstehungsbedingungen des Ursprungskörpers wurden aus mineralogischen, geochemischen und chronologischen Daten ermittelt. Der Tafassiten-Ursprungskörper muss vor den differenzierten Achondriten der CR-Gruppe und den CR1-3 Chondriten entstanden sein. Die Tafassite deuten deshalb darauf hin, dass silikatische Ursprungskörper schnell entstanden sind und zwar auch im äußeren Sonnensystem, wo die geringe Staubdichte und die langen Umlaufzeiten solch eine schnelle Akkretion erschweren sollten. Die Resultate zeigen außerdem, dass limitierte radiale Vermischung während dieser Periode in der Ursprungsregion auftrat.

Die terrestrischen Planeten im inneren Sonnensystem sind wahrscheinlich das Resultat der Akkumulation einer Vielzahl kleiner, sowohl primitiver als auch differenzierter Körper. In erster Näherung ist die chemische Zusammensetzung der Erde insgesamt sehr ähnlich den chondritischen Meteoriten. Jedoch weist die Erde verglichen mit den Chondriten eine stärkere Verarmung der moderat und leicht flüchtigen Elemente auf. Überdies zeigen Daten von massenunabhängigen Isotopen-Anomalien, dass im Vergleich zu allen anderen untersuchten Proben aus dem Sonnensystem die Erde die stärkste Anreicherung an s-Prozess-Isotopen aufweist. Mezger und Kollegen zeigen, dass es momentan nicht möglich ist, die verschiedenen chemischen und isotopischen Bestandteile zu definieren und zu quantifizieren, aus denen die Erde entstand. Eine bedeutende Komponente scheint in den bekannten extraterrestrischen Proben zu fehlen. Diese Komponente könnte aus dem inneren Sonnensystem stammen. Bislang haben Weltraummissionen Proben vom Mond und von Asteroiden gesammelt und die Probenentnahme vom Mars und seinen Monden ist geplant. Zusätzlich wären Proben von der Venus und vom Merkur sehr wichtig, um die Entstehung der terrestrischen Planeten besser eingrenzen zu können. Leider sind derartige Proben sehr schwer zugänglich.

Die Akkretion der Erde ist ein kontinuierlicher Prozess. Ungefähr 100 Tonnen an Material, größtenteils Staub, werden der Erde jeden Tag hinzugefügt. Aber auch größere Objekte kreuzen regelmäßig die Erdbahn. Netzwerke von Kameras und Wetterradar-Stationen helfen dabei, Feuerball-Ereignisse aufzuspüren und die Aufschlagsorte von Meteoriten einzugrenzen. Es ist noch einfacher, sie zu finden und zu konservieren, wenn ein Meteorit auf einem vereisten See einschlägt wie im Fall des Hamburg-Meteoriten, eines normalen H4-Chondriten, der am 16. Januar 2018 in Michigan einschlug. Heck und Mitarbeiter haben exklusiv drei Bruchstücke untersucht, die nur wenige Tage nach dem Einschlag gefunden wurden. Am meisten überraschte die Entdeckung, dass der Meteorit noch ~2600 verschiedene organische Verbindungen enthielt, obwohl er für etwa 25 Millionen Jahre nach seiner Entstehung einer thermischen Metamorphose bei bis zu 720 K (basierend auf Blei-Blei Messungen an Phosphaten) ausgesetzt war. Resultate zeigen, dass der 40-60 cm große Meteoroid vor etwa 12 Millionen Jahren von seinem Ursprungskörper weggeschleudert wurde, ohne dass dabei die Spuren der früheren thermischen Entwicklung beeinflusst wurden.

Im Zusammenhang mit der Entstehung der Erde wird auch eine mögliche mineralogische Schichtung des oberen und unteren Erdmantels seit langer Zeit diskutiert. Während Enstatit-Chondrite für viele Isotopen-Systeme die größte Übereinstimmung mit der Erde zeigen, entspricht ihre Zusammensetzung an Hauptelementen nicht der des oberen Erdmantels. Dieses Problem könnte durch ein niedrigeres Mg/Si-Verhältnis im unteren Mantel gelöst werden. Basierend auf akustischen Geschwindigkeitsmessungen an Bridgmanit postulieren Machino und Kollegen eine mögliche Mineralogie des unteren Mantels mit einer verglichen mit dem oberen Mantel Si-angereicherten Zusammensetzung mit Mg/Si = 1,14 (oberer Mantel: Mg/Si = 1,25). Dies würde bedeuten, dass 4,5 Milliarden Jahre der Mantelkonvektion nicht in der Lage waren, den gesamten Erdmantel zu homogenisieren.

In der heutigen Erde transportieren subduzierte Platten Wasser ins Innere der Erde. Marzotto und Kollegen kombinieren Experimente zur thermischen Leitfähigkeit von Ringwoodit mit eindimensionalen numerischen Modellen der Subduktion einer Platte. Die Experimente zeigen, dass die Aufnahme von Wasser die thermische Leitfähigkeit von Ringwoodit, dem Hauptbestandteil der unteren Übergangszone (520-670 km Tiefe), um bis zu 40 % senkt. Unter diesen Bedingungen kann die Anwesenheit von wasserhaltigem Ringwoodit in einer subduzierenden Platte die Zersetzung von wasserhaltigen Magnesium-Silikaten dort signifikant hinauszögern. Auf diese Weise ist es wahrscheinlicher, dass diese wasserhaltigen Phasen den unteren Erdmantel erreichen können.

3.2 Geochemie

Die Gesteine der Erde weisen im Vergleich zu denen anderer terrestrischer Planeten eine enorme chemische Vielfalt auf, obwohl jeder Planet aus ähnlichen Materialien entstanden ist. Diese Vielfalt ist ein Ergebnis der einzigartigen Evolution unseres Planeten. Um sie zu verstehen, müssen wir die chemischen Fraktionierungsprozesse untersuchen, die sich in Kern, Mantel und Kruste der Erde abgespielt haben.

Viele der in diesem Abschnitt des Jahrbuchs beschriebenen Studien zielen darauf ab, die chemischen Fraktionierungsprozesse durch Experimente im Labor zu untersuchen. Die Produkte dieser Experimente sind meist Silikatschmelzen, silikathaltige Fluide oder die nach Schmelz- oder Entwässerungsprozessen verbleibenden Restgesteine, die mit natürlichen Proben verglichen werden können. In den ersten drei Beiträgen dieser Sektion wird das großräumige Fraktionierungsereignis untersucht, das die Trennung des metallischen Erdkerns von den Silikaten des Erdmantels ermöglichte. Eine wichtige Fragestellung ist hier, welche Elemente die kernbildende Eisenschmelze aus dem Erdmantel entfernt hat. Der erste Beitrag verwendet Experimente mit laserbeheizten Diamant-Stempelzellen und ein neues numerisches Modell, um zu untersuchen, warum die Kernbildung nicht den größten Teil des Kohlenstoffs der Erde in den Kern transportiert hat. Durch die Modellierung der verschiedenen Stadien der Akkretion und Kernbildung wird deutlich, dass die Planetesimale, die den Kohlenstoff zur Erde

brachten, kein kernbildendes Metall enthielten. Dies liegt daran, dass sie sich in den äußeren Regionen des Sonnensystems gebildet hatten, wo das Metall oxidiert wurde. Diese Planetesimale fügten also nur dem Erdmantel Kohlenstoff hinzu. Obwohl später weitere Stadien der Kernbildung auftraten, war das Metall-Silikat-Gleichgewicht dabei auf eine Region um das sich abscheidende Kernmaterial beschränkt, sodass der Rest des Mantels nicht an Kohlenstoff verarmte.

Die nächste Studie untersucht, wie viel Wasserstoff im Erdkern noch vorhanden sein könnte. Dies ist sehr wichtig, weil der Wasserstoffgehalt der gesamten Erde nur unzureichend bekannt ist. Es ist extrem schwierig, den Wasserstoffgehalt von flüssigem Metall experimentell zu untersuchen, da der Wasserstoff nicht im Metall verbleibt, sobald die Probe auf Raumtemperatur abgeschreckt wird. In dieser Studie werden stattdessen *ab initio* Berechnungen durchgeführt, die zeigen, dass sich der Wasserstoff mit dem Druck zunehmend im Metall anreichert. Dementsprechend sollte sich etwa 1 Gew.-% Wasserstoff im Kern befinden. Die gleichen Simulationen sagen auch voraus, dass sich Silizium signifikant im Kern löst, während Mg fast vollständig im Silikatmantel verbleibt. Diese letztere Schlussfolgerung wird in der folgenden Studie bestätigt, die untersucht, ob MgO bei sehr hohen Temperaturen aus dem Mantel in den Kern gelangt sein könnte. Neuere Modelle haben vorgeschlagen, dass die spätere Entmischung von MgO aus dem Kern dazu beigetragen haben könnte, den Geodynamo der frühen Erde anzutreiben. Das würde erklären, warum die Magnetisierung alter Gesteine auf ein frühes Magnetfeld der Erde hindeutet. In dieser Studie wird jedoch festgestellt, dass die Menge an MgO, die im Kern gelöst werden kann, extrem gering ist und es keinen Hinweis darauf gibt, dass sie bei höheren Temperaturen zunehmen würde – was die Voraussetzung für eine Entmischung von MgO bei der Abkühlung der Erde wäre.

Die folgenden zwei Studien wurden durchgeführt, um Schmelzbildung im unteren Erdmantel zu untersuchen. In beiden Fällen geschieht dies mit dem Ziel, den Ursprung von Regionen mit niedrigen seismischen Wellengeschwindigkeiten aufzuklären, die durch das Vorhandensein von Schmelzen verursacht werden könnten. Schmelzexperimente erfordern sehr gut kontrollierte thermische Umgebungen, die in der laserbeheizten Diamant-Stempelzelle nur schwer zu erreichen sind. In der ersten Studie werden daher Multianvil-Experimente unter besser kontrollierbaren p,T-Bedingungen durchgeführt, die dem oberen Bereich des unteren Erdmantels entsprechen. Die Ergebnisse werden zur Entwicklung eines thermodynamischen Modells für die Schmelzbildung verwendet, das dann bis zur Basis des Mantels extrapoliert wird. Die Ergebnisse zeigen, dass die Zone mit extrem niedriger seismischer Geschwindigkeit an der Basis des Mantels wahrscheinlich nicht durch das Schmelzen von subduzierten basaltischen Gesteinen verursacht wird, da deren Schmelztemperatur ähnlich der des umgebenden Mantels sein sollte. Die zweite Studie untersucht die Verteilung von Eisen zwischen wasserhaltigen Schmelzen und Mineralen an der oberen Grenze des unteren Mantels. Seismische Beobachtungen deuten darauf hin, dass es in diesen Tiefen in einigen Regionen eine Schmelzanreicherung geben könnte, die aus der Stagnation der aufsteigenden Schmelze resultieren könnte, da die Schmelze dort die gleiche Dichte wie das umgebende Mantelgestein

hat. Die Dichte von Schmelzen hängt stark von ihrem Eisengehalt ab und in dieser Studie wird zum ersten Mal die Verteilung des Eisens zwischen den Mineralen des unteren Mantels und den Schmelzen bestimmt. Es wird erwartet, dass ein signifikanter Anteil des Eisens im unteren Erdmantel im oxidierten (Fe^{3+}) Zustand vorliegt. Die Ergebnisse zeigen jedoch, dass aufgrund der stärkeren Verteilung von oxidiertem Eisen in das Mantelmineral Bridgmanit der Eisengehalt der Schmelze nicht ausreicht, um eine ähnliche Dichte wie der umgebende Mantel zu erreichen. Die gebildeten Schmelzen würden wahrscheinlich vollständig aus dem unteren Mantel aufsteigen.

Die nächsten vier Studien in diesem Abschnitt beschäftigen sich mit der Bildung von Diamanten im Erdmantel, die einige der wenigen Beweise für die Zirkulation von Kohlenstoff im tiefen Erdinneren liefern. Die erste dieser Studien untersucht den Eisengehalt von winzigen Ferroperiklas (Eisen-Magnesiumoxid)-Einschlüssen, die in seltenen brasilianischen Diamanten aus dem unteren Erdmantel gefunden wurden. Da die Einschlüsse so klein sind, wird eine Mikrostrahl-Mössbauerspektroskopietechnik an einer Synchrotron-Röntgenquelle hoher Intensität eingesetzt. Die Einschlüsse enthalten sehr wenig Eisen, was bedeutet, dass die Bedingungen der Diamantbildung sehr reduzierend gewesen sein müssen. In der folgenden, Studie wurden Experimente durchgeführt, um die Nickelkonzentration von Ferroperiklas zu bestimmen, wenn er sich im Gleichgewicht mit einer Legierung aus metallischem Eisen und Nickel befindet. Die Ergebnisse zeigen, dass die Nickelkonzentrationen natürlicher Ferroperiklas-Einschlüsse in Diamanten durchaus damit übereinstimmen, dass sie im Gleichgewicht mit Metall im unteren Mantel waren. Dies bedeutet, dass der untere Mantel stark reduziert ist. Die folgende Studie baut auf diesem Szenario auf, indem sie untersucht, was mit einer solchen reduzierten, metallhaltigen Mineralvergesellschaftung des unteren Mantels passieren würde, wenn es einen Zufluss von Karbonatschmelze gäbe. Der reduzierte Zustand des unteren Mantels kann tatsächlich auf die starke Vorliebe des Mantelminerals Bridgmanit für oxidiertes Eisen zurückgeführt werden, die jeden verfügbaren Sauerstoff abpuffert. In dieser Studie wurde festgestellt, dass sich Diamanten bilden, wenn Karbonate mit einer solchen metallhaltigen Paragenese des unteren Mantels ins Gleichgewicht gebracht werden. Dies ist ein plausibles Szenario für die Bildung von Diamanten in der Tiefe, da Karbonatschmelzen von subduzierten lithosphärischen Platten in den reduzierenden unteren Mantel aufsteigen können. Faszinierend ist, dass mit zunehmendem Druck der Eisengehalt von Bridgmanit weiter ansteigt, was darauf hindeutet, dass der untere Mantel mit zunehmender Tiefe noch stärker reduziert werden kann. Die letzte Studie, die sich auf Diamanten bezieht, wurde durchgeführt, um den Oxidationszustand von Eisen in majoritischem Granat zu verstehen. Dieses Mineral wird auch als Einschluss in Diamanten gefunden, die unter Bedingungen der Übergangszone der Erde gebildet wurden. Das Ziel der Studie ist es, die Sauerstoff-Fugazität zu bestimmen, bei der das gesamte Eisen im majoritischen Granat im oxidierten Zustand ist. Diese Bedingungen werden bei einer nicht besonders hohen Sauerstoff-Fugazität erreicht. Aus der Tatsache, dass in natürlichen majoritischen Granateinschlüssen in Diamanten 30 % des Eisens im oxidierten Zustand vorliegen, lässt sich schließen, dass die Bedingungen, unter denen Diamanten in der Übergangszone gebildet werden, ebenfalls sehr reduziert sein können.

Die letzten vier Beiträge in diesem Abschnitt befassen sich alle mit Prozessen, die auftreten, wenn lithosphärische Platten, bestehend aus Mantel, ozeanischer Kruste und Sedimentschichten, in den Mantel subduziert werden. Der erste dieser Beiträge untersucht, wie sich der Redoxzustand von Serpentiniten während der Subduktion entwickelt. Die Serpentinisierung ist ein Hauptmechanismus, durch den Wasser in der ozeanischen Lithosphäre gebunden wird, aber durch dieser Prozess wird der Lithosphäre auch Eisen hinzugefügt, sowohl in Serpentinmineralen als auch durch die Bildung von Magnetit. Bei der Subduktion werden daher Wasser und Eisen in den Mantel transportiert. In dieser Studie wird ein Modell entwickelt, mit dem die Sauerstoff-Fugazität einer solchen Mineralparagenese berechnet werden kann. Die Ergebnisse zeigen, dass unabhängig vom Eisengehalt die Sauerstoff-Fugazität in einem sehr engen Bereich variieren muss sobald die Entwässerung des Serpentinits beginnt. Es wurde vorgeschlagen, dass sulfathaltige Fluide, die aus der Platte freigesetzt werden, den darüber liegenden Mantel oxidieren und den oxidierten Charakter der Inselbogenmagmen erklären könnten. Die Ergebnisse zeigen jedoch, dass der Oxidationszustand der Serpentinite unter dem Niveau bleibt, in dem Sulfate stabil wären. Obwohl Serpentinite relativ oxidiert sind, scheint es keinen Mechanismus zu geben, der diesen Redoxzustand in den darüber liegenden Mantel transferiert, wenn sie Wasser freisetzen. In der nächsten Studie werden die Phasenbeziehungen von wasserhaltigen Aluminosilikatphasen untersucht, um die Bedingungen zu bestimmen, unter denen eine wasserhaltige Teilschmelze gebildet wird, die möglicherweise flüchtige Stoffe aus subduzierten Platten entfernt. In dieser Vorstudie führten jedoch hohe Konzentrationen von Stickstoff, die den Experimenten hinzugefügt wurden, zur Bildung von ungewöhnlichen Glimmern, bei denen Kalium vollständig durch Ammonium ersetzt wird.

In der folgenden Studie wird die Rolle von Apatit bei der Bestimmung der Spurenelementsignatur von Fluiden, die subduzierte Sedimentschichten verlassen, untersucht. Sogenannte akzessorische Minerale, wie z. B. Apatit, sind in Gesteinen nur in geringen Anteilen vorhanden, können aber Spurenelemente sehr hoch anreichern. Wenn sich bestimmte Spurenelemente stark in akzessorischen Phasen anreichern, kann dies umgekehrt zu Verarmungen dieser Elemente in den freigesetzten Fluiden führen. In dieser Studie wird die Verteilung von Spurenelementen zwischen Apatit und anderen Mineralen untersucht, die sich innerhalb eines Sediments während der Subduktion gebildet haben. Die Ergebnisse zeigen, dass geologisch realistische Mengen von Apatit die Spurenelementzusammensetzungen von Subduktionszonenfluiden nicht signifikant beeinflussen können. Die Zusammensetzung der Fluide wird die stattdessen durch die normalen gesteinsbildenden Minerale bestimmt. Die letzte Studie in diesem Abschnitt untersucht die Rolle des Salzgehalts (NaCl) der Fluide in Subduktionszonen auf die Menge an Oxiden, die darin gelöst werden können. Zu diesem Zweck wurden Fluide mit unterschiedlichem Salzgehalt, die sich im Gleichgewicht mit Material basaltischer Zusammensetzung befanden, unter Bedingungen der Subduktionszone in einer Schicht aus Diamantpulver eingefangen und anschließend mittels induktiv gekoppelter Massenspektrometrie in Kombination mit Laserablation (LA-ICPMS) analysiert. Diese sog. Diamantfallenexperimente zeigen, dass eine Erhöhung des Chlorgehalts der Fluide auf

6 Gew.-% den Gesamtgehalt an gelösten Stoffen in der Flüssigkeit auf etwa 40 % verdoppelt. Es wurde weiterhin festgestellt, dass dieser Effekt des Salzgehalts mit zunehmendem Druck abnimmt. Die Ergebnisse deuten darauf hin, dass der Salzgehalt des Fluids mindestens genauso wichtig ist wie Druck und Temperatur, wenn es darum geht, den Gehalt an gelösten Stoffen und die Zusammensetzung der Fluide zu bestimmen, die aus der subduzierenden ozeanischen Kruste austreten und für die Metasomatisierung des darüber liegenden Mantels unter den Vulkanbögen der Subduktionszone verantwortlich sind.

3.3 Mineralogie, Kristallchemie und Phasentransformationen

Die Beschaffenheit von Mineralien und ihre Stabilität beeinflussen die Eigenschaften und Prozesse im tiefen Erdinneren erheblich. Alle Beiträge in diesem Abschnitt erforschen Phasenumwandlungen und/oder die Kristallchemie von Mineralen bei relevanten Druck-Temperatur-Zusammensetzungsbedingungen. Die ersten vier Beiträge berichten über neue Entdeckungen an $MgSiO_3$-Silikat-Polymorphen, AB_2O_4-Oxiden und A_2CO_4-Tetracarbonaten unter Verwendung verschiedener Hochdruckapparaturen in Verbindung mit *in situ*-Röntgenbeugung und Raman-Spektroskopie. Eine starke negative Temperaturabhängigkeit des Akimotoit-Bridgmanit-Übergangs kann die Stagnation von subduzierten kalten Platten oberhalb der 660-km-seismischen Diskontinuität verursachen und eine signifikante Absenkung der 660-km-seismischen Diskontinuität bis auf 750 km Tiefe erklären, die unterhalb von Subduktionszonen beobachtet wurde. Hochdrucküberg̈ange in $MgAl_2O_4$ sind wichtig für die Identifizierung und das Verständnis potentieller Wirtsminerale von Aluminium im Erdmantel. Die Phase vom $CaTi_2O_4$-Typ kann in basaltischen und kontinentalen Krustenzusammensetzungen über einen weiten Druckbereich stabil sein und die Entdeckung einer neuen $MgFe_2O_4$-Hochdruckphase liefert neue Erkenntnisse über den Redoxzustand des Erdmantels. Die Untersuchung von Calcium- (Ca_2CO_4) und Strontium- (Sr_2CO_4) Tetracarbonaten bei hohem Druck zeigt, dass Tetracarbonat-Polymorphe im System CaO-CO_2 unter den Bedingungen der Übergangszone der Erde und des obersten unteren Mantels stabil sein können.

Die nächsten vier Beiträge erforschen Substitutionsmechanismen von flüchtigen Spezies, die die Natur der geochemischen Kreisläufe beeinflussen. Neue Messungen an wasserhaltigem Forsterit zeigen, dass Protonen vorwiegend an Si- und nicht, wie bisher angenommen, an Mg-Kristallgitterplätzen substituieren. Dieser Substitutionsmechanismus wird mit Hilfe der Einkristall-Neutronenbeugung auch für Fe-haltigen Olivin nachgewiesen. Eisen ist das am häufigsten vorkommende Übergangsmetall im Erdmantel und liegt hauptsächlich als Fe^{2+} oder Fe^{3+} vor, sodass die Chemie der Eisendefekte die Kreisläufe flüchtiger Elemente beeinflussen kann. Neue Messungen von eisenhaltigem Bridgmanit zeigen, dass die Sauerstoffleerstellen mit zunehmendem Druck abnehmen. Der Einbau von Wasserstoff in Eisensulfid ist ein möglicher Mechanismus zur Entfernung von Wasserstoff während der sogenannten "Hadean Matte"-Periode der Erdgeschichte, in der sich der Erdkern aus einem frühen Magmaozean gebildet hat.

Ergebnisse von *in situ* Neutronenbeugungsexperimenten an Eisensulfid liefern in diesem Zusammenhang ein mögliches Szenario zur Erklärung des schnellen Anstiegs des Mantel-Oxidationszustandes nach der Kernbildung.

Die letzten fünf Beiträge untersuchen Materialien unter verschiedensten Bedingungen, von extremem Hochdruck bis hin zu Umgebungen an der sehr frühen Erdoberfläche. Innovative kernmagnetische Resonanzmessungen in der Diamantstempelpresse zeigen einen Kernspin-Crossover in dichtem Wasserstoff, der für die Stabilisierung der Magnetosphären von Gas- und Eis-Riesenplaneten wichtig sein könnte. Dichtefunktionaltheorie kombiniert mit Hochdruck-Kernspinresonanz zeigt tiefgreifende Veränderungen in der Protonendynamik von Eis-VII oberhalb von 130 GPa. Einkristall-Röntgenbeugung zeigt einen Übergang vom Verwey-Typ in der neuartigen Eisenoxidphase Fe_5O_6, einem potentiellen Endglied der unteren Oxidphasen im unteren Mantel. Der grundlegende Unterschied in der Löslichkeit von Fe(II) und Fe(III) in wässrigen Lösungen liefert eine Methode für die Behandlung von mit Antimon kontaminiertem Grundwasser und neue Einblicke in Prozesse in frühen Ozeanen durch Studien von Bändereisenerzen.

3.4 Physikalische Eigenschaften von Mineralen

Geophysikalische Methoden zur Erkundung des tiefen Erdinneren wie z. B. die Seismologie sind auf die Kenntnis der physikalischen Eigenschaften von Mineralen, Gesteinen und Schmelzen angewiesen. Nur mit einer soliden Datenbasis dieser Eigenschaften lassen sich geophysikalische Daten wissenschaftlich sinnvoll interpretieren. Daher werden in der experimentellen Mineralphysik große Anstrengungen unternommen, um die physikalischen Eigenschaften von Geomaterialien unter den Temperatur- und Druckbedingungen der tiefen Erde zu bestimmen. Neun Beiträge dieses Kapitels zielen darauf ab, das elastische Verhalten von Geomaterialien experimentell zu bestimmen, um ihre Ergebnisse mit geophysikalischen Daten aus verschiedenen Regionen des Erdinneren in Beziehung zu setzen. Dabei werden hauptsächlich vier Versuchstechniken angewendet.

Die ersten vier Studien nutzen die Einkristall-Röntgenbeugung gekoppelt mit Synchrotronstrahlung, um die Kompressibilität von Materialien zu untersuchen, die eine wichtige Rolle im Verhalten des unteren Erdmantels und des inneren Erdkerns spielen können. Im ersten Beitrag wird berichtet, dass oberhalb von 40 GPa ein Spin-Paarungs-Übergang in einer Fe-haltigen Al-Phase D auftritt, einer wasserhaltigen Phase, die unter den Bedingungen des unteren Erdmantels stabil sein könnte, was wichtige Konsequenzen für den Wasserhaushalt der Erde hat. In den nächsten beiden Studien wird die Kompressibilität von Al- und Al/Fe-haltigen Bridgmaniten untersucht. Im zweiten Beitrag wurde die Auswirkung des unterschiedlichen Mechanismus der Al-Substitution in Bridgmanit auf dessen Kompressibilität untersucht. Vorläufige Ergebnisse deuten darauf hin, dass dieser Effekt trotz der unterschiedlichen molaren Volumina der beiden Bridgmanit-Endglied-Komponenten minimal

ist. Der dritte Beitrag berichtet über die strukturelle Variation und Kompressibilität eines extrem Fe/Al-reichen Bridgmanits und deutet darauf hin, dass eine solch große Menge an Fe^{3+} zu einer Si/Fe-Ordnung an der oktaedrischen Stelle führen kann, was eine Verringerung der Symmetrie der orthorhombischen Perowskitstruktur zur Folge hat. Der vierte Beitrag untersucht die Hochdruckphasen im Ni-C-System, um die mögliche Chemie des Erdkerns besser zu verstehen und präsentiert die Kompressibilität eines neuartigen Ni_3C-Materials.

Im fünften Beitrag wird der Einfluss kleiner Schmelzmengen auf das elastische Verhalten von Olivin-Polykristallen mit Hilfe von Ultraschall-Interferometrie untersucht, um bestimmte Zonen niedriger seismischer Geschwindigkeit im oberen Erdmantel zu interpretieren, die möglicherweise Regionen mit partiellem Schmelzen darstellen.

In den folgenden drei Studien wurde Einkristall-Brillouin-Spektroskopie gekoppelt mit Röntgenbeugung verwendet, um den vollen elastischen Tensor von anisotropen Mineralen zu bestimmen. Im sechsten Beitrag wurde der volle elastische Tensor von Antigorit bei verschiedenen Drücken bis zu 5,2 GPa bestimmt. Dabei zeigte sich eine deutliche Verringerung der Anisotropie, die hauptsächlich auf die Erhöhung des elastischen c_{33}-Koeffizienten zurückzuführen ist. Im siebten Beitrag wurden die elastischen Eigenschaften von Fe-haltigem -AlOOH über den Bereich seiner strukturelle Phasenumwandlung gemessen, die bei demselben Druck auftritt, bei dem eine Fehlordnung der Wasserstoffbrückenbindung beobachtet wurde. Kurz vor dem Übergang wird eine große Erweichung des Kompressionsmoduls beobachtet, während das Material nach der Umwandlung deutlich steifer wird. Messungen des elastischen Tensors von Bridgmanit bei Drücken des unteren Erdmantels wurden in dem achten Beitrag verwendet, um seismische Wellengeschwindigkeiten für verschiedene Mineral-Zusammensetzungen zu berechnen und mit seismischen Beobachtungen zu vergleichen. Ein Mineral-physikalisches Modell, das aus Bridgmanit, Ferroperiklas und Ca-Perowskit besteht, steht in guter Übereinstimmung mit den Scherwellengeschwindigkeiten aus seismischen 1D-Modellen, während die Kompressionswellengeschwindigkeiten um mehr als 1 % langsamer sind als aufgrund der seismischen Modelle erwartet wird. Dies deutet darauf hin, dass die Substitution von Fe und Al in Bridgmanit neu überdacht werden muss.

Im neunten Beitrag wurde die Brillouin-Spektroskopie mit einem CO_2-Laser-Heizsystem gekoppelt, um Brillouin-Spektren bei hohen Drücken und Temperaturen für transparente Einkristalle von Pyrop zu sammeln. So wurden Wellengeschwindigkeiten bei verschiedenen Drücken bis zu 1900 K gesammelt, die zur Eingrenzung der thermoelastischen Eigenschaften dieses Minerals verwendet werden können.

Schließlich wurden im letzten Beitrag Messungen der Wärmeleitfähigkeit von -(Al,Fe)OOH durchgeführt, die eine große Variation der Wärmeleitfähigkeit über den Eisen-Spin-Übergang bei 30-45 GPa und Raumtemperatur ergaben. Dies bedeutet, dass das Vorhandensein dieser wasserhaltigen Phase zu einer außergewöhnlich niedrigen Wärmeleitfähigkeit im untersten Mantel führen kann.

3.5 Fluide, Schmelzen und ihre Wechselwirkung mit Mineralen

Die ersten drei Beiträge in diesem Kapitel beschäftigen sich mit dem Verhalten von flüchtigen Bestandteilen in Subduktionszonen. Serpentin ist ein wasserhaltiges Mineral, das in der subduzierten Platte Wasser in große Tiefen transportieren kann. Die Dehydratation von Serpentin ist möglicherweise eine Hauptquelle von Fluiden in Subduktionszonen. Die Permeabilität von Serpentinit beeinflusst, wie sich dieses Fluid verteilt und wie es sich durch den Mantel bewegt. Der erste Beitrag beschreibt entsprechende Permeabilitäts-Messungen unter realistischen Druck- und Temperaturbedingungen. Die Daten zeigen, dass die Permeabilität bei der Entwässerung des Serpentins stark ansteigt, während gleichzeitig ihre Anisotropie verschwindet. Die bedeutet, dass die freigesetzten Fluide wahrscheinlich nicht lokal fokussiert werden, sondern sich durch das gesamte Gesteinsvolumen ausbreiten und daher sehr stark mit dem umgebenden Gestein wechselwirken. Neuere theoretische Studien haben Hinweise darauf geliefert, dass die Fluide in Subduktionszonen nicht nur aus einfachen anorganischen Molekülen wie H_2O und CO_2 bestehen, sondern möglicherweise auch organische Verbindungen wie Azetat unter hohem Druck und hoher Temperatur stabil sind. Diese Vorhersagen haben großes Aufsehen erregt und es wurde spekuliert, dass diese organischen Verbindungen beispielsweise auch eine Rolle bei der Entstehung von Diamanten spielen könnten. Direkte experimentelle Belege für die Stabilität dieser Moleküle unter den relevanten Bedingungen fehlten aber bisher weitgehend. Ein Beitrag in diesem Jahresbericht beschäftigt sich daher mit der Stabilität von Azetat in Wasser bei 5 GPa und 600 ˚C. Ein Teil der Experimente wurde in einer Piston-Cylinder-Apparatur mit Silberkapseln durchgeführt, teilweise wurde aber auch die Zusammensetzung der Fluide direkt *in situ* mit Hilfe von Raman-Spektroskopie in extern beheizten Diamantstempelzellen untersucht. Die Ergebnisse waren allerdings negativ. Man kann zwar beim Aufheizen des Acetats unter Druck sehr interessante chemische Reaktionen beobachten, aber bei 5 GPa und 600 ˚C, wo Acetat nach den theoretischen Vorhersagen stabil sein sollte, war keine Spur davon mehr vorhanden. Fluide spielen möglicherweise auch eine Rolle bei der Entstehung von Erdbeben in Subduktionszonen. Tiefe Erdbeben wurden manchmal zurückgeführt auf die schlagartige Umwandlung von metastabilem Olivin in Hochdruckphasen innerhalb der subduzierten Platte. Wasser im Olivin beschleunigt jedoch diese Umwandlung und es ist daher schwer verständlich, wie Olivin in einer Wasser-haltigen Platte überhaupt in einem metastabilen Zustand verbeiben sollte. Eine mögliche Lösung für diesen scheinbaren Widerspruch liefert der nächste Beitrag: Wenn der Olivin mit bestimmten wasserhaltigen Mineralen wie "Phase A" koexistiert, dann bevorzugt das Wasser diese Phasen so stark, dass der Olivin praktisch wasserfrei ist.

Flüssigkeitseinschlüsse liefern wohl die direktesten Hinweise auf die Zusammensetzung von Fluiden in Kruste und Mantel. Diese in Kristallen eingeschlossenen Tröpfchen von Flüssigkeiten und Gasen sind jedoch nicht immer leicht zu interpretieren. Eine gleichmäßige Verteilung der Einschlüsse in einem Kristall gilt normalerweise als Hinweis für einen "primären" Ursprung, d. h. für eine Bildung der Einschlüsse während dem Wachstum des Kristalls. Eine Studie in diesem Kapitel zeigt jedoch mit Hilfe von Kathodolumineszens-Bildern, dass dies nicht so ist. Synthetische Flüssigkeitseinschlüsse werden manchmal auch

benutzt, um in Hochdruckexperimenten Fluide einzuschließen und sie dann unter Normalbedingungen zu Untersuchen. Das nächste Projekt in diesem Kapitel benutzt diese Methode, um die kritische Kurve im System H_2O-H_2 bis 4.5 GPa zu untersuchen. Die Daten zeigen ein merkwürdiges Verhalten um 2.5 GPa, in einem Druckbereich wo auch frühere Untersuchungen bereits Hinweise auf ein anomales Verhalten von Wasser gefunden haben. Neben Wasser oder Wasserstoff ist auch Stickstoff eine flüchtige Komponente, die ständig zwischen dem Mantel und der Atmosphäre ausgetauscht wird. Vulkanische Aktivität ist der wichtigste Mechanismus für die Entgasung von Stickstoff aus dem Mantel. Die Effizienz der Entgasung hängt hier vor allem von den Mineral/Schmelze-Verteilungskoeffizienten von Stickstoff im Mantel ab. Der folgende Beitrag beschreibt die ersten Messungen des Verteilungskoeffizienten von Stickstoff zwischen basaltischer Schmelze, Olivin, Pyroxenen, Plagioklas und Granat. Die Daten zeigen, dass Stickstoff in den Mineralen sehr inkompatibel ist, wenn auch nicht ganz so stark wie Argon.

Die Viskosität von Silikatschmelzen kontrolliert den Eruptionsmechanismus von Vulkanen, aber auch andere Prozesse, wie etwa die Kinetik der Trennung von Kern und Mantel in der frühen Erdgeschichte. Drei Beiträge beleuchten verschiedene neue Aspekte der Viskosität von Silikatschmelzen. Neuere Studien haben gezeigt, dass sich bei vulkanischen Prozessen manchmal Nano-Partikel bilden. Der Einfluss dieser Partikel auf Viskositäten wird in einem laufenden Projekt untersucht. Ein neues, theoretisch fundiertes numerisches Modell erlaubt eine bessere Vorhersage der Viskosität wasserhaltiger Schmelzen bei unterschiedlichen Temperaturen. Neue technische Entwicklungen in der Multianvil-Technologie haben es schließlich ermöglicht, erstmals die Viskosität einer Peridotit-Schmelze bis zu den Drücken des unteren Mantels zu messen. Diese Daten sind wichtig für die Modellierung der Trennung von Metall und Silikat im Magmenozean in der frühen Erdgeschichte. Dieses Problem wird auch untersucht im letzten Beitrag dieses Kapitels, das sich speziell mit dem Einfluss des Nickels auf die Transporteigenschaften von flüssigem Eisen unter hohem Druck beschäftigt. *Ab initio*-Simulierungen zeigen, dass Nickel beispielsweise die Diffusion von Kohlenstoff in flüssigem Eisen verlangsamt, was die Effektivität der Anreicherung von Kohlenstoff im Kern verringert.

3.6 Rheologie und Metamorphose

Die Rheologie beschreibt quantitativ, wie sich Materialien als Reaktion auf nicht-hydrostatische Spannungen verformen und fließen, während die Metamorphose der Prozess ist, durch den sich die Mineralogie und Textur von Gesteinen an die Druck- und Temperaturänderungen im Erdinneren anpasst. Rheologie und Metamorphose sind eng miteinander verbunden und beide können ähnliche geologische Prozesse und Gesteinseigenschaften beeinflussen. Die Festkörperdiffusion kann beispielsweise das viskose Fließen von Gesteinen bei hohen Temperaturen kontrollieren und ist auch ein wichtiger steuernder Faktor bei der Metamorphose. Gesteinstexturen, wie z. B. die Korngröße und ihre Entwicklung mit der Zeit, sind sowohl für die Rheologie als auch für die Metamorphose wichtig.

Die experimentelle Untersuchung der Rheologie des tiefen Erdmantels ist wesentlich für das Verständnis der Mantelkonvektion und anderer geodynamischer Prozesse. Solche Studien sind jedoch schwierig, da sowohl die differentielle Spannung als auch die Verformungsrate als Funktion von Temperatur und Druck bestimmt werden müssen. Darüber hinaus sind die experimentellen Verformungsraten um Größenordnungen schneller als die Deformation im Erdmantel, was bedeutet, dass große Extrapolationen der Ergebnisse notwendig sind, deren Zuverlässigkeit oft unsicher ist. Eine indirekte Herangehensweise an dieses Problem ist die Untersuchung der Diffusionsraten in Mantelmineralen bei hohen Drücken und Temperaturen, da dieser Prozess für die Kontrolle der Rheologie wichtig ist. Die Korngrößenentwicklung bei hohen Temperaturen ist ebenfalls ein wichtiger Parameter, der die Rheologie beeinflussen kann, und seine Entwicklung mit der Zeit kann ebenfalls experimentell untersucht werden.

Der erste Beitrag stellt die Ergebnisse einer Studie zur Interdiffusion zwischen Al und Si+Mg in Majorit-Granat (ein wichtiges Mineral im Erdmantel im Tiefenbereich ~ 550-900 km) und Pyrop-Granat vor. Das Diffusionsexperiment wurde bei 18,5 GPa und 1750 °C für 300 Minuten an einem Fe-freien System durchgeführt und das Ausmaß der Diffusion wurde mittels Transmissionselektronenmikroskopie untersucht. Es wurde sowohl Korngrenzen- als auch Volumendiffusion beobachtet und das Ausmaß der Volumendiffusion ist ähnlich dem, das in einer früheren Studie von Fe-haltigem Majorit beobachtet wurde. Die extrem niedrige Diffusionsgeschwindigkeit ist in derselben Grössenordnung wie die Raten der Si- und Mg-Selbstdiffusion in Bridgmanit, dem am häufigsten vorkommenden Mineral im unteren Erdmantel.

Die Kinetik des Kornwachstums von polykristallinem Olivin bei hohem Druck ist das Thema des zweiten Beitrags. Die Geschwindigkeit des Kornwachstums wurde bei Drücken bis zu 12 GPa untersucht, im Gegensatz zu früheren Studien, die bei relativ niedrigen Drücken (bis zu 1,2 GPa) durchgeführt wurden. Es wird festgestellt, dass das Kornwachstum mit steigendem Druck deutlich langsamer wird. Dies hat Auswirkungen auf die Deformationsmechanismen und die Rheologie des oberen Mantels und kann bedeuten, dass ein Übergang vom Versetzungskriechen zum Diffusionskriechen in einer geringeren Tiefe stattfindet als bisher angenommen.

Der dritte und vierte Beitrag dieses Abschnitts befasst sich mit der geodynamischen Modellierung. Diese Methode erlaubt, eine Vielzahl von Prozessen in der Erde zu verstehen, einschließlich der Mantelkonvektion, Plattentektonik, Bildung von geologischen Störungen und tiefer Erdbeben. Der erste Beitrag untersucht die Ursachen des Abbrechens von subduzierten Platten, bei dem sich ein spezifisch schwerer Teil von der subduzierenden Lithosphäre löst und in den Mantel absinkt. Drei mögliche Mechanismen werden untersucht: strukturelle Schwächung durch Einschnürung, Materialschwächung durch Korngrößenreduktion unter Verwendung eines zweiphasigen Kornschädigungsmodells und thermische Schwächung durch Schererwärmung. Die Ergebnisse deuten darauf hin, dass die

Kornschädigung die anfängliche Ursache für die Ablösung der Platte ist, mit zunehmender Zeit aber die thermische Schwächung immer wichtiger wird.

Ozeanische Transformstörungen sind extrem ausgeprägte Verwerfungen, an denen die mittelozeanischen Rücken seitlich entlang der Störung versetzt werden. Der zweite Beitrag zur Geodynamik untersucht den Mechanismus, durch den solche Transformstörungen initiiert werden. Die Ergebnisse zeigen, dass die Korngrößenreduktion die Hauptursache ist und dass die Lebensdauer solcher Verwerfungen durch die Kinetik des Kornwachstums gesteuert wird.

Der letzte Beitrag dieses Kapitels befasst sich mit der Quantifizierung der Größe von Antiphasendomänen in Omphaziten aus Eklogiten. Solche Domänen bilden sich während der Metamorphose als Ergebnis der Kationenordnung. Die Größe von Antiphasendomänen hängt von der Maximaltemperatur, der Dauer der Metamorphose und der Abkühlungsrate ab und kann daher Informationen über die metamorphe Geschichte von Hochdruckgesteinen liefern. In der vorliegenden Studie wurde die Größenverteilung von Antiphasendomänen untersucht, was zeigt, dass die durchschnittliche Größe möglicherweise nicht der geeignetste Parameter ist, um solche Merkmale zu charakterisieren.

3.7 Materialwissenschaften

Forschung in Materialchemie und -physik am Bayerischen Geoinstitut profitiert von einer einzigartigen Kombination aus Synthesemöglichkeiten bei hohem Druck, der zunehmenden Möglichkeit, Proben unter Druck *in situ* zu untersuchen und Erfahrung in theoretischer Festkörperphysik. In diesem Jahresbericht stellen wir Forschungsergebnisse für Stickstoff und zu Nitriden, Karbiden sowie Hydriden auf der Basis von Übergangsmetallen vor. In den Beiträgen dieses Kapitels spielt die *in situ* Einkristall-Röntgenbeugung in der Diamantstempelzelle, die in den vergangenen Jahren – auch mit Hilfe von Wissenschaftlern des Bayerischen Geoinstituts – an verschiedenen Synchrotron-Anlagen entwickelt wurde, eine zentrale Rolle.

Feste Nitrid-Verbindungen – und das ihnen zugrunde liegende Element Stickstoff – sind von großem wissenschaftlichen Interesse, da die bei hohem Druck sehr anpassungsfähige N-N Bindung ein großes Potential als Material mit hoher Energiedichte hat, und Stickstoff-Verbindungen damit Kandidaten für neuartige Treib- und Explosivstoffe sind. Der erste Beitrag des Kapitels zeigt, dass Stickstoff bei einem Druck von mehr als 100 GPa die Struktur von schwarzem Phosphor annimmt. Dies was aufgrund systematischer Betrachtungen für die Elemente der Stickstoff-Gruppe bereits angenommen worden, der experimentelle Nachweis dafür wird aber erst hier geführt. Der zweiten Beitrag zeigt mit Hilfe der Kombination von Röntgenbeugung und Elektronenstruktur-Berechnungen die Variabilität von N_2 Anionen auf: Bei 50 GPa sind in Y_5N_{14} zwei Typen von N_2 Dimeren vorhanden, $[N{=}N]^{2-}$ und $[N{\equiv}N]^{3-}$, wobei im letzteren die N-N Bindungslänge signifikant länger ist.

Yttrium ist auch die Basis für das Hochdruckkarbid Y_4C_5, das im dritten Beitrag vorgestellt wird, wobei Karbide als Materialien mit hohem Schmelzpunkt und einer großen Härte von Interesse sind. Ähnlich zu Y_5N_{14} zeigt auch Y_4C_5, bei 44 GPa in der Diamantstempelzelle synthetisiert, eine ungewöhnliche Struktur. Hier tritt Kohlenstoff sowohl als C_2 Dimer und C_3 Trimer auf, und in beiden Komplexen fällt der C-C Abstand zwischen Werte für einfache und doppelte Kohlenstoffbindungen. Eine Analyse der Ladungsdichte, die mit Hilfe der Dichtefunktionaltheorie berechnet wurde, zeigt einen metallischen Zustand für Y_4C_5 und formale Ladungen für die Kohlenstoff-Gruppen von $[C_2]^{5-}$ und $[C_3]^{6-}$.

Zusätzlich zu Röntgenbeugung und Elektronenstruktur-Berechnungen nutzt der letzte Beitrag des Kapitels auch Proton-Kernspinresonanz-Spektroskopie (NMR), um die Natur und Umgebung von Wasserstoff in Eisen- und Kupferhydriden zu untersuchen. Metallisches FeH und Cu_2H zeigen über einen beschränkten Druckbereich eine Abweichung vom erwarteten freien-Elektronen-ähnlichen Verhalten, das mit Hilfe der berechneten Ladungsdichte mit der Bildung von elektronischen Wechselwirkungen auf dem Wasserstoffgitter verstanden werden kann, was auch zur metallischen Leitfähigkeit der Hydride beiträgt. Der Abstand zwischen Wasserstoffatomen, bei dem dieses Verhalten auftritt ist deutlich größer als zuvor angenommen wurde. Da Wasserstoff einen wichtigen Beitrag zur Hochtemperatur-Supraleitung in Metallhydriden bei hohem Druck spielt, erfordert diese Beobachtung eine weitere Untersuchung mit zusätzlichen experimentellen und theoretischen Methoden.

3.8 Methodische Entwicklungen

Die Entwicklung neuartiger experimenteller, analytischer und numerischer Techniken sind wissenschaftliche Herausforderungen, durch die unerwartete Ergebnisse erzielt werden können. Methodische Entwicklung erfolgten in diesem Jahr auf neun Gebieten, die im Folgenden zusammengefasst werden. Fünf Arbeiten beschäftigen sich mit der Vielstempel (Multi-Anvil)-Apparatur, eine mit der Kolben-Zylinder-Apparatur, eine mit der Diamantstempelpresse, eine mit numerischer Modellierung und eine mit NMR-Spektroskopie.

Ishii et al. berichten im ersten Abschnitt, dass der Druckbereich von Vielstempel-Pressen mit Karbid-Stempeln auf 52 GPa bei einer Temperatur von 2000 K erhöht werden konnte. Mit dieser Technik untersuchten sie Phasenbeziehungen in einem basaltischen System in Tiefen des Erdmantels bis zu 1300 km.

Mafische und ultramafische Schmelzen spielen bei verschiedenen geochemischen Prozessen im Erdmantel eine wichtige Rolle. Die Kenntnis der Schmelzeigenschaften ist für die Untersuchung der Mantelgeochemie extrem wichtig. Die nachträgliche Analyse von zu Glas abgeschreckten Schmelzen ermöglicht es, eine Vielzahl von Schmelzeigenschaften zu bestimmen. Jedoch sind ultramafische Schmelzen aufgrund der begrenzten Abkühlungsraten in Hochdruckapparaturen bei hohen Drücken nur schwer abzuschrecken. Bondar et al. haben

durch die Entwicklung einer Schnellabschrecktechnik die Abkühlrate von Vielstempelpressen um eine Größenordnung erhöht und weltweit zum ersten Mal erfolgreich wasserhaltige ultramafische Schmelzen zu Gläsern abgeschreckt.

Hohe Drücke sind in terrestrischen Planeten mit hohen Temperaturen verbunden, aber bei den planetaren Mänteln von Gasriesen und ihren eisigen Satelliten ist das nicht der Fall. Eine Entwicklung, die Hochdruck-Kryo-Experimente in der Vielstempelpresse ermöglicht, wird von Howard und Walte beschrieben. Dieses System ist bereits für Kryo-Experimente im Einsatz und soll in Zukunft für *in situ*-Experimente mit Neutronenstrahlung zur Untersuchung eisiger Sonnensystemkörper genutzt werden.

Die Kenntnis der rheologischen Eigenschaften ist für das Verständnis der Mantel-Dynamik unerlässlich. Die Vielstempelpresse mit sechs unabhängig verfahrbaren Stempeln ermöglicht die triaxiale Verformung von Mineral- und Gesteinsproben unter den Drücken des oberen Mantels. Die deviatorischen Spannungen in den Proben können mit Hilfe der Röntgenbeugungsanalyse unter Verwendung von Synchrotronstrahlung bestimmt werden, was aber am BGI vor Ort nicht möglich ist. Dolinschi und Frost entwickeln daher eine Technik zur Messung von Probenspannungen *in situ* unter Verwendung piezoelektrischer Kristalle. Der vierte Beitrag berichtet über ihre aktuellen Ergebnisse dieser In-situ-Spannungsmessung bei Raumtemperatur.

Die Messung von Ultraschallgeschwindigkeiten in Mantelmineralen zur Bestimmung ihrer Zustandsgleichungen ist eine wichtige Aufgabe in den experimentellen Geowissenschaften. Obwohl die Geschwindigkeiten von Mineralen als Funktion von Druck und Temperatur gemessen werden müssen, sind die Druckunsicherheiten bei Experimenten erheblich, da die Probendrücke anhand einer in separaten Experimenten ermittelten Kalibrierkurve abgeschätzt werden. Neri et al. haben versucht, den Probendruck durch Messung der Schallgeschwindigkeiten von Granat-Einkristallen als Standardmaterial zu bestimmen und berichten im fünften Beitrag über aktuelle Ergebnisse dieses Versuchs.

Die Kolben-Zylinder-Presse ist eine der meistgenutzten Hochdruckapparaturen. Der Mechanismus der einachsigen Kompression der Kolben-Zylinder-Apparatur erzeugt jedoch oft heterogene Proben-Temperatur-Felder aufgrund der Stauchung der Heizung. Um dieses Problem zu unterdrücken, wurde ein neuer Einsatz entwickelt, der hauptsächlich aus NaCl besteht. Audetat et al. untersuchten Temperaturverteilungen in verschiedenen Kolben-Zylinder-Experimenten mit NaCl-Druckmedien, indem sie die CaO- und TiO_2-Gehalte in Titanit-gesättigter Albit-Schmelze in den Probenkapseln kartierten.

Die Kernspinresonanzspektroskopie (NMR) ist eine leistungsfähige Methode zur Untersuchung der Spinzustände von Übergangsmetallen. Meier und seine Kollegen haben diese Technik an die Hochdruckumgebung in einer Diamantstempelpresse angewandt. Im letzten Jahr verfolgten sie die hochauflösende Spin-Entkopplungstechnik in der paramagnetischen Resonanz unter Verwendung von δ-(Al,Fe)OOH als Testprobe von Hochdruckmineralen.

Der letzte Beitrag betrifft die Entwicklung der numerischen Modellierung. Im Allgemeinen wurde das Deformationsregime der Plattentektonik durch numerische Simulationen nicht gut reproduziert. Marzotto et al. untersuchten die Auswirkungen der rechnerischer Gitterauflösung und einer Fließspannungsbegrenzung auf die Modellierung der Plattentektonik. Sie zeigen, dass hohe Gitterauflösungen notwendig sind, um die Lithosphärenstruktur realistisch darzustellen.

3. Research Projects

3.1 Earth and Planetary Structure and Dynamics

Both astronomical observations of protoplanetary discs and geochemical data for meteorites suggest that planet formation begins very early after star formation. Records of condensation in the solar system started ~ 4.57 billion years ago when refractory calcium-aluminium-rich inclusions (CAIs) formed, and therefore CAIs serve as the start of the chronology of solar system formation. Meteorite studies provide evidence that many planetesimals, the building blocks of planets, formed rapidly and differentiated into a core, mantle and crust shortly afterwards, before the end of formation of chondrules and thus chondrites. This early differentiation of meteorite parent bodies was powered by the decay of short-lived radioactive isotope ^{26}Al (half-life ~ 0.7 Myr). The mass-independent isotopic anomalies in meteorites have also revealed a fundamental dichotomy that existed in the solar protoplanetary disc. Non-carbonaceous (NC) and carbonaceous (CC) meteorite parent bodies formed within two distinct reservoirs, representing the inner and outer regions of the disc respectively. The NC meteorite parent bodies also appear to have generally accreted earlier (< 0.5-3 Myr after solar system formation) and to be more thermally metamorphosed than those of carbonaceous chondrite meteorites (~ 2 to 4 Myr) which are more commonly aqueously altered. For terrestrial planets, models based on Hf-W and Fe-Ni short-lived isotope systematics propose that Mars had reached 90 % of its final mass within 5 million years after CAIs. Earth experienced a more protracted accretion history lasting up to 100 Myrs with the Moon-forming event, known as the giant impact, delivering about 10 % of its current mass. After core formation ceased, the late accretion occurred over 100s of Myrs, delivering another ~ 0.5 % of Earth's mass. The planetary materials added after core formation were critical sources of siderophile and volatile elements to the silicate Earth.

The first contribution in this section describes a coupled numerical approach where disk formation models and planetesimal thermal evolution models are used to study the early evolution of solar system bodies. The results indicate that migration of the water ice line, where temperatures are sufficiently low in the protoplanetary disk and solid water ice can form, causes two distinct bursts of planetesimal formation separated in space and time. These two distinct reservoirs in the inner and the outer solar system evolve in two modes due to different initial abundances of ^{26}Al. The results are in agreement with accretion chronology from NC and CC meteorites, water content and mass divergence of inner and outer Solar System.

The meteorite sampling of differentiated parent bodies among carbonaceous chondrites is relatively rare compared to NC meteorites, and the transition from primitive to differentiated bodies is not observed in CC meteorites. The study by Ma and collaborators describes a new and earliest group of primitive achondrites, with the proposed name of Tafassites, which originate from the carbonaceous region. They use mineralogical, geochemical and chronological records to constrain the formation conditions of their parent body. They show that the Tafassite parent body accreted before CR-related differentiated achondrites and CR1-

3 chondrites formed. Tafassites therefore indicate that rocky parent bodies accreted rapidly and successively even in the outer solar system where lower dust density and longer orbital periods should challenge such fast accretion timescales. These results also imply that limited radial mixing also occurred throughout that period within this region.

The terrestrial planets of the inner solar system are likely the result of the accumulation of numerous smaller primitive as well as differentiated bodies. To first approximation, the chemical composition of the bulk Earth bears great similarities to chondritic meteorites. However, Earth shows a much stronger depletion of the moderate to highly volatile elements compared to chondrites. In addition, mixing trends of mass-independent isotope anomalies reveal that the Earth is most enriched in s-process isotopes compared to all other bulk solar system materials. Mezger and collaborators show that it is currently not possible to fully define and quantify the different chemical and isotopic materials that formed the Earth. A major component seems to be missing in the extant collections of extra-terrestrial samples which may be sourced in the inner solar system. So far spacecraft missions succeeded in returning planetary samples from the Moon and asteroids, and sample returns from Mars and its moon Phobos are planned. Additionally, samples from Venus and Mercury, although very challenging to acquire, would be of great interest and importance in order to constrain the accretion of the terrestrial planets.

Earth's accretion is a continuous process. About 100 metric tons of materials are added every single day to Earth, mostly as dust. But larger objects regularly cross Earth's path. Camera and weather radar station networks help to detect fireball events and narrow down potential meteorite fall locations. It is even better to find and preserve them when a meteorite lands on ice like the Hamburg meteorite, an H4 ordinary chondrite, which fell in Michigan on 16 January 2018. A consortium study led by Heck extensively studied three stones recovered only days after the fall event. The most surprising finding was that the meteorite still contained ~ 2,600 different organic compounds beside its thermal metamorphic history at up to 720 K for about 25 Ma (constrained by Pb-Pb ages of Ca-phosphates) after its accretion. Results show that the 40-60 cm meteoroid was ejected from its parent asteroid about 12 Ma ago without affecting its earliest records of thermal evolution.

As we try to constrain the formation of the Earth, the mineralogical stratification of Earth's upper and lower mantle has remained a subject of debate. This question is critical for understanding Earth's building blocks and in order to interpret geophysical and geochemical data. While enstatite meteorites are the closest match to Earth's composition for many isotopic systems, their bulk major elemental budget is problematic when compared to the upper mantle composition as constrained by peridotites. Better constraints on the Mg/Si of the lower mantle can provide new clues regarding a potential deep Si-rich reservoir other than the Earth's core. Based on acoustic velocity measurements of bridgmanite, Machino and collaborators deduced a possible mineralogy for the lower mantle with a distinctive Si-enriched composition with Mg/Si = 1.14 relative to the upper mantle (Mg/Si=1.25). These results imply that 4.5 billion years of mantle convection was unable to homogenize Earth's whole mantle.

In modern Earth, slabs transport water into Earth's interior. Marzotto and colleagues combine experiments on ringwoodite thermal conductivity and 1D numerical models of slab subduction. The experiments show that incorporation of water reduces thermal conductivity of ringwoodite, the main constituent of the lowermost mantle transition zone (520-670 km depth), by up to 40 %. The numerical models demonstrate that under these circumstances the presence of hydrous ringwoodite in a subducting slab can significantly delay the decomposition of dense hydrous magnesium silicates present in a slab. This way it becomes more likely that these hydrous phases can reach Earth's lower mantle.

a. *Earliest isotopic and chemical bifurcation of planetary building blocks (G.J. Golabek, T. Lichtenberg/Oxford and J. Drążkowska/Munich; M. Schönbächler and T. Hands/Zurich)*

Recent astronomical and geochemical evidence point to early spatial and temporal fragmentation of the planet formation process, whose physical origins remain disputed. Here we use a coupled numerical model to investigate the influence of the build-up of the solar protoplanetary disk on the timing and internal evolution of forming protoplanets. We find that the orbital drift of the water iceline can generate two temporally and spatially distinct bursts of planetesimal formation. These sample different source regions of interstellar materials and experience limited intermixture. Driven by internal radiogenic heating, these planetary reservoirs compositionally evolve in two modes and based on this recover accretion chronology, thermochemical pattern, and mass divergence of inner and outer Solar System. Our numerical experiments suggest that the earliest interplay between disk physics and geophysical evolution of accreting planetesimals initiated the present-day observed chemical and isotopic dichotomy of the Solar System planets.

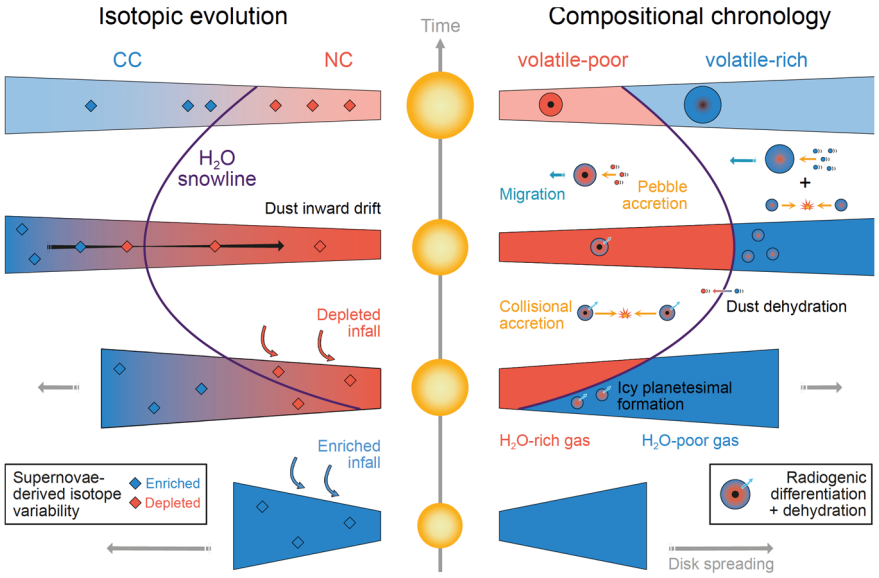

Fig. 3.1-1: Schematic illustration of early Solar System accretion chronology based on numerical experiments. Isotope variability (left) across the disk due to varying composition of infall material is retained by the traffic-jam of inward-drifting dust grains at the water iceline. The formation of two distinct planetesimal populations initiates divergent evolutionary pathways of inner and outer Solar System (right) due to the combined effects of internal radiogenic heating and secular variation of the dominant mode of planetary growth.

b. *Tafassites, a new group of carbonaceous chondrites and primitive achondrites (N. Ma and A. Bouvier, in collaboration with M. Trieloff, W. Schwarz and T. Ludwig/Heidelberg)*

Several equilibrated chondrite and achondrite meteorites (such as the ungrouped primitive achondrite Tafassasset) have been recently recovered in the vast Saharan desert. They have been linked to the altered CR1-3 chondrites based on their similar mass-independent anomalies in ^{17}O and ^{54}Cr isotopes. Four Tafassasset-like meteorites grouped as CR6 or CR7 and Tafassasset were examined for their mineralogy and textures, and phosphate trace element compositions and Pb-Pb ages. We found that Tafassasset-like meteorites should form a new carbonaceous chondrite to primitive achondrite class to which we provisionally suggest the name of Tafassites.

Tafassite meteorites are characterised by: 1) a highly equilibrated texture ranging from porphyritic (T6 chondrite) to poikilitic/protogranular T7 primitive achondrite; 2) mineralogy comprised of homogeneous FeO-rich olivine (Fa_{27-38}), Ca-poor pyroxene (Fs_{22-30}), minor clinopyroxene (as exsolution lamellae when T_{peak} > 1080 °C), intermediate plagioclase ($An_{44-52}Ab_{46-53}Qr_{1-3}$, heterogeneous when disturbed by silicate partial melting) abundant Fe-Ni metal, troilite, Al-rich chromite (~ $Mg_{0.2}Fe_{0.8}Al_{0.4}Cr_{1.5}Ti_{0.1}O_4$) and trace merrillite; 3) oxygen isotopic signature broadly similar to CR1-3 chondrites; 4) ancient retrograde metamorphic age obtained by Pb-Pb phosphate dating between 4549 ± 16 Ma to 4561 ± 6 Ma 2σ (closure temperature 720± 50 K for grain 25-65 μm and assuming a cooling rate of 10K/My); 5) nucleosynthetic anomalies (*i.e.*, ^{54}Cr, ^{17}O) in close similarity to carbonaceous chondrites.

These characteristics indicate a new meteorite group that probably derives from one to potentially several common parent bodies which accreted early in regions further out than ordinary and enstatite chondrites within the protoplanetary disc. They subsequently experienced extreme thermal metamorphism that span the chondrite-(primitive achondrite) transition. Their thermal history is similar to other groups of primitive achondrites (*e.g.*, acapulcoites, lodranites, winonaites) with an early accretion (T_{acc} 1.0 ± 0.2 My) of a small (< 25 km in radius) parent body followed by commonly supersolidus annealing (T_{peak} up to 1800 K) and fast cooling (300-400 K/My in the 1200-700 K range).

Tafassites probably originated from a parent body different from the CR1-3 chondrites based on incompatible bulk compositions, lack of continuous metamorphic sequence (*e.g.*, absence of petrographic types 4-5), fundamentally different accretion and thermal histories (T_{acc} =1.0 ± 0.2 Myr for Tafassites vs. T_{acc} =3.5± 0.5 Myr for CR chondrites based on chondrule formation ages, extreme thermal metamorphism vs. dominant aqueous alteration) (Fig. 3.1-2). The similarity in oxygen isotope and nucleosynthetic anomalies between the two groups should rather reflect the similar region of accretion within the protoplanetary disk but with a time gap of ~ 2.5 Myr between the formation of the parent bodies of the two meteorite groups. Such rapid accretion of carbonaceous materials in the outer regions of the protoplanetary disk where orbital periods are much longer has major implications for understanding the onset of planetary accretion.

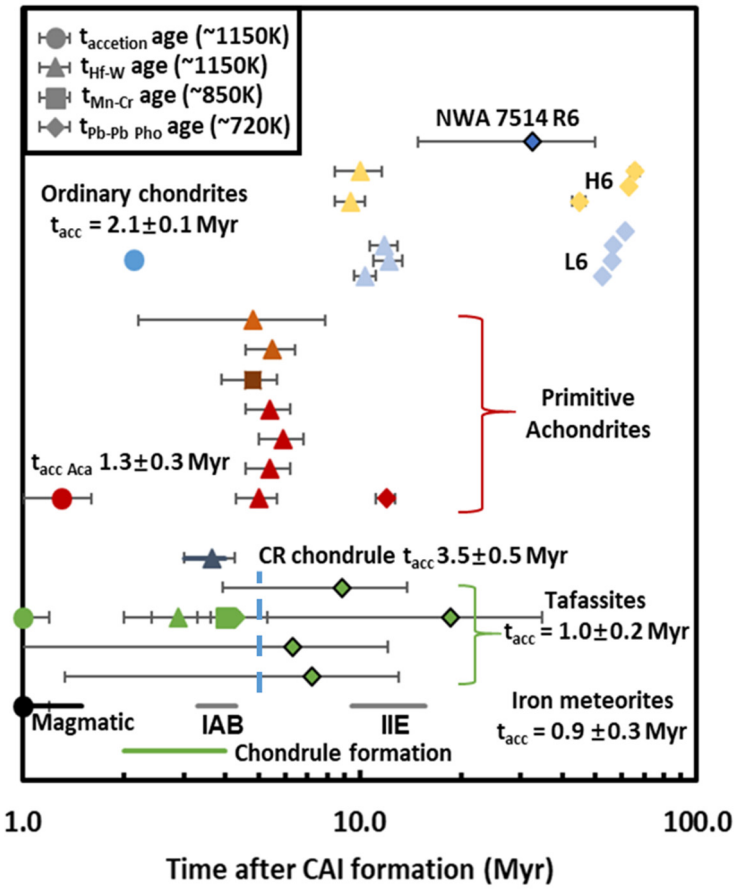

Fig. 3.1-2: Pb-Pb phosphate ages of Tafassites (green diamonds, this work) and R6 chondrite (blue diamond, this work) obtained by SIMS measurements compared with literature data obtained using Al-Mg ages for CR chondrules and using other radiometric methods (Pb-Pb, Mn-Cr or Hf-W) with different closure temperatures (indicated in the inset) based on mineral separation of silicate, chromite and metal phases for other groups of meteorites. Error bars are 2σ.

c. *Accretion of the Earth-missing components? (K. Mezger/Bern, M. Schönbächler/Zürich and A. Bouvier)*

Primitive meteorites preserve the chemical and isotopic composition of the first aggregates that formed from dust and gas in the solar nebula during the earliest stages of solar system evolution. Gradual increase in the size of solid bodies from dust to aggregates and then to planetesimals finally led to the formation of planets within a few to tens of million years after the start of condensation. Thus, the rocky planets of the inner solar system are likely the result of the accumulation of numerous smaller primitive as well as differentiated bodies.

The chemically most primitive known meteorites are chondrites and they consist mostly of metal and silicates. Chondritic meteorites are derived from distinct primitive planetary bodies that experienced only limited element fractionation during formation and subsequent differentiation. Different chondrite classes show distinct chemical and isotopic characteristics, which may reflect heterogeneities in the solar nebula and the slightly different pathways of their formation. To a first approximation the chemical composition of the bulk Earth bears great similarities to primitive meteorites. However, for some elements there are striking and significant differences. The Earth shows a much stronger depletion of the moderate to highly volatile elements compared to chondrites. In addition, mixing trends of specific isotopes reveal that the Earth is most enriched in s-process isotopes compared to all other analysed bulk solar system materials.

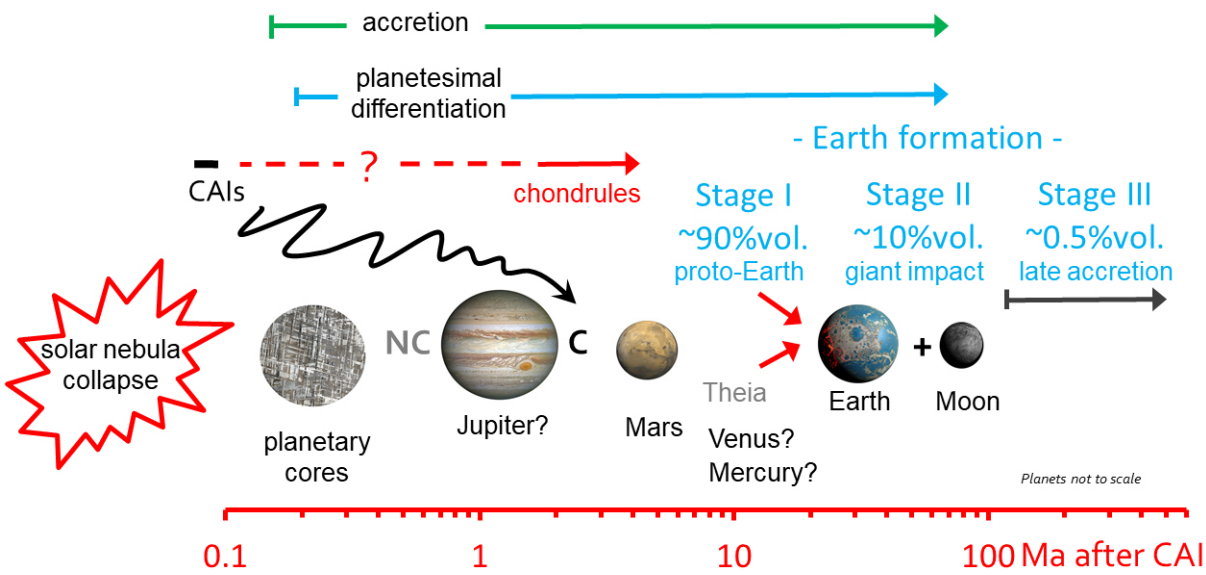

Fig. 3.1-3: Summary of timescales for the accretion and differentiation of planetary materials and their connection to Earth's formation (split here into 3 main stages). The isolation of non-carbonaceous (NC) and carbonaceous (C) chondrite reservoirs with distinct isotopic signatures over 2-4 Ma has been linked to the formation of Jupiter within 1-2 Ma after CAIs.

It is currently not possible to fully define and quantify the different chemical and isotopic materials that formed the Earth, because a major component seems missing in the extant collections of extra-terrestrial samples. Variations in nucleosynthetic isotope compositions as well as the strong depletion of moderately and strongly volatile elements points towards a source in the inner solar system for this missing material. It is conceivable that Venus and Mercury contain a much larger fraction of this missing component. Thus, for a complete reconstruction of the conditions that led to the formation of the inner solar system planets (Mercury to Mars) samples from the inner planets Venus and Mercury are of great interest and importance and should be sought as potential targets for future sample return missions. High precision chemical and isotopic analyses in the laboratory of rocky material from inner solar system bodies could complete the knowledge on the chemical, isotopic and mineralogical make-up of the solar nebula just prior to planet formation and enhance our understanding of the evolution of the solar nebula in general and the formation of the rocky planets in particular.

d. *The fall, recovery, classification, and initial characterization of the Hamburg, Michigan H4 chondrite (P.R. Heck and J. Greer/Chicago, A. Bouvier, and 27 co-authors (Heck* et al. *Meteoritics and Planetary Science 2020)*

A fireball was observed in several United States Midwest states and in Ontario, Canada and was tracked on the Nasa's weather radar as the meteoroid flew across the sky on the evening of 16 January 2018. It struck near Hamburg, Michigan with 1 kg of fragments recovered by public and professional hunters onto the frozen surfaces of the Strawberry and Bass lakes within days

after the fall. The meteor also produced an atmospheric shockwave equivalent to a magnitude 2.0 earthquake. Three of the meteorite pieces were donated to the Field museum for our consortium including 30 international researchers from the United States, Germany, Canada, and China. These fragments of Hamburg were found onto the frozen surface of Strawberry Lake within 3 days after the fall and showed minimal signs of terrestrial weathering or contamination.

Petrology, mineral chemistry, trace element and organic chemistry, and O and Cr isotopic compositions are characteristic of H4 chondrites. Cosmic ray exposure ages based on cosmogenic ^{3}He, ^{21}Ne, and ^{38}Ar are about 12 Ma, and roughly agree with each other. Noble gas data as well as the cosmogenic ^{10}Be concentration point to a small 40–60 cm diameter meteoroid. Microanalyses of phosphates using LA-qICPMS give an average Pb-Pb age of 4549 ± 36 Ma. This is in good agreement with the average SIMS Pb-Pb phosphate age of 4535.3 ± 9.5 Ma and U-Pb Concordia age of 4535 ± 10 Ma. The weighted average age of 4541.6 ± 9.5 Ma reflects the protracted metamorphic history of the H chondrite parent body after its accretion in the inner solar system. A similar ^{40}Ar-^{39}Ar age of 4532 ± 24 Ma indicates that no major impact or thermal event occurred later in its evolutionary history.

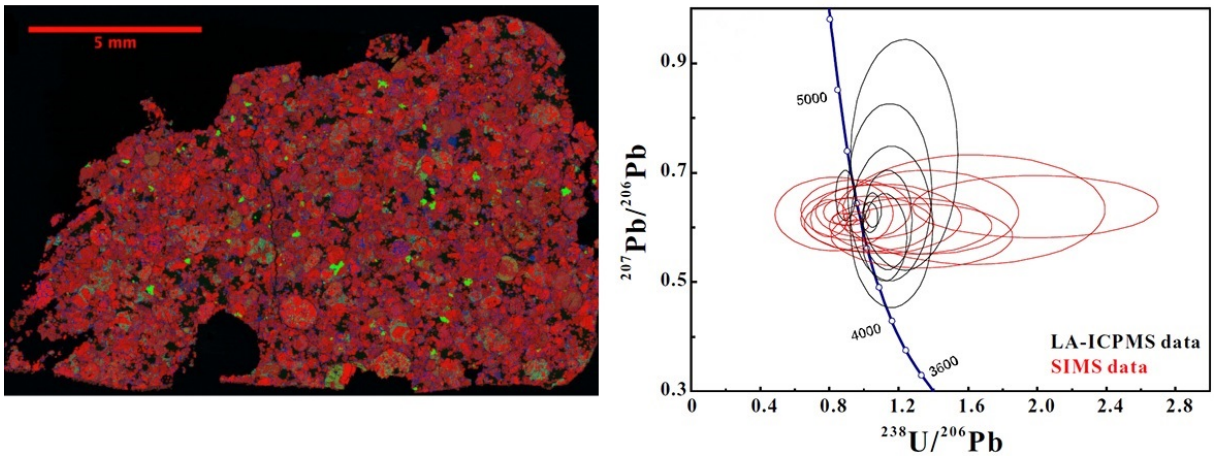

Fig. 3.1-4: Left: Composite RGB EDS map of the Hamburg ordinary chondrite. Red = Mg; green = Ca; blue; Al. Right: Comparison of the SIMS U-Pb data (in red) with those of LA-ICP-MS data obtained in Ca-phosphates (in black) in a Tera–Wasserburg diagram providing a weighted average Pb-Pb age of 4541.6 ± 9.5 Ma. Figures from Heck *et al.* (2020).

The meteorite is an H4 chondrite is a relatively rare subtype of a class of meteorites common in collections. The most surprising finding was that the meteorite still contained 2,600 different organic compounds beside its thermal metamorphic history at up to 720K for about 25 Ma after its accretion. It was ejected from its parent asteroid without affecting its earliest records of thermal evolution. There are only 10 to 15 meteorite fall events with recovered fragments every year. In 2020, two new carbonaceous chondrites groups have been identified and promise exciting future research and discoveries.

e. *Experimental evidence for silica-enriched Earth's lower mantle with ferrous iron dominant bridgmanite (I. Mashino and M. Murakami/Zurich, N. Miyajima and S. Petitgirard/Zurich)*

Identification of the chemical compositions of the Earth's upper and lower mantle provides critical implications for the geochemical, geophysical, seismological and cosmochemical models of the Earth. While the Mg/Si ratio of the upper mantle has been constrained at approximately ~ 1.25 based on geochemical and petrological observations, the Mg/Si ratio of the lower mantle still remains unknown because of a lack of direct observations and conclusive experimental results. To uncover these issues, we have conducted sound velocity measurement of iron-bearing bridgmanite (Brd) in a diamond anvil cell up to 124 GPa using Brillouin scattering spectroscopy.

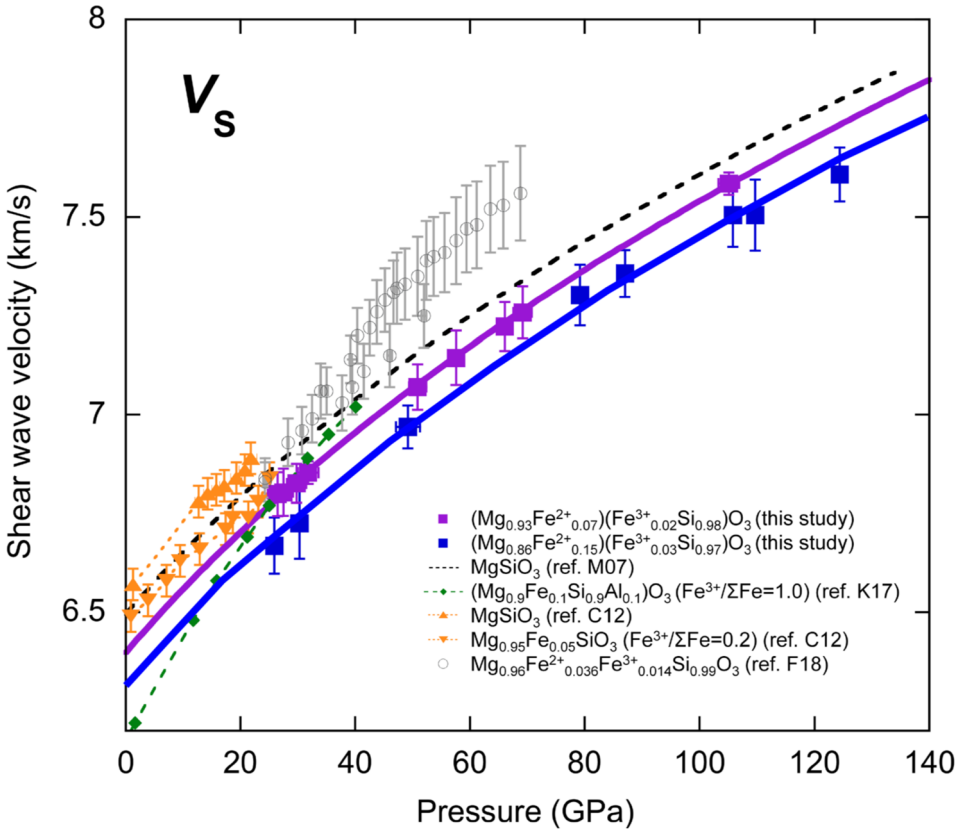

Fig. 3.1.5: Shear wave velocity profiles of Brd as a function of pressure at 300 K. Blue and purple squares show the shear wave velocities of $(Mg_{0.86}Fe^{2+}_{0.15})(Fe^{3+}_{0.03}Si_{0.97})O_3$ and $(Mg_{0.93}Fe^{2+}_{0.07})(Fe^{3+}_{0.02}Si_{0.98})O_3$ Brd, respectively. Third-order Eulerian finite strain fits are shown by solid lines. Black dotted lines show the shear wave velocity profiles of $MgSiO_3$ from M07 (Murakami *et al.*, Earth Planet. Sci. Lett., 256:47, 2007) by Brillouin measurements. Orange upward and downward-pointing triangles show the shear wave velocity profiles of $MgSiO_3$ and $Mg_{0.95}Fe^{2+}_{0.04}Fe^{3+}_{0.01}SiO_3$ Brd from C12 (Chantel *et al.*, Geophys. Res. Lett., 39:2, 2012) by ultrasonic measurements, green diamonds shows that of $(Mg_{0.9}Fe_{0.1}Si_{0.9}Al_{0.1})O_3$ Brd from K17 (Kurnosov *et al.*, Nature 543:543, 2017) by Brillouin scattering measurements, and grey circles shows that of $Mg_{0.96}Fe^{2+}_{0.036}Fe^{3+}_{0.014}Si_{0.99}O_3$ Brd from F18 (Fu *et al.*, Geophys. Res. Lett., 45:4725, 2018) by Brillouin scattering measurements, respectively.

In this study, we obtained the acoustic velocities for two different Fe-Brd compositions with $(Mg_{0.93}Fe^{2+}_{0.07})(Fe^{3+}_{0.02}Si_{0.98})O_3$ and $(Mg_{0.86}Fe^{2+}_{0.15})(Fe^{3+}_{0.03}Si_{0.97})O_3$ from 25.9 GPa to 124.4 GPa at ambient temperature conditions (Fig. 3.1.5). In the model, we assume a simplified lower mantle lithology with a two-phase mixture of $(Mg_{0.93}Fe^{2+}_{0.07})(Fe^{3+}_{0.02}Si_{0.98})O_3$ Brd measured in this study and $(Mg_{0.79}Fe_{0.21})O_3$ Fp from previous experimental study (Murakami *et al.*, Nature, 485:90, 2012). We compared the calculated V_S profiles with one-dimensional global seismic model of PREM. The latter is best fitted by a mixture of 88 % Brd and 12 % Fp by volume for the T-K geotherm (Katsura *et al.*, Phys. Earth Planet. Inter., 183:212, 2010), and 92 % Brd and 8 % Fp by volume for the O-A geotherm (Anderson, Philos. Trans. Royal Soc. A, 306:21, 1982) (Fig. 3.1.6). Our lower mantle model shows a distinctive Si-enriched composition with Mg/Si of 1.14 relative to the upper mantle (Mg/Si=1.25), which implies that the mantle convection has been inefficient enough to chemically homogenize the Earth's whole mantle.

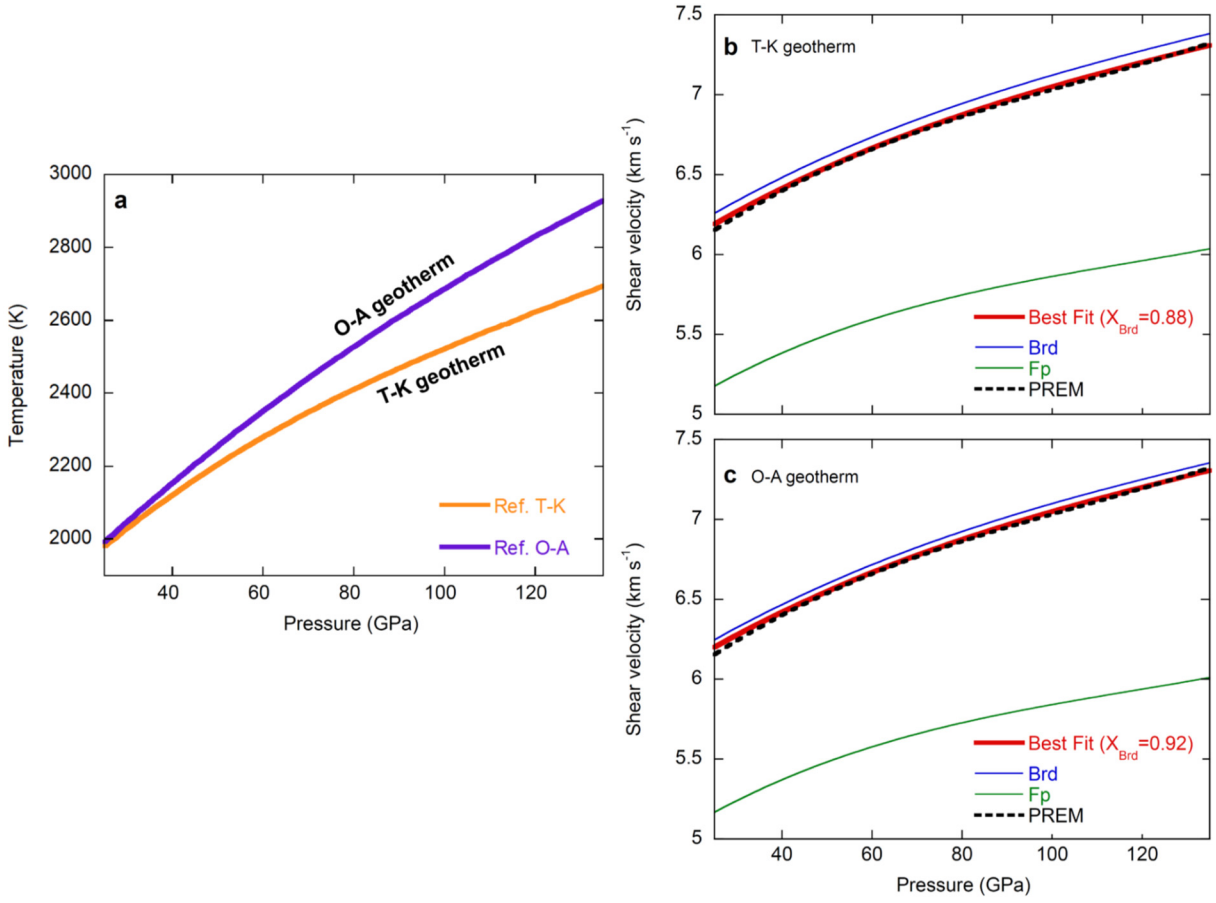

Fig. 3.1-6: Lower-mantle geotherms and calculated shear-wave velocity profiles. a, Representative lower-mantle geotherms for T-K (Katsura *et al.*, Phys. Earth Planet. Inter., 183:212, 2010) and O-A (Anderson, Philos. Trans. Royal Soc. A, 306:21, 1982). b and c, Calculated shear wave velocity profiles for T-K (b) and O-A (c). Calculated shear wave velocity profiles of Fe-Brd (blue lines), Fp (green lines) and PREM (dashed black lines). The best-fit models to PREM are shown as red curves. The uncertainties fall in the line thicknesses, which derived from the uncertainties of the shear strain derivative of the Grüneisen parameter η_{S0}.

f. *Effect of water on lattice thermal conductivity of ringwoodite and its implications for the thermal evolution of descending slabs (E. Marzotto, W.-P. Hsieh/Taipei, T. Ishii, K.-H. Chao/Hawaii, G.J. Golabek, M. Thielmann and E. Ohtani/Sendai)*

Lattice thermal conductivity Λ, is the physical parameter that controls heat transfer through solids. In minerals, heat is transported by phonon vibration. Changes in the lattice structure due to different P-T conditions, and the presence of impurities, alters the phonon mean-free-path. Is thus fundamental to constrain the effect of these parameters on Λ, in order to study the thermal evolution of geological bodies. In the present work, we measured the effect of water C_{H2O} and pressure P on ringwoodite thermal conductivity by combining DAC with Time-Domain Thermo-Reflectance (TDTR). Ringwoodite is the olivine high-pressure polymorph which is stable in the lower Mantle Transition Zone (520-660 km). It is believed that it represents up to 80 vol. % of the harzburgitic slab, and it can potentially host 1.5-2 wt. % water.

Ringwoodite samples with increasing water content were synthesized by performing multianvil experiments with a 4/10 assembly. Starting materials were San Carlos olivine powder and 3-10 wt. % distilled water. High quality samples were selected through XRD, chemical composition was determined with EMPA (~ 8.5 wt. % FeO), and unpolarized FTIR was employed to measure the water concentration of the synthesized batches (0.11, 0.47, 1.73 wt. % H_2O).

For TDTR measurements, each sample was coated with ~ 90 nm thick Al film as a thermal transducer. Crystals were loaded into a DAC, along with a ruby sphere for pressure determination. We employed 400 μm Ø cullet size diamond, a Re gasket, and silicone oil as the pressure medium. Measurements were performed at room temperature and high pressures up to 25 GPa (~700 km). The incorporation of 1.73 wt. % water in ringwoodite results in ~ 40 % drop of Λ, with respect to the 0.11 wt. % sample. The presence of H_2O in ringwoodite potentially provides a mechanism to maintain a cold slab core.

To test this hypothesis, we studied the thermal evolution of a descending slab by means of 1D numerical modeling. We assumed a slab entirely made by ringwoodite progressively heated by the warm ambient mantle. In the upper part of the slab we prescribed the presence of an hydrous layer. The parameterized equation derived from our measurements allowed us to calculate Λ for different P and C_{H2O}. Heat diffusion was modeled by solving the Fourier Law with the Finite Difference method. We compared the temperature evolution of an hydrous slab with the one of a completely dry reference case. A total of 240 simulations were performed in this study, by varying hydrous layer thickness (5-40 km) and ringwoodite water content (0.1-1.5 wt. %.).

Our calculations reveal that the presence of hydrous ringwoodite significantly delays heat propagation through the slab (Fig. 3.1.7). This effect might hinder the decomposition of temperature sensitive hydrous minerals (in particular DHMS), enabling them to reach the lower mantle. Our results have an impact on the deep water cycle, by providing a mechanism to deliver water down to the lower mantle.

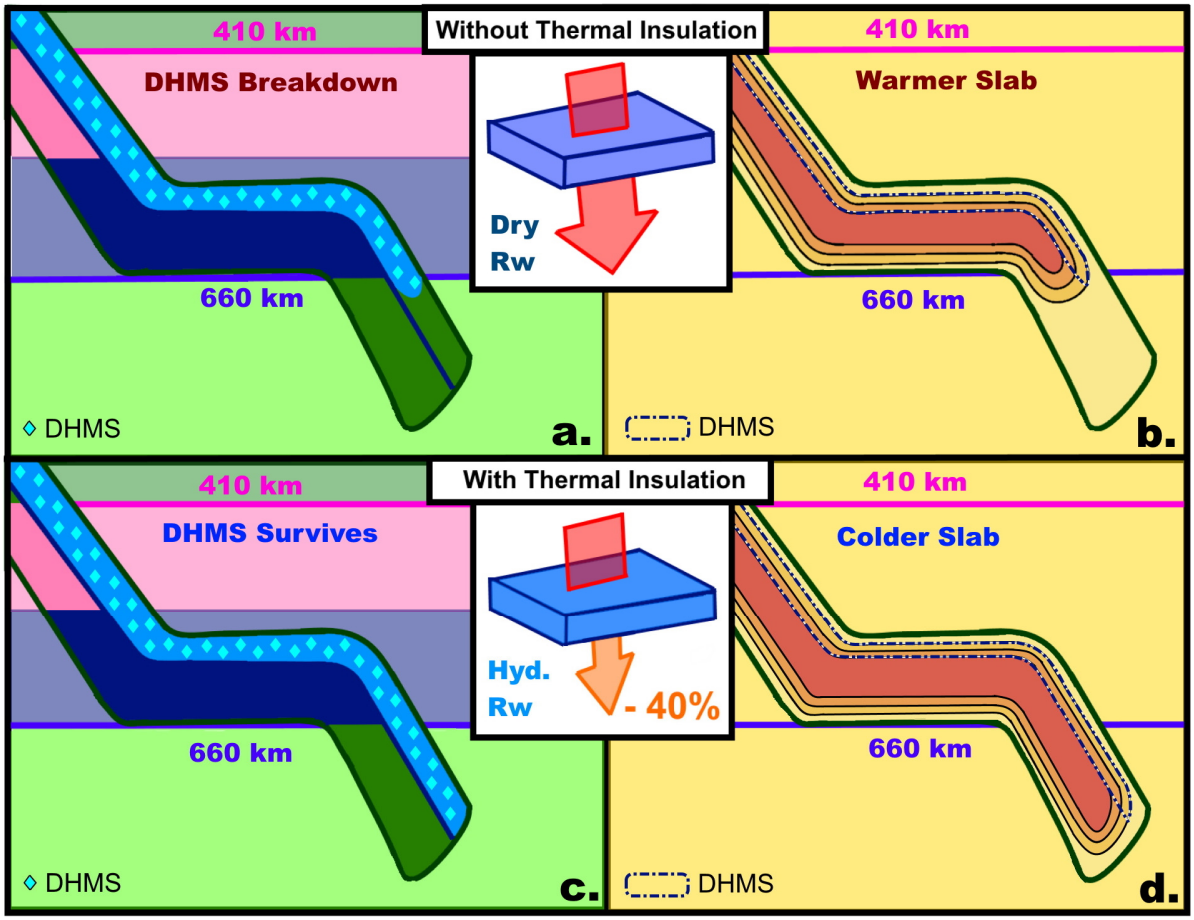

Fig. 3.1-7: The sketch shows the thermal state of a descending slab (outlined in green), crossing the MTZ (410-660 km). The colour scale in the right panels (b. And d.) indicates the temperature field (T) of the slab and the ambient mantle: bright colours for high T, and dim colours for low T. The dashed blue line highlights the stability field of temperature-sensitive Dense Hydrous Magnesium Silicates (DHMS). Ringwoodite (blue) is the dominant mineral phase (> 60 vol. %) stable in the lower MTZ (520-660 km), and the presence of water in its structure causes ~ 40 % reduction in the lattice thermal conductivity. We compare the thermal state of a slab with (c. and d.) and without (a. and b.) the insulation provided by hydrous ringwoodite. The slab composed by dry ringwoodite is not capable of protecting the DHMS from the high T reached during the descent. The presence of hydrous ringwoodite significantly hampers heat transport, providing a colder environment suitable for the survival of DHMS.

3.2 Geochemistry

The Earth's rocks have enormous chemical diversity compared to those of other terrestrial planets, even though each planet was formed from similar materials. To understand the origin of this diversity, which is a crucial outcome of the unique evolution of our planet, we need to comprehend the chemical fractionation processes that have occurred between and within Earth's layers.

Many of the studies described in this section of the yearbook are designed to place constraints on chemical fractionation processes by reproducing them in the laboratory. The products of these experiments are often silicate melts or fluids or the rock residues remaining after melting or dehydration processes, which can be compared with natural samples to evaluate whether the conditions of the experiments reproduce those of the studied fractionation events. In the first three reports of this section the large-scale fractionation event that occurred as the Earth's metallic core separated from the outer silicates of the mantle is examined in order to understand which elements the core-forming liquid removed from the mantle. The first of these contributions uses the results of laser-heated diamond anvil cell experiments and a new numerical model to examine why core formation did not strip most of the Earth's carbon into the core, as experiments would predict. By modelling the various stages of accretion and core formation it becomes apparent that the planetesimals (asteroid-size bodies) that brought carbon to the Earth contained no core forming metal because they formed in the outer regions of the solar system where metal became oxidized. These planetesimals, therefore, added carbon only to the mantle. Although later stages of core formation occurred, metal-silicate equilibration was limited to a region around the separating core material, leaving the rest of the mantle undepleted in carbon.

The next study examines how much hydrogen may have been extracted to the core, which is important because the hydrogen content of the Earth as a whole is very uncertain. It is extremely difficult to study the hydrogen content of liquid metal experimentally because hydrogen does not remain in the metal once it is recovered to room pressure and temperature for analysis. In this study *ab initio* computer calculations are performed instead, which show that hydrogen partitions increasingly into the metal with pressure. The results predict that about 1 wt. % hydrogen is in the core. The same simulations also predict that silicon partitions significantly into the core, whereas Mg remains almost entirely in the silicate mantle. This latter conclusion is confirmed in the following study that examines whether MgO could have entered the core from the mantle at very high temperatures. Recent models have proposed that the exsolution of MgO from the core may have helped to power the early Earth's geodynamo, explaining why ancient rocks indicate that the Earth had a magnetic field. In this study, however, the amount of MgO entering the core is found to be extremely low and with no indication that it would increase at higher temperatures.

The following two studies were performed to examine melting of the Earth's lower mantle, in both cases to explain the origin of regions exhibiting low seismic wave velocities, which might arise from the presence of deep magma layers. Melting experiments require very well controlled

thermal environments, which can be challenging to achieve in the laser heated diamond anvil cell. In the first study, therefore, multianvil experiments are performed under more controllable conditions of the top of the lower mantle and the results are used to develop a thermodynamic model for melting, which is then extrapolated to the base of the mantle. The results show that the ultra-low seismic velocity zone at the base of the mantle is unlikely to be caused by melting of subducted basaltic rocks, because their melting temperature should be similar to that of the surrounding mantle. The second study examines the partitioning of iron between hydrous melts and minerals at the top of the lower mantle. Seismic observations have indicated that there may be a melt layer at these depths under some regions, which might result from melt stagnation due to the melt having the same density as the surrounding mantle rocks. The density of melts depends strongly on their iron content and in this study the partitioning of ferric iron between lower mantle minerals and melts is determined for the first time. A significant portion of the iron in the lower mantle is expected to be in the ferric state. However, the results indicate that because ferric iron partitions more strongly into the lower mantle mineral bridgmanite, the iron content of the melt is not sufficient for its density to be similar to the surrounding mantle and any melts formed would tend to rise out of the lower mantle.

The next four studies in this section are related to the formation of diamonds in the mantle, which provide some of the only evidence for the circulation of carbon in the Earth's deep interior. The first of these investigates the ferric iron contents of tiny ferropericlase (iron-magnesium oxide) inclusions found in rare lower-mantle diamonds from Brazil. As the inclusions are so small a micro-beam Mössbauer spectroscopy technique is employed at a synchrotron high intensity X-ray source. The inclusions are found to contain very little ferric iron, which means that the conditions of diamond formation must have been quite reducing, *i.e.*, with little available oxygen. In the following related study experiments were performed to determine the nickel concentration of ferropericlase when it is in equilibrium with iron-nickel metal. The results show that the nickel concentrations of natural ferropericlase inclusions in diamonds are quite consistent with them having been in equilibrium with metal in the lower mantle. This further supports the idea that the lower mantle is quite reduced. The following study further builds on this scenario by considering what would happen to such a reduced, metal-bearing, lower mantle assemblage if there was an influx of carbonate melt. The reduced nature of the lower mantle can actually be traced back to the strong preference of the lower mantle mineral bridgmanite for ferric iron, which scavenges any available oxygen. In this study when carbonates are equilibrated with such a metal bearing lower mantle assemblage, diamonds are found to form. This is a plausible scenario for deep diamond formation because carbonate melts may rise into the reducing lower mantle from subducted lithospheric plates. What is intriguing is that with increasing pressure the ferric iron content of bridgmanite is found to increase further, implying that the lower mantle may become even more reducing with depth. The final study related to diamonds is performed to understand the oxidation state of iron in majoritic garnet, which is also found as inclusions in diamonds formed at conditions of the Earth's transition zone. The aim of the study is to find the extent of oxidation, *i.e.*, the oxygen fugacity, at which all iron in majoritic garnet is in the ferric state. These conditions are found for an oxygen fugacity which is not particularly high. Given that natural majoritic garnet inclusions in diamonds have been found with 30 % of the iron in the ferric state, the implication

is that the conditions where diamonds are formed in the transition zone may also be quite reduced.

The final four contributions in this section all deal with processes occurring as lithospheric slabs, comprising mantle, oceanic crust and sediment layers, are subducted into the mantle. The first of these examines how the redox state of serpentinites will evolve during subduction. Serpentinization is a major mechanism through which water is bonded into the oceanic lithosphere, but this process also adds ferric iron both in serpentine minerals and through the formation of magnetite. Upon subduction water and ferric iron are, therefore, carried into the mantle and in this study a model is developed from which the oxygen fugacity of such an assemblage can be calculated. The results show that once dehydration of the serpentinite commences, the oxygen fugacity is constrained to vary over a very narrow range, regardless of the ferric iron content. It has been proposed that sulphate-bearing fluids released from the slab might oxidize the overlying mantle and explain the oxidized nature of island arc magmas. However, the results show that the oxidation state of serpentinites remains below the level where sulphates would be stable. Although serpentinites are relatively oxidized, there seems to be no mechanism to communicate this redox state with the overlying mantle when they release water. In the next study phase relations of aluminosilicate hydrous phases are examined to determine the conditions where hydrous partial melting takes place that may remove volatiles from subducting slabs. In this preliminary study, however, high concentrations of nitrogen added to the experiments resulted in the formation of unusual micas where the potassium cation is entirely replaced by ammonium.

In the following study the role of apatite in determining the trace element signature of fluids leaving subducted sedimentary layers is examined. So called accessory minerals, such as apatite, are present in only small proportions in rocks but can potentially contain very high concentrations of what would otherwise be considered trace elements. If certain trace elements partition strongly into accessory phases, this can cause depletions in these elements in the released fluids. In this study trace element partitioning is examined between apatite and other minerals formed within a subducting sediment composition. The results demonstrate that geologically realistic amounts of apatite cannot significantly influence the trace element compositions of subduction zone fluids, which are instead controlled by the presence of more dominant hydrous minerals. The final study in this section examines the role of fluid salinity (NaCl) in determining how much rock can be dissolved by hydrous fluids during subduction of the oceanic crust. For this purpose, fluids with varying salinity, in equilibrium with material of basaltic composition, were trapped at subduction zone conditions within a layer of diamond powder and subsequently analysed by laser ablation inductively coupled mass spectrometry. These diamond trap experiments reveal that raising the chlorine content of the fluid to 6 wt. % doubles the total solute content of the fluid to approximately 40 %. This effect of salinity is found to decrease with increasing pressure. The results imply that fluid salinity is at least as important as pressure and temperature in determining the solute content and composition of fluids leaving subducting oceanic crust, which are responsible for metasomatizing the overlying mantle beneath arc volcanos.

a. *Partitioning of carbon between the mantle and core during Earth's accretion (D.C. Rubie, I. Blanchard/Potsdam and S. Jacobson/Minnesota)*

The element carbon plays a critical role in the Earth because it is essential for the origin and development of life on the planet. There have been many studies of how carbon partitions between the mantle and core during Earth's early differentiation. These involved experimental determinations of metal-silicate partition coefficients for carbon and their dependence on parameters such as pressure, temperature and oxygen fugacity. Most studies have concluded that carbon is strongly siderophile (metal-loving) such that it should have partitioned almost entirely into Earth's core, leaving the mantle strongly depleted in the element. In contrast to this prediction, the concentration of carbon in Earth's mantle is relatively high (around 140 ppm according to most studies). Based on high metal-silicate partition coefficients and simple models of core formation, the only way that such high mantle concentrations could be achieved is by the addition of almost all mantle carbon during Earth's late accretion after core formation was complete. However, the feasibility of this idea is not widely accepted.

Most previous experimental investigations of the metal-silicate partitioning of carbon have been performed at pressure-temperature conditions ($\leq$ 13 GPa and $\leq$ 2500 K) that are much lower than the *P-T* conditions under which Earth's core is considered to have formed. We performed laser-heated diamond anvil cell experiments and have thus determined metal-silicate partition coefficients at 41-79 GPa and 3600-4000 K (see BGI Annual Report 2018). The results show that carbon becomes significantly less siderophile at such conditions, compared with the low *P-T* results. We have applied these new partitioning results in a state-of-the-art model that combines the processes of accretion and core-mantle differentiation and, in particular, treats core formation as a multistage process. The model is based on N-body accretion simulations that start with around 100-200 Mars-size embryos embedded in a protoplanetary disk consisting of several thousand much smaller planetesimals. Planets grow from the embryos through collisions with other embryos and planetesimals. Most collisions involve a core formation event that involves accreted metal equilibrating with silicate liquid in an impact-induced magma ocean before segregating to the core. Using a mass balance/element partitioning approach, the evolving compositions of Earth's mantle and core are tracked throughout accretion. We assume that the concentration of carbon in starting bodies is defined by a gradient such that concentrations increase with increasing heliocentric distance as a result of it being a volatile element and due to decreasing temperatures in the protoplanetary disc. The gradient is defined by the average concentration ($C_{>4.5AU}$) in fully-oxidized planetesimals that originated in the outer solar system beyond 4.5 AU and the heliocentric distance ($D_{C=0}$) at which the C concentration becomes zero (Fig. 3.2-1). We assume that the metal of the cores of impacting bodies equilibrates with only a small fraction of the silicate mantle of growing Earth after an accretional collision event. This fraction is quantified using a model of the hydrodynamic interaction of metal and silicate as an impactor's core sinks in the magma ocean. Bodies that originate from beyond 4.5 AU are fully oxidized and therefore contain no metal; thus, when these are accreted there is no core-forming event and siderophile elements, including carbon, are mixed into Earth's mantle.

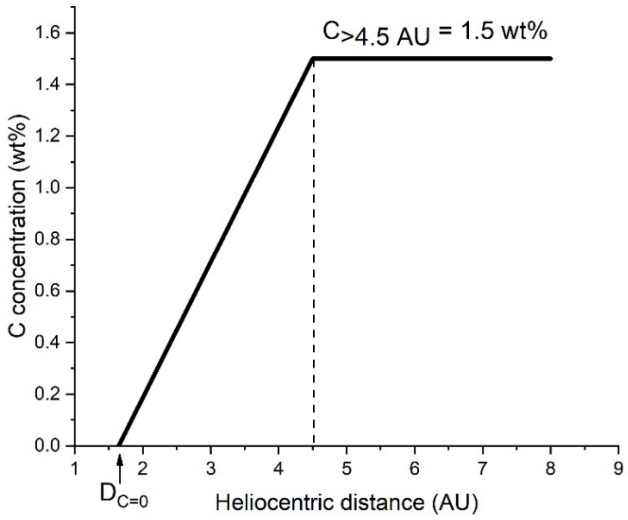

Fig. 3.2-1: An example of a carbon concentration profile for starting embryos and planetesimals in the protoplanetary disc that results in modelled carbon concentrations in the bulk Earth of 725 ppm and in the mantle of 140 (±20) ppm (Fig. 3.2-2). $C_{>4.5\ AU}$ is the average C concentration in bodies originating from beyond 4.5 AU. The parameters $D_{C=0}$ and $C_{>4.5\ AU}$ are strongly corrected (Fig. 3.2-3).

In order to model the concentrations of carbon in the mantle and core during Earth's accretion we used published estimates of the bulk silicate Earth (BSE) C concentration (140±40 ppm) and Earth's bulk C concentration (730±300 ppm). The modeled concentrations of C in the mantle, core and bulk Earth depend strongly on C concentrations in the bodies that accrete to form the Earth. Figure 3.2-1 shows an example of a compositional gradient for carbon in starting embryos and planetesimals that results in a bulk Earth concentration of 725 ppm and a final mantle concentration of 140 ppm (Fig. 3.2-2). However, the profile shown in Figure 3.2-1 is not unique because the parameters $C_{>4.5\ AU}$ and $D_{C=0}$ are strongly correlated and, in addition, we need to take account of the uncertainty on Earth's bulk C concentration. Figure 3.2-3 shows that the parameter space that results in a final Earth bulk concentration of 730±300 ppm and a mantle concentration of 140 ±40 ppm approximately covers the ranges $C_{>4.5\ AU}$ = 1.0-2.2 wt. % and $D_{C=0}$ = 1.0-2.0 AU. The calculated carbon content of Earth's core lies in the range 0.08 - 0.3 wt. % across this parameter space.

There are two reasons for the successful prediction of Earth's mantle carbon concentration using our accretion/differentiation model, in contrast to previous studies that were based on relatively simple core formation scenarios. First, bodies originating from the outer solar system are fully oxidized and therefore contain no metal. Thus, as described above, there is no core formation event when they are accreted and the delivered carbon remains in the mantle. Second, when differentiated metal-bearing bodies are accreted, the metal of the impactor only equilibrates with a small fraction of the target's mantle, the value of which depends on the size of the impactor's core and the depth of the magma ocean. Consequently, core formation events are extremely inefficient at removing carbon from the bulk of the mantle and transferring it to the core.

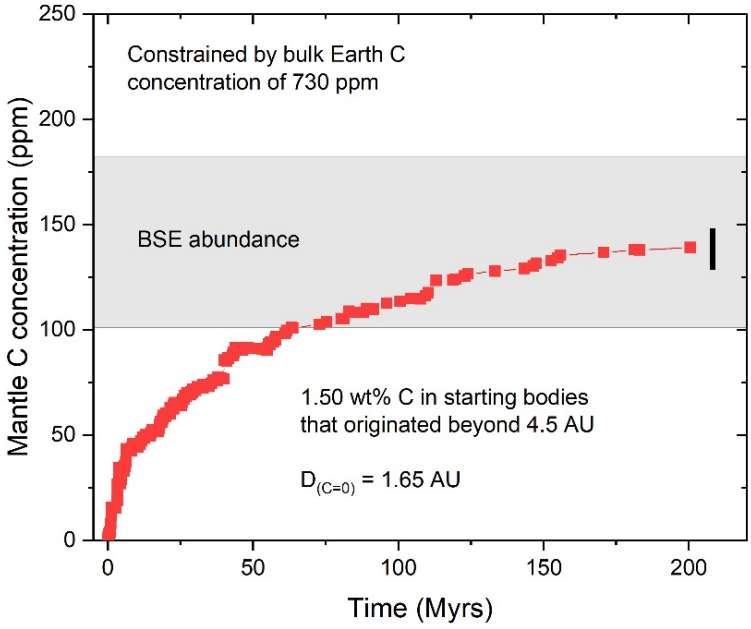

Fig. 3.2-2: Evolution of the modelled carbon concentration in Earth's mantle as a function of time during accretion. Each red symbol represents an accretion event. The carbon concentrations in starting bodies are shown in Figure 3.2-1. The vertical black error bar shows the result of propagating the uncertainties on partitioning parameters.

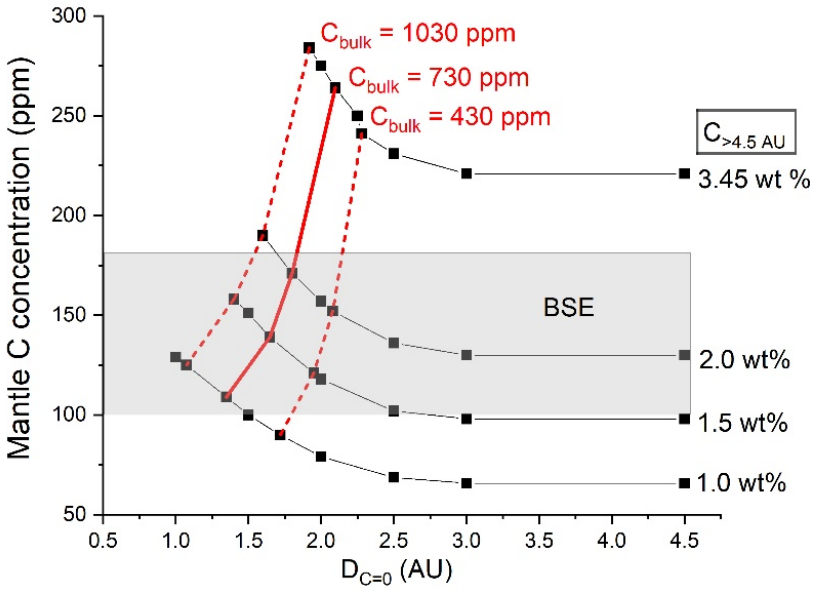

Fig. 3.2-3: Effects of varying the C concentration gradient in starting bodies (Fig. 3.2-1) on the final mantle C concentration. The mantle concentration is plotted as a function of the heliocentric distance at which the C concentration in starting bodies is zero ($D_{C=0}$). The four black curves show this relationship for different average C concentrations ($C_{>4.5\ AU}$) in bodies originating beyond 4.5 AU that range from 1.0 to 3.45 wt. %. The solid red line connects values that result in a bulk Earth C concentration of 730 ppm and the dashed red lines bracket a ±300 ppm uncertainty on this concentration. The shaded region shows the bulk silicate Earth (BSE) C concentration.

b. *Strong sequestration of hydrogen into the Earth's core during planetary differentiation (L. Yuan and G. Steinle-Neumann)*

The Earth's core is the main repository for some of the chemical elements on our planet, and determining its composition is a major goal in understanding the state and evolution of Earth's interior. A large number of elements have been proposed to account for the density deficit of the core, *i.e.*, its lower density compared to pure iron. Among them is hydrogen, the most abundant element in the universe whose budget on Earth is uncertain as it is volatile and escapes Earth's gravitational field readily. Despite its importance, the amount of hydrogen in the core is poorly understood as it is extremely difficult to measure the hydrogen content of iron metal recovered from experiments at high pressure and temperature.

We explore the partitioning behaviour of hydrogen between coexisting metal and silicate melts at conditions of the magma ocean and the current core–mantle boundary with the help of density functional theory molecular dynamics (DFT-MD). We perform simulations with the two-phase and thermodynamic integration methods. Two-phase simulations model element partitioning directly, mimicking an experiment by putting metallic and silicate phases in direct contact in a simulation cell, and then tracking the distribution of hydrogen atoms between the two liquids as the system approaches equilibrium (Fig. 3.2-4a). Simulations start from initial configurations where six hydrogen atoms each are located in the silicate and metallic liquids.

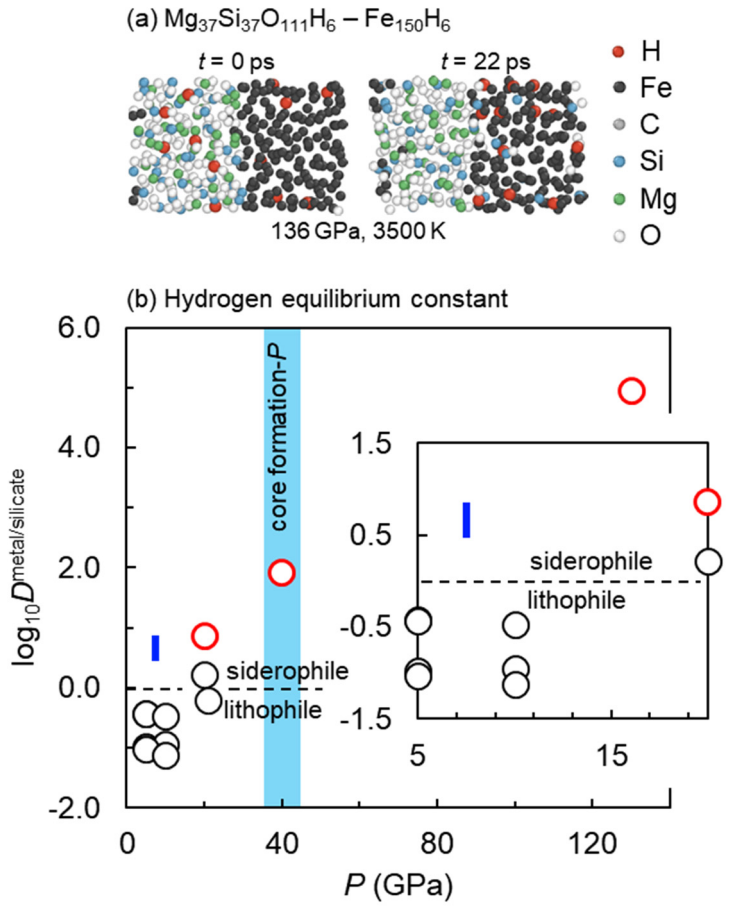

Fig. 3.2-4: (a) Initial and final configurations for the two-phase simulations of silicate ($Mg_{37}Si_{37}O_{111}H_6$) and metal liquid ($Fe_{150}H_6$) in contact. (b) Hydrogen metal–silicate partitioning coefficients computed via Gibbs energy differences from the DFT-MD simulations using thermodynamic integration (red circles). Experimental data (black circles: Clesi *et al.*, 2018, Sci. Adv. 4: e1701876; blue bar: Okuchi, 1997, Science 278: 1781-1784) are shown for comparison.

At all *P–T* conditions considered (20-130 GPa and 2500-4000 K), we observe diffusion of hydrogen atoms from the silicate to the metallic phase, leading to an accumulation of hydrogen in iron. We quantify the hydrogen metal–silicate partition coefficient ($D^{metal/silicate}=c^{metal}/c^{silicate}$, which is defined by the ratio of molar fractions of H_2O in Fe metal, c^{metal} and $MgSiO_3$ silicate, $c^{silicate}$) by thermodynamic integration (Fig. 3.2-4b). We find that hydrogen is weakly siderophile at low pressure (20 GPa and 2500 K), and becomes much more strongly so with pressure, suggesting that hydrogen partitioned into the core in a significant amount during core segregation and is stable there. Based on our results, the core likely contains ~ 1 wt. % H, assuming single-stage formation and equilibration at 40 GPa.

Our two-phase simulations further suggest that also significant amounts of silicon partition into the core, whereas magnesium remains almost entirely in the silicate phase. This preferred incorporation of silicon hints at an explanation for the elevated Mg/Si ratio of the bulk silicate Earth relative to chondritic compositions.

c. *The incorporation of Mg into core-forming melts during the accretion of terrestrial planets (L. Man and D.J. Frost)*

Energetic impacts during terrestrial planet-formation, such as the Moon-forming giant impact, released enormous amounts of energy which caused large-scale (or even global) melting. Under such extreme pressure and temperature conditions, interaction between metallic iron and silicate melts occurred during multiple magma ocean events as the metallic melts gravitationally separated into the core. It has been widely accepted that light elements, such as O, S, C, H, and Si may have dissolved into core-forming metallic melts during this phase of differentiation, which is consistent with geophysical and geochemical observations and experimental results. In addition, recent experimental and theoretical studies showed that even the least siderophile major element, Mg, could substantially partition into the core at very high temperatures. It has been proposed that subsequent exsolution of MgO as the core cooled may have contributed to thermochemical convection in the core that might explain the occurrence of an ancient terrestrial magnetic field before the inner core is projected to have formed. However, detailed melting phase relations of the Mg-bearing iron alloy have not been investigated by experiments, and large discrepancies exist concerning the influence of temperature and oxygen concentration on Mg solubility among previous studies.

In this study, we performed multianvil experiments in the Fe-FeO-MgO system from 2500 to 3300 K at 23 GPa. Starting materials with varied O and Mg concentrations were used to obtain different redox conditions. The samples were quenched by switching off the power after being kept at the target temperature for 0.5 to 2 min. The chemical compositions of each phase in the quenched samples were measured using the electron microprobe. Figure 3.2-5 shows the textures and compositions of a representative sample. Quenched melts consisted of mixtures of iron metal and magnesiowustite, which crystallized from a single, homogeneous liquid phase

during quenching. As shown in the Figure 3.2-6, significant amounts of MgO (up to several mol. %) can dissolve into the Fe-FeO melts when the O concentration in the melts is sufficiently high. It can be seen that the solubility of MgO in the iron-rich melt is controlled by the O content but remains very low at the O contents expected for the core. The melting phase relations of Fe-FeO-MgO determined in this study will be used to constrain the energy sources of the early geodynamo and the light element budgets in terrestrial planetary cores.

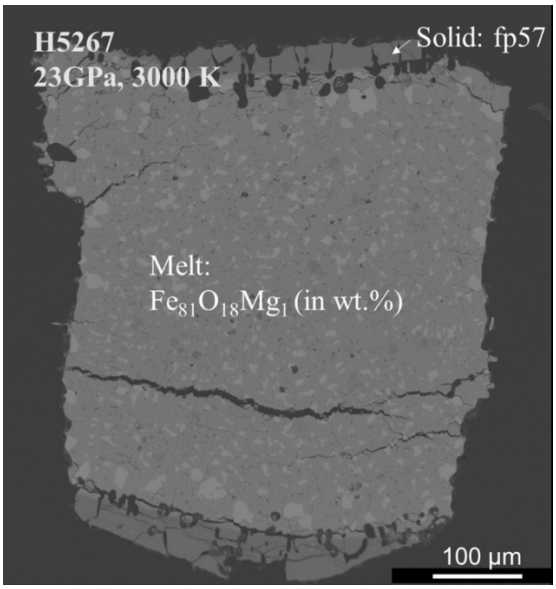

Fig. 3.2-5: A representative sample containing Fe-FeO-MgO liquid quenched from 23 GPa and 3000 K.

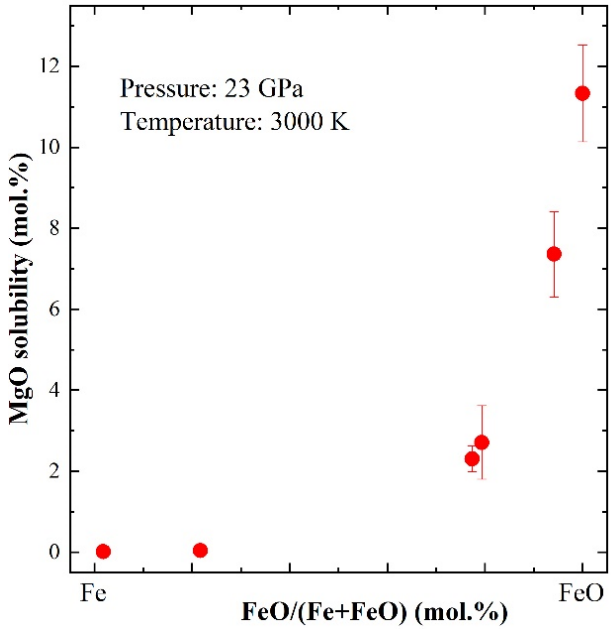

Fig. 3.2-6: The solubility of MgO in Fe-FeO-MgO melts with varied O content. All of the experiments shown in this graph were performed at 23 GPa and 3000 K.

d. *The $MgSiO_3$-SiO_2 eutectic at lower mantle pressure determined using multianvil experiments (J. Yao, D.J. Frost and G. Steinle-Neumann)*

Silicate melting has shaped the chemical and physical evolution of planetary interiors, from magma ocean formation during accretion to the subsequent continuing extraction of melt. For the Earth, the latter is dominated by the ongoing formation of mid-ocean ridge basalt (MORB) from mantle peridotite and the possible presence of melt near the core-mantle boundary (CMB), where it serves as an explanation for the occurrence of seismic ultra-low velocity zones (ULVZ). Given a silica content of $X_{SiO_2} = 0.45$, with $X_{SiO_2} = SiO_2/(SiO_2 + MgO)$, for the bulk silicate Earth, many high-pressure (P) experiments on melting relations have focused on compositions in the peridotite system MgO-$MgSiO_3$, and have provided robust results in terms of the location of the eutectic, constraining the composition at which the liquidus phase switches from MgO periclase to $MgSiO_3$ bridgmanite, and the solidus temperature (T).

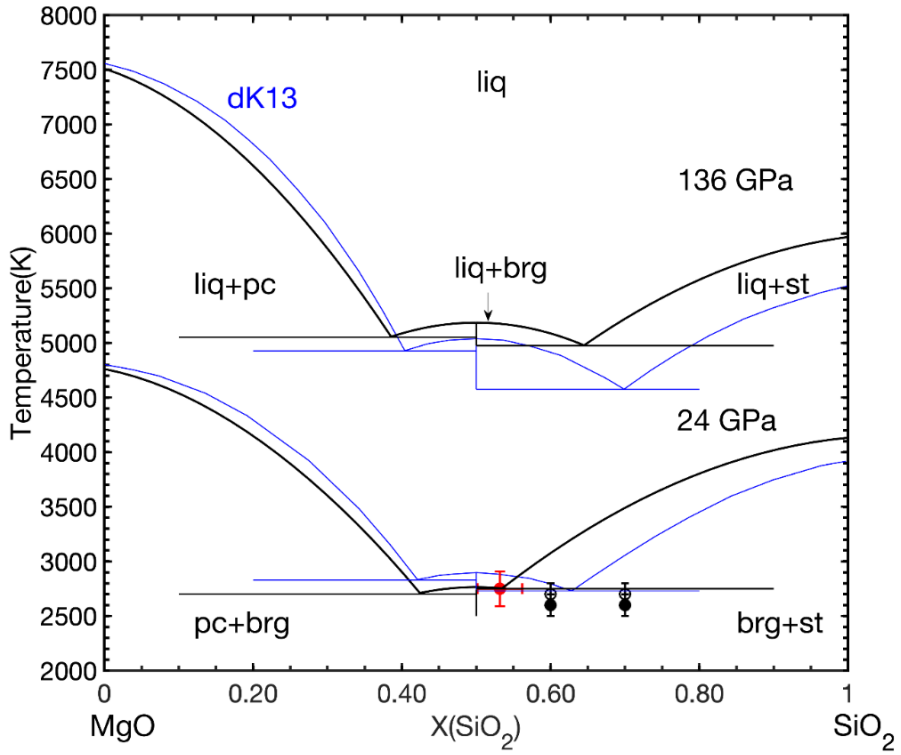

Fig. 3.2-7: MgO-SiO_2 melting relations computed from our thermodynamic model at 24 GPa (bottom black graph), based on the experiments performed in the $MgSiO_3$-SiO_2 system, combined with previous result for the MgO-$MgSiO_3$ system. The eutectic composition (red circle with error) is determined based on an experiment for $Mg_{0.4}Si_{0.6}O_{1.6}$ at T=2700±100 K (black semi-filled circle); starting compositions and T of additional experiments are also shown, with the filled black circles for the experiments at T=2600±100 K indicating that the experiments remained below the solidus. Melting relations at P=136 GPa (top black graph) computed from our model. For comparison we include melting relations from the model of de Koker *et al.* (EPSL 361, 58, 2013) (dK13, blue) both at P=24 GPa and P=136 GPa. Abbreviations: pc-periclase, brg-bridgmanite, st-stishovite, liq-liquid.

Silica-enriched reservoirs in the Earth, primarily associated with subducted MORB crust, have been considered as potential sources for partial melt near the CMB, which makes melting relations for the entire MgO-SiO_2 join at high *P* a topic of geological significance. Multianvil (MA) experiments create stable conditions in terms of *P* and *T*, and provide sufficient material for a reliable chemical analysis. We have, therefore, determined melting relations in the $MgSiO_3$-SiO_2 system at 24 GPa in the MA press. For a starting composition of $Mg_{0.4}Si_{0.6}O_{1.6}$ at 2700 K we find large stishovite crystals (liquidus phase) coexisting with quenched melt with $X_{SiO_2} = 0.53 \pm 0.03$ (Fig. 3.2-7). Using the eutectic locations and temperatures for MgO-$MgSiO_3$ and $MgSiO_3$-SiO_2, we formulate a thermodynamic model for melting phase relations in the MgO-SiO_2 system. For a model with a minimum number of parameters, we describe the liquid with the oxide components MgO and SiO_2 with a binary symmetric solution model, and use MgO periclase, $MgSiO_3$ bridgmanite and SiO_2 stishovite as solid phases, creating the phase diagram shown in Figure 3.2-7. As we perform MA experiments only at 24 GPa, we cannot model an explicit *P* dependence of the Margules interaction parameter; and any *P* dependence hinges on the equation-of-state parameters of the endmembers, and on the *T* increase with *P* via the *T* dependence of the Margules parameter.

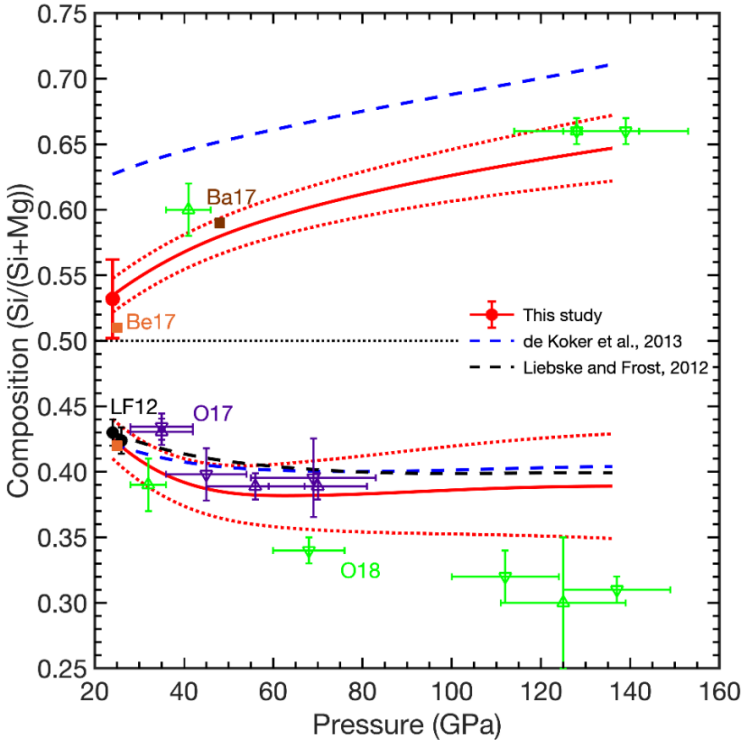

Fig. 3.2-8: Eutectic compositions in the MgO-SiO_2 system in the *P* range 24-136 GPa. Filled circles show eutectic liquid compositions based on our multianvil experiments (red) and those by Liebske and Frost (EPSL 345, 159, 2012) (LF12, black). Previous experimental data in the diamond anvil cell (O17, O18 and Ba17) and computational values (Be17) are included for comparison. Results from our model are shown by the red solid curves with uncertainties from Monte Carlo simulations given by the dotted curves; they are compared to previous models by Liebske and Frost (EPSL 345, 159, 2012) (black dashed curve) and de Koker *et al.* (EPSL 361, 58, 2013) (blue dashed curves).

We find that with increasing P the stability range of bridgmanite as the liquidus phase increases, with the eutectic points moving further away from enstatite composition Fig. 3.2-8). The eutectic for MgO-$MgSiO_3$ agrees well with many previous studies, while for $MgSiO_3$-SiO_2, our values agree with some of the prior experiments. At lowermost mantle conditions, we predict the basaltic eutectic at $X(SiO_2)=0.65\pm0.03$ (Fig. 3.2-7,-8). The solidus T for both the basalt and peridotite system are quite similar (Fig. 3.2-7) such that a preferred melting of MORB near the CMB appears unlikely as a cause of the ULVZ.

e. *The composition and redox state of partial melts generated at the top of the lower mantle (R. Huang, T. Boffa Ballaran, C.A. McCammon and D.J. Frost)*

Zones of low seismic velocity have been proposed beneath the 660-discontinuity based on observations of seismic P-to-S conversions. This could indicate the presence of a melt layer produced through dehydration as material is transported downwards out of the mantle transition zone, due to a decrease in the amount of water that can be stored in mineral structures. However, the composition, and particularly the iron content, of such a melt layer is still poorly constrained, although important for estimating the likely melt density and therefore buoyancy. In this study, we have investigated ferrous and ferric iron partitioning between bridgmanite (Brg) and coexisting melt and a thermodynamic model has been derived to describe the composition of Brg and melt as a function of oxygen fugacity (fO_2) at 25 GPa and 1973 K.

For the starting material $Mg_{0.93}Fe_{0.07}Si_{0.93}Al_{0.07}O_3$ pyroxene was mixed with 5 wt. % $(Mg_{0.9}Fe_{0.1})O$ and 15 wt. % Fe metal. Ir was also added to monitor the fO_2 of the experiments. Different amounts of water (5-20 wt. %) were added to each experiment using a syringe or as $Mg(OH)_2$ and the capsules were welded closed. High-pressure experiments were performed using a multianvil press at 25 GPa and 1973 K. The composition of the run products was measured using the electron microprobe and the $Fe^{3+}/\Sigma Fe$ ratios in Brg and melt were determined by Mössbauer spectroscopy. All recovered samples contained Brg, ferropericlase (Fp) and quenched microcrystals from the melt. A consistent fO_2 of iron-wustite (IW) + 2 log units was obtained. The compositions of Brg in all experiments are similar with 0.07 cations per formula unit (pfu) Al and 0.15-0.16 pfu Fe due to the oxidation of Fe metal by reaction of H_2O. The fitting results from Mössbauer spectroscopy reveal $Fe^{3+}/\Sigma Fe$ ratios of Brg between 0.42 (7) and 0.54 (7). The Fe/(Mg+Fe) ratios of the melt from all experiments fall in a narrow range between 0.33 and 0.38, which is twice more than the ratio of coexisting Brg but lower than Fp with a Fe/(Mg+Fe) ratio of 0.45-0.55. The $Fe^{3+}/\Sigma Fe$ ratio of melt in one experiment (S6840) was determined to be 0.31(5) by Mössbauer spectroscopy. By comparing with previous studies where melts coexisted with Brg and Fp, the (Mg+Fe)/Si ratio of the partial melt decreases monotonically from 5.2 at 1573 K to 1.2 at 2600 K and seems to be independent of the Fe content of the melt and the experimental fO_2. Any hydrous partial melt produced at the top of the lower mantle at temperatures < 2000 K would, therefore, be MgO-rich and SiO_2-poor with a (Mg+Fe)/Si ratio > 2.5.

In experiment S6840 the mineral/melt partition coefficient for Fe^{3+} is calculated to be 0.52, which is higher than partition coefficients for Fe^{3+} determined at upper mantle conditions but still implies that Fe^{3+} is incompatible in Brg. However, the Fe contents of both melt and Brg were higher in the experiments than expected in the mantle and the Brg Al concentration was lower. A model is therefore required in order to slightly extrapolate these compositions to those of the mantle. For Brg we use a thermodynamic model described in the BGI Annual Report (2019), which describes Brg Fe^{3+} content as a function of composition and fO_2. As shown in Figure 3.2-9 this model, shown by the dotted curve, fits the experimental data point extremely well, even though it was not used in the development of this model. Two melt models were employed, one where Mg, Fe^{2+} and Fe^{3+} mixing is assumed to be ideal (Model A) and one where non-ideal mixing is considered (Model B). Based on these models, in conjunction with a mass balance calculation, partial melt compositions produced at the top of the lower mantle within a pyrolite composition can be calculated as a function of fO_2 and melt fraction. Mineral and melt compositions predicted by the models for a pyrolite composition are shown by the solid lines in Figure 3.2-9. Due to the higher Al content of the mantle composition and the lower bulk Fe

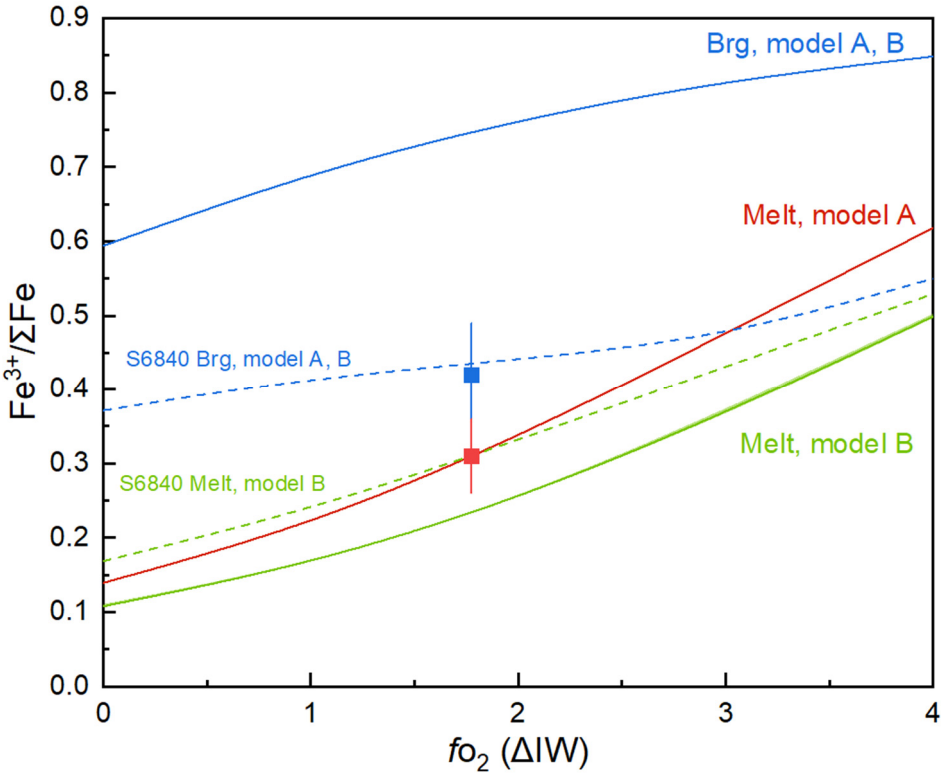

Fig. 3.2-9: Experimentally determined $Fe^{3+}/\sum Fe$ ratios for coexisting Brg (blue symbol) and melt (red symbol) and the corresponding mineral and melt models for these data (dashed lines) as a function of oxygen fugacity. Solid lines show the model curves calculated for a pyrolite composition. The $Fe^{3+}/\sum Fe$ ratio of melt calculated using model A does not depend on the melt composition because it assumes ideal mixing. Melt model B considers non-ideal mixing, which causes the melt $Fe^{3+}/\sum Fe$ ratio in equilibrium with pyrolite mantle to decrease slightly compared to the experiment due to the lower bulk Fe content.

content, Brg is predicted to have a much higher Fe^{3+} content than the melt for a comparable fO_2. The uncertainty due to the activity composition relations assumed for the melt are relatively small (approximately 5 %) and at an fO_2 of IW the melt $Fe^{3+}/\Sigma Fe$ ratio is still expected to be above 0.1. Under these conditions Fe^{3+} is predicted to become compatible in Brg.

The density calculated for the hydrous partial melt composition at topmost lower mantle conditions falls within a narrow range between 3.8-3.9 g/cm^3 regardless of the water content (15 wt. %-30 wt. %), melt fraction (0.1 wt. %-1 wt. %) or fO_2 (IW – IW+4) that is assumed. This is much lower than the density of the surrounding lower mantle at this depth but may be close to the density at the base of the transition zone. As previously proposed, if hydrous mantle is dragged into the lower mantle, melts may be produced that rise back into the transition zone and crystalize, thereby creating a continuous cycle.

f. *Ferropericlase inclusions from ultra-deep diamonds: a synchrotron XRD and Mössbauer study (I. Koemets, E.S. Kiseeva/Cork, D.A. Zedgenizov/Novosibirsk, H. Kagi/Tokyo, A. Aslandukova, S. Khandarkhaeva, T. Fedotenko/Bayreuth, L.S. Dubrovinsky, G. Aprilis/Grenoble, K. Glazyrin/Hamburg)*

The lower mantle (LM) is the largest silicate reservoir on Earth and contributes ~ 50 % of the mass of the entire planet. The composition of the LM in comparison with the upper mantle or crust is rather simple, in peridotitic/pyrolitic lithologies it consists of ~ 70 % of bridgmanite $(Mg,Fe)SiO_3$, with small amounts of Al, ~ 20 % ferropericlase (Mg,Fe)O, and ~ 10 % Ca-perovskite ($CaSiO_3$) that can also act as a host for alkali metals and other incompatible elements. In metabasaltic/eclogitic lithologies, ferropericlase is absent, while in addition to bridgmanite and Ca-perovskite, stishovite and two Al-bearing phases (NAL and CF) are present. Most of the information concerning LM phases has been obtained experimentally from synthetic or natural precursors, and the only evidence representing natural high-pressure deep mantle environments comes from inclusions in diamonds. LM inclusions in diamonds are extremely rare and have been found mostly in the Juina area in Brazil. Such inclusions were observed in alluvial diamonds and in those coming from a few kimberlite pipes. Bridgmanite inclusions are usually expected to transform into upper mantle phases upon ascent, while ferropericlase is expected to be preserved. To date, there are ~ 130 inclusions of ferropericlase reported in the literature, spanning a range of #Mg between ~ 12 and ~ 90, and containing significant amounts of Ni (up to 1.5 wt. % NiO), Mn (up to 1.6 wt. % MnO), Cr (up to 2.5 wt. % Cr_2O_3), Na (up to 1.4 wt. % Na_2O) as well as < 1 wt. % of SiO_2, Al_2O_3, TiO_2 and K_2O.

In this study we selected three ferropericlase inclusions from São Luiz, Juina (Fig. 3.2-10) and analysed them for their oxidation state using Synchrotron-based Mössbauer Spectroscopy (SMS) (beamline ID18 at the European Synchrotron Radiation Facility, Grenoble). Prior to analysing them by SMS, we used single-crystal X-ray diffraction (XRD) analysis (beamline P02 at PETRA III, Hamburg) to confirm their phase purity. For the synchrotron study, the

inclusions were brought to the diamond surfaces by double sided polishing and their size was ~ 70*50 µm with thickness ~ 10-30 µm. The XRD analysis showed that all inclusions were single-phase ferropericlase, and their composition refined from their structure is in general agreement with the electron microprobe analysis:

- SL14: $(Fe_{0.263}\ Mg_{0.737})O$, a= 4.2292(1) Å
- SL14_2: $(Fe_{0.287}\ Mg_{0.713})O$, a= 4.2392(2) Å
- SL24: $(Fe_{0.164}\ Mg_{0.836})O$, a= 4.2309(2) Å

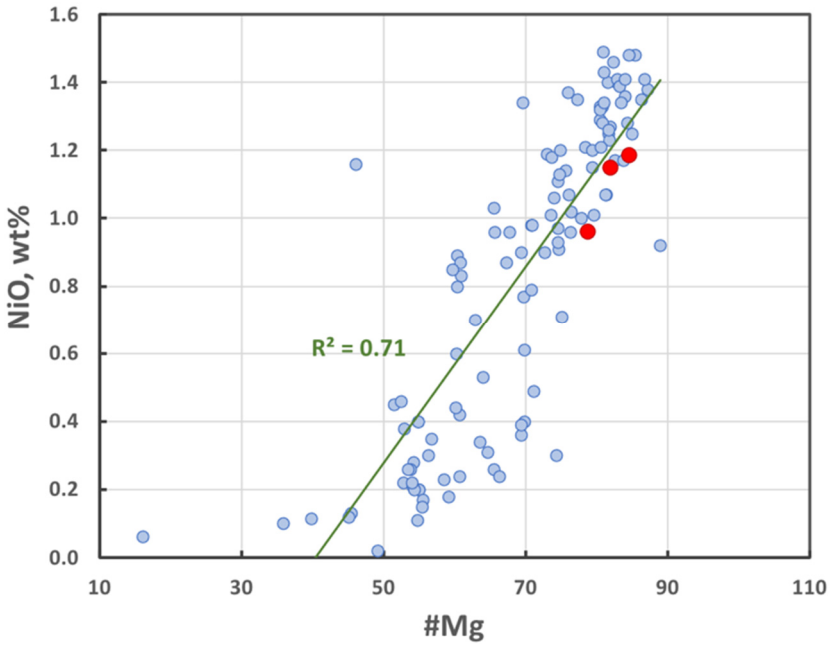

Fig. 3.2-10: Compositions of ferropericlase inclusions from Juina, Brazil. Blue circles are literature data, red circles are ferropericlase crystals from this study.

SMS results (Fig. 3.2-11) confirmed previous findings that natural ferropericlase inclusions incorporate only little amounts of ferric iron into their structure. Previous studies using conventional Mössbauer sources have measured up to 6 % Fe^{3+}/Fe_{tot}, in ferropericlase from Kankan (Guinea) and studies that have used the flank method have found 10-12 % Fe^{3+}/Fe_{tot} in the inclusions from Kankan, São Luiz and Juina kimberlites. The SMS signal does not exhibit any finite ferric iron contribution in the studied ferropericlases. However, because these inclusions are thin and they have low Fe content (natural ^{57}Fe abundance is ~ 2.1 %), the Mössbauer effect in these samples is weak and absorption reaches only 4-10 %, depending on the sample. Longer acquisition times will not improve resolution due to background intensity scatter. Our estimations show that despite a high beam intensity and good focusing optics at the ID18 beamline, Fe^{3+} detection limit for the samples used in this study is ≤ 5 % and currently available methods (free from exposing inclusions to the atmosphere) cannot effectively improve this value.

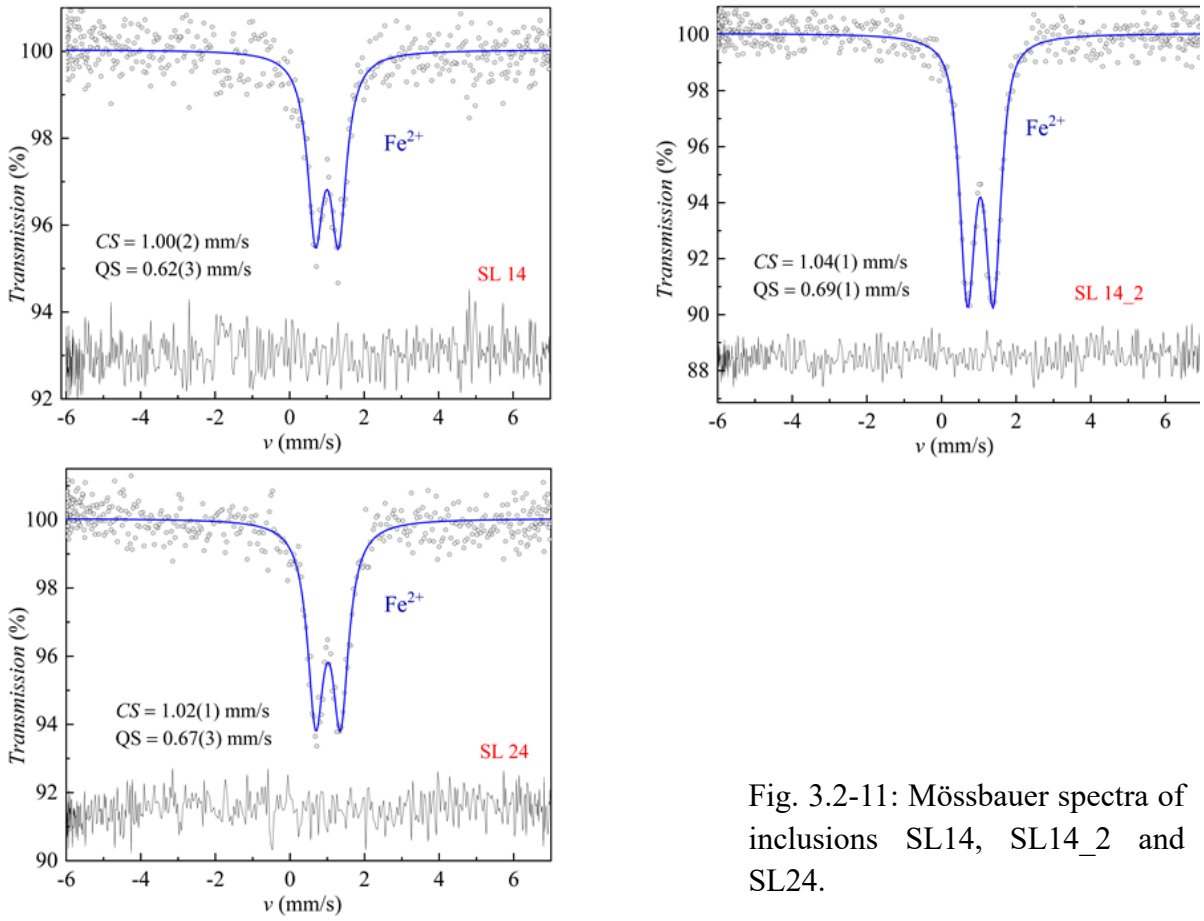

Fig. 3.2-11: Mössbauer spectra of inclusions SL14, SL14_2 and SL24.

g. *The partitioning of nickel between iron metal and ferropericlase at lower mantle conditions (E. Obengo, R. Huang and D.J. Frost)*

It has been proposed that as a result of the strong preference of Al-bearing bridgmanite for ferric iron, that approximately 1 wt. % of metal may precipitate in the lower mantle. Ferric iron forms by oxidation of ferrous iron as it is simultaneously reduced to iron metal in a charge disproportionation reaction. Nickel would also partition into this metal leaving the remaining oxides and silicates depleted in this element, however, it is also known that Ni becomes less siderophile (metal loving) at high pressures. It is important to be able to determine the Ni content of metal in the lower mantle because it will also influence how much metal is formed. Furthermore, as can be seen in the previous contribution by Koemets *et al.*, ferropericalse inclusions that are found in some rare sublithospheric diamonds also contain Ni. If these inclusions formed in the presence of metal then the Ni content of the inclusions may provide constraints on the conditions at which these inclusions were formed. Currently, however, data on the Ni content of ferropericlase in equilibrium with Fe-rich metal do not exist at lower mantle conditions.

To investigate the distribution of nickel between (Mg,Fe)O ferropericlase and iron-nickel alloy at conditions near the top of the lower mantle, multianvil experiments were conducted at 22

GPa and temperatures between 1300 °C and 1900 °C. A series of four ferropericlase compositions were employed with Mg/(Fe+Mg) molar ratios between 0.2 and 0.8 and containing 5 mol. % NiO. These compositions were mixed with 10 wt. % iron metal. Samples were loaded into four-hole alumina capsules so that all four compositions could be equilibrated in a single experiment. Recovered samples were analysed with the electron microprobe to determine the chemical compositions, from which metal/ferropericlase Ni-Fe distribution coefficients, $K_D = (X_{Ni}/X_{Fe})_{metal}/(X_{NiO}/X_{FeO})_{oxide}$, where X_{Ni} is, for example, the mole fraction of Ni in the Fe-Ni alloy, were determined.

Values of K_D were found to have a negative dependence on increasing temperature and ferropericlase MgO content *i.e.*, Ni becomes less siderophile. Comparison with previous studies performed at lower pressures indicates that Ni also becomes less siderophile with pressure. Although thermodynamic data to model these results appears to be well determined and very little uncertainty should exist, when models for K_D are compared with the experimental data they show a much smaller temperature and ferropericlase MgO dependence. This can be seen in Figure 3.2-12 where the term RTln(K_D) is plotted from the experimental data as a function of the ferropericlase MgO content, where R is the gas constant and T is temperature. If Fe-Ni mixing in the two phases were ideal this term should be equal to the Gibbs free energy difference of the Ni-Fe exchange reaction, *i.e.*, $Ni_{metal}+FeO_{oxide}=Fe_{metal}+NiO_{oxide}$. Shown for

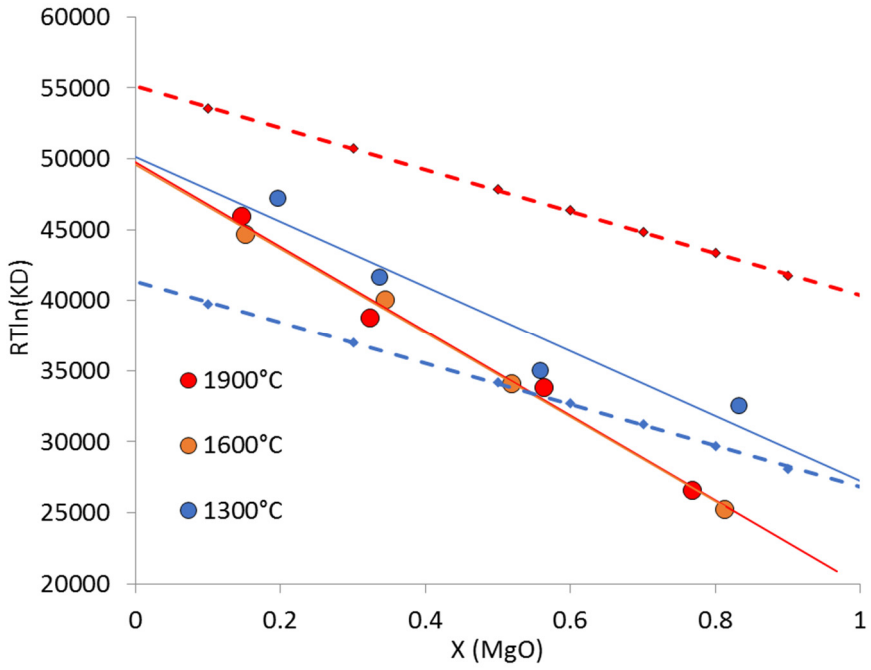

Fig. 3.2-12: RTln(K_D) as a function of the ferropericlase MgO mole fraction (X) determined experimentally at 1300 ° C, 1600 °C and 1900 °C and at 22 GPa. Linear fits have been plotted through these data. Two thermodynamic model calculations are performed at the same pressure and 1300 °C and 1900 °C. These calculations assume a metal $X_{Ni} / (X_{Ni} + X_{Fe}) = 0.5$ which is very similar to the experimental data. In comparison the thermodynamic model predicts a shallower slope and a much greater temperature dependence compared to the experimental data.

comparison are thermodynamic calculations, based on relatively well determined estimates of the Gibbs energy difference, which show a clearly much larger temperature variation and a different slope. While the difference in slope between the models and the experiments can be attributed to non-ideal mixing in the metal and oxide, the strong difference in temperature dependence implies a much smaller entropy for the exchange equilibrium than previously considered.

The origin of these discrepancies is hard to determine and requires further study. However, for ferropericlase formed in a peridotite composition at the top of the lower mantle the experimental data indicate a Ni-Fe K_D of approximately 6, which is lower than expected based on the extrapolation of previous data. If, as previous studies have suggested, there is approximately 1 wt. % of Fe-rich metal in the lower mantle then the experimental results indicate that ferropericlase should contain approximately 1 wt. % of Ni and the metal should contain approximately 18 wt. % Ni, if the lower mantle has the same composition as the upper mantle. This Ni content is in very good agreement with that found for ferropericlase inclusions in deep mantle diamonds, implying that they may well have formed in equilibrium with iron metal.

h. *Iron oxidation state of carbonated lower mantle assemblages: Implications for the redox conditions in subducting slabs and diamond stability (S. Dominijanni, C.A. McCammon, V. Stagno/Rome, D.J. Frost, T. Boffa Ballaran, V. Cerantola/Hamburg, in collaboration with T. Arimoto and T. Irifune/Matsuyama)*

Carbon is transported into the deep mantle in the form of both carbonates and elemental carbon. Natural evidence of carbonates from Earth's interior comes from sub-lithospheric diamonds, which host carbonate phases in equilibrium with minerals such as ferropericlase and bridgmanite. The mobility and residence time of carbon in the subducting slab is controlled by the local oxygen fugacity (fO_2), which determines whether carbon can occur in its oxidised form (carbonate and CO_2-rich melts) or as elemental carbon (graphite/diamond and carbide). Although several studies have emphasised the role of fO_2 on the fate of subducted carbonates, little is known about the Fe oxidation state in ferropericlase and bridgmanite at redox conditions where diamonds form by reduction of carbonates (either solid or liquid).

We examine the effect of pressure and temperature on ferric/ferrous ratios in bridgmanite and ferropericlase at fO_2 conditions buffered by the coexistence of diamonds and carbonates. Experiments were performed using a multianvil apparatus at 25 to 50 GPa and between 1000 and 1700 °C with sintered diamond anvils at the GRC (Ehime University). The starting material used for the experiments consisted of a mixture of natural magnesite, graphite, synthetic ferropericlase, glass with bridgmanite-like composition, and Fe-Ni alloy loaded in a graphite capsule as a representation of a simplified lower mantle mineral assemblage. Iridium powder was also added as a redox sensor to determine the oxygen fugacity (Fig. 3.2-13a). Chemical and textural analyses of the recovered samples were performed using the electron microprobe and the scanning electron microscope. Phase identification was performed using an X-ray microdiffraction technique. *In situ* synchrotron Mössbauer source spectroscopy was used to determine the $Fe^{3+}/\Sigma Fe$ ratios in bridgmanite and ferropericlase.

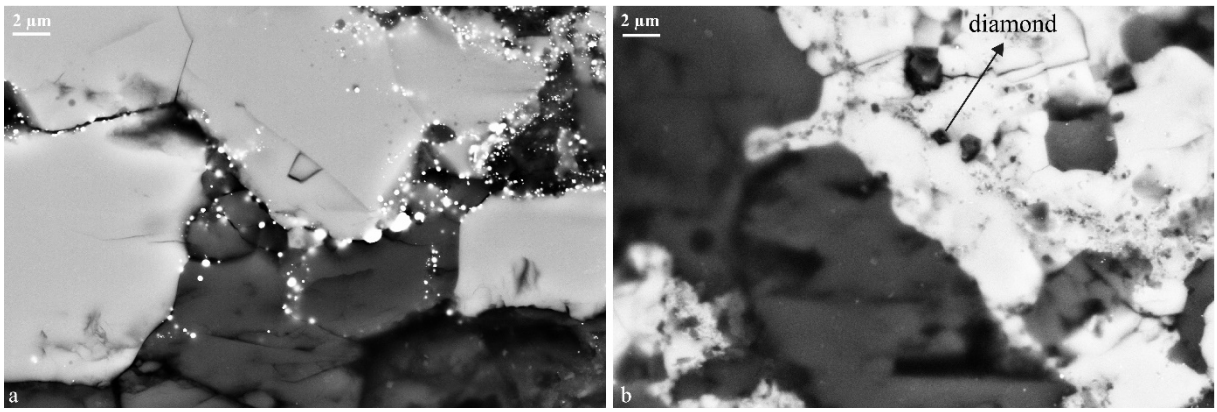

Fig. 3.2-13: a) Back scattered electron image of a run product showing coexisting ferropericlase (light grey), magnesite (dark grey) and Fe-Ir alloy (bright spots). The Fe activity in Fe-Ir alloy was used to calculate the oxygen fugacity; b) Diamond formation (black regions) by redox freezing of magnesite (dark grey) in equilibrium with Ni-enriched ferropericlase (light grey). Experimental conditions of both runs are 25 GPa and 1500 °C.

Preliminary results show that $Fe^{3+}/\Sigma Fe$ in bridgmanite increases with increasing pressure and decreases with increasing temperature, while $Fe^{3+}/\Sigma Fe$ in ferropericlase decreases as both pressure and temperature increase. Furthermore, we observed that $Fe^{3+}/\Sigma Fe$ in ferropericlase increases with increasing fO_2, while the crystal chemistry of bridgmanite controls the incorporation of Fe^{3+} in the bridgmanite structure. Textural observations show the formation of Ni-rich ferropericlase and diamonds by simultaneous reduction of magnesite and oxidation of Fe-Ni alloy (Fig. 3.2-13b). No textural evidence of redox reaction was found near bridgmanite. The preliminary results of this study suggest that the influx of carbonates into the lower mantle from subducting slabs can promote diamond formation through redox freezing, with a consequent rise of oxygen fugacity above the iron-wustite buffer.

i. *Oxidation state of Fe in synthetic Na-rich majorite with implications for the origin of superdeep diamonds (G. Marras and V. Stagno/Rome, C.A. McCammon, L. Bindi/Florence, in collaboration with T. Irifune and S. Greaux/Matsuyama, P. Scarlato/Rome)*

Majorite is a mineral with tetragonal structure that occurs in the upper mantle transition zone with variable abundance ranging from ~ 20 vol. % within peridotitic assemblages (P-type) to ~ 80 vol. % within deeply subducted oceanic crust (E-type). Recent findings of natural pyroxenitic majorites included in diamonds from South Africa showed a linear relation of their Fe oxidation state ($Fe^{3+}/\sum Fe$ up to 30 %) with mantle redox state similar to reports for synthetic P-type majorites; while eclogitic (E-type) majorites showed even higher $Fe^{3+}/\sum Fe$ values up to about 90 %. However, little is known about the maximum amount of Fe^{3+} that E-type majorites can incorporate when they form at highly oxidised conditions.

To address this question, we synthesised majorite directly from reduced glass with omphacitic composition mixed with 25 % Re and ReO_2 (1:1 mole ratio) to act as redox buffer. Experiments were carried out at 18 and 24 GPa and 1000 °C using an 840-ton Walker-type at the National Institute of Geophysics and Volcanology in Rome. The recovered run products were identified by powder and single crystal X-ray diffraction, micro-Raman and -FTIR, and both scanning electron microscopy and electron microprobe. The Na-rich majorites have the general formula $(Mg_{2.80}Na_{0.20})(Al_{1.79}Si_{0.15}Mg_{0.06})Si_3O_{12}$ but contain approximately 4 wt. % iron oxide. In addition, $Fe^{3+}/\sum Fe$ was determined using point source ^{57}Fe Mössbauer spectroscopy on double-polished Re capsules with 600 µm thickness. Spectra were fitted with Lorentzian line shapes. Results showed the presence of only Fe^{3+} in the majorite structure (Fig. 3.2-14a). Hyperfine parameters are consistent with values reported in the literature for Fe^{3+} in tetrahedral coordination (Fig. 3.2-14b).

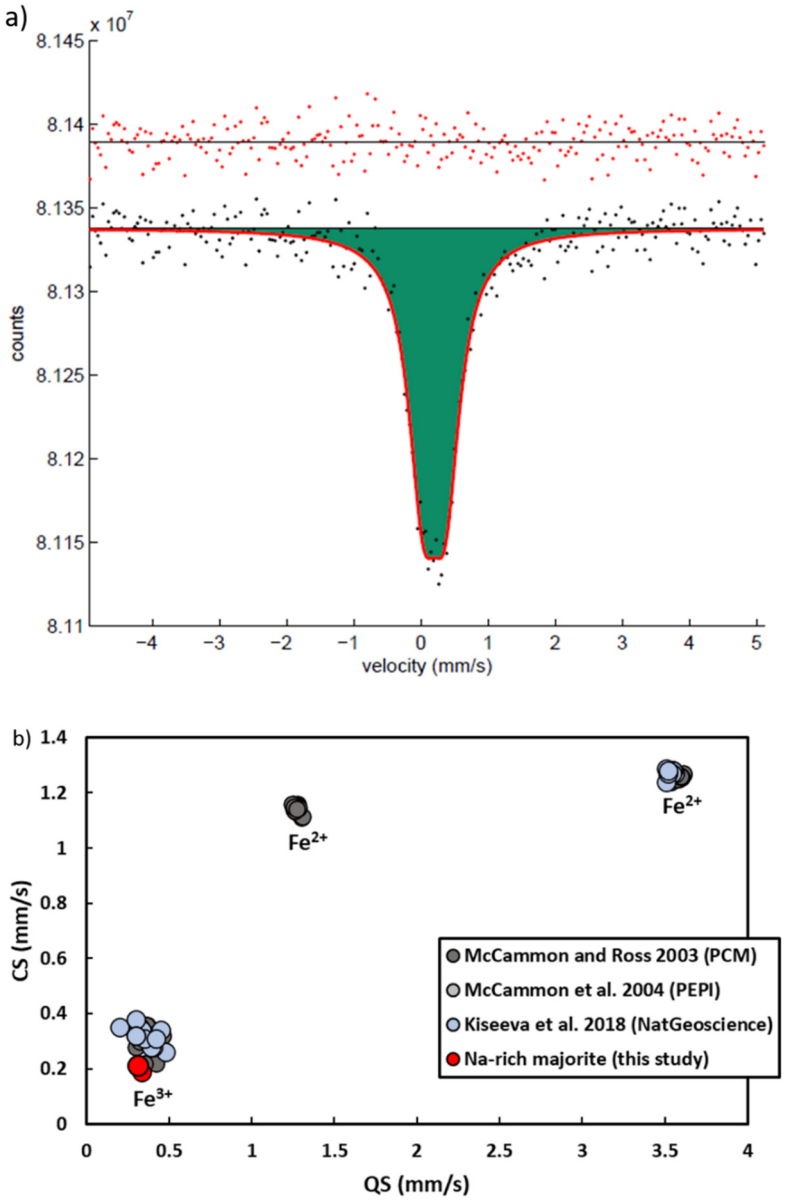

Fig. 3.2-14: a) Room temperature Mössbauer spectrum of Na-rich eclogitic majorite fitted with one doublet assigned to Fe^{3+}, b) Hyperfine parameters plotted with literature data for both natural (Kiseeva *et al.* 2018, Nat. Geo, 11: 144) and synthetic (McCammon and Ross 2003, Phys. Chem. Minerals 30: 206; McCammon *et al.* 2004, Phys. Earth Planet. Inter., 143: 157) majorites.

Our results appear to be in good agreement with previous investigations of $Fe^{3+}/\sum Fe$ in hydrous P-type majorites where a predominance of Fe^{3+} was observed (Fig. 3.2-15). In addition, the possibility for E-type majorite to host Fe entirely as Fe^{3+} has important implications for the formation of diamonds by redox reaction as well as for the rheology of subducted slabs.

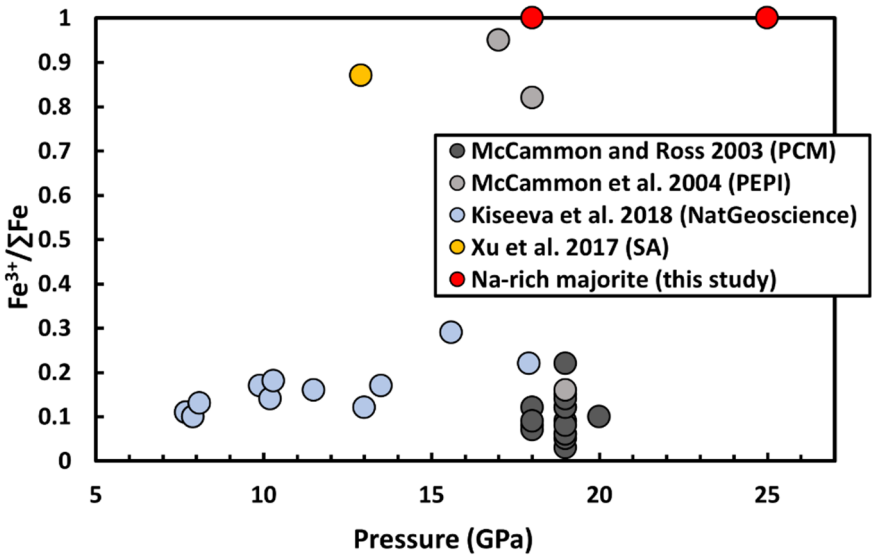

Fig. 3.2-15: Variation of $Fe^{3+}/\sum Fe$ with pressure for natural E-type majorite (Xu *et al.* 2017, Sci. Adv., 3: e1601589) compared to natural and synthetic P-type majorites.

j. *The oxygen fugacity of serpentinites during subduction (L. Eberhard, D.J. Frost and C.A. McCammon)*

Serpentinites formed at the ocean floor contain a significant amount of magnetite but the serpentine minerals themselves also have a large ferric Fe component. The bulk $Fe^{3+}/\Sigma Fe$ ratio of typical serpentinites is in the range of 0.2-0.6. Although the dehydration of serpentinites in subduction zones is well investigated, the effect of ferric Fe on mineral phase relations has not been examined to date. This study is aimed at determining the relationship between the ferric Fe content and the oxygen fugacity fO_2 in subducted serpentinites. The oxygen fugacity will ultimately determine the redox state of fluids produced by serpentinite dehydration.

We performed multianvil experiments on natural antigorite ($Fe^{3+}/\Sigma Fe$ = 0.3) and lizardite ($Fe^{3+}/\Sigma Fe$ = 0.7) powders across the serpentine dehydration reaction at subduction zone conditions. The fO_2 was buffered by various metal-oxide pairs or monitored through a sliding redox sensor. Mössbauer spectroscopy was used to determine the $Fe^{3+}/\Sigma Fe$ ratio of the run products. In lizardite the $Fe^{3+}/\Sigma Fe$ ratio increases with increasing fO_2 and decreases with increasing temperature. The results also revealed a preferred partitioning of Fe^{3+} onto the serpentine octahedral site at elevated PT conditions. Stoichiometric relations indicate ferric Fe to be charge balanced by Al on the tetrahedral site, which can be described by the ferri-alumina-Tschermak component $Mg_2Fe^{3+}AlSiO_5(OH)_4$. For antigorite, the tetrahedral site was found to

not equilibrate within experimental time scales, although sliding redox sensors adjusted to the oxygen fugacity imposed by the antigorite samples. Comparison of the experimental data from lizardite with natural antigorite samples showed that Al and Fe^{3+} contents of lizardite behave similarly to antigorite with respect to pressure and temperature. This allowed lizardite to be used as an analogue for antigorite in the development of a thermodynamic description of the ferric iron component. Thermodynamic properties for the new ferri-alumina-Tschermak endmember were derived for both lizardite and antigorite. These data allow the fO_2 resulting from ferric-ferrous iron equilibria to be calculated for a serpentinite assemblage during subduction.

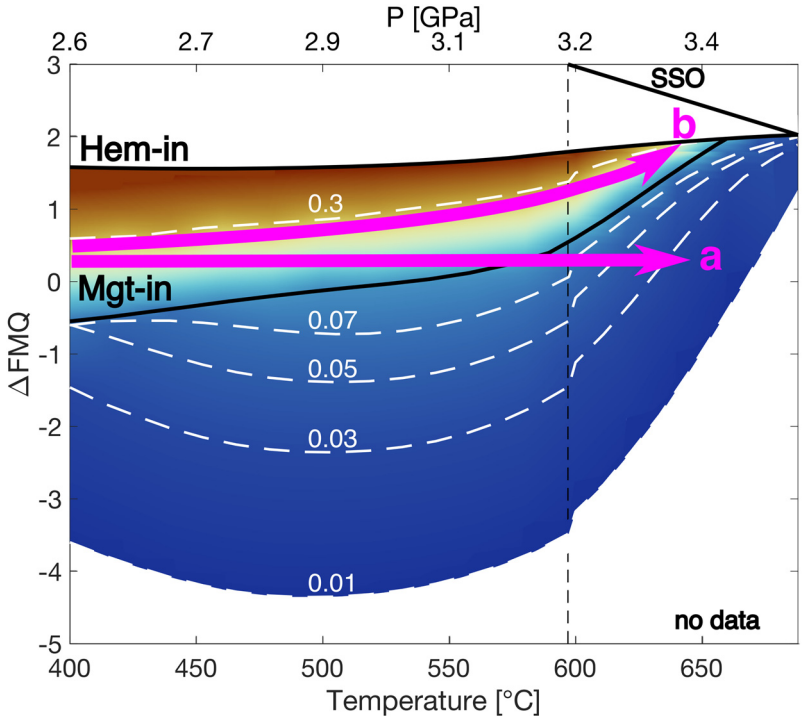

Fig. 3.2-16: The fO_2 calculated along a *PT*-gradient of the northern Honshu subduction zone. Shown are also the Mgt-in, Hem-in and sulphide-sulphate equilibrium (SSO). The vertical line marks the onset of the serpentine dehydration reaction. Contours show the bulk $Fe^{3+}/\Sigma Fe$ ratio of the serpentinite rock. Colours show regions of different bulk $Fe^{3+}/\Sigma Fe$ ratio between 0.01 and 0.4. Serpentinites with higher $Fe^{3+}/\Sigma Fe$ ratios have an fO_2 buffered at the magnetite-hematite equilibrium. Path "a" and "b" show two different evolutions for subducted serpentinites. In "a" the fO_2 is fixed *i.e.*, buffered externally by a redox equilibrium. The $Fe^{3+}/\Sigma Fe$ ratio decreases and Mgt disappears at T>550 °C. "b" indicates a fixed bulk $Fe^{3+}/\Sigma Fe$ ratio, in which case the fO_2 increases and converges towards the magnetite-hematite equilibrium.

Figure 3.2-16 shows the evolution of the fO_2 for a typical serpentinite during subduction as obtained from the thermodynamic model combined with mass balance calculations. The mineralogy and the fO_2 were found to strongly depend on the bulk $Fe^{3+}/\Sigma Fe$ ratio. If the fO_2 were fixed, which might arise from an external redox buffer present in the subducted

assemblage potentially involving a fluid phase, the bulk $Fe^{3+}/\Sigma Fe$ ratio of a serpentinite would decrease during subduction (path "a" in Fig. 3.2-16). Serpentinites with a bulk $Fe^{3+}/\Sigma Fe$ ratio below 0.1 will leave the Mgt-stability field. However, reduction can only occur if a complementary oxidation reaction can take place. Serpentinites do not generally contain large amounts of organic material or graphite, which might contribute to such an external redox reaction. Since the sulphide-sulphate equilibrium (SSO) is more than 2 log unites above the FMQ buffer, sulphur also cannot serve as a redox partner. It is thus more likely that the bulk $Fe^{3+}/\Sigma Fe$ ratio in the serpentinite remains constant during subduction and the fO_2 changes instead. In this case subducting serpentinites will evolve towards higher fO_2 (path "b" in Fig. 3.2-16). For typical serpentinites the fO_2 is constrained in a narrow range between ΔFMQ+0.5 - ΔFMQ+2 and reaches the magnetite-hematite equilibrium at temperatures > 550 °C. The coexistence of magnetite and hematite will further buffer the fO_2. Fluids released from subducted serpentinites have an fO_2 above the FMQ buffer but still below the SSO equilibrium. They would consequently contain oxidised carbon but reduced sulphur species. Even though serpentinites represent a relatively oxidised lithology in subduction zones, there does not seem to be a viable mechanism for communicating their oxidation state with the overlying mantle wedge through the dehydration process.

k. *Melting phase relations of subduction zone minerals (C. Melai and D.J. Frost, in collaboration with Y. Furukawa, A. Ishida, A. Suzuki/Sendai and E. Füri/Nancy)*

Subduction zones play a key role in the exchange of volatile components between Earth's external and internal reservoirs. As the different assemblages comprising layers within the subducting oceanic lithosphere undergo prograde metamorphism a sequence of hydrous mineral phases is produced that are important not just for the passage of water into the mantle but also for other volatile components such as nitrogen, halogens and potentially noble gases. In this study we are examining the phase relations of hydrous aluminosilicate minerals that form in sedimentary layers during early prograde metamorphism of the oceanic lithosphere that may be potential hosts for such volatile components. As these sedimentary layers often encounter conditions where they undergo partial melting, it is important experimentally to be able to identify conditions where such hydrous minerals can be directly equilibrated with partial melts. A further complication is that if partitioning of volatile components is to be studied, it is important to be able to quench these melts as glasses, which depends to some extent on the compositions of the melts and pressure of the experiments. The goal is to ultimately constrain partition coefficients for trace and volatile elements between hydrous minerals and melts.

In order to investigate hydrous aluminosilicate melting phase relations, natural mineral starting compositions were selected of montmorillonite, $(Na,Ca)_{0.33}(Al,Mg)_2(Si_4O_{10})(OH)_2 \cdot nH_2O$, and phengite $K(AlMg)_2(OH)_2(SiAl)_4O_{10}$. Experiments were performed in the multianvil at subarc conditions of 2-4 GPa and temperatures between 600-900 °C. Glycine ($C_4H_5NO_2$) was added to some experiments to examine nitrogen partitioning and experiments were run both under

oxidizing (RuO_2) and reducing (provided by the C residual product of the glycine decomposition) conditions. Run products were investigated using the electron microprobe and with X-ray diffraction.

Preliminary results show that the montmorillonite composition at 750 °C under both oxidizing and reducing conditions crystalizes a phengite structured phase with ammonium substituted entirely for potassium, as the bulk composition contains no potassium, which coexists with partial melt. The melt is found to quench to a homogeneous glass which contains some bubbles. The fact that the presence of nitrogen has stabilized an ammonium bearing mineral, that likely does not exist in the Earth and that the glasses contain some bubbles implies that the samples have been doped too highly in additional volatile components. At higher temperatures of 900 °C the composition is almost entirely melted but coexists with large crystals of the amphibole gederite $Mg_2(Mg_3Al_2)(Si_6Al_2)O_{22}(OH)_2$. In the phengite experiments at both reducing and oxidising conditions the run product comprises phengite, coesite and some rutile crystals and starts to coexist with pockets of partial melt at 750 °C. From a study of the phase relations we aim to identify the conditions where volatile components such as nitrogen may be passed to higher pressure phases and constrain the proportion of volatiles lost from the slab due to partial melting.

l. *The role of residual apatite in controlling the trace element budget of subduction zone fluids (M. Putak Juriček and H. Keppler)*

Reports from studies on natural eclogites from exhumed HP and UHP terranes suggested that most of the trace element budget of residual slab lithologies may be stored in accessory minerals. Consequently, the subduction zone fluids equilibrating with eclogites at peak metamorphic conditions were expected to be depleted in specific trace elements, which could be mostly retained by key accessory phases.

Apatite is a very common accessory mineral observed in eclogites. Its structure allows for incorporation of a number of trace elements. Considerable amounts of Sr^{2+}, Ba^{2+}, Pb^{2+} and Eu^{2+} had been observed to readily substitute for the seven-fold coordinated Ca^{2+} in both natural and synthetic apatites. When a trivalent cation, such as REE^{3+}, substitutes for Ca^{2+}, charge compensation can be achieved by replacement of a $(PO_4)^{3-}$ group by $(SiO_4)^{4-}$. Quadrivalent elements, such as U^{4+} and Th^{4+}, had been reported to replace 2 Ca^{2+} by forming a vacancy in the apatite structure. Considering that many of these elements are often used as a proxy to elucidate different subduction zone processes, the role of apatite in the partitioning of trace elements between metamorphic slab lithologies and various subduction zone fluids (aqueous fluids, hydrous silicate melts, supercritical fluid-melt mixtures) needs to be carefully investigated. In a previous experimental study, the trace element partitioning between apatite and hydrous silicate melts had been investigated at pressures of 2.5 to 4.5 GPa and temperatures between 750 and 1050 °C. These experiments demonstrated that in equilibrium with a silicate

melt, apatite has no strong effect on the trace element budget of the melt phase. Somewhat in contrast to the results of that study, extremely REE-enriched apatites had been found in Dabieshan (China) coesite-bearing eclogites. However, Dabieshan eclogites had experienced a fairly low geothermal gradient and thus may have been fluxed with dilute aqueous fluids at peak metamorphic conditions instead of having experienced partial melting. Therefore, the possibility arises that in equilibrium with aqueous fluids, which should be the dominant mobile phase in cold-to-moderate-temperature subduction zones, apatite may retain REE much more efficiently.

To test this hypothesis, we performed a two-week piston cylinder experiment at 3.5 GPa and 600 °C using a trace element doped GLOSS (GLObal Subducting Sediment) starting material. Phosphorous was introduced via the fluid phase by diluting concentrated phosphoric acid with distilled H_2O. The initial fluid:rock ratio was 1:3 and the added amount of phosphorous corresponded to approximately 1 wt. % P_2O_5 by the weight of solid material. The high concentration of P_2O_5 was necessary to produce a sufficient proportion of apatite for analysis. The sample was embedded in epoxy and all mineral compositions were measured by electron microprobe and LA-ICP-MS to determine major and trace element concentrations, respectively. Microprobe major element oxide concentrations (CaO for apatite and SiO_2 for silicates) were used as internal standards for LA-ICP-MS analyses. At the investigated conditions, the phosphorous-bearing GLOSS composition produced a metamorphic equilibrium assemblage consisting of clinopyroxene, phengite, lawsonite, garnet, coesite and accessory apatite, rutile and allanite. The sample contained several apatite grains > 15 µm in diameter, which were suitable for LA-ICP-MS analysis. We used the measured mineral compositions to determine trace element partition coefficients between all major minerals and apatite (Fig. 3.2-17).

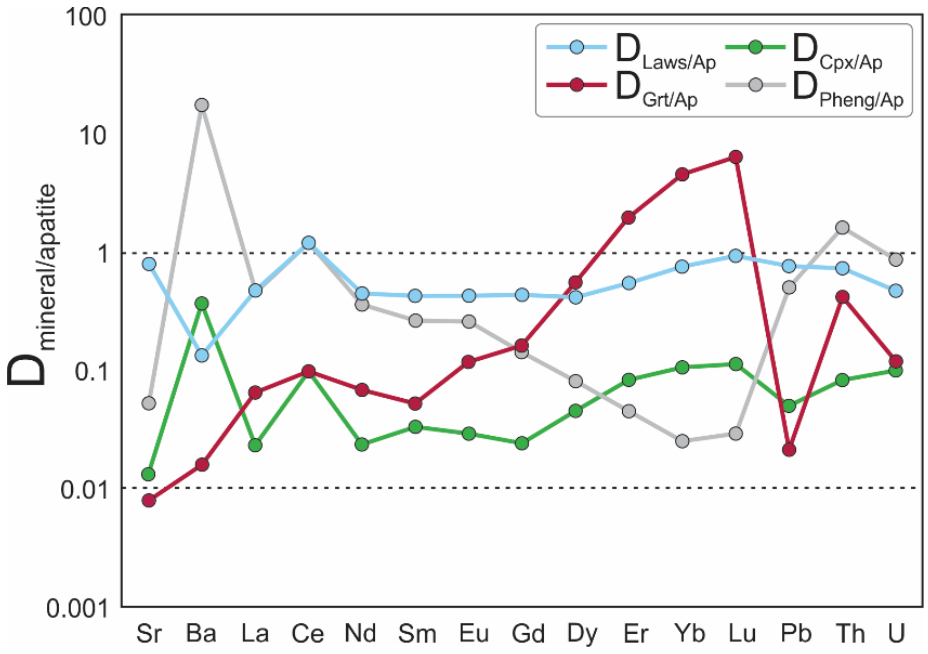

Fig. 3.2-17: Experimentally measured mineral/apatite trace element partition coefficients.

The average reported P_2O_5 concentration of both subducting sediments and MORB is around 0.2 wt. % and, given the stoichiometric proportion of P_2O_5 in apatite, no more than 0.5 wt. % of apatite should be present in slab lithologies of most subduction zones worldwide. In addition, due to the high solubilities of phosphorous in garnet and kyanite, reported by a previous study, the proportion of apatite at sub-arc depths may be significantly lower than 0.5 wt. %, since most of the phosphorous budget could be stored in garnet. Since the proportion of apatite in slab lithologies is an order of magnitude lower than the proportions of other solid phases, it cannot exert considerable control over the subduction zone fluid composition unless $D_{fluid/apatite}$ are at least two orders of magnitude lower than $D_{fluid/mineral}$ for clinopyroxene, phengite, lawsonite and garnet. The results presented in Figure 3.2-17 indicate that is not the case – most of the measured $D_{mineral/Ap}$ are generally higher than 0.01 for the trace elements of interest. In particular, there is very little trace element fractionation between apatite and lawsonite. At peak metamorphic conditions, phengite and lawsonite are expected to be the main hosts for Sr, Ba, REE, Pb, Th and U in eclogitic residues. Additionally, a considerable proportion of the HREE budget may be stored in garnet.

The results of this study suggest that even along low geothermal gradients, the role of apatite in controlling the trace element budget of subduction zone fluids should be negligible and observations of REE-rich apatites in Dabieshan eclogites are likely reflecting secondary enrichment processes operating at low temperatures. Furthermore, the results underline the importance of direct measurements of trace element partition coefficients at subduction-zone-relevant pressures and temperatures. While the information from natural samples is invaluable, the interpretation of primary mineral assemblages in HP and UHP eclogites is not straightforward due to retrograde overprinting and other exhumation-related processes.

m. *The bulk composition of saline fluids released from the basaltic layer of the subducted slab (G. Rustioni, A. Audétat and H. Keppler)*

Aqueous fluids are liberated from subducting oceanic slabs when hydrous minerals contained in them break down. Such fluids are likely responsible for melting in the mantle wedge and therefore for triggering arc magmatism. However, although considerable effort has been dedicated to characterize such fluids, their exact composition is still largely unknown. Previous work focused mainly on how the composition of the fluid is affected by the pressure and temperature at which it is released by the slab. However, several studies demonstrated that fluid salinity is also a key parameter that needs to be considered for major and trace elements solubility in aqueous fluids. The eclogite-water ± NaCl system was therefore studied at different pressures and temperatures in order to understand the effect Cl on the bulk composition of a fluid released from the basaltic layer of the subducted slab.

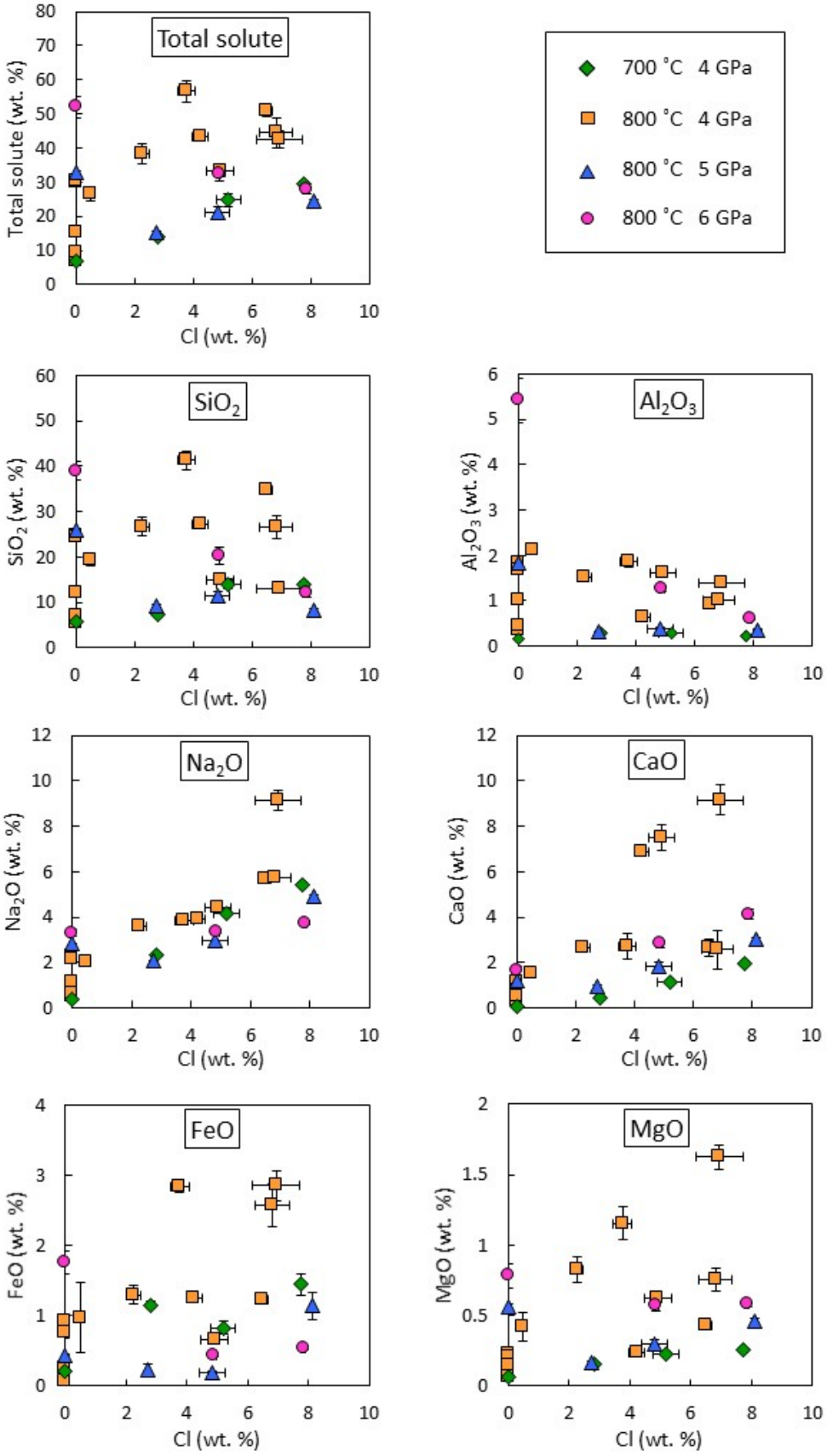

Fig. 3.2-18: Bulk composition of saline fluids in equilibrium with an eclogitic assemblage from diamond trap experiments conducted at 4 - 6 GPa and 700-800 °C.

High-pressure experiments were conducted using either a piston cylinder or multianvil apparatus at conditions ranging from 4 to 6 GPa and 700 to 800 °C with durations of 3-7 days. In these experiments, the diamond trap technique was used to determine the composition of the fluid. This method uses a diamond powder layer between two layers of MORB starting material. During the experiment, it is assumed that only the fluid phase can circulate inside the diamond trap. Therefore, any solid material found in this portion of the capsule after the experiment is attributed to the precipitation from the fluid during quench and is thus regarded as a fluid component. The composition of the fluid was determined by laser ablation ICP-MS performed on the frozen diamond trap after each experiment, so that both solid precipitates and the frozen fluid could be analyzed together.

The results from these experiments are shown in Figure 3.2-18. The total solute content (considering SiO_2, Al_2O_3, Na_2O, CaO, FeO, MgO and Cl) appears to be highly dependent on fluid salinity, and the average ranges from about 20 wt. % in experiments conducted in the absence of Cl to about 40 wt. % for experiments with more than 6 wt. % of Cl. Temperature also seems to have a significant effect on the bulk composition, but the enhancement in solubility caused by increasing salinity at 4 GPa is similar both at 700 and 800 °C. On the other hand, increasing pressure appears to decrease the effect of Cl at 5 GPa or even reverse it at 6 GPa, where fluids with high salinity yield lower solute contents. In each experiment, SiO_2 represents the major solute, accounting alone for about 65 % of the total solute content. Both SiO_2 and Al_2O_3 are not particularly sensitive to fluid salinity at low pressure, being more affected by increases in pressure and temperature. At 6 GPa however, a markedly decrease in their solubility with addition of Cl is observed. On the other hand, Na_2O and CaO concentration in the fluid is mainly controlled by fluid salinity, which enhances their solubility. A similar behaviour is observed for FeO and MgO at 4 GPa, while at higher pressures, the effect of salinity appears to be again reduced for both oxides. Overall, the results of this study show that fluid salinity is a very important parameter to consider together with pressure and temperature for the determination of the bulk composition of a fluid released during subduction by the basaltic layer of the slab.

3.3 Mineralogy, Crystal Chemistry and Phase Transformations

The nature of minerals and their stabilities profoundly affect properties and processes of Earth's deep interior. This section highlights new discoveries and ongoing progress related to basic questions about the Earth and other planets. All contributions explore phase transformations and/or crystal chemistry of minerals at relevant pressure-temperature-composition conditions. The first four contributions report new discoveries involving $MgSiO_3$ silicate polymorphs, AB_2O_4 oxides and A_2CO_4 tetracarbonates using different high-pressure apparatus coupled with *in situ* X-ray diffraction and Raman spectroscopy. A strong negative temperature dependence of the akimotoite-bridgmanite transition can cause stagnation of cold slabs above the 660-km seismic discontinuity and explain significant depression of the 660-km seismic discontinuity observed down to 750 km beneath subduction zones. High-pressure transitions in $MgAl_2O_4$ are important for identifying and understanding potential hosts of aluminium in Earth's mantle. The $CaTi_2O_4$-type phase may be stable in basaltic and continental crust compositions over a wide pressure range and discovery of a new $MgFe_2O_4$ high-pressure phase provides new insight for understanding mantle redox state. Exploration of calcium (Ca_2CO_4) and strontium (Sr_2CO_4) tetracarbonates at high pressure demonstrates that tetracarbonate polymorphs in the system CaO-CO_2 may be stable under conditions of Earth's transition zone and uppermost lower mantle.

The next four contributions explore substitution mechanisms of volatile-related species that influence the nature of geochemical cycles. New measurements of hydrous forsterite indicate that protons substitute predominantly on Si sites, not Mg sites as previously inferred. This substitution mechanism is demonstrated to occur also in Fe-bearing olivine using single crystal neutron diffraction. Iron is the most abundant transition metal in Earth's mantle and exists primarily as Fe^{2+} or Fe^{3+}, so iron defect chemistry can influence volatile cycles. New measurements of ferric iron-dominated bridgmanite show that oxygen vacancies decrease with increasing pressure. The incorporation of hydrogen into iron sulphide is a viable mechanism to remove hydrogen during the ancient "Hadean Matte" period. Results from *in situ* neutron diffraction experiments on iron sulphide provide a possible scenario to explain the rapid increase in mantle oxidation state following core formation.

The final five contributions probe materials at wide-ranging conditions from extreme high pressure to ancient environments on Earth's surface. Innovative nuclear magnetic resonance measurements in the diamond anvil cell reveal nuclear spin crossover in dense hydrogen which may be important for stabilising magnetospheres of gas and ice giant planets. Density functional theory combined with high-pressure nuclear magnetic resonance shows profound changes in proton dynamics of ice-VII above 130 GPa. Single crystal X-ray diffraction reveals a Verwey-type transition in the novel iron oxide phase Fe_5O_6, a potential endmember of lower mantle oxides. The profound difference in solubility of Fe(II) and Fe(III) in aqueous solutions provides a mechanism for the treatment of antimony-contaminated groundwater, and new insight into processes in ancient oceans through studies of banded iron formations.

a. *Strong negative temperature dependence of the akimotoite-bridgmanite transition in $MgSiO_3$ using a multianvil press with* in situ *X-ray diffraction (A. Chanyshev, T. Ishii, E.J. Kim, S. Bhat/Hamburg, D. Bondar, R. Farla/Hamburg and T. Katsura)*

The 660-km seismic discontinuity is the boundary between Earth's upper and lower mantle, and is attributed to the bridgmanite-forming reaction, presumed to be the dissociation of ringwoodite to bridgmanite plus ferropericlase (post-spinel phase transition). A number of seismic studies have showed a significant depression of the 660-km seismic discontinuity down to 750 km beneath subduction zones. Recent experimental studies have revealed that the post-spinel phase transition has a negative but gentle Clapeyron slope (-0.9 MPa/K on average), which varies the depth of the 660-km seismic discontinuity within 630-670 km and therefore cannot cause depressions beneath subduction zones. One of the most likely candidates to explain the deep depression of the 660-km seismic discontinuity is the akimotoite-bridgmanite phase transition, since it has a steep Clapeyron slope (-3.2 MPa/K) and occurs at similar pressures to the post-spinel transition. Moreover, akimotoite is expected to be an abundant mineral in harzburgitic and pyrolitic layers of subducting slabs in the transition zone.

Our recent studies at the SPring-8 synchrotron facility have suggested that conventional high-pressure/-temperature experiments to determine phase boundaries might contain significant errors because of drastic changes in sample pressure upon heating and therefore lead to misidentification of stable phases due to sluggish kinetics. In order to obtain reliable phase relations that avoid these problems, we have re-determined the akimotoite-bridgmanite phase transition boundary in $MgSiO_3$. Experiments were performed at beamline P61B at DESY (Hamburg, Germany) using a multianvil press with *in situ* X-ray diffraction following a new strategy: (1) phase stability was determined by the change in abundance of already coexisting akimotoite and bridgmanite, not by the formation of bridgmanite from akimotoite; (2) two diffraction patterns of the sample were collected at a fixed press load and temperature to observe the growth of stable phases without sudden pressure changes associated with temperature changes; and (3) experimental conditions were kept close to the phase boundary in order to maintain coexistence of two phases.

Transition pressures of the akimotoite-bridgmanite boundary over the temperature range 1250-2085 K were found to be 20.5-24.5 GPa, which correspond to 585-680 km depth (Fig. 3.3-1). The transition has a steep negative boundary (-21.2 MPa/K) at temperatures below 1300 K. The boundary extrapolated to 1100-1250 K (temperatures of a cold slab at the studied pressures) is located at 24.5-27.3 GPa, corresponding to depths of 680 to 750 km. Therefore, the akimotoite-bridgmanite transition can significantly depress the 660-km seismic discontinuity down to 750 km beneath cold subduction zones. Above 1300 K the transition boundary flattens out and the slope is estimated to be -2.7 MPa/K. Phase transformations with negative Clapeyron slopes hinder mantle convection because of induced positive buoyancy forces. The extremely steep Clapeyron slope of the akimotoite-bridgmanite transition at low temperatures can therefore cause stagnation of cold slabs above the 660-km seismic discontinuity, which is consistent with seismic observations beneath cold subduction zones, *e.g.*, Tonga zone.

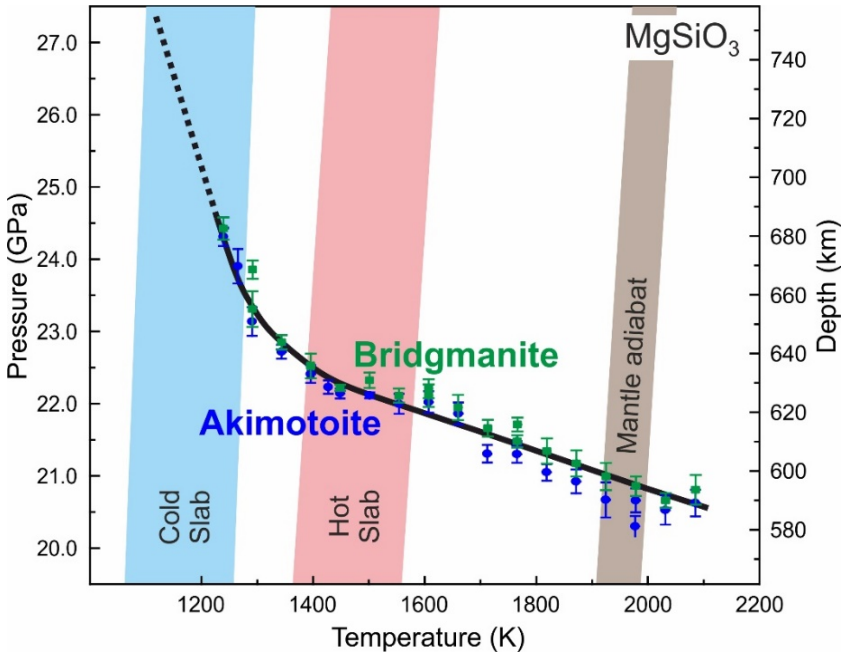

Fig. 3.3-1: Comparison of the $MgSiO_3$ akimotoite-bridgmanite phase transition boundary (solid black curve) with pressure-temperature (P-T) profiles in Earth's mantle. The dotted line represents linear extrapolation of the boundary below 1290 K. Green squares and blue circles indicate the P-T conditions where the ratio of bridgmanite to akimotoite increased or decreased, respectively.

b. *Crystal structures of new low-density $CaFe_2O_4$-related and $CaTi_2O_4$-type $MgAl_2O_4$ phases (T. Ishii, G. Criniti, E. Bykova, L.S. Dubrovinsky, T. Katsura, H. Arii/Miyazaki; H. Kojitani and M. Akaogi/Tokyo)*

High-pressure polymorphs of $MgAl_2O_4$ with calcium ferrite (CF)- and calcium titanate (CT)-type structures are important and abundant components of basalt, upper continental crust, and sediment assemblages that are stable under lower-mantle conditions. High-pressure transitions in $MgAl_2O_4$ have thus been an important subject for identifying and understanding potential hosts of aluminium in Earth's mantle.

In this study, we synthesised single crystals of CT-type and new low-density $CaFe_2O_4$ (LD-CF)-related $MgAl_2O_4$ at 27 GPa and 2500 ºC, and also CT-type $MgAl_2O_4$ at 45 GPa and 1727 ºC using conventional and advanced multianvil technologies, respectively. The structures of CT-type and LD-CF-related $MgAl_2O_4$ were determined by single-crystal X-ray diffraction. Figure 3.3-2 shows the crystal structures of $MgAl_2O_4$ high-pressure polymorphs and their density relationship. The CT-type phase (Z = 4, space group: *Cmcm*) has an AlO_6 octahedral site and a MgO_8 bicapped trigonal prism with two longer cation-oxygen bonds. The LD-CF-related phase has a novel structure with orthorhombic symmetry (Z = 4, space group: *Pnma*). The structural framework is comprised of tunnel-shaped spaces constructed of edge- and corner-shared AlO_6 and a 4+1 AlO_5 trigonal bipyramid in which MgO_5 trigonal bipyramids are

accommodated. CF-type $MgAl_2O_4$ also has the same space group (*Pnma*), but a slightly different atomic arrangement with Mg and Al coordination numbers of 8 and 6, respectively. The LD-CF-related phase has the lowest density (3.50 g/cm^3) among $MgAl_2O_4$ polymorphs, despite high-pressure synthesis from a spinel-type phase (3.58 g/cm^3), indicating that the LD-CF-related phase formed via back transformation from a high-pressure phase during sample recovery. Combined with previously determined phase relations, the phase transition between CF- and CT-type $MgAl_2O_4$ is expected to have a steep Clapeyron slope. Therefore, the CT-type phase may be stable in basaltic and continental crust compositions at temperatures higher than the average mantle geotherm over the wide pressure range of the lower mantle. The LD-CF-related phase could occur in shocked meteorites and used for estimating shock conditions.

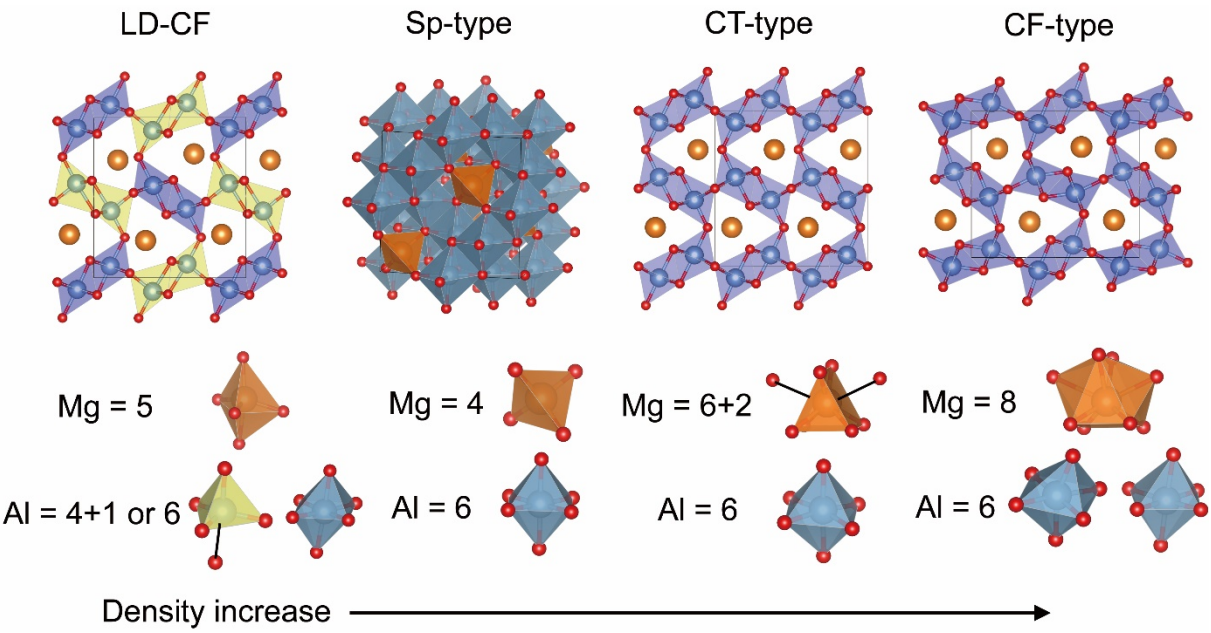

Fig. 3.3-2: Structural comparison of $MgAl_2O_4$ compounds at ambient conditions. Densities of $MgAl_2O_4$ phases increase from left to right. Numbers below the structures give coordination numbers of Mg and Al. The longest oxygen-cation bonds in the polyhedra are indicated by thick black lines, which contribute correspondingly less to cation coordination. Blue octahedra and yellow trigonal bipyramids accommodate Al cations. Orange spheres indicate Mg cations. In the Sp-type phase, Mg cations are accommodated in tetrahedral sites. Red spheres indicate oxygen atoms and unit cells are shown as thin solid lines.

c. *Discovery and crystal structure of a new $MgFe_2O_4$ high-pressure phase (T. Ishii, N. Miyajima, R. Sinmyo/Tokyo, H. Kojitani/Tokyo, D. Mori/Higashimita, Y. Inaguma/Tokyo and M. Akaogi/Tokyo)*

Crystal structures and phase relations of spinel-structured minerals at high pressure and temperature are important for understanding the physics and chemistry of Earth's mantle,

particularly its redox state. Spinel-type $MgFe_2O_4$ and its high-pressure phase have been found in diamonds and shocked meteorites. Therefore, high-pressure and high-temperature phase relations in the $MgFe_2O_4$ system can provide information about diamond formation and shock events involving meteorites. High-pressure forms of spinel-type $MgFe_2O_4$ have been intensively investigated, including reports of an unknown $MgFe_2O_4$-structured phase.

In this study, we synthesised a previously unknown $MgFe_2O_4$ phase (space group, *Pnma*) at 25-27 GPa and 1000-1200 °C. We determined its crystal structure using powder X-ray diffraction and transmission electron microscopy and investigated its compression behaviour in a diamond anvil cell. So far, $CaFe_2O_4$-, $CaTi_2O_4$-, and $CaMn_2O_4$-type structures have served to define the high-pressure spinel-type structures. Rietveld analysis of the novel compound revealed that it has features similar to those of conventional high-pressure structures, but its cation arrangement is very different (Fig. 3.3-3). This phase has a Z-shaped framework of edge-sharing $(Mg,Fe)O_6$ octahedra, with the other Mg and Fe cations randomly occupying one tetrahedral and two octahedral sites in tunnel spaces within the framework. The structure is similar to $Na_x(Fe,Ti)_xTi_{2-x}O_4$ phase ($0.75 \leq x \leq 0.9$) with $(Fe,Ti)O_6$ Z-shaped framework and tricapped-prism sites for Na. Compression data show ~ 6 % volume reduction at 16-20 GPa. The recovered phase may have transformed during decompression from a $Na_x(Fe,Ti)_xTi_{2-x}O_4$-type structure by shifting of cations in the tunnel spaces, probably due to cation-size misfit. Based on known phase relations, this phase may occur in impact craters and shocked meteorites and possibly plays an important role as a P-T indicator for shock events. The discovery of the novel $MgFe_2O_4$ phase highlights the necessity for careful phase identification of high-pressure phases of spinel-type structures by crystal structure refinement in experimental run products and natural samples due to their crystallographic similarity.

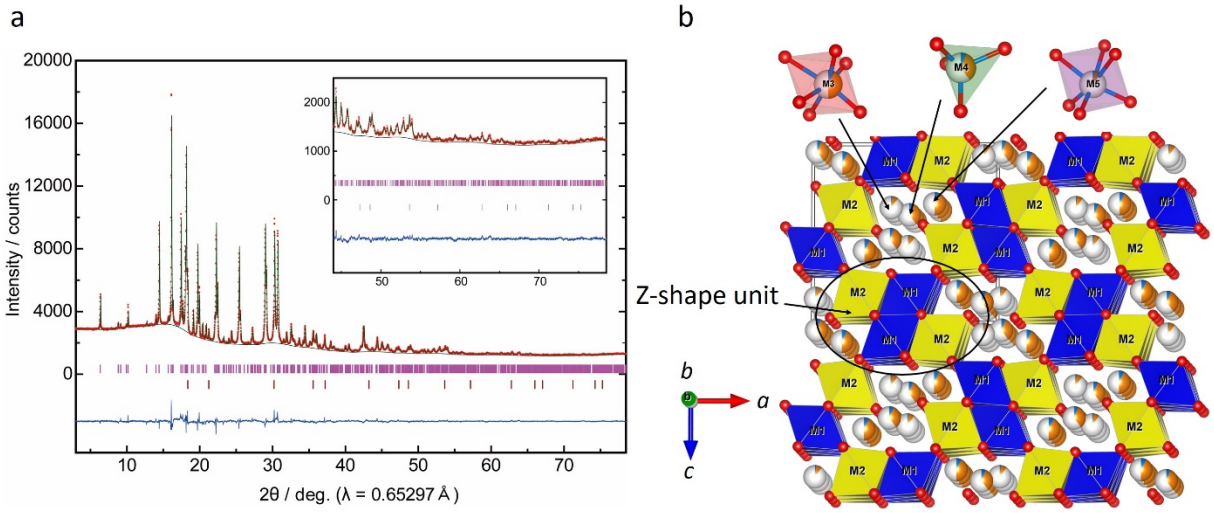

Fig. 3.3-3: a) Rietveld analysis of $MgFe_2O_4$ high-pressure phase. b) Crystal structure of novel $MgFe_2O_4$ high-pressure phase.

d. *Synthesis and characterisation of calcium (Ca_2CO_4) and strontium (Sr_2CO_4) tetracarbonates under extreme conditions (D. Laniel/Bayreuth, J. Binck and B. Winkler/Frankfurt, S. Vogel/Munich, T. Fedotenko/Bayreuth, S. Chariton/Chicago, V. Milman/Cambridge, V. Prakapenka/Chicago, W. Schnick/Munich, L.S. Dubrovinsky and N.A. Dubrovinskaia/ Bayreuth)*

Compared to the amount of carbon expected based on cosmochemical data, the amount in Earth's exosphere is small, suggesting that a significant amount of carbon is trapped in Earth's interior. As a mechanism for removing carbon from the exosphere and delivering it deep into the mantle, subduction of carbonates has focused considerable attention on this class of compounds. A remarkable discovery has been the so-called tetracarbonates – a novelty in the carbonate family – in which sp^3-hybridisation leads to the formation of CO_4^{4-} tetrahedra instead of the usual triangular sp^2-hybridised CO_3^{3-} groups. Up to now, tetracarbonates were synthesised at pressures > 70 GPa, which suggested that only the deep lower mantle could provide the required conditions for their occurrence. However, recent theoretical studies have indicated that tetracarbonate polymorphs in the system CaO-CO_2 may be stable at pressures and temperatures corresponding to conditions of Earth's transition zone and uppermost lower mantle.

We therefore investigated both the Ca-C-O as well as the Sr-C-O systems under extreme pressure and temperature conditions. From Raman spectroscopy as well as synchrotron single-crystal X-ray diffraction measurements, we found clear evidence for formation of the tetracarbonates Ca_2CO_4 and Sr_2CO_4, where the two compounds were determined to be isostructural. While Sr_2CO_4 was only studied at 92 GPa, its calcium counterpart was successfully synthesised between 20 GPa (~ 1800 K) and 89 GPa (2500 K) (Fig. 3.3-4). This

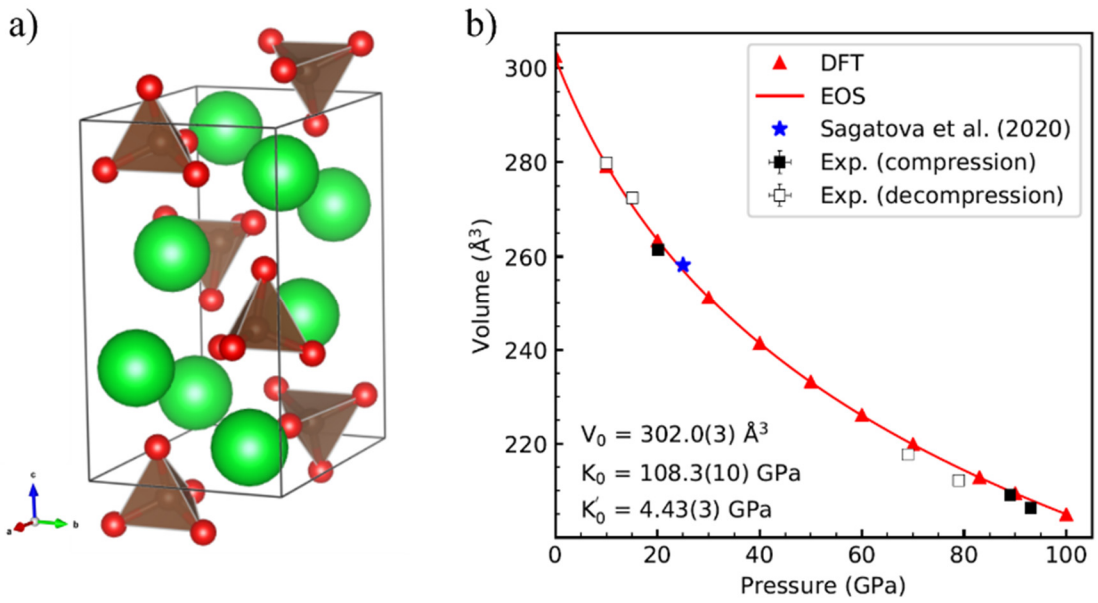

Fig. 3.3-4: a) Crystal structure of Ca_2CO_4 at 20 GPa. b) Pressure-volume evolution of the Ca_2CO_4 phase.

broad pressure-temperature stability range suggests the existence of Ca_2CO_4 in Earth's transition zone and most of the lower mantle. Density functional theory-based calculations indicate that, at least in the athermal limit, the phase assemblage $Ca_2CO_4 + 2SiO_2$ is more stable than 2 $CaSiO_3$ + CO_2 at high pressures. Our findings show that the sp^2-sp^3 transition in carbonates can be studied at pressures accessible using large-volume presses and thus may provide new insight into the deep global carbon cycle.

e. *Proton substitution mechanism in forsterite (H. Fei and T. Katsura)*

Protons can be incorporated into the crystal structure of olivine in either the Mg or Si sites. Since different incorporation mechanisms may have different effects on the point defect chemistry of olivine, understanding incorporation mechanisms is essential for investigating dynamics and geochemical circulation in the upper mantle. However, questions still remain about which site dominates for proton incorporation in olivine and have been under debate for decades. Previous experimental high-pressure studies indicate that the water solubility in olivine is nearly proportional to the water fugacity in the system, suggesting that protons mainly occupy Mg sites by the reaction:

$2\ H_2O + Mg_2SiO_4 = (4H)SiO_4 + 2\ MgO.$

In contrast, nuclear magnetic resonance studies and first-principle calculations suggest that the main proton components are attributed to Si sites substituted by four protons according to the following reaction:

$2\ H_2O + Mg_2SiO_4 = Mg_2(4H)O_4 + SiO_2.$

Measurements of Mg/Si atomic ratio as a function of water content and comparison with the ideal chemical formula can provide constraints for understanding proton substitution mechanisms in minerals. However, owing to the low solubility of water in olivine, the deviation of the Mg/Si ratio from the ideal formula is small, even for water-saturated systems, and thus conclusive results are difficult to obtain.

In this study, we carefully compared Mg/Si ratios in dry and hydrous Fe-free olivine by electron microprobe (EPMA). Five forsterite samples were prepared: a) hydrous forsterite with 2800 wt. ppm water synthesised from MgO, SiO_2, and $Mg(OH)_2$ with bulk composition $Mg_{2.2}SiO_{4.2}$ + 15 wt. % H_2O, (b) hydrous forsterite with 530 wt. ppm water synthesised from MgO, SiO_2, and $Mg(OH)_2$ with bulk composition $Mg_2Si_{1.1}O_{4.2}$ + 15 wt. % H_2O, (c) hydrous forsterite with 540 wt. ppm water synthesised from dry forsterite single crystal and $PtO_2.xH_2O$ as the starting material, (d) dry forsterite single crystal without water source, (e) dry forsterite single crystal as a standard for EPMA analysis. Samples (a)-(d) were prepared at 8 GPa, 1250 °C using a

multianvil press. The water content of the samples was determined by infrared spectroscopy analysis (Fig. 3.3-5).

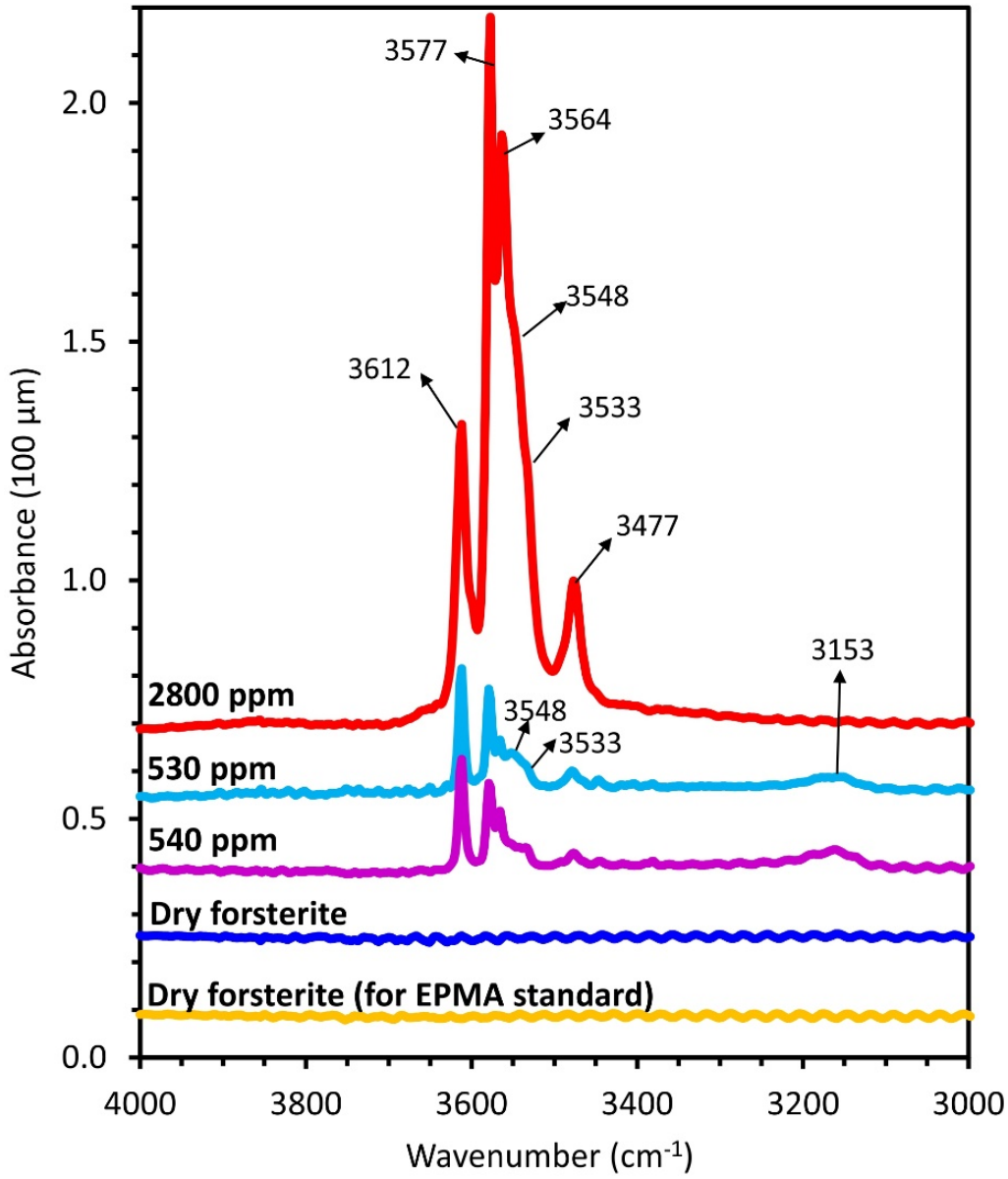

Fig. 3.3-5: Unpolarised FTIR spectra of five forsterite samples. The thickness of all samples is 100 µm. No baseline correction or thickness normalisation was performed on the spectra in this figure.

The results of EPMA analysis are shown in Figure 3.3-6. The sample with 2800 wt. ppm water has a Mg/Si atomic ratio of 2.044 ± 0.011. In contrast, the Mg/Si ratios in the 530 and 540 wt. ppm water samples are 2.010 ± 0.009 and 2.006 ± 0.006, respectively, whereas dry forsterite has a Mg/Si ratio of 1.999 ± 0.007. Therefore, with higher water content, the Mg/Si ratio is clearly higher, and demonstrates that protons are predominantly incorporated into Si sites in hydrous forsterite.

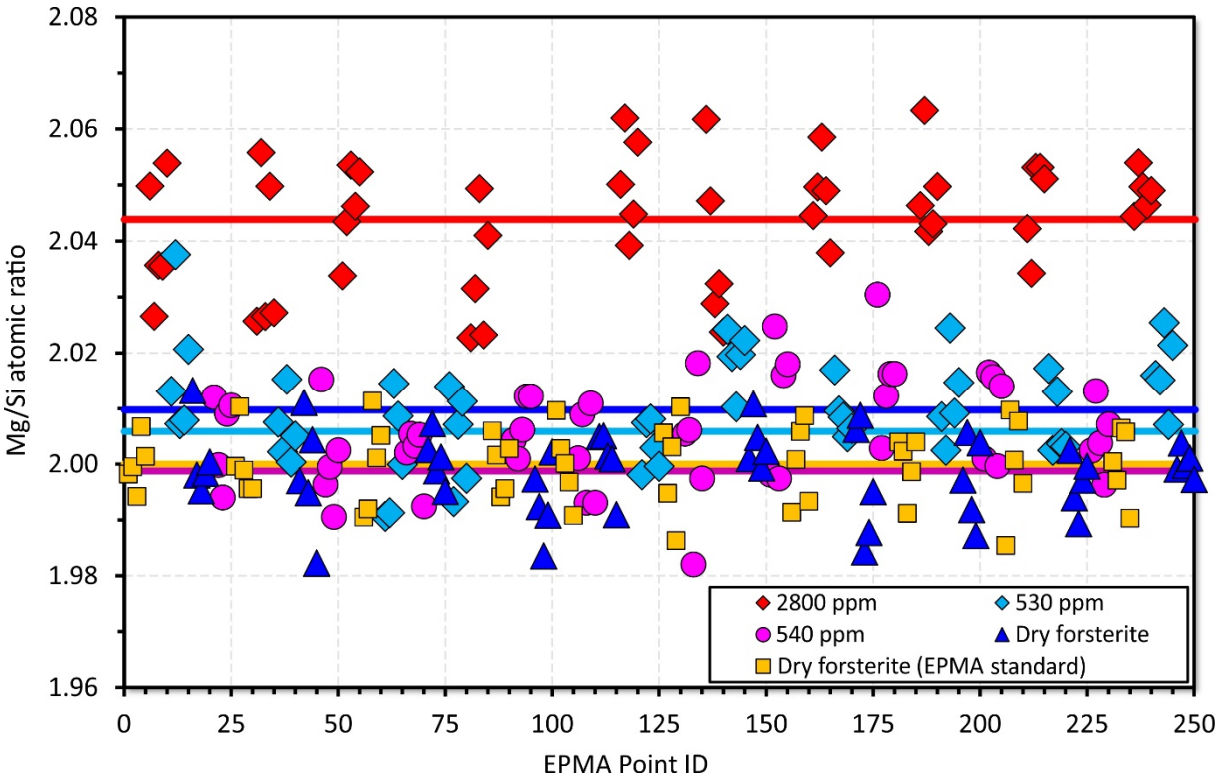

Fig. 3.3-6: Mg/Si atomic ratios in five forsterite samples. Although data points are largely scattered due to the resolution of EPMA, the sample with 2800 ppm water clearly has a higher Mg/Si ratio than samples with lower water content or dry samples. The five samples were analysed sequentially, *i.e.*, five points were analysed on each sample, with 25 points for the five samples in one cycle, for a total of 10 cycles (250 points) of measurements. No data points were discarded in the EPMA analyses.

f. *Understanding the hydrogen incorporation mechanism in olivine (N. Purevjav, T. Boffa Ballaran, H. Fei, A.C. Withers and T. Katsura, in collaboration with C. Hoffmann/Oak Ridge)*

Olivine is the predominant mineral in Earth's upper mantle. Thus, studying the crystal chemistry of olivine provides essential clues for understanding the physical and chemical properties of the upper mantle. Olivine can incorporate several hundreds to thousands ppm of water/hydrogen in its structure. Such hydrogen can be substituted by either Mg or Si cations in its crystal structure, which can significantly alter elemental diffusivity, electrical conductivity, and rheology of the host mineral. The effect of water on these physical properties has been intensively studied; however, the exact mechanisms by which hydrogen is incorporated into the crystal structure is still a matter of debate. Moreover, water content and hydrogen incorporation mechanisms in olivine seem to be greatly influenced by synthesis pressure and SiO_2 activity.

Single-crystal neutron diffraction is by far the most powerful technique for probing hydrogen in minerals. In this study, we aim to understand the hydrogen incorporation mechanisms in hydrous olivine crystals at various pressures and SiO_2 activity conditions in Fe-bearing and Fe-

free systems using single-crystal neutron diffraction in combination with polarized infrared (IR) spectroscopy for elucidating hydrogen positions and incorporation mechanisms in the olivine structure at an atomic scale.

We performed multianvil experiments in the MgO-SiO_2-$Mg(OH)_2$ and MgO-SiO_2-$Mg(OH)_2$-FeO systems at 10-12 GPa and 1523 K over heating durations of 48-96 h to produce chemically homogenous large single crystals of olivine. We successfully recovered hydrous forsterite and hydrous olivine single crystals up to 1 mm in size, which are suitable for single-crystal neutron diffraction. Absence of inclusions and/or twinning within recovered crystals was confirmed using single-crystal X-ray diffraction. Crystals with H_2O content of 0.2-0.3 wt. % were measured at the single-crystal neutron diffractometer TOPAZ at Oak Ridge National Laboratory (Fig. 3.3-7). Preliminary structure refinements suggest that substitution of hydrogen by Si at the tetrahedral site could be the dominant mechanism, at least in Fe-bearing olivine (Fig. 3.3-8).

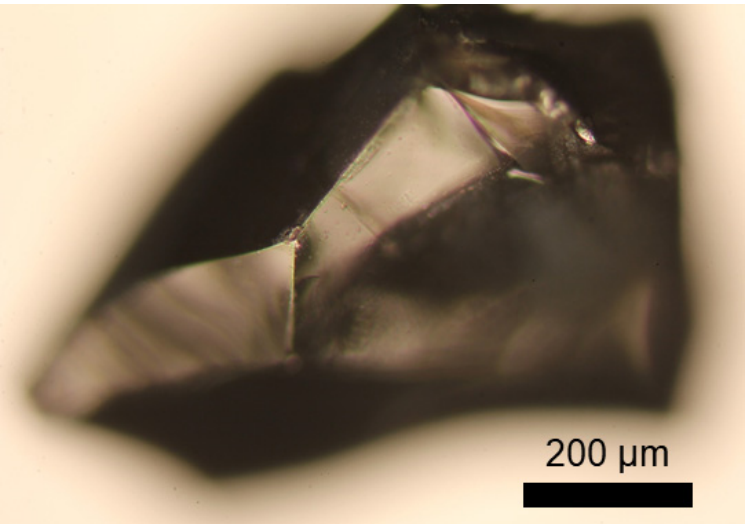

Fig. 3.3-7: Representative single crystal of hydrous forsterite synthesised by multianvil experiments. The crystal was measured at TOPAZ at Oak Ridge National Laboratory.

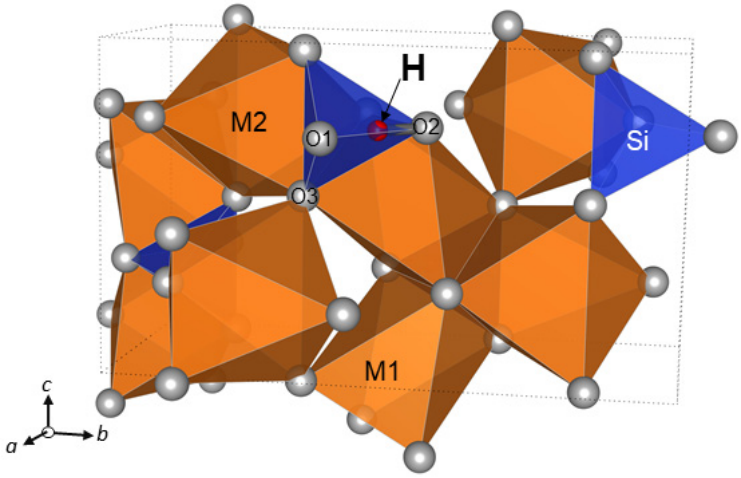

Fig. 3.3-8: Preliminary structure refinement of Fe-bearing olivine. Mg and Fe atoms are located at octahedral sites M1 and M2, and Si atoms are located at tetrahedral sites. There are three types of oxygen, O1, O2, and O3. The red sphere denotes the refined hydrogen position in the olivine structure.

g. *Pressure destabilises oxygen vacancies in bridgmanite (H. Fei, Z. Liu/Jilin, R. Huang, S. Kamada/Sendai, N. Hirao/Sayo, S. Kawaguchi/Sayo, C.A. McCammon and T. Katsura)*

Bridgmanite, the most abundant mineral in the lower mantle, can incorporate significant amounts of ferric Fe although the valence state of the A site (Mg and Fe^{2+} site) and B site (Si site), respectively, are 2+ and 4+, in the primary chemical formula $(Mg,Fe^{2+})SiO_3$. Fe^{3+} may be substituted into the crystal structure of bridgmanite by a charge-coupled mechanism, in which both the A and B sites are occupied by Fe^{3+} following the reaction, $Mg_A^{\times} + Si_B^{\times} \rightarrow Fe_A^{\bullet} + Fe_B'$, or by an oxygen-vacancy mechanism, in which only the B site is occupied by Fe^{3+} with additional oxygen vacancies, $Si_B^{\times} \rightarrow Fe_B' + 1/2\,V_O^{\bullet\bullet}$. As a result, $FeFeO_3$ and $MgFeO_{2.5}$ components, respectively, are formed. The different substitution mechanisms produce different types of defect species. As a result, physical properties of bridgmanite including atomic diffusivity, elasticity, plasticity, and electrical conductivity will be controlled by the substitution mechanisms of Fe^{3+} under lower mantle conditions.

In this study, we investigated the substitution mechanism of Fe^{3+} in Al-free bridgmanite in the MgO-SiO_2-Fe_2O_3 system as a function of pressure. Experiments were performed at 2300 K and 27, 33 and 40 GPa using a multianvil press. 7/3 (for 27 GPa) and 5.7/1.5 (for 33 and 40 GPa) cell assemblies with a $LaCrO_3$ heater were used. Run products consisted of coexisting bridgmanite, ferropericlase, and $MgFe_2O_4$-phase. Chemical compositions of bridgmanite were analysed by electron microprobe. $Fe^{3+}/\Sigma Fe \approx 100$ % was confirmed by both in-house and synchrotron Mössbauer source spectroscopy.

As shown in Figure 3.3-9, $FeFeO_3$ content in bridgmanite decreases from 7.7 to 5.3 mol. %, whereas the $MgFeO_{2.5}$ content decreases from 2.2 to ~ 0 %, with increasing pressure from 27 to 40 GPa. The oxygen vacancy substitution mechanism is therefore dramatically suppressed

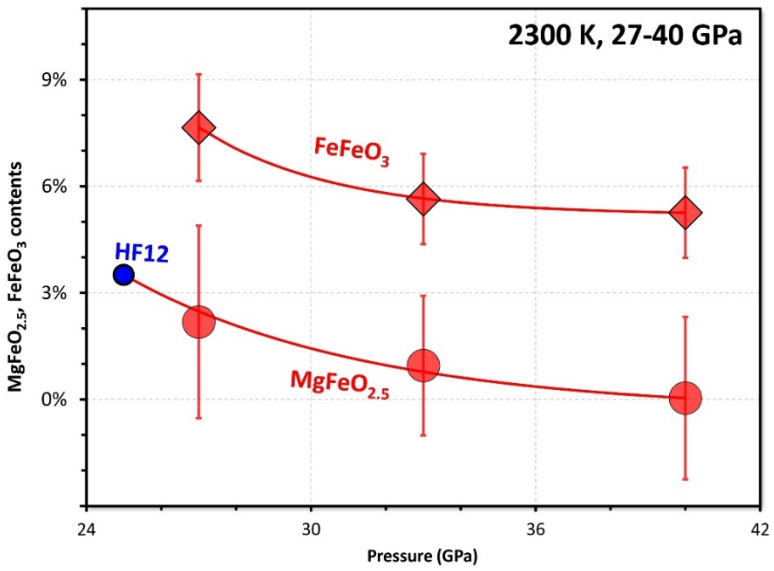

Fig. 3.3-9: $MgFeO_{2.5}$ and $FeFeO_3$ content in bridgmanite. The maximum $MgFeO_{2.5}$ content reported by HF12 (Hummer and Fei, Am. Min. 97, 1519-1521, 2012) at 25 GPa, 1970 ~ 2070 K is also shown for comparison.

by pressure. Oxygen vacancies can be produced by ferric iron in bridgmanite in the topmost lower mantle and in harzburgitic layers of subducted slabs, but the concentrations should decrease rapidly with increasing depth. The reduction in vacancies may potentially explain the viscosity increase in the lower mantle at 800 ~ 1200 km depth because viscosity is inversely proportional to atomic diffusivity, which is controlled by the defect concentrations.

h. *Deuterium content and site occupancy in iron sulphide at high pressure and high temperature using* in situ *neutron diffraction (S. Abeykoon, C. Howard, S. Dominijanni, L. Eberhard, D.J. Frost, T. Boffa Ballaran and A. Kurnosov, in collaboration with H. Terasaki/Okayama; T. Sakamaki, A. Suzuki and E. Ohtani/Sendai; A. Sano-Furukawa and J. Abe/Tokai)*

Earth evolved towards a habitable environment through many different stages over 4.5 Ga of geological history. The rapid increase in the oxidation state of the mantle after core formation (by 3.4 Ga) is one of the key processes that has not been fully understood. It is frequently proposed that the mantle was oxidised after the main phase of core formation had finished due to delivery of water during a late impact event, giving rise to the reaction $H_2O + 2FeO = Fe_2O_3 + H_2$. The question remains, however, as to how resulting H_2 was removed from the mantle to prevent it reversing the oxidation process. It has been proposed that iron sulphide was the main phase to separate to the core during the period termed the "Hadean Matte". Since iron sulphide can incorporate hydrogen, its segregation into the core may have been a viable mechanism to remove H_2. Studies on hydrogen incorporation into FeS, however, are very challenging, since any incorporated H_2 exsolves from the FeS structure during quenching; therefore, measurements have to be done *in situ* at high pressures and high temperatures. The aim of this study is to use neutron diffraction to detect the amount of hydrogen incorporation into high-pressure polymorphs of FeS.

We performed *in situ* time-of-flight neutron diffraction experiments on the FeS–H(D) system up to 12 GPa and 1400 K using a six axis multianvil high-pressure press at the J-PARC neutron beamline facility in Japan. Thermal decomposition of deuterated ammonia borane (ND_3BD_3) supplied deuterium to the FeS starting material during heating at high pressure and powder diffraction profiles were collected over 3-12 GPa and 900-1400 K. Rietveld structure refinements were performed on the collected diffraction patterns in order to determine the amount of deuterium incorporated into the structure of FeS.

Phase transformations of FeS to high-pressure and high-temperature polymorphs that were observed in this study agree with published X-ray diffraction studies on FeS. Our data shows that the deuterium content in the NiAs-type FeS-V phase increases with increasing pressure at temperatures higher than 1000 K. Rietveld structure refinement of neutron diffraction data collected at 7.8 GPa and 1300 K resulted in a total deuterium site occupancy (x) = 0.77(12) (Fig. 3.3-10a, see figure caption for details), that corresponds to about 1.7 wt. % of deuterium

in FeS. We also followed the volume expansion of FeS occurring at constant P and T conditions over about 17 hrs. Results show a good correlation with the increase of deuterium occupancy over this period, reaching a maximum after 8 hours of heating (Fig. 3.3-10b). Therefore, FeS may indeed be a candidate for segregating hydrogen to the core during the late stage of core formation, allowing oxidation of the mantle to occur.

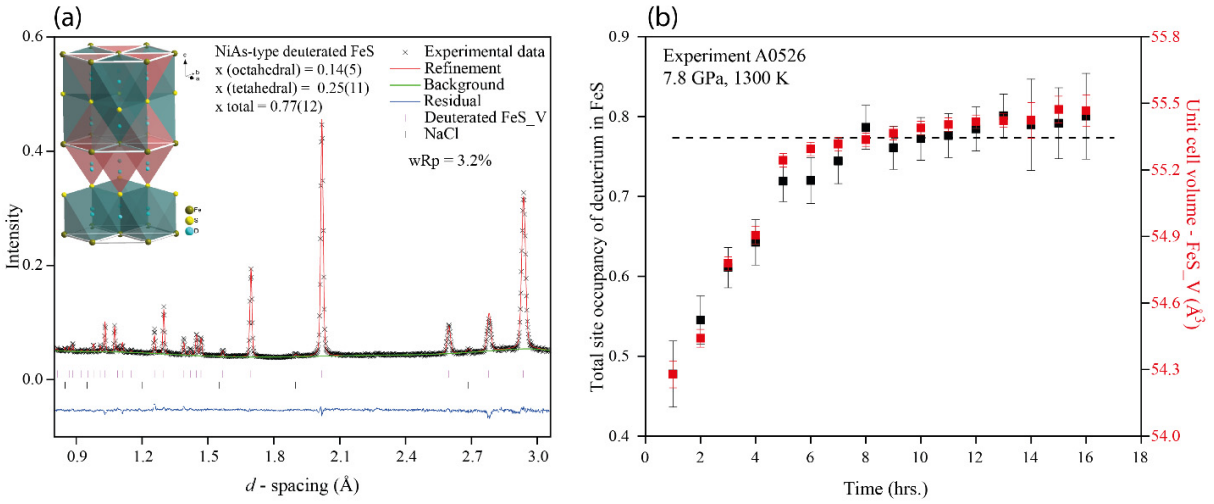

Fig. 3.3-10: a) Rietveld structural refinement of NiAs-type FeS-V structure from neutron powder diffraction data collected at 7.8 GPa, 1300 K (run# 61306). The structural model implies that both octahedral (O) and tetrahedral (T) positions usually vacant in the FeS structure are occupied by deuterium. The resulting crystal structure of deuterated NiAs-type FeS-V (hexagonal–*P*63/*mmc*, Z = 2) is shown (inset). The deuterium atom positions represented as blue spheres are only partially occupied. b) Total deuterium site occupancy (left y-axis) and volume expansion (right y-axis, red) of NiAs-type FeS-V structure plotted as a function of time at 7.8 GPa and 1300 K. The black dashed line represents the total deuterium occupancy (0.77 ± 0.12) obtained by fitting diffraction data collected during the final 10 hrs of heating.

i. *Electronic and structural properties of compressed dense hydrogen (T. Meier, D. Laniel/Bayreuth, M. Pena-Alvarez/Edinburgh, F. Trybel, S. Khandarkhaeva, A. Krupp, J. Jacobs/Grenoble, N.A. Dubrovinskaia/Bayreuth and L.S. Dubrovinsky)*

Hydrogen, the most abundant element in our universe, is one of the most enigmatic molecular compounds when subjected to extreme pressures and temperatures. Lack of core electrons and small molecular masses render H_2 subject to substantial nuclear quantum correlations such as zero-point motions, tunnelling, and structural complexity far exceeding expectations for such a "simple molecular system". Furthermore, despite predictions of a metallic and room-temperature superconducting phase at megabar pressures, experimental claims fall short of unequivocal proofs due to current limitations in laboratory methods and techniques accessible to the high-pressure community.

A promising emerging high-pressure technique is *in situ* nuclear magnetic resonance (NMR) in diamond anvil cells (DACs), which has been developed in BGI over the course of the last years. As NMR probes the response of the nuclear spin system and is particularly sensitive to hydrogen atoms, it presents the ideal tool to engage in high-pressure studies of molecular H_2. Technical limitations, like sufficient pressure generation and stability as well as spectral resolution, previously limited its application to below 20 GPa.

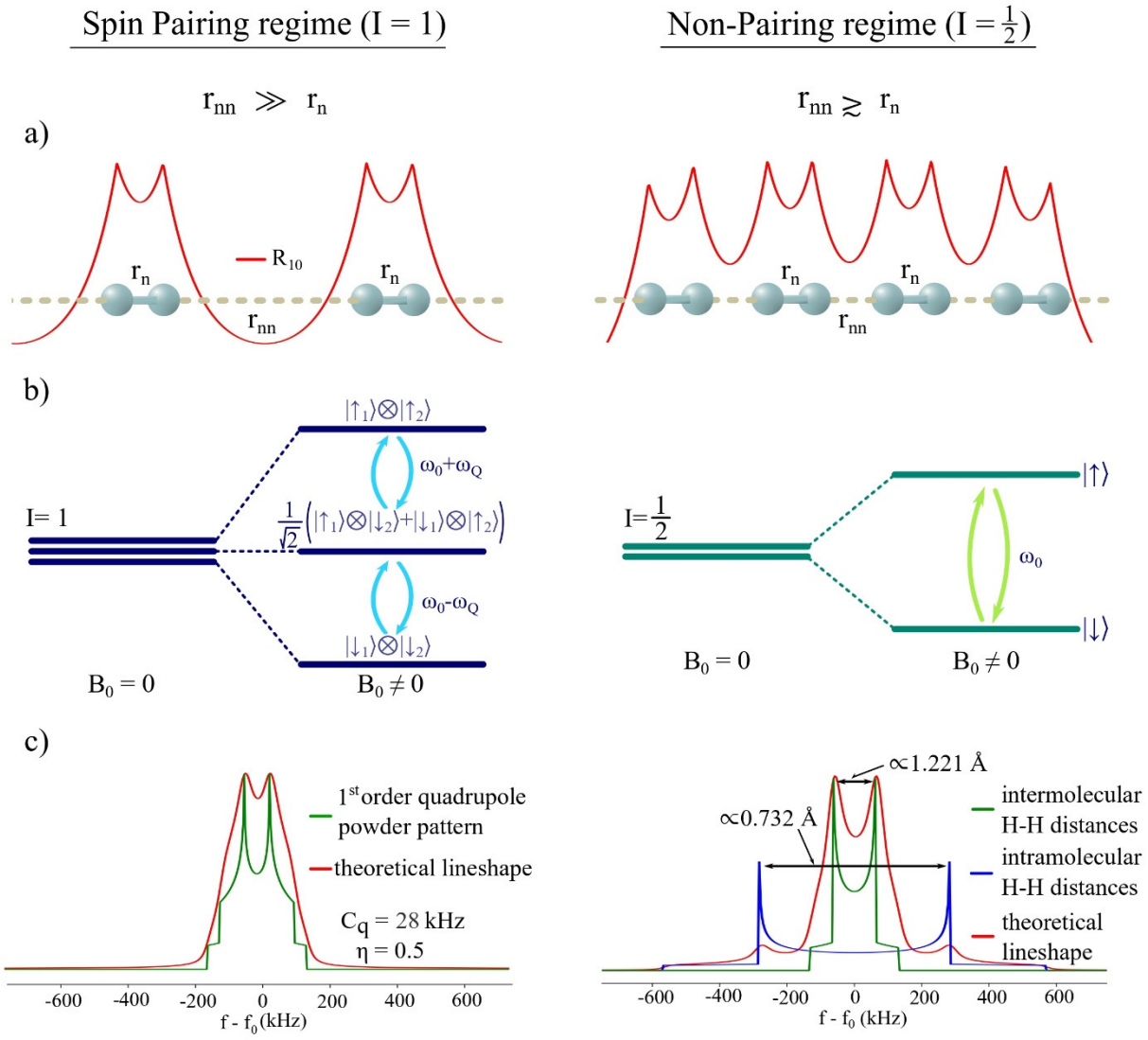

Fig. 3.3-11: Overview of both spin-pairing and non-pairing regimes. a) Schematic representation of the wave function overlap (red lines) of H_2 molecules. b) Schematic representation of the nuclear spin energy levels under the influence of an external magnetic field B_0 for the pairing (*i.e.*, quadrupole interaction) and non-pairing (dipole-dipole interaction) regimes. c) Theoretical line shapes in the pairing and non-pairing regime. $\omega_0 = 2\pi f_0$ denotes the Larmor frequency of the hydrogen nuclei, and ω_Q, η and C_q are the quadrupole frequency, the asymmetry parameter and the quadrupole coupling constant, respectively.

In 2019 we were able to demonstrate that high resolution-high sensitivity NMR in DACs is possible using static homonuclear ^{1}H decoupling by application of a rotating radio frequency field leading to significant improvements in spectral resolution at pressures up to 70 GPa on a sample of molecular hydrogen. With these developments, we were able to investigate the response of the hydrogen nuclear spin system.

One of the most striking properties of molecular hydrogen is the coupling between molecular rotational properties and nuclear spin orientations, giving rise to the spin isomers ortho- and para-hydrogen. At high pressure, as intermolecular interactions significantly increase, the free rotation of H_2 molecules is increasingly hindered, and consequently a modification of the coupling between molecular rotational properties and the nuclear spin system can be anticipated. To date, high-pressure experimental methods have not been able to observe nuclear spin states at pressures approaching 100 GPa and consequently the effect of high pressure on nuclear spin statistics could not be directly measured. We present *in situ* high-pressure nuclear magnetic resonance data on molecular hydrogen in its hexagonal phase I up to 123 GPa at room temperature. While our measurements confirm the presence of ortho-hydrogen at low pressures, above 70 GPa we observe a crossover in nuclear spin statistics from a spin-1 quadrupolar to a spin-1/2 dipolar system, evidencing the loss of spin isomer distinction (Fig. 3.3-11). These observations represent a unique case of a nuclear spin crossover phenomenon in quantum solids. Future experiments will be focused on elucidating high-pressure structural candidates of phases III and IV which cannot be uniquely resolved with complementary structural probes like X-ray diffraction.

j. *Proton dynamics in high-pressure ice-VII from density functional theory (F. Trybel, T. Meier and G. Steinle-Neumann, in collaboration with M. Cosacchi and V.M. Axt/Bayreuth)*

The discovery of ice-VII inclusions in diamonds from Earth's mantle highlights the importance of this high-pressure phase of water for planetary interiors beyond icy satellites in our solar system and potentially H_2O-dominated exosolar planets. At room temperature (T), water crystallizes as ice-VII at pressures (P) above 2 GPa, in a structure based on a body-centred cubic arrangement of oxygens with two possible proton positions along the diagonal O-O direction (dOOd) that are occupied randomly but assumed to follow the ice rules: each oxygen atom is covalently bound to two hydrogen atoms and each resulting water-like unit forms two hydrogen bonds to other oxygen atoms. In ice-VII, a double-well potential along the O-O direction can be found under correlated proton movement that changes significantly under compression. With increasing P, the O-H···O bond continuously symmetrises to form ice-X, a process that has been of great interest in high-P physics and chemistry.

Using Kohn-Sham (KS) density functional theory (DFT), we trace the potential by displacing all, six and a single proton (Fig. 3.3-12a), along dOOd to investigate proton dynamics and explore symmetrisation under compression. We build ice-VII cells with 384 atoms (lattice

constants between l = 3.35 Å and 2.55 Å), following the ice rules. All protons are simultaneously moved by the same amount along the respective dOOd (22 steps); calculated energies are interpolated, and the optimal proton position at each l is determined. We obtain a double-well potential at low compression and observe a continuous transition to a single well with decreasing l. In previous path-integral-based studies, a collective motion of six protons in a hexagonal configuration was identified without breaking the ice rules. We follow this suggestion and move six protons in such a configuration and obtain potentials almost perfectly corresponding to the all-proton case in terms of energy per proton (Fig. 3.3-12a), with the double-well character steadily decreasing with decreasing lattice constant. Under further compression, the high-P single well becomes increasingly localised. Moving a single proton along dOOd in the ice-rule conforming cell leads to an asymmetric single-well potential, with the minimum corresponding to one of the minima in the double well obtained from the collective displacement of all protons (Fig. 3.3-12a), which also converges to a symmetric potential at increasing compression. By breaking the ice rules, it is possible to create environments in which a single proton experiences a double-well potential when moved along dOOd; four different cases of ice-rule breaking configurations (Fig. 3.3-12 aa-ad) can be distinguished by oxygen/proton ratio and symmetry. Based on the barrier height and distance between the minima for all six cases, two groups can be distinguished: ice-rule violating structures lose the double-well character at a smaller compression, compared to the ice-rule conforming structures.

Many high-P techniques do not provide access to the potential itself, but the electron density close to the protons by X-rays, and the response of the lattice to an excitation of phonon modes by Raman, infrared or Brillouin spectroscopy can be measured. High-P NMR spectroscopy, by contrast, enables the investigation of effective proton dynamics by performing a lineshape analysis. To compare with the latter results, we use a matrix exponential formalism to solve the time-dependent (t-dependent) Schrödinger equation for a wave packet in the one-dimensional potentials obtained from the DFT-based sampling. We determine the probability of finding the proton in the left half of the double-well potential, $p(x<0)$ and its Fourier transform, $p(k)$, to quantify tunnelling in the system (Fig. 3.3-12b). Choosing the position of the initial state (x_0) at the minimum of the respective potential leads to a non-zero overlap between the ground state and the first excited state and therefore a non-zero transition frequency as long as x_0 is not central. This frequency is calculated from the energy difference between the ground state and the first excited state of the eigenvalue spectrum of the Hamiltonian (Fig. 3.3-12b). Once the minimum of the potential is at the centre of dOOd, no overlap between the ground state (symmetric) and the first excited state (antisymmetric) is expected, and the amplitude of this frequency in $p(k)$ should vanish, indicating the completion of the symmetrisation.

If we compare the amplitude of the transition frequency as a function of P with an NMR lineshape analysis (Fig. 3.3-12c), we find that the hexagonal configuration reproduces the P-dependence of the data at room T well: a strong increase in amplitude up to $P \approx 20$ GPa, a plateau to $P \approx$ 80-90 GPa, and a subsequent drop. This supports the understanding that charge

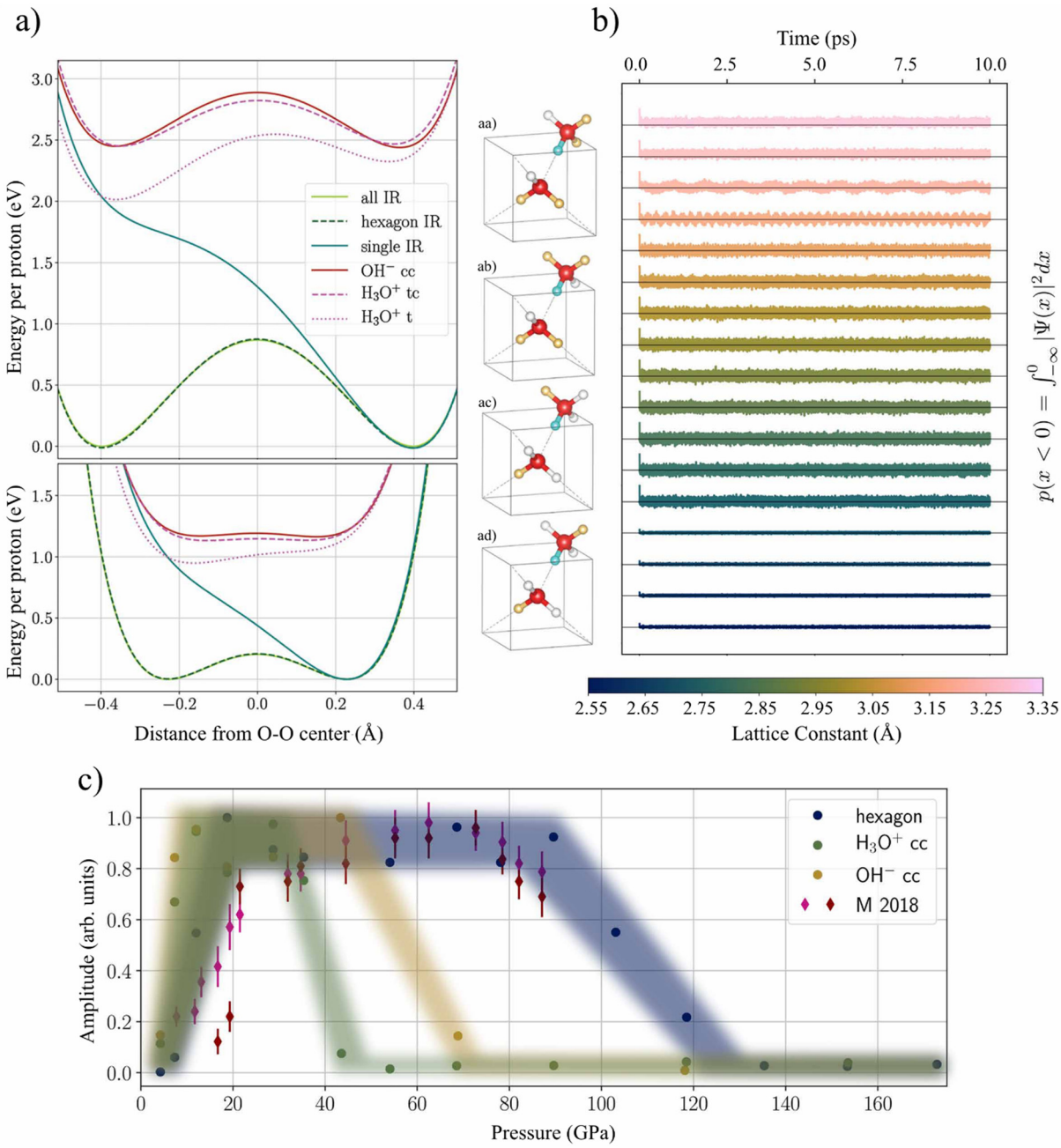

Fig. 3.3-12: a) Energy of different proton configurations in ice-VII for $l = 3.35$ Å ($P \approx 4$ GPa, top) and $l = 2.95$ Å ($P \approx 27$ GPa, bottom) and (aa-ad) visualisation of configurations with a single-H ice-rule (IR) violation: O is shown in red, unoccupied H positions in white, occupied ones in gold, and sampled H in blue. Potentials are for the collective motions of all protons and in a hexagonal configuration and a single H, all obeying IR. Two potentials for IR-breaking arrangements are shown, bracketing the potential of the IR-breaking structures – without and with conjugation of the associated charge defect. b) Probability of finding H in the left half of the potential p ($x < 0$) as a function of time for the hexagonal configuration: at $l < 3.2$ Å ($P > 9$ GPa) p ($x < 0$) starts to oscillate with decreasing wavelength, and for $l < 2.7$ Å ($P > 90$ GPa) the amplitude of p ($x < 0$) collapses. c) Corresponding amplitudes of the transition in $p(k)$. Diamonds in magenta and purple show the result of a peak analysis of NMR experiments by Meier et al. (Nat. Commun. 9, 2766, 2018) (M 2018).

balance tends to be maintained, and therefore tunnelling is dominantly correlated, represented by the hexagonal configuration. We do not find a sharp phase transition in cubic ice between the emergence of ice-VII at 2 GPa and 200 GPa, well in the stability field of ice-X, rather described a gradual change from a double- to a single-well potential, and we predict related changes in proton dynamics. Based on our results we can distinguish regions of characteristic proton dynamics and potential (at room T): (i) for 2 GPa < P < 20 GPa, protons become increasingly delocalised, as the potential barrier decreases; (ii) for 20 GPa < P < 90 GPa, protons tunnel in a fashion well represented by correlated hexagons; (iii) for 90 GPa < P < 130 GPa, symmetrisation occurs and the system becomes less dynamic; (iv) for P > 130 GPa, the potential is fully symmetric and no proton dynamics are expected for an initially symmetric state.

k. *Room-temperature Verwey-type transition in Fe_5O_6 (S.V. Ovsyannikov, M. Bykov/Hamburg; S.A. Medvedev and P.G. Naumov/Dresden; A. Jesche and A.A. Tsirlin/Augsburg, E. Bykova/Hamburg, I. Chuvashova/Cambridge, A.E. Karkin/Yekaterinburg, V. Dyadkin and D. Chernyshov/Grenoble, L.S. Dubrovinsky)*

The existence of phase transitions or crossover points in strongly correlated oxides are of considerable interest from both fundamental and applied perspectives, and may be relevant to geosciences. We therefore investigated crystals of a novel mixed-valent iron oxide with an unconventional Fe_5O_6 stoichiometry. We found that Fe_5O_6 undergoes a Verwey-type charge-ordering transition that is concurrent with a dimerization in iron chains and ensuing formation of novel Fe-Fe chemical bonds. We established that the minimal Fe-Fe distance in the octahedral chains is a key parameter that determines the type and temperature of charge ordering.

Single crystals of Fe_5O_6 were synthesised at high-pressure high-temperature (HP-HT) conditions at 14-16 GPa and 1200-1400 °C in 1200-tonne multianvil presses at BGI. For their preparation we used stoichiometric mixtures of Fe_3O_4 and Fe. At ambient conditions Fe_5O_6 crystals adopt an orthorhombic *Cmcm* structure, in which iron cations fill linear chains of both octahedra (crystallographic sites Fe1 and Fe2) and the trigonal prisms (Fe3) (Fig. 3.3-13c). A bond-valence-sum (BVS) analysis of Fe-O bond lengths in this structure returns BVS values of 2.57(6), 2.43(7), and 1.97(4) for Fe1, Fe2, and Fe3 atoms, respectively. Thus, the bigger prismatic Fe3 sites are filled with Fe^{2+}, likewise, the two inequivalent octahedral sites are filled with mixed Fe^{2+}/Fe^{3+} ions.

We carried out temperature-dependent single crystal X-ray diffraction of Fe_5O_6 from 293 K down to 80 K at SNBL (Swiss-Norwegian Beam Line, ESRF, Grenoble, France) with a wavelength of 0.6884 Å. Upon cooling below room temperature, a well-ordered array of superlattice reflections appears in diffraction patterns of Fe_5O_6 single crystals (Fig. 3.3-13a,b). This fact indicates the emergence of an additional structural order. We solved the crystal structure of this low-temperature phase, labelled as Fe_5O_6–II, in the $P2_1/m$ monoclinic space group. Fe-Fe distances in octahedral chains in this phase display a pronounced separation into

pairs, resulting in the formation of dimers (Fig. 3.3-13d). Figure 3.3-14a shows that upon the phase transition a single Fe-Fe periodicity of 2.877 Å along the octahedral iron chains turns into a periodicity of two alternating distances; these distances correspond to the dimers (short distance) and the gaps between them (long distance). A BVS analysis of Fe-O bond lengths in this lattice indicates that the iron ions filling the octahedral sites keep their non-integer valences of about +2.5. Hence, we can conclude that the dimers in the Fe_5O_6–II structure are composed mainly of a pair of Fe^{2+} and Fe^{3+}, in which one electron simultaneously belongs to both iron ions (Fig. 3.3-13d). Thus, the phase transition leads to stabilisation of a "formal" fractional oxidation state of ~ +2.5 for octahedrally-coordinated iron cations. This fractional oxidation state is not a result of "mathematical averaging" of Fe^{2+} and Fe^{3+} valences, because such a model does not explain the formation of the dimers.

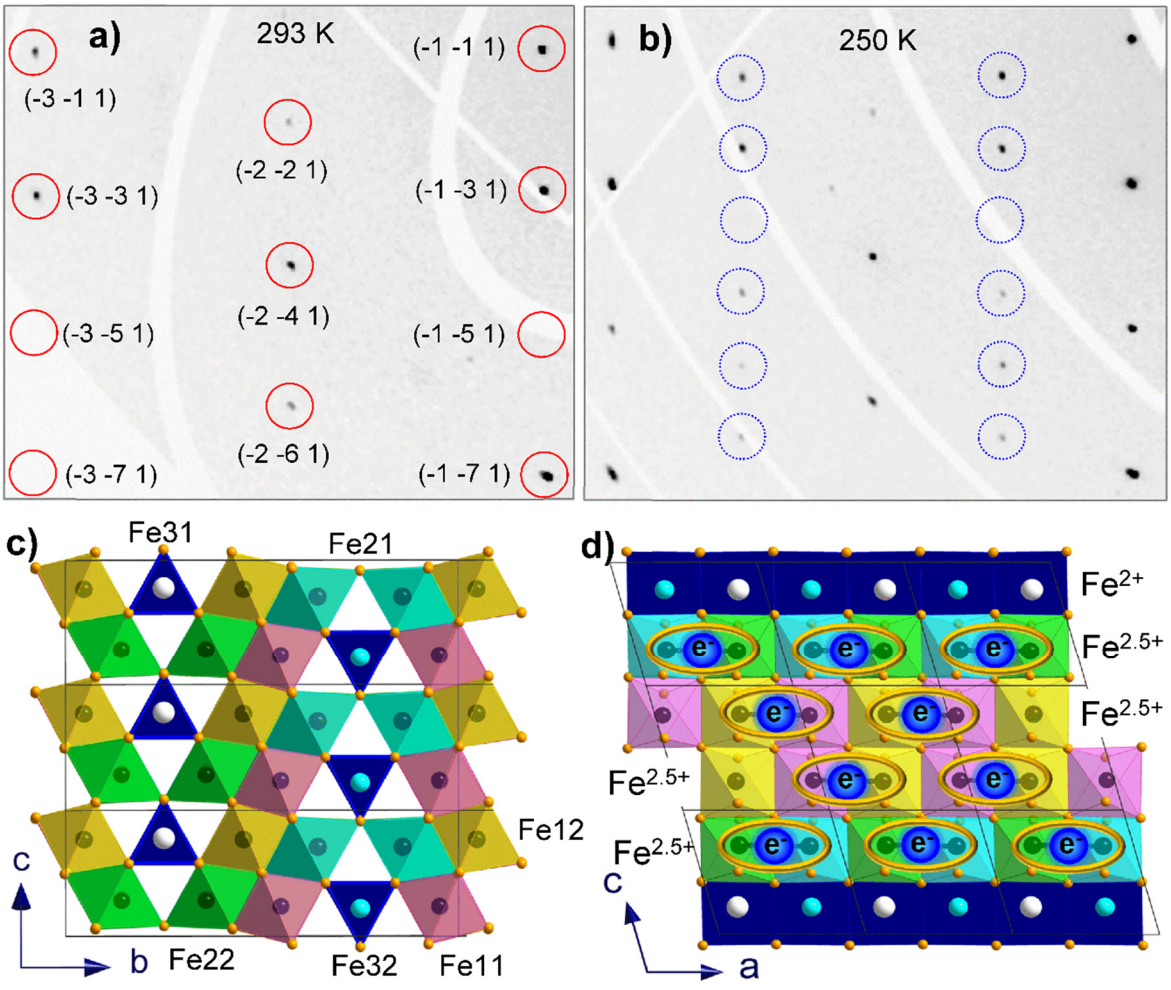

Fig. 3.3-13: Examples of reciprocal lattice planes (*hk1*) of Fe_5O_6 at a) 293 K and b) 250 K demonstrating the appearance of superlattice reflections (highlighted by blue circles) upon the phase transition from the original Fe_5O_6-I phase (a) to the low-temperature Fe_5O_6-II phase (b). Positions of the basic structural reflections in (a) are highlighted by red circles and indexed. Two projections (c,d) of the crystal structure of the Fe_5O_6-II phase showing the formation of Fe-Fe dimers with one shared electron in chains of octahedrally-coordinated iron ions. The cations labels are given in (a).

The normal Fe-Fe bond length value in α-Fe metal is about 2.48 Å, whereas in complexes containing metal clusters it was found to be always longer, in the range of 2.5-2.7 Å. The shortest Fe-Fe distances of ~2.78 Å in the Fe_5O_6–II structure at 260 K are in the Fe1 chains of Fe11 and Fe12 octahedra (Fig. 3.3-13c,d); with decreasing temperature these distances are reduced to ~2.68 Å (Fig. 3.3-14a). This behaviour of the crystal structure of the Fe_5O_6–II phase points to the formation of the Fe-Fe bonds and their strengthening with cooling below the transition point.

The temperature dependence of electrical resistivity for two crystals of Fe_5O_6 shows an abrupt increase in resistivity below 280-290 K (Fig. 3.3-14b). A derivative of one of these curves suggests a midpoint of this transition at 275 K. Thus, the structural distortion in Fe_5O_6 is accompanied by a significant increase in the electrical resistivity. At room temperature, the electrical resistivity of these Fe_5O_6 crystals amounts to ~ 7 mΩcm (Fig. 3.3-14b). Hence, Fe_5O_6 is a good electrical conductor at room temperature, and like magnetite, it can be characterised by a high concentration of low-mobile carriers associated with hopping charges. The Fe_5O_6–II phase is apparently semiconducting with an activation energy of about 0.1 eV (inset in Fig. 3.3-14b), which corresponds to a band gap value of E_g=2 E_a ~ 0.2 eV.

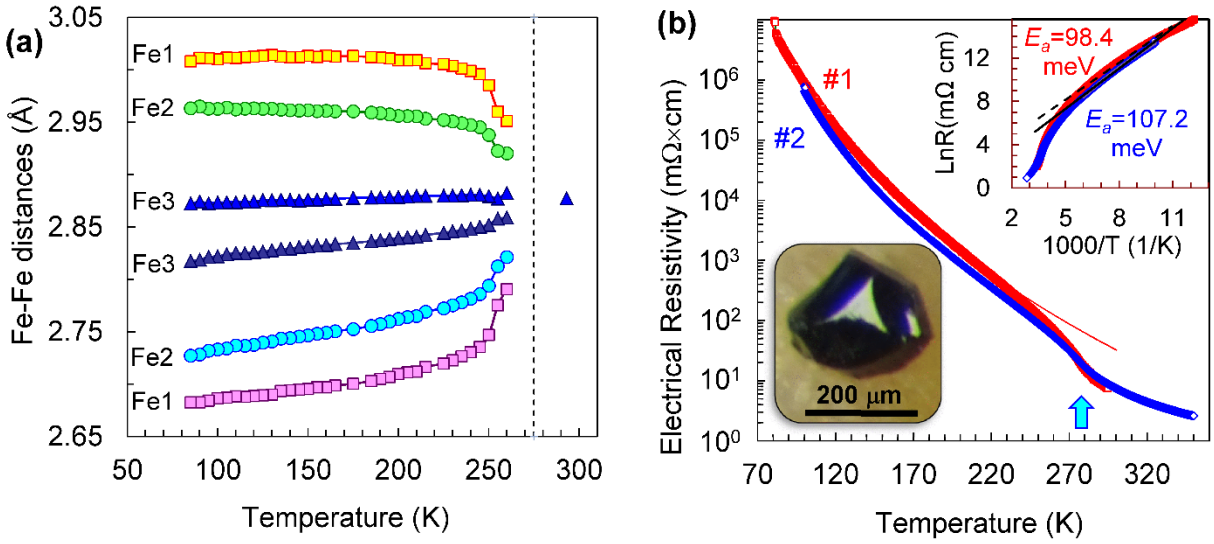

Fig. 3.3-14: a) Temperature dependence of two characteristic Fe-Fe distances within each chain of iron cations along the a-axis (Fig. 3.3-13d). Two Fe-Fe distances in the octahedral chains Fe1 and Fe2 correspond to the dimers (short distance) and the gaps between them (long distance). The dashed vertical line at 275 K indicates the midpoint of the transition. b) Temperature dependence of electrical resistivity of Fe_5O_6 for two single crystals (#1, #2) at 0.3 GPa. The inset shows the determination of the activation energy in the charge-ordered phase.

l. *Influence of antimony on Fe(II) oxidation to iron oxyhydroxide (C.A. McCammon, in collaboration with K. Hockmann, L. Wegner, B. Planer-Friedrich and S. Peiffer/Bayreuth; E. Burton/Lismore, G. Auchterlonie/Brisbane and B. Morgan/Sydney)*

Fe(II) is soluble in a wide range of environments and is thermodynamically stable under anoxic conditions, but can be easily oxidised to insoluble Fe(III) phases. For example, banded iron formations (see contribution by Szlachta in this Annual Report) likely formed by precipitation of ferrihydrite (hydrous iron oxyhydroxide) due to oxidation of Fe(II) that was dissolved in ancient oceans. The chemistry of the aqueous environment strongly influences the oxidation process and resulting precipitates. Dissolved antimony is of particular interest due to its toxicity and role as an environmental contaminant. Our ongoing experiments have revealed that increasing concentrations of antimony favour formation of the rarely reported phase feroxyhyte (δ'-FeOOH) instead of lepidocrocite (γ-FeOOH), and suggest that antimony is mainly incorporated into the feroxyhyte structure instead of being adsorbed on the surface. To further investigate the nature of iron oxyhydroxide phases with respect to antimony, we undertook a study using Mössbauer spectroscopy.

Fe(II) solutions were prepared to which Sb(V) was added to achieve molar Sb:Fe ratios of 1:100, 1:25, 1:10, and 1:4 as well as an Sb-free control. Oxygen was bubbled through the solutions and precipitates were collected at the end of the experiment. Mössbauer spectra were measured at both room temperature and 80 K of all precipitates as well as reference samples of lepidocrocite and feroxyhyte. At room temperature all spectra show a quadrupole doublet assigned to Fe^{3+}, which can be either lepidocrocite or feroxyhyte since both are paramagnetic. However, at 80 K, feroxyhyte is magnetically ordered while lepidocrocite is not, which enables a clear distinction of phases (Fig. 3.3-15). Our results agree with X-ray diffraction data and show that Sb-free, 1:100 and 1:25 samples contain only lepidocrocite, while the 1:4 sample

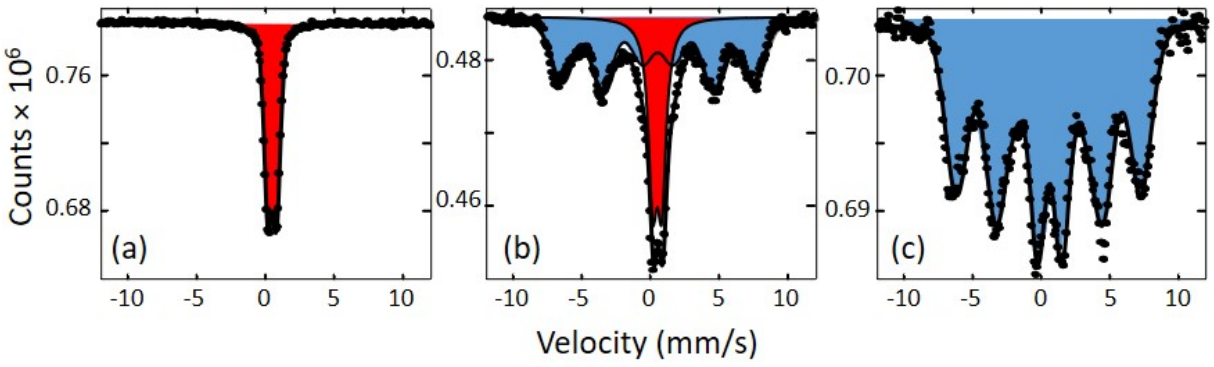

Fig. 3.3-15: Mössbauer spectra at 80 K of precipitates obtained from oxidation of solutions with Sb:Fe ratios of (a) 1:100, (b) 1:10 and (c) 1:4. Spectra were fit to a quadrupole doublet assigned to lepidocrocite (red) and/or a sextet with magnetic field distribution assigned to feroxyhyte (blue).

contains only feroxyhyte and the 1:10 sample shows a mixture. The hyperfine magnetic field of feroxyhyte produced from Fe-Sb solutions (33 T) is substantially less than the magnetic field of pure feroxyhyte (46 T), consistent with incorporation of diamagnetic Sb^{5+}. Similarly, the strong distribution of hyperfine magnetic fields (*i.e.*, asymmetric line broadening) is consistent with the large variation in Fe^{3+} next-nearest neighbour environments expected when the high field strength cation Sb^{5+} is substituted into the crystal lattice. These results support the possibility of coprecipitation as a promising approach for the treatment of Sb-contaminated waters.

m. *Microstructure of banded iron formations as a window to ancient oceans (V. Szlachta and C.A. McCammon, in collaboration with J. M. Byrne/Bristol)*

Banded iron formations (BIFs) are layered, Fe- and Si-rich marine sedimentary deposits that formed prior to and during the Great Oxidation Event. Although the mechanisms responsible for their characteristic, alternating layers of chert and iron oxide are still under debate, it is generally accepted that the main iron-bearing phases, hematite and magnetite, are secondary reaction products. Precipitation of primary minerals (mainly ferrihydrite) from seawater likely involved microbial activity, while the role of microbes in transforming ferrihydrite to magnetite and hematite is still open. Unravelling these processes provides important constraints on redox cycling in ancient oceans and ultimately on atmospheric evolution. Mössbauer spectroscopy is a useful tool for studying iron-bearing phases in BIFs. Our previous work using a synchrotron Mössbauer source showed intriguing results on a section from the Kuruman BIF (South Africa), but also the puzzling observation of asymmetric area ratios. One possible interpretation was preferred orientation, which has implications for spectral deconvolution as well as the microstructure. To address this question and also investigate BIF oxidation state more thoroughly, we undertook a combined study using Mössbauer spectroscopy and electron backscatter diffraction (EBSD).

We prepared a 150 µm thick section (Fig. 3.3-16) from the same rock used in the previous study, which we used to collect Mössbauer spectra over length scales from 500 µm to 1 cm. We also prepared a thin section from the same rock for EBSD analysis. Mössbauer results show a large variation in bulk $Fe^{3+}/\Sigma Fe$ across the different bands (Fig. 3.3-16), which can be attributed to varying abundances of iron oxides. We also found large deviations of the magnetite Fe^{2+}/Fe^{3+} ratio to more oxidised and more reduced values, which is consistent with recent models for microbial redox cycling of magnetite. EBSD data confirm that preferred orientation is present for both hematite and magnetite. Hematite grains show a slight preference for the basal plane (which contains the magnetic moment) to be aligned with BIF layers, while cubic axes of magnetite grains also show a similar slight tendency to be aligned with BIF layers. These orientations are consistent with Mössbauer area ratio asymmetry. There is little evidence for extensive deformation of the Kuruman BIF, suggesting that preferred orientation was either inherited from primary deposition processes or that it developed through microbial transformation to iron oxides.

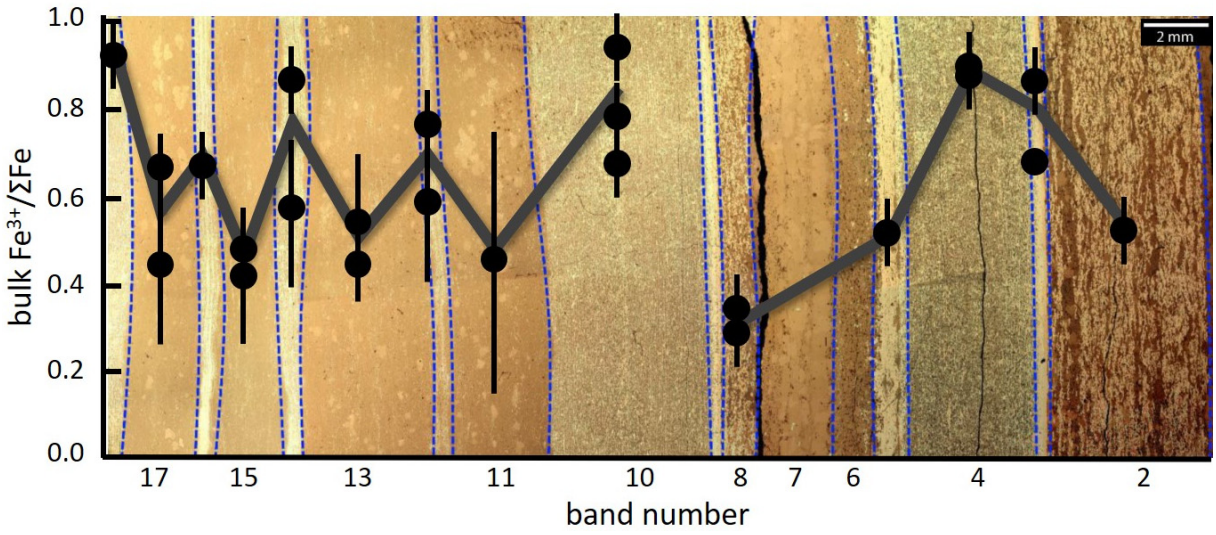

Fig. 3.3-16: Reflected light image of a section from the Kuruman banded iron formation. A plot of bulk $Fe^{3+}/\Sigma Fe$ values (solid circles) measured from each band is superimposed on the image. The trend lines (dark grey) highlight the contrast between oxidised bands (lighter due to higher reflectivity) and more reduced bands (darker due to lower reflectivity). Band boundaries are indicated by blue dashed lines.

3.4 Physical Properties of Minerals

Geophysical methods of exploration of the Earth's deep interior such as seismology rely crucially on the knowledge of the physical properties of minerals, rocks and melts. Only a sound database of these properties allows geophysical data to be interpreted in a scientifically meaningful way. Therefore, a large effort is made in experimental mineral physics to determine physical properties of geomaterials under the temperature and pressure conditions of the deep Earth. Nine contributions of this chapter aim to determine experimentally the elastic behaviour of geological materials in order to relate their results to geophysical data from different regions in the interior of the Earth using four main experimental techniques.

The first four studies make use of single-crystal X-ray diffraction coupled with synchrotron radiation to investigate the compressibility of materials which may play an important role in defining the behaviour of the Earth's lower mantle and inner core. In the first contribution a spin crossover transition is reported to occur above 40 GPa in a Fe-bearing Al-phase D, a hydrous phase which may be stable at Earth's lower mantle conditions with important consequence for the Earth's water budget. The next two studies investigate the compressibility of Al and Al/Fe-bearing bridgmanites. In the second contribution the effect of the different mechanism of Al substitution in bridgmanite on its compressibility has been investigated. Preliminary results suggest that such effect is minimal in spite of the different molar volumes of the two bridgmanite end-member components. The third contribution reports about the structural variation and compressibility of an extremely Fe/Al-rich bridgmanite and suggests that such large amount of Fe^{3+} may give rise to Si/Fe ordering at the octahedral site with consequent reduction in symmetry of the orthorhombic perovskite structure. The fourth contribution aims at constraining the high-pressure phases in the Ni-C system to better understand the possible chemistry of the Earth's core and presents the compressibility of a novel Ni_3C material.

In the fifth contribution the influence of small amounts of melt on the elastic behaviour of olivine polycrystals is investigated using *in house* ultrasonic interferometry with the goal to interpret certain seismically detected low-velocity zones in the upper mantle, which may represent regions of partial melting.

The following three studies have used single-crystal Brillouin spectroscopy coupled with X-ray diffraction to determine the full elastic tensor of anisotropic minerals. In the sixth contribution the full elastic tensor of antigorite has been determined at different pressures up to 5.2 GPa showing a major reduction in anisotropy mainly due to the increase of the c_{33} stiffness coefficient. In the seventh contribution the elastic properties of Fe-bearing δ-AlOOH have been measured across its structural phase transformation which occurs at the same pressure at which disorder of the hydrogen bond has been observed. Just before the transition a large softening of the bulk modulus is observed, whereas after the transformation, the material becomes significantly stiffer. Measurements of the elastic tensor of bridgmanite at pressures of the

Earth's lower mantle have been used in the eight contribution to calculate seismic wave velocities for different mineral assemblages to compare with seismic observations. A mineral-physics model consisting of bridgmanite, ferropericlase and Ca-perovskite is in good agreement with shear wave velocities reported in 1D seismic models, whereas the compressional wave velocities are more than 1 % slower than expected from the seismic models, suggesting that substitution of Fe and Al in bridgmanite needs to be reconsidered.

In the ninth contribution Brillouin spectroscopy has been coupled with a CO_2 laser heating system to collect Brillouin spectra at high pressures and temperatures for transparent single-crystals of pyrope. Wave velocities have been therefore collected at several different pressures up to 1900 K and they can be used to constrain the thermoelastic properties of this mineral.

Finally in the last contribution measurements of the thermal conductivity of δ-(Al,Fe)OOH have been performed, observing in a large variation of the thermal conductivity across the iron spin transition at 30-45 GPa and room temperature, suggesting that the presence of this hydrous phase may give rise to an exceptionally low thermal conductivity at the lowermost mantle conditions.

a. *Structural disorder and compressibility of Fe-bearing aluminous phase D (G. Criniti, T. Ishii, A. Kurnosov and T. Boffa Ballaran, in collaboration with K. Glazyrin and R. Husband/Hamburg)*

The stability of dense hydrous magnesium silicates (DHMSs) in mafic and ultramafic subducted lithologies at depth larger than 200 km has opened new scenarios for water transport in the lower mantle. Among DHMSs, Mg-free Al-phase D (nominally $Al_2SiO_6H_2$) was found to be stable up to 2100 °C at 26 GPa, *i.e.*, more than 700 °C higher than Al-free phase D (nominally $MgSi_2O_6H_2$) at the same pressure. The remarkably high dissociation temperature of Al-phase D at lower mantle pressures is believed to be related to Al-Si disordering and to the strengthening of H-bonds that are induced by Al incorporation. However, the structure of Al-phase D was investigated only at ambient conditions and high-pressure diffraction studies of phase D conducted so far have focused only on Mg-rich compositions. In this study, we report on the compressibility of an Fe-bearing and partially disordered Al-phase D up to approximately 50 GPa obtained by means of single-crystal X-ray diffraction using a diamond anvil cell.

Al-phase D crystals were synthesized in a Kawai-type multianvil apparatus at 27 GPa and 1700 °C from a starting mixture of FeOOH, $Al(OH)_3$ and SiO_2 in molar proportion 2:6:2. The recovered sample consisted of large crystals of Fe-bearing Al-phase D with chemical composition $Al_{1.73}Fe_{0.29}Si_{0.98}O_6H_{2.02}$ and (Al,Si,Fe)OOH with a $CaCl_2$-type structure. Single-crystal X-ray diffraction measurements at ambient conditions indicate that the space group symmetry of $Al_{1.73}Fe_{0.29}Si_{0.98}O_6H_{2.02}$ is $P\bar{3}1m$. Diffuse scattering is observed in 2D diffraction

images along the *c*-axis and in the odd 00*l* planes, which suggests short range ordering of Si, Al and Fe cations at the octahedral sites. A structural refinement revealed partial disorder of the cations in four distinct octahedral sites, with site occupancies ranging from 0.19 to 0.74. Our structural model lies in between those of Al-bearing Mg-phase D, where three partially disordered sites exist, and the Al-phase D endmember, having four sites equally populated.

We investigated the variation of the unit-cell lattice parameters of Fe-bearing Al-phase D at high pressure by means of single-crystal X-ray diffraction in diamond anvil cell (DAC) at the beamline P02.2 of PETRA III (Hamburg). A high-quality single crystal of approximately 15 x 15 x 10 μm^3 was loaded together with a ruby sphere and a piece of Au in DACs equipped with diamonds having 350 µm (run 1) and 250 µm culets (run 2). The sample chambers were obtained by laser drilling a Re foil indented to 53 µm and 35 µm respectively, and He was loaded as quasi-hydrostatic pressure-transmitting medium. Pressure-volume data up to 40 GPa can be fitted with a 3rd-order Birch-Murnaghan equation of state (Fig. 3.4-1), yielding V_0 = 83.68(2) A^3, K_0 = 166.3(15) GPa and K_0' = 4.45(12). At pressures higher that 40 GPa, the behaviour of Fe-bearing phase D starts to deviate from the equation of state, as observed both in the pressure-volume data (Fig. 3.4-1) and in the *f-F* plot (Fig. 3.4-1, inset). The observed volume decrease and elastic softening can be explained with the high-spin (HS) to low spin (LS) crossover in Fe^{2+} which was previously reported in Fe-bearing Mg-phase D at similar pressures.

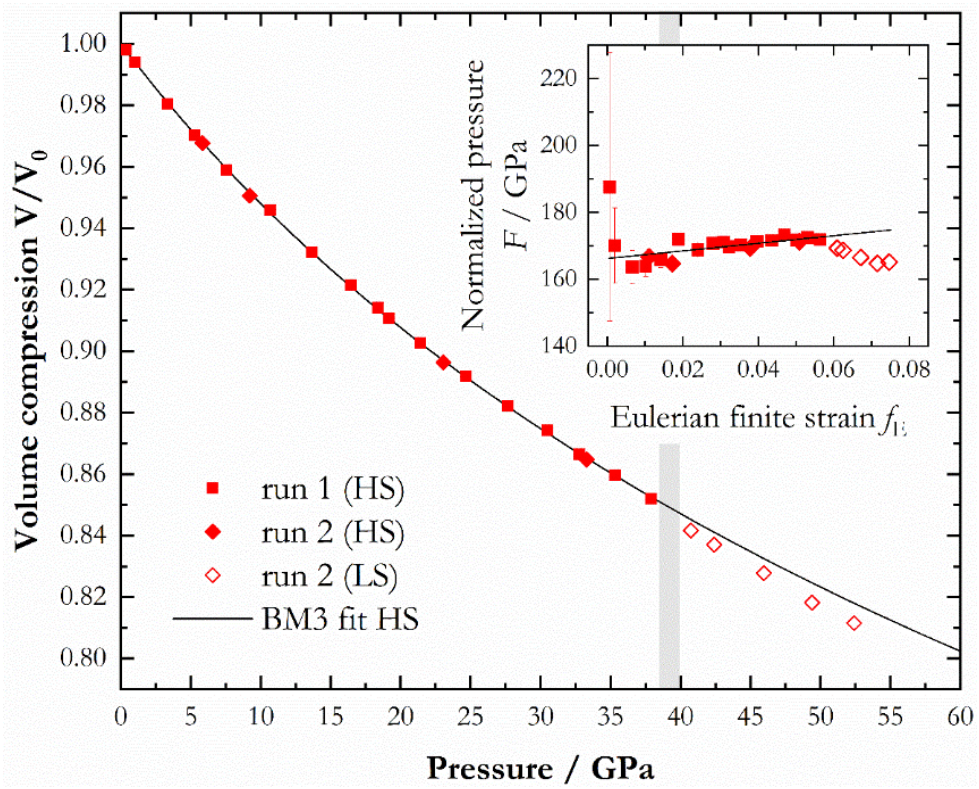

Fig. 3.4-1: Volume compression of Fe-bearing Al-phase D as a function of pressure. The grey shaded area represents the onset of the spin crossover. In the inset, the *f-F* plot provides further evidence of the elastic softening and volume reduction accompanying the spin crossover.

b. *Crystal chemistry and compressibility of Fe-free aluminous bridgmanite (G. Criniti, A. Kurnosov, T. Boffa Ballaran and D.J. Frost; in collaboration with Z. Liu/Jilin, K. Glazyrin and R. Husband/Hamburg)*

$MgSiO_3$-rich bridgmanite is widely accepted to be the most abundant mineral of the Earth's lower mantle. Al incorporation in the structure of bridgmanite is expected at lower mantle conditions in both mafic and ultramafic systems, and was reported to occur via $Fe^{3+}AlO_3$ and $AlAlO_3$ charge coupled (CC) substitutions, and via $MgAlO_{2.5}$ oxygen vacancy (OV) substitution. Because the OV mechanism is favored in MgO rich systems, such as pyrolite (Mg/Si ~ 1.3), it is believed that bridgmanite preferentially incorporates Al trough OV substitution at shallow lower mantle conditions. However, the complex crystal chemistry of Fe-bearing bridgmanite makes it difficult to tightly constrain the effect of $AlAlO_3$ and $MgAlO_{2.5}$ components, while all Fe-free samples analyzed so far were polycrystalline and therefore their structural refinements lack the precision necessary to constrain small structural changes. Furthermore, it was predicted that the incorporation of Al via OV mechanism has a greater effect on the bulk modulus relative to the CC substitution mechanism, but the experimental approach could not corroborate such a feature due to scarce characterization of the samples prior or after high-pressure experiments. For this reason, we decided to synthesize Fe-free Al-bearing bridgmanite crystals with different CC and OV contents at 25-27 GPa and 1773-2000 K using a mixture of $MgSiO_3$ enstatite, Al_2O_3 corundum and H_2O or $MgCl_2$ as flux materials.

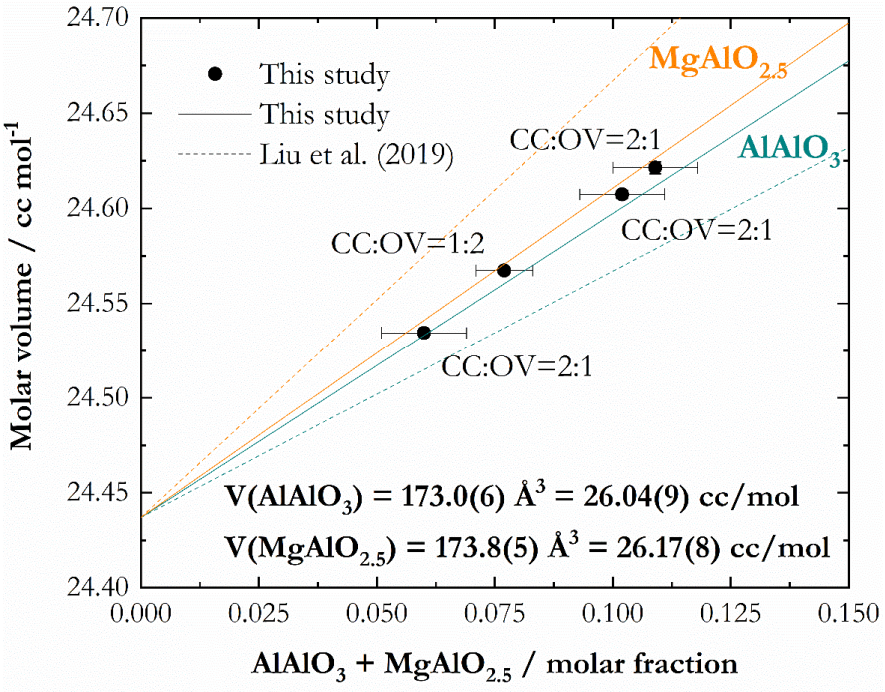

Fig. 3.4-2: Molar volume of aluminous bridgmanite as a function of Al content in the octahedral site of bridgmanite. Solid lines represent the dependence on OV and CC substitution determined in this study from single-crystal diffraction data; for comparison trends determined from polycrystalline samples are also reported (Liu *et al.*, 2019. *Earth Planet. Sci. Lett*. 523).

Single crystals recovered from high-pressure experiments were characterized by electron microprobe and single-crystal X-ray diffraction at ambient conditions. Our analyses on samples with different CC and OV concentrations reveal that the refined molar volume of the OV end member is larger than the CC end member, although the difference is much smaller than previously reported (Fig. 3.4-2).

In order to assess the effect of the two substitution mechanisms on the thermoelastic properties of Al-bridgmanite, we plan to conduct high-pressure and high-temperature single-crystal X-ray diffraction experiments in the diamond anvil cell (DAC). In a preliminary experiment, two high-quality single crystals with equal Al contents, but different degrees of CC and OV substitutions, were loaded in the same DAC together with a ruby sphere and a piece of Au. A Re gasket was indented to a thickness of 50 µm using diamonds with 350 µm culets, and laser drilled to create a sample chamber of 210 µm diameter. Helium was gas-loaded as a quasi-hydrostatic pressure transmitting medium. Compression experiments at room temperature were performed at the beamline P02.2 (DESY, Hamburg) and results are displayed in Figure 3.4-3. Pressure-volume datasets were fitted using a 2nd-order Birch-Murnaghan equation of state, yielding so far almost identical values of isothermal bulk modulus K_{T0}, equal to 243.5(11) GPa and 241.9(16) GPa for CC-rich and OV-rich samples respectively.

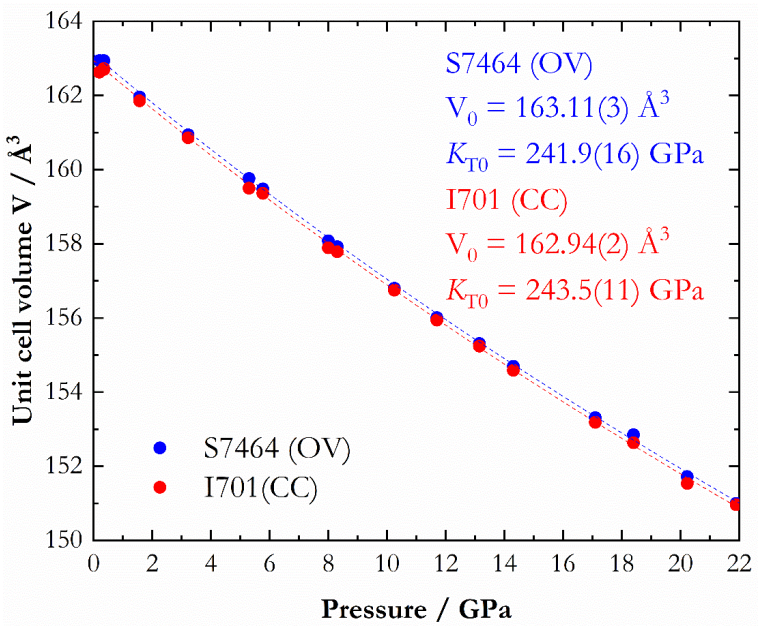

Fig. 3.4-3: Unit cell volume of two Al-bridgmanite samples with different OV and CC content as a function of pressure. Dotted trend lines represent 2nd-order Birch-Murnaghan fits of pressure-volume datasets.

c. *Equation of state and structure of Si-poor perovskite (I. Koemets, E. Koemets, T. Ishii, L. Dubrovinsky in collaboration with K. Glazyrin/Hamburg)*

The lower mantle constitutes more than half of the Earth's interior by volume and is believed to consist predominantly of bridgmanite (perovskite-structured $(Mg,Fe)(Si,Al)O_3$) and up to approximately 20 % ferropericlase (Mg,Fe)O by volume. Thus, the physical properties, crystal chemistry, and stability of bridgmanite at high pressures and temperatures are critical for

understanding the structure and dynamics of our planet, as well as the interior of other terrestrial planets and exoplanets. Ever since the application of laser heated diamond anvil cell (LHDAC) techniques coupled with X-ray diffraction allowed the major components of the lower mantle to be identified, investigations of perovskite-structured silicates have been a popular focus of mineral physics studies. Over the decades there have been several claims that bridgmanite undergoes structural transformations or that is not chemically stable at all conditions within the lower mantle. So far, however, only one phase transition in (Mg,Fe)(Si,Al)O_3 bridgmanite has been unambiguously confirmed, namely to a $CaIrO_3$-type structure phase (often called post-perovskite, PPv) above 125 GPa and at high temperatures. However, it is still unknown the maximum amount of Fe and Al that can be substituted in the orthorhombic perovskite structure of bridgmanite. Here we present a study of $Mg_{0.207(1)}Fe_{0.861(3)}Al_{0.648(1)}Si_{0.261(2)}O_3$ silicate perovskite that shows strong diffuse scattering implying a possible transformation to a double-perovskite structure having lower symmetry at larger Fe^{3+} content.

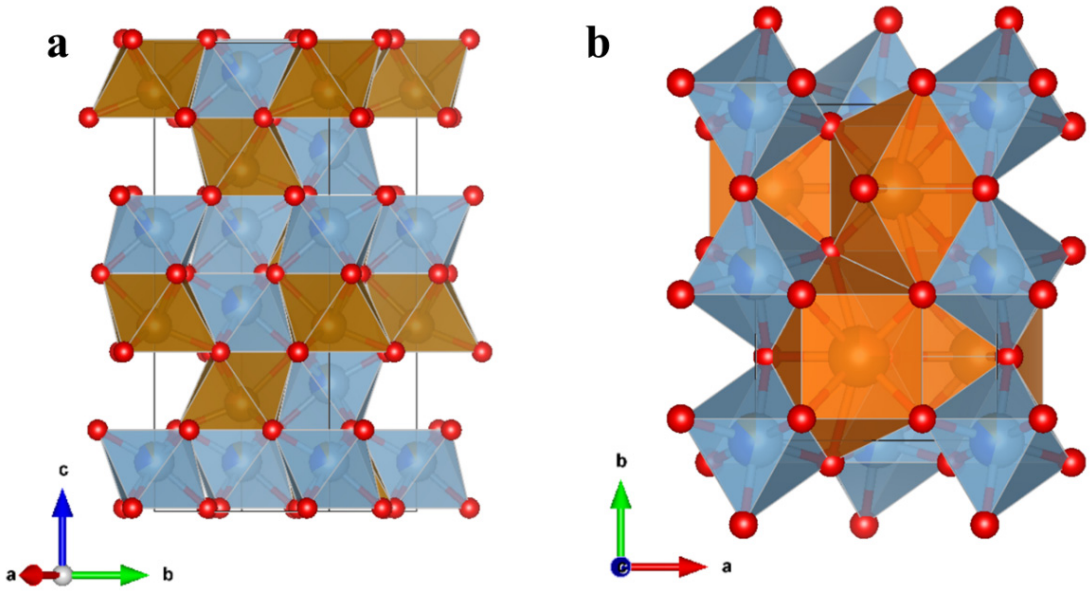

Fig. 3.4-4: The structure of $Mg_{0.207(1)}Fe_{0.861(3)}Al_{0.648(1)}Si_{0.261(2)}O_3$ consists of two types of polyhedra: Fe,Mg-bearing (orange) and Fe,Al,Si-bearing (blue). a) $LiNbO_3$-type structure ($R3c$) at ambient conditions where only octahedral sites are present and b) $GdFeO_3$-type perovskite ($Pnma$) at 30 GPa consisting (as determined from single crystal XRD data) of larger A-sites with mixed occupancy ($Fe_{0.75}Mg_{0.25}$) and B-sites that contain approximately 10 % of Fe.

Crystalline material with the composition $Mg_{0.207(1)}Fe_{0.861(3)}Al_{0.648(1)}Si_{0.261(2)}O_3$ has been synthesised in a Kawai-type multianvil apparatus (IRIS-15) at the Bayerisches Geoinstitut, University of Bayreuth. Starting materials consisted of $MgSiO_3$ + $FeAlO_3$ + Fe_2O_3 and PtO_2 was added to ensure a high oxygen fugacity. The synthesis was performed at a pressure of 27 GPa and a temperature of 2000 K. The recovered phase at ambient conditions has a black colour and crystallizes in a $LaNbO_3$-type structure (space group $R3c$) with unit-cell lattice parameters a = 4.908(2) Å and c = 13.153(5) Å (Fig. 3.4-4a). Recovered crystals were compressed up to

60 GPa in a BX90-type diamond anvil cell with 250-µm culet Bueler-Almax diamonds. We used rhenium as a gasket material and neon gas as the pressure-transmitting medium. At each pressure point, we collected single crystal X-ray diffraction data at beamline P02.2 at DESY, Hamburg.

Upon compression, the $LiNbO_3$-structured phase transforms to a distorted $GdFeO_3$-type perovskite structure with space group *Pnma* (Fig. 3.4-4b). Fitting pressure-volume data with a 2nd order Birch-Murnaghan EoS resulted in a bulk modulus K_0 = 234(9) GPa (Fig. 3.4-5). After transformation into the silicate perovskite phase the $Mg_{0.207(1)}Fe_{0.861(3)}Al_{0.648(1)}Si_{0.261(2)}O_3$ sample shows strong diffuse scattering along **c***, implying the presence of local ordering of Si and Fe^{3+} at the octahedral sites and that changes in composition could make a lower-symmetry structure, such as double perovskite, energetically favourable.

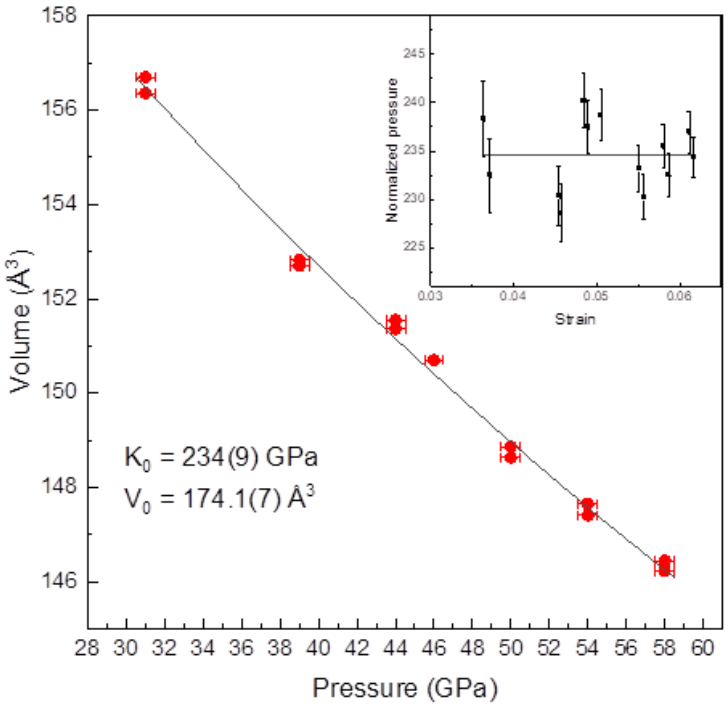

Fig. 3.4-5: Unit-cell volume variation with pressure of a Fe/Al-rich bridgmanite with composition $Mg_{0.207(1)}Fe_{0.861(3)}Al_{0.648(1)}Si_{0.261(2)}O_3$. Experimental points obtained in different compressional runs have been fitted with a 2nd order Birch-Murnaghan equation of state (solid line).

d. *Synthesis and compressibility of novel nickel carbide at pressures of Earth's outer core (T. Fedotenko, S. Khandarkhaeva. L. Dubrovinsky and N. Dubrovinskaia in collaboration with P. Sedmak/Grenoble and K. Glazyrin/Hamburg)*

Nickel is known to be the second most abundant element in the Earth's core after iron. Cosmochemical models and studies of meteorites suggest that Earth's core contains about 5

wt. % of Ni and up to 10 wt. % of light elements. The high abundance of carbon in the solar system suggests that this element can be one of the most likely candidates as a light element in the Earth's core. The intermediate Fe-C compounds, *i.e.*, Fe_3C and Fe_7C_3, were suggested to be the most likely candidates for the carbon-bearing phases in Earth's core, as they were found to be stable at relevant pressures and temperatures. Fe_3C decomposes into a mixture of solid Fe_7C_3 and hcp-Fe at above 145 GPa upon laser heating at temperatures of above 3400 K.

Contrary to the binary iron-carbon system, the Fe–Ni–C and Ni–C systems at high *PT* conditions are still poorly constrained. The mineral cohenite, $(Fe,Ni,Co)_3C$, which is isostructural to cementite Fe_3C, was found in iron meteorites and predicted to be stable at high pressures. However, a pure-Ni cementite-type phase (Ni_3C) has never been reported before.
Here, we report the synthesis and EOS of a novel high-pressure phase of nickel carbide (Ni_3C) obtained in a laser heated diamond anvil cell (LHDAC). A piece of a Ni powder was clamped between two thin layers of LiF from both sides and loaded inside a sample chamber of a BX90-type diamond anvil cell equipped with Boehler–Almax type diamonds (with culet diameter of 80 μm). We used LiF as pressure-transmitting medium and thermal insulation to minimize dissipation of heat through the diamonds. The sample was pressurized up to 184(5) GPa and laser-heated up to 3500(200) K by scanning of the Ni sample with a laser beam. High-pressure single-crystal and powder X-ray diffraction (SCXRD) experiments were carried out at the extreme conditions' beamline P02.2 (DESY, Hamburg, Germany; $\lambda = 0.29$ Å, the beam size ~ 2 × 2 μm^2) and material science beamline ID11 (ESRF, Grenoble, France; $\lambda = 0.30996$ Å, the beam size ~ 0.5 × 0.5 μm^2).

A direct reaction between Ni and carbon from the diamond anvil resulted in the synthesis of a new compound indexed as orthorhombic. In order to localize the point of interest, high-resolution two-dimensional X-ray diffraction mapping was realized at ID11 beam line at the ESRF (Fig. 3.4-6).

The reaction products consist of numerous very small single crystals that were identified using synchrotron single-crystal XRD. The structure solution and refinement (final $R_1 = 6.4$ %) revealed the cementite-type orthorhombic structure (space group *Pnma, #62*; a = 4.520(3) Å, b = 5.8014(17) Å, c = 4.009(4) Å at 184(5) GPa) and the Ni_3C chemical composition. The diamond anvil cell was then studied under stepwise decompression but unfortunately no diffraction pattern from Ni_3C was observed below 75 GPa. It is still unclear whether the quality of the sample deteriorated or the Ni_3C phase decomposed/amorphized during decompression. The pressure-volume data of Ni_3C was fitted to a 3rd order Birch-Murnaghan (BM3) EOS and gave the following parameters: $V_0 = 147.7(8)$ Å^3; $K_0 = 157(10)$ GPa, $K' = 7.8(6)$ (Fig. 3.4-7).

The EOS parameters of cementite-type Ni_3C are close to those of Fe_3C ($K_0 = 165(4)$ GPa, $K' = 5.99$ (9)). Thereby, the presence of Ni in the alloy likely should not affect significantly the elastic properties of Fe-Ni-C system, but may potentially change the carbon distribution. Due to the stability of Ni_3C at conditions of the Earth's outer core, it may be considered as one of the likely candidates to carbon-bearing phases in the core along with Fe_7C_3.

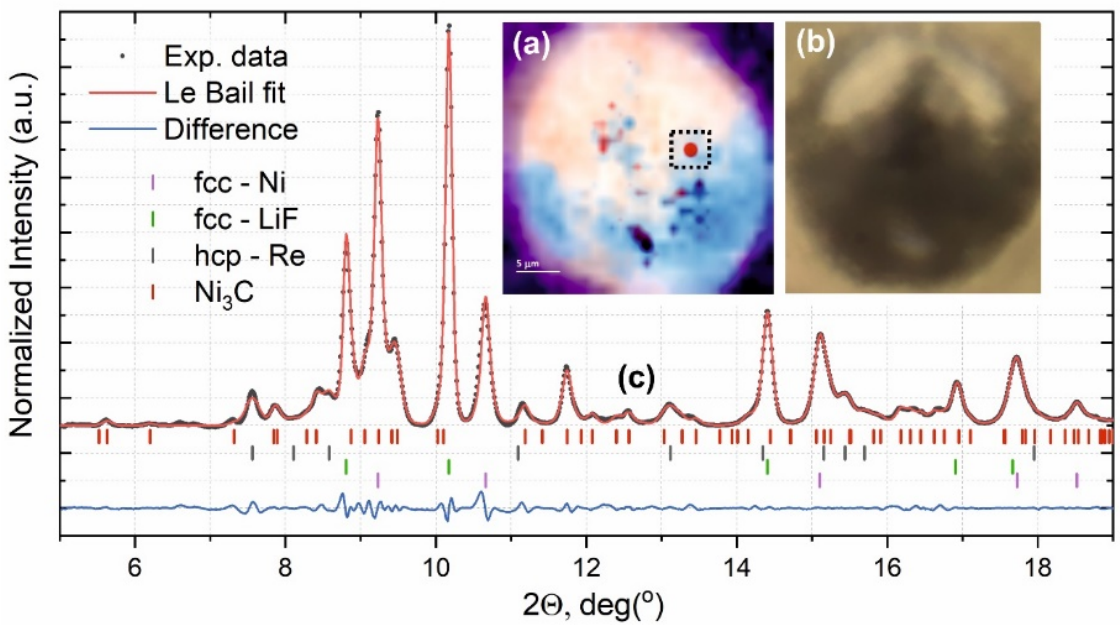

Fig. 3.4-6: (a) Two-dimensional X-Ray diffraction mapping of the sample chamber of a diamond anvil cell. The color map allows to distinguish between the present phases. The intensity of the colors is proportional to the intensity of particular reflections: the dark purple region beyond the pressure chamber corresponds to the Re gasket; the blue region represents the reflections of Ni and the orange region represents the reflections of LiF. The red region indicates the presence of the new compound Ni_3C. (b) View of the same sample chamber under optical microscope. (c) Powder diffraction pattern collected from the sample at the position highlighted by the black dotted square on the XRD color map in (a).

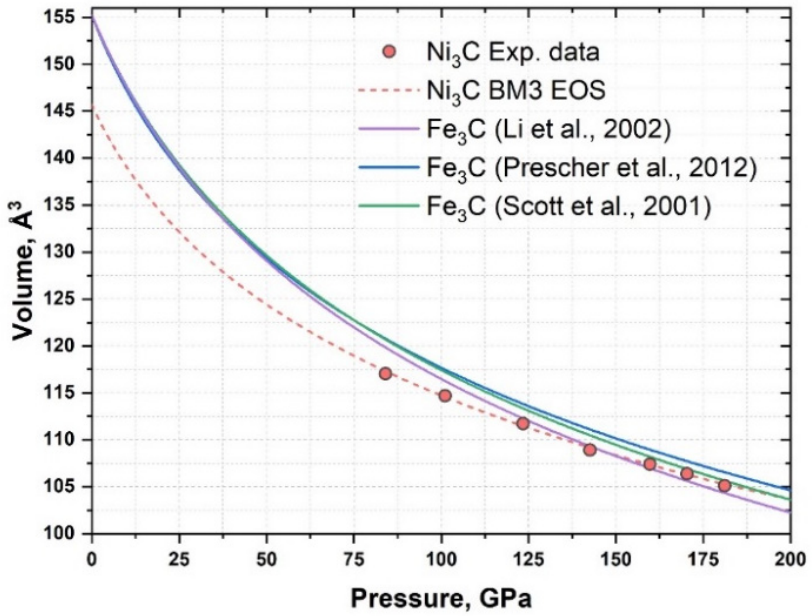

Fig. 3.4-7: The pressure-volume dependence of Ni_3C synthetized at 184 GPa and ~ 3500 K. Red dots represent experimental data, the dashed red curve is the BM3 EOS fit (V_0 = 147.7(8) Å^3; K_0 = 157(10) GPa, K' = 7.8(6)). Solid purple, blue and green lines correspond to the EOSes of Fe_3C obtained in different studies.

e. *Seismic signature of iron-sulfide melt accumulation in the upper mantle (A. Néri and D.J. Frost)*

The Earth's upper mantle can show evidence for long-term low seismic wave speeds. Classical explanations are either the presence of raised temperatures or of melt, both affecting locally the elastic properties of the material. However, some low seismic velocity regions are located in old tectonic settings which have not experienced tectonic activity for more than ≈ 50 Myr. This rules out thermal anomalies as their lifetimes are much shorter than these timescales. The presence of melt may only provide a satisfactory explanation if it is able to remain immobile on such timescales. Indeed, silicate and carbonate melts are able to form percolative interconnected networks at low melt fractions (< 1 vol. %), making them highly mobile. Metallic or sulfide melts, however, have much larger interconnection thresholds (volume fraction at which a phase forms a percolative network) and are likely more plausible candidates.

Ultrasonic interferometry is an *in situ* technique that allows the elastic properties of samples to be determined at high pressures and temperatures. This technique is adapted for use in large-volume multianvil presses, however it requires an accurate knowledge of the pressure-temperature conditions during the experiment in order to study the behaviour of mixtures and is, therefore, mostly employed at synchrotron facilities where *in situ* X-ray measurements can be made. Following the development of an internal pressure sensor for "in-house" measurements (see contribution by Dolinschi *et al.*, section 3.8), the seismic signal of mixtures of olivine and iron-sulfide melts will be determined.

Literature studies suggest that the phase relations of a liquid in a crystalline matrix controls the elastic properties of the mixture. Depending on the wetting behaviour of the melt, the surface area of contact between the melt and the matrix varies. At equilibrium, this behaviour is dictated by the minimization of interfacial energies, increasing the contact lengths of low energy cost and decreasing that of high energy cost. Repeated dihedral angle measurements at triple junctions allow the interfacial energy budget within a sample to be estimated. At a fixed dihedral angle, different melt fractions most likely affect the surface area of contact between the melt and the silicate; both dihedral angle and melt fraction are then distilled into a parameter called contiguity that corresponds to the ratio of the solid - solid contact surface area to the total surface contact area (solid - solid and solid - liquid). Both dihedral angles and contiguity can be estimated from image analysis of samples. Figure 3.4-8A shows a sample composed of olivine and troilite in a 95:5 volume ratio, the dihedral angle of the troilite melt is ≈ 135° and contiguity is relatively high due to the rounded shape of the melt pockets. The relation between contiguity and dihedral angles determined at low angles (< 80°) will be extended for larger values with results obtained in this study. From contiguity, theoretical parametrizations allow to predict the compressional and shear wave velocities (Fig. 3.4-8B and C respectively). This experimental work brings critical information to verify and potentially to improve these geometric models.

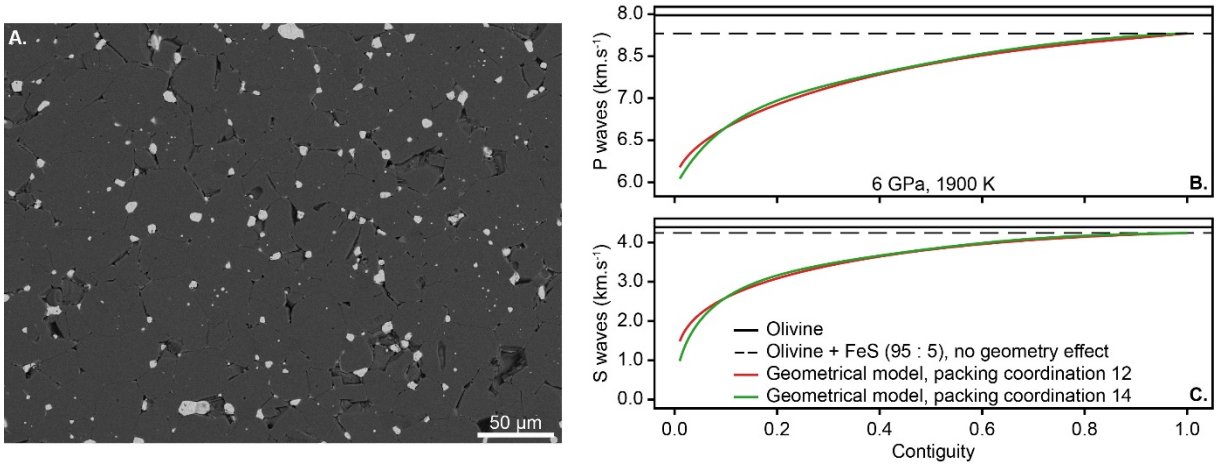

Fig. 3.4-8: (A.) SEM-BSE image of a sample bearing 95 vol. % of olivine (dark phase) and 5 vol. % of troilite (light phase). (B.) and (C.) show the effect of contiguity on P- and S-waves of an olivine - troilite mixture in similar proportions as the experiment shown in (A.).

f. *First experimental constraints on the full elastic properties of antigorite single crystals at high-pressure conditions (N. Satta, T. Boffa Ballaran and A. Kurnosov in collaboration with H. Marquardt/Oxford)*

The interaction between surface and Earth's interior water reservoirs is crucial for the geological evolution of our planet. Water is mostly delivered into the Earth's interior by means of subduction of oceanic slabs, *i.e.*, portions of oceanic lithosphere forced to sink down by plate tectonics. Antigorite is a hydrous phyllosilicate that forms as result of the alteration of mafic minerals, and is thought to be among the main mineralogical constituents of oceanic slabs up to 180-200 km depth. In fact, with a stability field that extends up to 5 GPa at 650 ˚C, and a water storage capacity of ~ 13 wt. %, antigorite governs the input of water into the Earth's interior. Experimental evidence has shown that if a subducting slab follows a cold geotherm, antigorite could be preserved down to depths that allow the formation of dense hydrous magnesium silicate phases, stabilizing part of the initial water budget possibly down to Earth's lower mantle. On the other hand, if the slabs follow a hot geotherm, the raising temperatures would most likely induce an earlier breakdown of antigorite, resulting in a complete release of water that would end up hydrating the overlying mantle wedge, triggering arc magmatism and seismic activity in the whole subduction region. Consequently, quantifying the distribution with depth of antigorite in subducting slabs is crucial to understand global scale processes in subduction zones and to provide tight constraints on the overall water budget that may be transported into the deep Earth's interior.

Seismology uses remote-sensing approaches to explore regions of the Earth's interior that would be otherwise inaccessible. In the last decades, the coupling between seismological observations and the experimental-based knowledge of the elastic properties of minerals led to a rapid improvement of our understanding of the mineralogical structures in the Earth's interior.

However, when it comes to the elasticity of antigorite, tight experimental constraints are missing. Therefore, our ability to accurately map the presence of this hydrous mineral, hence the distribution of water in subducting slabs, is strongly hampered.

The aim of this study is to characterize the single-crystal elastic properties of antigorite under high-pressure conditions relevant to its stability field. Two large, high-quality single crystals of antigorite (m = 17, where m is the number of the unique tetrahedra along the length of the structural modulation) were carefully selected based on their crystallinity from a batch of natural samples from Val Malenco (Italy). The selected crystals were first oriented parallel to complementary crystallographic orientations, and then double-sided polished to a final thickness of ~ 20 µm. The two polished platelets and a ruby sphere were loaded together in a diamond anvil cell. Helium was used as a pressure-transmitting medium. For each pressure point, acoustic wave velocities were probed along the 360˚ azimuth for a total of 38 different crystallographic directions (19 for each platelet) by means of Brillouin scattering measurements. The compressional wave velocities collected at different pressures are shown in Figure 3.4-9. The measured wave velocities together with density obtained using X-ray diffraction data collected at each pressure point were used to obtain the 13 independent and non-zero elastic stiffness coefficients (c_{ij}) of antigorite up to 5.17(2) GPa.

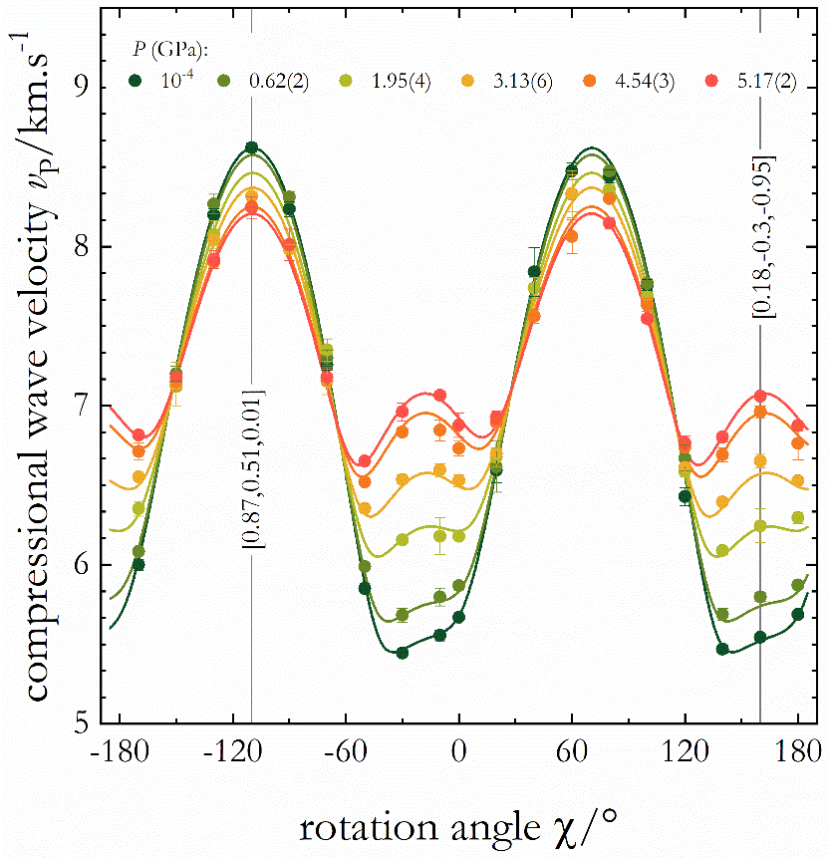

Fig. 3.4-9: Compressional wave velocities at different pressures of one of the two investigated antigorite crystals as a function of the rotation angle. Solid circles represent observations, while solid curves are calculated values resulting from the c_{ij} best-fit.

Antigorite shows a rapid reduction of the compressional wave anisotropy with pressure. This reduction is associated with a marked stiffening of the *c*-axis, which is described by the monotonic and large increase (~ 100 %) of the c_{33} up to ~ 6 GPa (Fig. 3.4-10). These results suggest that pressure is mostly accommodated through a reduction of the interlayer distance, in agreement with what is predicted by theoretical studies.

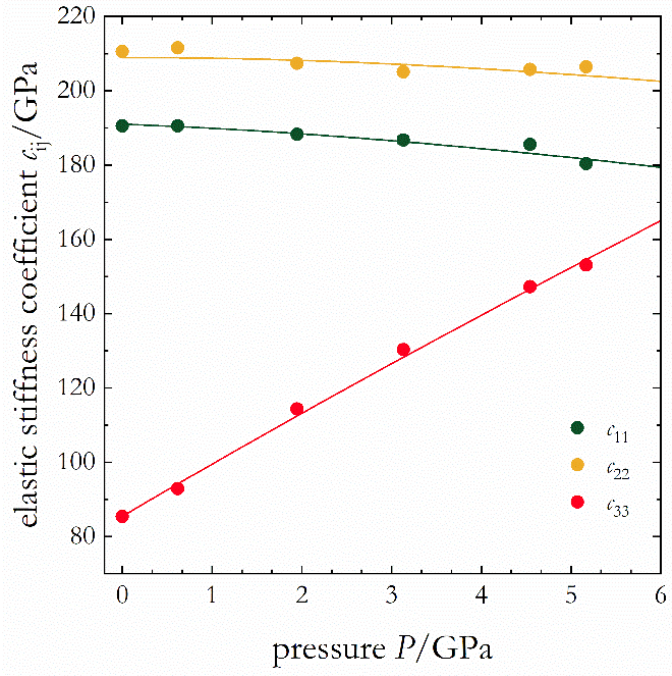

Fig. 3.4-10: Variation with pressure of the elastic coefficient c_{11}, c_{22} and c_{33} of antigorite. Solid lines are fit to the c_{ij} using third order finite strain equations.

g. *Single-crystal elasticity of δ-(Al,Fe)OOH: Relation between P-induced H-bond evolution and elastic properties (N. Satta, G. Criniti, T. Ishii, T. Boffa Ballaran and A. Kurnosov, in collaboration with H. Marquardt/Oxford)*

The Earth's mantle is likely the largest reservoir of terrestrial water in our planet. Remote sensing approaches used by seismology provide a viable way to picture the Earth's interior and thus its hydration state. However, a precise knowledge of the elastic properties of hydrous minerals is critical to locate hydrous regions in the Earth's mantle and to constrain their degree of hydration. At lower mantle depths, δ-AlOOH, ε-FeOOH and phase H ($MgSiO_2(OH)_2$) are expected to form a solid solution having a $CaCl_2$-type structure (space group *Pnnm*) and are believed to be the most important carrier of water in MORB-like rocks within subducted slabs. δ-AlOOH and ε-FeOOH have lower symmetry at ambient conditions (space group $P2_1nm$) and undergo a phase transition to the *Pnnm* phase associated with the symmetrization of the hydrogen bonds. Recent neutron diffraction experiments on δ-AlOOH revealed that the pressure-induced evolution of the hydrogen bond passes through an acentric, and then disordered state before reaching the centered symmetric configuration. A similar proton order-disorder sequence has been already observed in H_2O ice - although at much higher pressure, suggesting that proton disordering may be a common precursor of hydrogen bond

symmetrization. As δ-(Al,Fe)OOH constitutes a case study for understanding the evolution of the elastic properties of H-bonded compounds across the hydrogen bond symmetrization, we have investigated the structural and elastic properties of δ-(Al,Fe)OOH single crystals at high pressure using Brillouin scattering and X-ray diffraction in a diamond anvil cell (DAC).

Large single crystals of δ-($Al_{0.97}Fe_{0.03}$)OOH were synthetized in a Kawai-type multianvil apparatus at 21 GPa and 1150 °C from a mixture of $Al(OH)_3$ and $^{57}Fe_2O_3$. A Mössbauer spectrum of the recovered crystals shows that all Fe is present as ferric. Two high-quality single crystals were oriented, double-sided polished to a thickness of ~ 13 µm and cut into half-circles using a focused ion beam prior to loading into the DAC (Fig. 3.4-11).

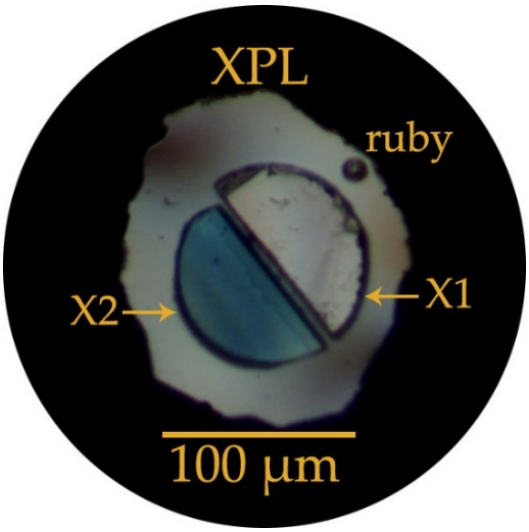

Fig. 3.4-11: The X1 and X2 FIB-cut double-sided polished platelets of δ-(Al,Fe)OOH crystals investigated in this study at a pressure of 23.8 GPa inside the DAC sample chamber loaded with He. Picture was taken under cross polarized light.

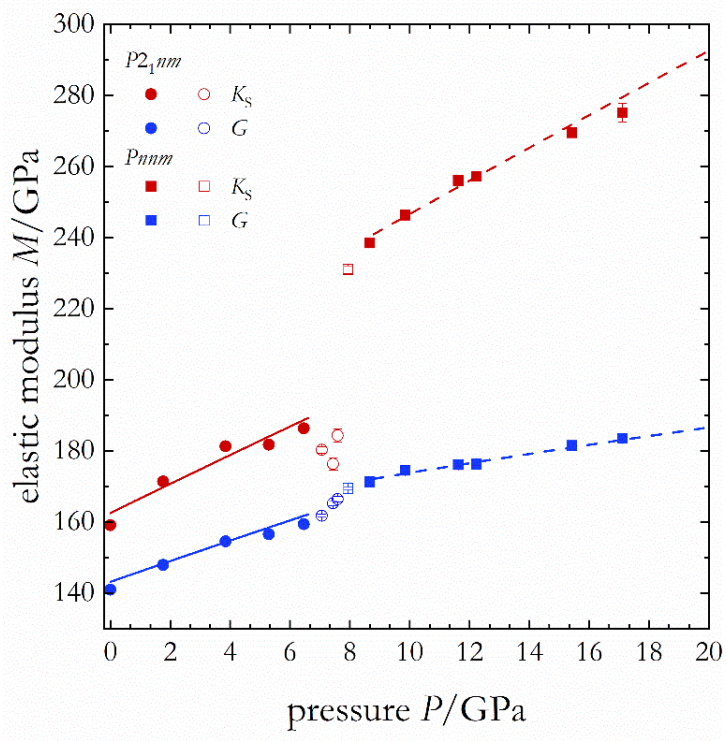

Fig. 3.4-12: Aggregate elastic moduli of δ-(Al,Fe)OOH as a function of pressure. A large softening of the bulk modulus is observed between 6.46(2) and 8.67(1) GPa, whereas the shear modulus variation is continuous through the $P2_1nm$ to *Pnnm* phase transition. Solid and dashed lines are equation of state fittings of the $P2_1nm$ and *Pnnm* phases, respectively. Open symbols were not included in the fit.

Simultaneous X-ray diffraction and Brillouin scattering measurements were performed up to 17.2 GPa, while X-ray diffraction experiments were carried out up to 23.8 GPa. Brillouin scattering measurements reveal that some of the elastic stiffness coefficients as well as the bulk modulus (K_S) of δ-$(Al_{0.97}Fe_{0.03})OOH$ undergo elastic softening just below the onset of the phase transition, followed by a stiffening of more than 50 GPa at about 7.6 GPa (Fig. 3.4-12). High-resolution X-ray diffraction measurements consistently show a subtle decrease in the unit cell volume accompanying the elastic softening of the low-pressure phase.

h. *Seismic profile of the Earth's lower mantle from single-crystal elasticity measurements of bridgmanite at high pressure (G. Criniti, A. Kurnosov, T. Boffa Ballaran and D.J. Frost)*

The combination of seismic observation and mineral physics data constitutes a unique tool to understand the structure and evolution of the deep Earth's interior. However, to date, elasticity data on both compressional (v_P) and shear (v_S) wave velocities of $MgSiO_3$-rich bridgmanite, the most abundant mineral of the lower mantle, are limited to shallow lower mantle conditions, hampering the resolution of mineral physics models. Here, we report the first experimental constraints on v_P and v_S of $MgSiO_3$ bridgmanite up to approximately 80 GPa using single-crystal Brillouin scattering in a diamond anvil cell, allowing us to calculate the pressure dependence of the adiabatic bulk modulus (K_{S0} = 257.1(6) GPa, K_{S0}' = 3.71(4)) and of the shear modulus (G_0 = 175.6(2) GPa, G_0' = 1.86(1)). Combining our results with literature data we built a self-consistent thermodynamic model to calculate seismic wave velocities along a lower mantle adiabat for a primitive upper mantle bulk composition in the FeO-CaO-MgO-SiO_2 (CFMS) system, which is currently the most complex system for which sufficient thermodynamic and thermoelastic data exist. Temperature was calculated self-consistently along an adiabatic profile assuming 1960 K at 24 GPa and the distribution of Fe^{2+} and Mg in bridgmanite and ferropericlase was calculated from mass balance and a pressure-temperature dependent distribution coefficient. Seismic wave velocities of $MgSiO_3$ bridgmanite and a phase assemblage consisting of bridgmanite, ferropericlase and Ca-perovskite (CFMS system) as a function of depth are shown in Fig. 3.4-13.

Velocities for single phase $MgSiO_3$ bridgmanite are faster than those reported in seismic models, showing that a perovskitic lower mantle would be too stiff in both v_P and v_S to fit 1D seismic profiles. In the CFMS system, there is excellent agreement between the calculated v_S and the seismic models throughout the whole lower mantle, with residuals never exceeding 0.6 %, while the v_P perfectly overlaps with 1D seismic models along the whole depth interval considered here. Although the striking agreement between our mineral physical model for the CFMS system and 1D seismic models points towards a pyrolytic lower mantle, the exclusion of Al and Fe^{3+} from the model is likely to have an effect on the calculated velocities. Al-bearing bridgmanite in a pyrolitic bulk composition has an Fe^{3+}/Σ Fe ratio of approximately 0.5. This would cause ferropericlase to become more Mg-rich and bridgmanite more Fe-rich, but the overall change of v_P and v_S is expected to cancel out to

this effect into a model for the entire bridgmanite stability field is not currently possible, as further experiments are needed to determine the proportion and stability of the $FeAlO_3$ component in bridgmanite at deep lower mantle conditions.

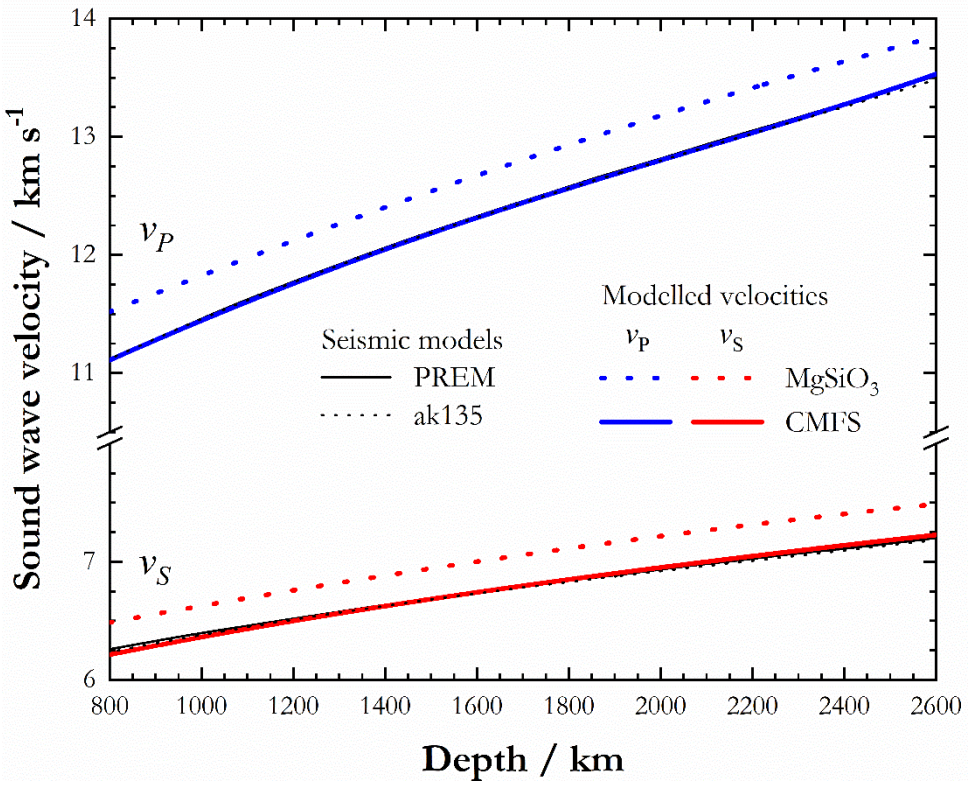

Fig. 3.4-13: P- and S-wave velocities of $MgSiO_3$ bridgmanite (dotted colored lines) and a lower mantle assemblage determined for a primitive mantle composition (solid colored line) calculated as a function of depth. 1D seismic models PREM (Dziewonski & Anderson, 1981, *Phys. Earth Planet. Inter.*, 25, 297, solid black lines) and ak135 (Kennett *et al.*, 1995, *Geophys. J. Int.*, 122, 108, dotted black lines) are shown for comparison.

i. *Simultaneous high-pressure and high-temperatures acoustic wave velocities of pyrope by means of Brillouin spectroscopy coupled with a CO_2 laser heating system. (A. Kurnosov, G. Criniti, T. Boffa Ballaran, A.C. Withers, S. Khandarkhaeva and D.J. Frost)*

The interpretation of seismic observations requires mineral physics models which can be constructed using the high-pressure high-temperature elastic properties of candidate materials of the Earth's interior. Ideally, the variation of the full elastic tensor of these materials and their density with pressure and temperature is needed in order to apply strong constraints not only on wave velocities, but also on possible anisotropic behaviour of the mantle rocks. The full elastic tensor of any material can be determined by means of single-crystal Brillouin spectroscopy, which however, requires the use of transparent samples that cannot be heated by conventional laser equipment used to reach realistic mantle *P,T*-conditions. In the last years, therefore, we have focused our effort in optimizing the use of a flexible CO_2 laser heating setup

(see previous BGI annual report) which has the advantage of using a laser wavelength being absorbed by samples which are transparent for visible and near infrared light, thus enabling us to reach high temperatures also during Brillouin spectroscopy. One of the important rock-forming minerals extensively studied is pyrope given its abundance in the Earth's mantle and transition zone. However, single-crystal elastic data available so far in the literature have been obtained only at room pressure and high temperature, at high pressure and room temperature or at high pressures and moderate temperatures (less than 800 K), whereas ultrasonic measurements at high pressure and high temperature have been performed only on polycrystalline pyrope.

Several single-crystals of pyrope have been selected, double-sided polished to a thickness of 18-20 μm and loaded into a diamond anvil cell between two thin layers of KBr or KCl, which provide a relatively soft pressure-transmitting medium (especially at high temperatures) as well as good insulation from the diamond. The two salts have been preferred to Ar or Ne because the thermal conductivity of noble gases is rapidly increasing with pressure and becoming too large already at the pressures of few GPa, requiring a very high laser power for heating at high pressures. KBr is a slightly better insulator compared to KCl, but it could be used only below 8 GPa because above such pressures the shear wave velocity signal of pyrope was masked by that of the pressure medium (Fig. 3.4-14), such that KCl was used at higher pressures.

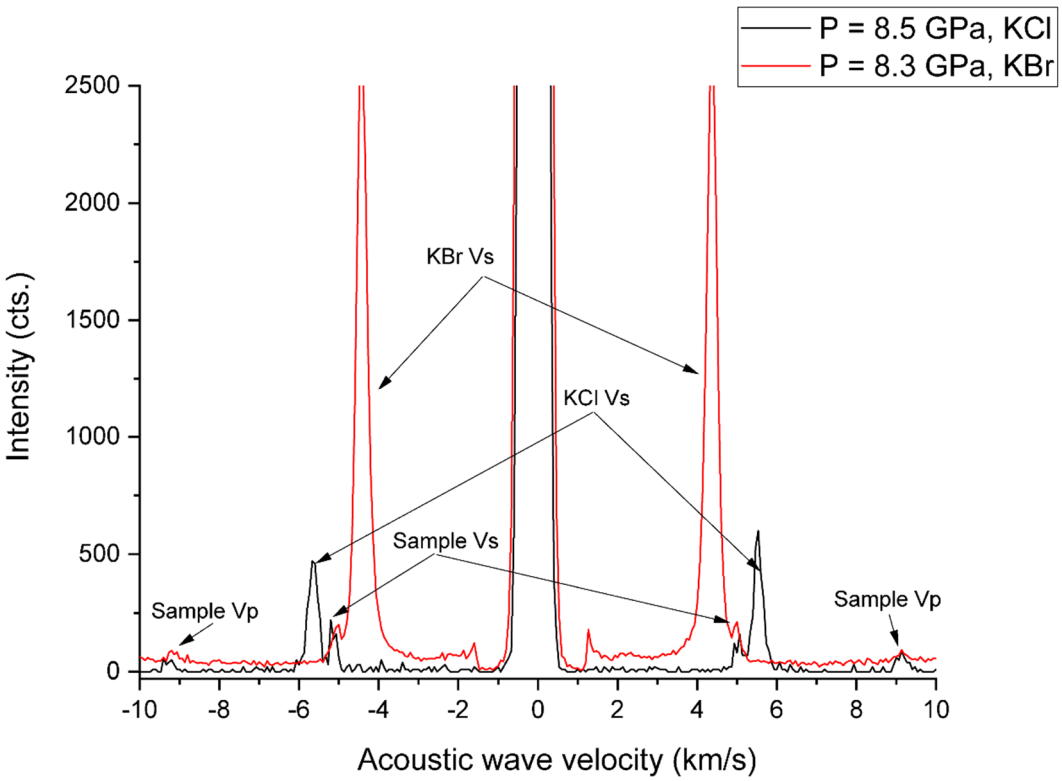

Fig. 3.4-14: Brillouin spectra collected at room temperature and at ~ 8.5 GPa for a crystal of pyrope loaded between two layers of KBr (red) and KCl (black). The v_s signal of pyrope is very close to the v_s signal of KBr and disappears under it at high temperatures.

The single crystals of pyrope were heated at different pressures using a fan-cooled CO_2 laser coupled to a commercially available Hollow Silica Core Waveguide and a cage system that contains ZnSe optics to focus the laser radiation to the sample inside the DAC. The temperature during heating was measured through the Brillouin collecting optics in order to measure the thermal emission spectra from the same part of the sample from which the Brillouin spectrum is collected. The DAC was reloaded several times with new single-crystals of pyrope, because the surface of the sample was ruined after few heating cycles over a relatively long period of time in order to obtain good quality Brillouin spectra. Pressure at high temperature was determined from the fluorescence signal of a Sm-doped YAG ($Y_3Al_5O_{12}$) garnet loaded together with pyrope, since such signal depends on pressure and it is insensitive to temperature.

So far, we have collected the Brillouin spectra at different pressures up to 11.5 GPa and at temperatures between 298 K and 1900 K. The measured acoustic wave velocities are shown in Figure 3.4-15 together with resistive heating data from the literature collected at ambient pressure up to 1070 K. The thermodynamic properties of pyrope at high pressures and high temperatures will be obtained by fitting the measured wave velocities with a self-consistent model which makes use of a finite strain equation for capturing the variation of the elastic moduli with pressure and of the Debye temperature, its first and second logarithmic volume derivatives and the shear strain derivative of the Grüneisen parameter to take into account the variation of the vibrational frequencies with pressure at high temperatures.

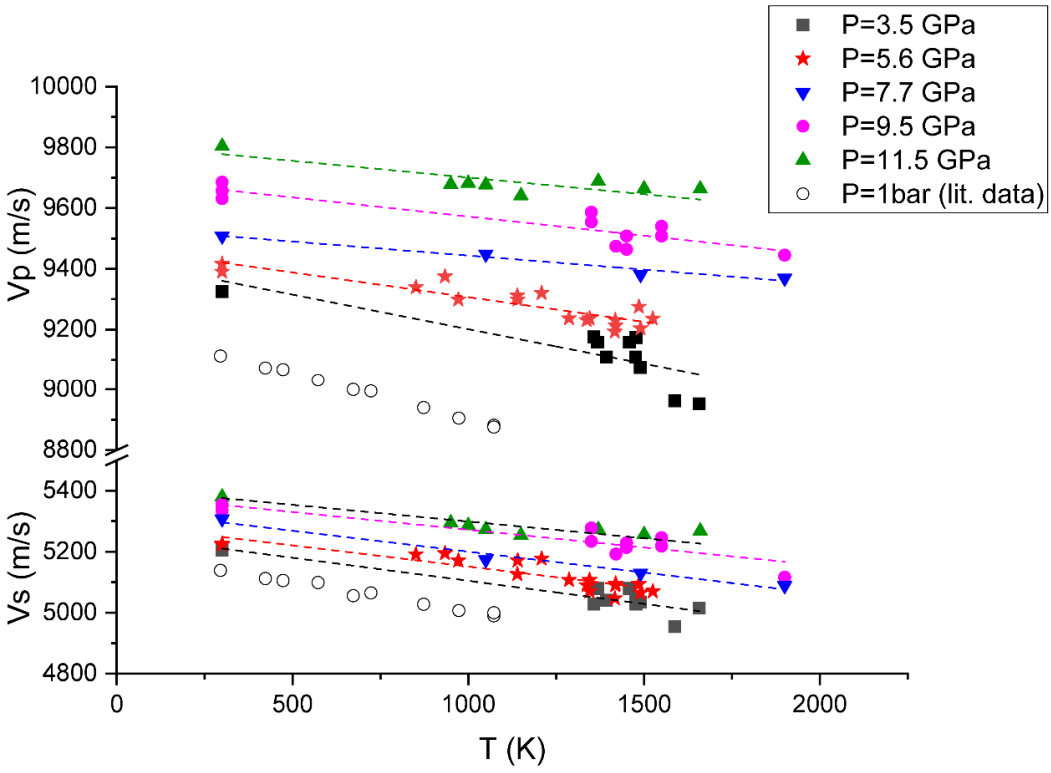

Fig. 3.4-15: Variation with temperature of the acoustic wave velocities of pyrope measured at different pressures up to 11.5 GPa; dashed lines are linear fits to the data for each pressure.

j. *Spin transition of iron in δ-(Al,Fe)OOH induces thermal anomalies in Earth's lower mantle (E. Ohtani/Sendai, W.-P. Hsieh, K.-H. Chao and F. Deschamps/Taipei, J. Tsuchiya/Matsuyama and T. Ishii)*

Seismic anomalies observed in the Earth's deep mantle are conventionally considered to be associated with thermal and compositional anomalies, and possibly partial melt of major mantle phases. However, through deep water cycle, impacts of hydrous minerals on geophysical observables and on the deep mantle thermal state and geodynamics remain poorly understood. We measured thermal conductivity of δ-(Al,Fe)OOH, an important water-carrying mineral in the Earth's deep interior, to lowermost mantle pressures at room temperature. The thermal conductivity varies drastically by twofold to threefold across the spin transition of iron at 30-45 GPa and room temperature, resulting in an exceptionally low thermal conductivity at the lowermost mantle conditions. As δ-(Al,Fe)OOH is transported to the base of the lower mantle, its exceptionally low thermal conductivity may serve as a local thermal insulator, promoting high-temperature anomalies and the formation of partial melt and thermal plumes at the base of the mantle, strongly influencing thermo-chemical profiles in the region and fate of Earth's deep water cycle.

3.5 Fluids, melts and their interaction with minerals

The first three contributions in this chapter investigate the behavior of volatiles, notably water and aqueous fluids, in subduction zones. Serpentine is a hydrous mineral that may be a major carrier of water in the subducted slab and serpentine dehydration may be one of the main sources of fluids in subduction zones. In order to understand how this fluid will distribute and migrate through the mantle, it is important to study the permeability of serpentinites upon dehydration. Such data, obtained under realistic pressure and temperature conditions, are reported in the first study of this chapter. The data show that permeability strongly increases upon serpentine dehydration, but the anisotropy of the permeability disappears. This implies less efficient focusing and more pervasive flow of fluids, therefore allowing for more widespread fluid-rock equilibration. While subduction zone fluids were usually considered to be dominated by simple inorganic species, such as H_2O and CO_2, recently several theoretical studies suggested the stability of organic species, such as acetate under high P,T conditions. These predictions have received a lot of attention and they have been used to explain various phenomena, including the formation of diamonds. However, direct evidence for the stability of these organic species under the relevant conditions was so far mostly lacking. Therefore, one contribution in this report looked at the predicted stability of acetate in subduction zone fluids at 5 GPa and 600 °C. The experiments were carried out both in silver capsules inside a piston cylinder press and by direct *in situ* observation of the speciation by Raman spectroscopy in an externally-heated diamond anvil cell. The results were, however, negative: While there is very interesting chemistry going on in the acetate solution upon heating, at the predicted stability field at 5 GPa and 600 °C, all acetate appears to be gone. Fluids and volatiles may also be involved in earthquakes that originate from subduction zones. Deep focus earthquakes were sometimes attributed to the rapid conversion of metastable olivine to its high-pressure polymorphs in the subducted slab. However, since water is known to greatly accelerate this transformation, the persistence of metastable olivine is hard to reconcile with the presence of abundant water in the slab. A possible solution for this apparent contradiction is presented in the next contribution: If the olivine coexists with certain hydrous minerals, such as "phase A", water partitions so strongly into these phases that the olivine is nearly dry.

The most direct evidence for the composition of fluids in crust and mantle comes from fluid inclusions. These droplets of fluid trapped in crystals are, however, not always easy to interpret. Usually, a uniform distribution of the fluid inclusions throughout a crystal is considered as evidence for their "primary" origin, *i.e.*, for trapping during the growth of the crystal. However, by using cathodoluminescence images of quartz crystals, a study in this chapter shows that this is not so. Synthetic fluid inclusions are sometimes also used as tools to trap and to study fluids from high-pressure experiments. The next contribution in this chapter uses this technology to look at the critical curve in the H_2O-H_2 system to 4.5 GPa. The data show a curious behavior around 2.5 GPa, *i.e.*, in a pressure and temperature range were some previous studies also observed some anomalies in the equation of state of pure water. Aside from water or hydrogen, nitrogen is another important volatile that is cycled between the mantle and the atmosphere.

The most important mechanism for nitrogen degassing from the mantle is volcanic activity. The efficiency of volcanic processes for nitrogen degassing is mostly controlled by the mineral/melt partition coefficients of nitrogen in the mantle. The following contribution reports first measurements of nitrogen partition coefficients between basaltic melt and olivine, pyroxenes, plagioclase, and garnet. The data suggest that nitrogen is highly incompatible, but slightly less so than argon.

The viscosity of silicate melts is a fundamental property that controls the style of volcanic eruptions as well as the kinetics of core-mantle separation in early Earth history. Three contributions look at various novel aspects of silicate melt viscosities. Recent studies have shown that nanoparticles sometimes form in melts during volcanic processes and these objects may have a major effect on bulk viscosities, which is being investigated by an ongoing research program. A new, theory-based fitting model allows a better prediction of the viscosity of hydrous silicate melts at variable temperatures. Finally, major advances in multianvil technology allowed for the first time to measure the viscosity of peridotite melts to lower mantle conditions. Such data are important for modelling the separation of iron metal from silicate melt during the magma ocean and core formation event in early Earth history. This problem is also addressed in the last contribution in this chapter, which looks at the effect of nickel on transport properties of molten iron under high pressure. *Ab initio* simulations show that nickel for example slows down the diffusivity of carbon in the molten metal, which influences the efficiency of carbon sequestration into the core.

a. *Changes in permeability during mineral dehydration at high pressure and high temperature (L. Eberhard, P. Eichheimer, M. Thielmann, G.J. Golabek and D.J. Frost, in collaboration with M. Nakamura and A. Suzuki/Sendai)*

Within subduction zones, fluids are released through dehydration reactions. An important reaction is the dehydration of antigorite that occurs in subducting lithosphere at 650-700 °C and 2.5 - 3 GPa:

$$Mg_{48}Si_{34}O_{85}(OH)_{62} = 14\ Mg_2SiO_4 + 20\ MgSiO_3 + 31\ H_2O \qquad (1)$$

The permeability of the subducted serpentinite is a critical parameter that controls how the fluid migrates towards the mantle wedge. Previous permeability measurements that were limited to near room pressure conditions revealed a strong permeability anisotropy in foliated serpentinites at room temperature. A higher fluid flux is measured parallel to the foliation, which would focus the fluid flow parallel to the slab surface and result in channelized flow in places where the foliation was crossed. Such focusing is important when considering the removal of soluble components from the slab. In previous low-pressure studies, a strong increase in permeability upon dehydration was also observed. However, conventional methods to determine the permeability are limited to pressures below 100 MPa.

We developed a multianvil setup to determine the permeability experimentally at high P,T conditions. This allows for the first time to determine permeabilities at subduction zone conditions. Oriented serpentinite drill cores were prepared from natural samples. The drill cores were placed into an MgO sleeve and welded shut in a gold capsule (Fig. 3.5-1a). Fluid released from the serpentine cylinder migrates towards the MgO and forms brucite (Fig. 3.5-1b) through the reaction

$$MgO + H_2O = Mg(OH)_2 \qquad (2)$$

The fluid flux q, *i.e.*, the total discharged fluid during the experiment, was obtained from the volume of brucite formed. Neglecting plastic deformation effects on the serpentine cylinder, the volume change according to the antigorite dehydration reaction (1) can be used to calculate a first order estimate of the fluid pore pressure. The permeability is then obtained from Darcy's law. Figure 3.5-1b shows the results of an experiment performed at 3.5 GPa and ~ 800 °C, where an anomalously thin brucite layer was formed.

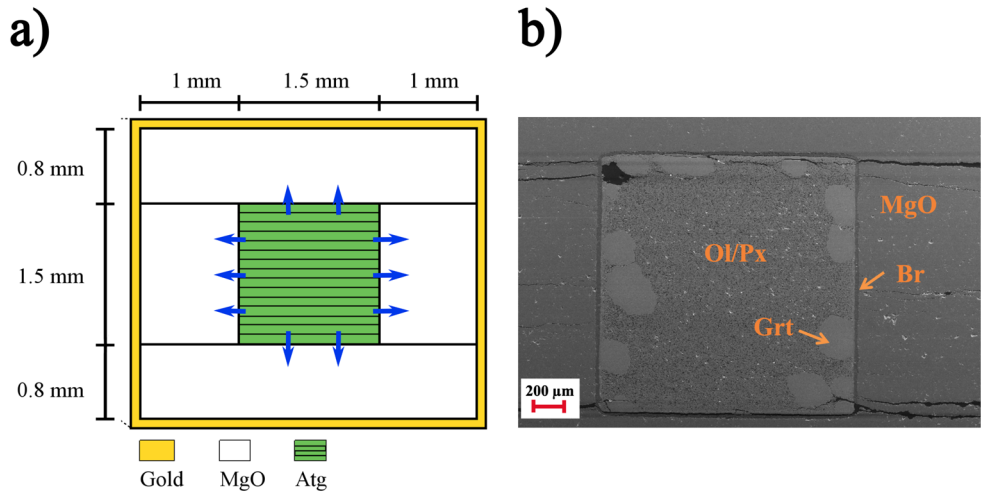

Fig. 3.5-1: Serpentine dehydration experiments. a) A sketch of the experimental setup. A serpentinite drill core is placed into an MgO sleeve. The foliation of the serpentine is either parallel of horizontal to the cylinder axis. Fluids released from the serpentinite migrate towards the MgO (indicated by blue arrows) and form brucite. b) SEM image of a run product. In this example, high-temperature dehydration results in the formation of olivine (Ol), pyroxene (Px) and garnet (Grt). A layer of brucite (Br) is formed within the MgO sleeve from fluids released during dehydration. In this experiment, performed at 3.5 GPa and ~ 800 °C, the brucite layer is anomalously thin, because of the low pore fluid pressure at these conditions.

This can be explained by the fact that above 3 GPa, reaction (1) results in a negative volume change, which causes a fluid underpressure. In the absence of an overpressure to drive the fluid into the MgO, brucite is formed only through a small amount of compaction from the surrounding multianvil assembly. Very large garnet crystals (> 200 µm) have also formed due to the high levels of pore fluid.

At temperatures below serpentine dehydration, additional fluid sources can be used to make similar permeability estimates, but these show serpentine to be essentially impermeable to water at the experimental timescales. This is consistent with experiments performed at ambient conditions which reveal permeabilities of $1x10^{-22}m^2$. Upon the onset of dehydration, however, the permeability strongly increases by several orders of magnitute at 2.5 GPa. No anisotropy in permeability is observed. These findings indicate that, although anisotropic fluid flux was measured at low pressure, the mineralogical changes during dehydration result in a loss of anisotropy and thus a pervasive fluid flux. Within subduction zones pervasive fluid flux will result in an effective fluid migration into the mantle wedge and a larger fluid-rock interaction.

b. *On the stability of acetate in subduction zone fluids (V. Szlachta, K. Vlasov and H. Keppler)*

Recent theoretical studies have predicted the stability of acetate as a major species in subduction zone fluids *e.g.*, at 5 GPa and 600 °C. The occurrence of abundant organic species in these fluids could have a major effect on their solvent properties and the processes occurring during fluid-rock interaction. In particular, the formation of diamonds has been suggested to involve such fluids containing organic species. However, the stability of acetate or other organic molecules in aqueous fluids at high pressure and high temperature was never experimentally confirmed. We therefore carried out a series of *in situ* and quench experiments in order to test this hypothesis.

We used a sodium acetate (CH_3COONa) solution as starting material in all experiments. In piston cylinder experiments at 5 GPa and 600 °C, this solution was filled together with silica glass powder into thick-walled silver capsules. Since silver is poorly permeable for hydrogen under run conditions, the idea was that the acetate solution would buffer the oxygen fugacity into its intrinsic stability range. Experiments were carried out as a time series, starting from zero time up to 24 hours run duration. After quench, the retrieved samples were studied by Raman spectroscopy. However, in none of the samples from piston cylinder experiments (and a few multianvil experiments) any acetate could be detected (Fig. 3.5-2a,b). Instead, some carbonaceous material (disordered and impure "graphite") had formed, suggesting decomposition of the acetate at run conditions.

The behavior of the acetate solution was also studied by *in situ* Raman spectroscopy in an externally heated diamond cell up to 4.65 GPa and 600 °C. While some new hydrocarbon species were detectable during the heating process, at the final run conditions acetate appeared to have completely decomposed (Fig. 3.5-2c); carbonaceous material was again prominent in the run products after quench to room temperature (Fig. 3.5-2d). Taken together, our data therefore strongly suggest that organic molecules are not major carbon species in subduction zone fluids. However, the presence of traces of such molecules is still possible and requires further study. The discrepancy between our experimental results and previous theoretical predictions is likely related to inaccuracies in the thermodynamic potentials of the organic species at high-pressure and high-temperature conditions.

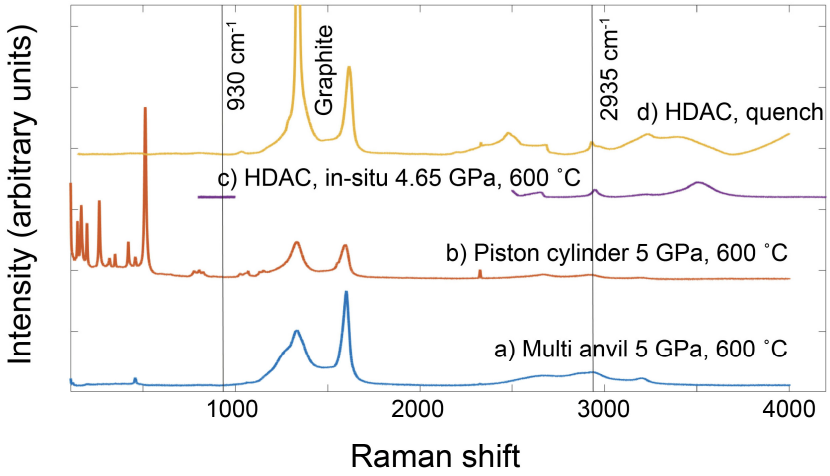

Fig. 3.5-2: Raman spectra of sodium acetate solutions at high pressure and temperature or of quench products. Marked are the positions of the 930 cm^{-1} band (C-C stretching) and of the 2935 cm^{-1} band (C-H stretching) of acetate. In particular, the first band is never detected in any of the spectra, showing the absence of acetate species. Decomposition of acetate at run conditions is also suggested by the abundance of carbonaceous material ("graphite").

c. *Water partitioning between olivine and its polymorphs and hydrous phases under water-undersaturated conditions (T. Ishii, in collaboration with E. Ohtani/Sendai)*

Deep-focus earthquakes are sometimes attributed to the delayed transformation of metastable olivine in the subducted slab. This interpretation seems to require dry subducting slabs, as water strongly enhances the reaction rate of olivine. On the other hand, many geochemical and geophysical observations and mineral physics data have shown that water is present in subducting slabs as hydroxyl groups in both hydrous and nominally anhydrous minerals, implying that subducting slabs are hydrated. The possible presence of metastable olivine in wet slabs is thus difficult to explain.

In this study, we investigated the partitioning of water between forsterite or wadsleyite and a major dense hydrous magnesium silicate (hydrous phase A) under water-undersaturated conditions in a multianvil press. A single crystal of forsterite or wadsleyite was enclosed in a powder mixture of forsterite, brucite and quartz (8:2:0 or 4:2:1 in molar ratio) inside a gold capsule. The recovered samples show the single crystal inside a matrix of forsterite or wadsleyite and hydrous phase A (±clinopyroxene) (Fig. 3.5-3). Water contents of the recovered single crystals were measured by Fourier transform infrared (FTIR) spectroscopy. Forsterite or wadsleyite coexisting with hydrous phase A contain less than 1 ppm and ≈300 ppm of water, respectively, which translates into kinetically dry conditions (Fig. 3.5-3).

Our results imply that olivine and wadsleyite may show dry transformation kinetics even in wet slabs, resolving the paradox of metastable olivine in wet slabs. Moreover, the water contents in

olivine and its polymorphs will dramatically increase by dehydration of hydrous phases. Therefore, deep-focus earthquakes and strong slab deformation leading to stagnant slabs may be produced by the transformation of olivine in water-undersaturated wet slabs. These processes could be the consequence of the dehydration of hydrous minerals and the subsequent rapid phase transformation of olivine (Fig. 3.5-4).

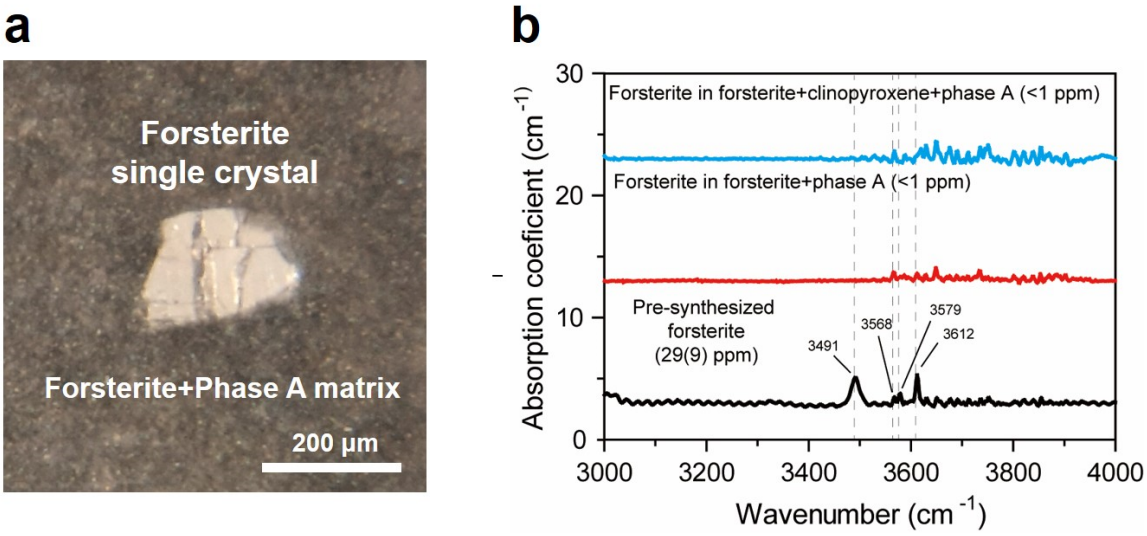

Fig. 3.5-3: (a) A representative photograph of a cross-section of a sample recovered from 10 GPa and 800 °C after 72 hours. The surrounding part of the forsterite single crystal is a matrix of forsterite + hydrous phase A. FTIR spectra of the forsterite single crystal indicate less than 1 ppm of water. (b) Representative unpolarized FTIR spectra from the recovered single crystals of forsterite.

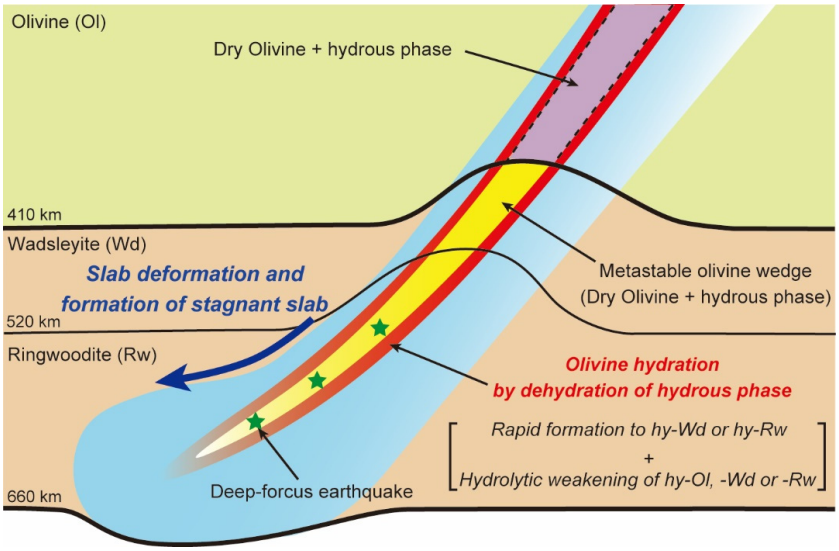

Fig. 3.5-4: (a) Slab deformation and the formation of a stagnant slab and their possible relation to the dehydration of hydrous phases. The presence of hydrous phases and of a dry metastable olivine core along the isotherms is shaded as yellow. In the temperature region of the slab above 1000 °C (red shaded area), dehydration of hydrous phases and the resulting increase of water fugacity increases the water content in olivine and its high-pressure polymorphs, which may cause slab deformation that results in a stagnant slab.

d. *Post-entrapment migration and compositional modification of quartz-hosted fluid inclusions (A. Audétat and D. Zhang/Wuhan)*

Fluid inclusions are small droplets of fluids that were trapped in minerals during or after their growth. They provide important information on the physicochemical nature of geological fluids. In most studies it is assumed that fluid inclusions remained perfectly isochoric and compositionally closed systems after their formation. However, there is increasing evidence that in many cases this is not true. A typical situation is shown in Figure 3.5-4a. In that sample, seemingly well-preserved, negative-crystal-shaped vapor and brine inclusions occur randomly within the host quartz. Based on their random distribution such fluid inclusions are commonly classified as primary, *i.e.*, having formed at the same time as the surrounding host. However, cathodoluminescence images (Fig. 3.5-5b) clearly demonstrate that these fluid inclusions are not of primary origin, but rather formed along pseudo-secondary or secondary trails and subsequently migrated away from these trails, leaving behind strings of dark-luminescent quartz.

During migration, the fluid inclusions changed their volume in order to reach the same internal pressure as outside. In most cases, this resulted in a reduction of the inclusion volume, hence in higher fluid density, and consequently, in lower homogenization temperatures. This is why many fluid inclusion assemblages display ± horizontal trends in liquid-vapor homogenization temperature vs. salinity diagrams (Fig. 3.5-6). Some of these trends cross the halite saturation curve, producing fluid inclusions that homogenize via halite dissolution. Some of the latter fluid inclusions imply very high minimum entrapment pressures and for this reason, they have previously been interpreted as having accidentally trapped solid halite. However, the present study suggests that most of these fluid inclusions experienced post-entrapment reduction in inclusion volume, which in some cases was accompanied by loss of H_2O and, consequently, with an increase in fluid salinity.

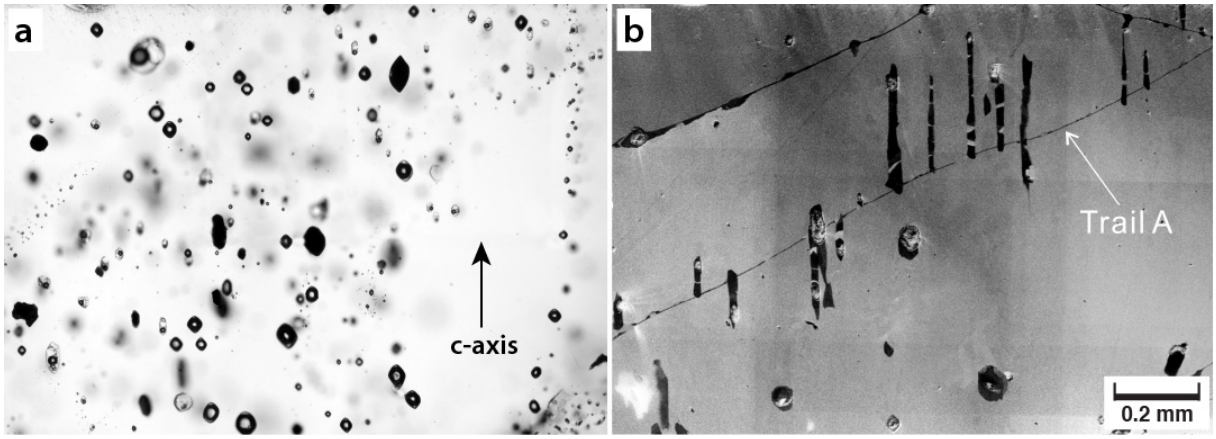

Fig. 3.5-5: (a) Transmitted-light photomicrograph of seemingly randomly distributed fluid inclusions in quartz. (b) Same field of view in a cathodoluminescence image. The elongated, dark-luminescent quartz patches parallel to the c-axis of the crystal suggest that many of the fluid inclusions originally occurred along trail A and subsequently migrated up or down in c-axis direction.

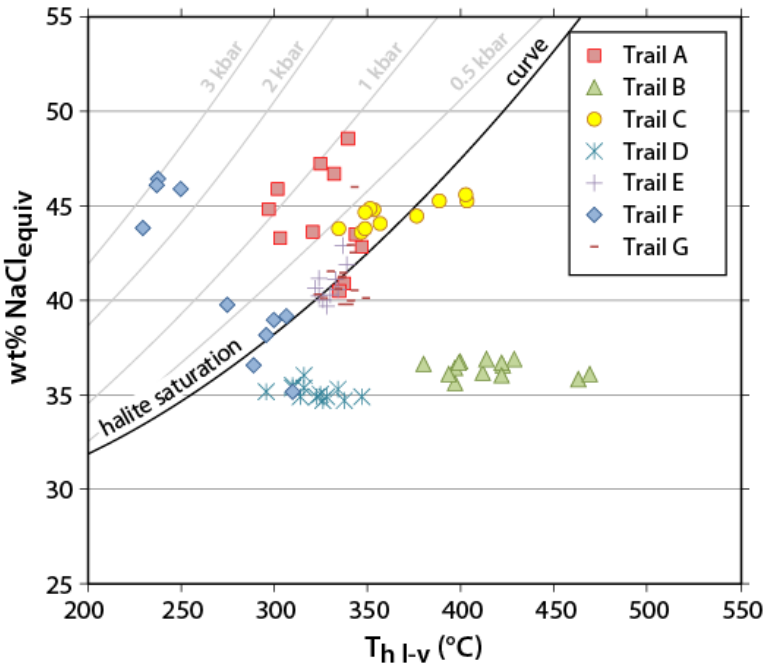

Fig. 3.5-6: Liquid–vapor homogenization temperature versus salinity of brine inclusions in seven different fluid inclusion assemblages within a single quartz crystal. Note the sub-horizontal trends displayed by three assemblages, and the high minimum entrapment pressures implied by some of the inclusions within the halite saturated field.

e. *The critical curve in the H_2-H_2O system to 4.5 GPa (K. Vlasov and H. Keppler)*

Oxygen fugacity in the upper part of the mantle is close to the FMQ buffer and becomes more reducing with depth, approaching the iron-wustite buffer only at ~ 200 km depth. However, sometimes extremely reduced mineral assemblies originate from shallow depths, containing phases such as moissanite SiC or Ti_2O_3.

A plausible mechanism for forming such extremely reduced domains was previously discovered at Bayerisches Geoinstitut. Experiments showed that at shield geotherm conditions, H_2O and H_2 are immiscible, and reducing H_2 fluid may be exsolved from a supercritical fluid as temperature drops. This work established the critical curve in the H_2-H_2O system from 1.5 to 2.6 GPa. With a slope of 400 °C/ GPa the H_2-H_2O critical curve, when extrapolated, would imply that at transition zone conditions those two species remain immiscible. However, in hotter parts of the mantle, such as plumes, they may still form a single fluid, that may unmix in colder domains of sinking slabs. The correct understanding of the behavior of hydrogen in the mantle, thus, requires additional experimental evidence, that may be obtained from experiments at pressures higher than 3 GPa.

Continuing the previous studies at Bayerisches Geoinstitut, we synthetized fluid inclusions in the piston cylinder apparatus with a ½" talc-pyrex assembly. Thermally shocked samples of

olivine were loaded together with water into a Pt-Rh capsule and sealed by arc welding. To control oxygen fugacity at Fe-FeO buffer level, this capsule was placed into an external iron capsule with FeO and water. At the end of the run experiments were quenched, olivine crystals were cut and polished. Fluid inclusions were investigated by Raman spectroscopy.

We performed a series of runs from 3 GPa to 4.5 GPa and established the position of the critical curve of H_2-H_2O in that pressure interval (Fig. 3.5-7). At lower temperatures, three types of fluid inclusions were observed – ones with pure H_2, pure H_2O, and a mixture of both (Fig. 3.5-7, open green circles). At higher temperatures only the H_2-H_2O mixed inclusions were present in the samples (Fig. 3.5-7, filled green circles). The critical curve shows a curious behavior, with an apparent inflection near 2.7 GPa. Additional experiments are required to confirm whether this effect is real. However, an anomalous behavior of water under these conditions was already described in the literature as observed from brucite dehydration experiments.

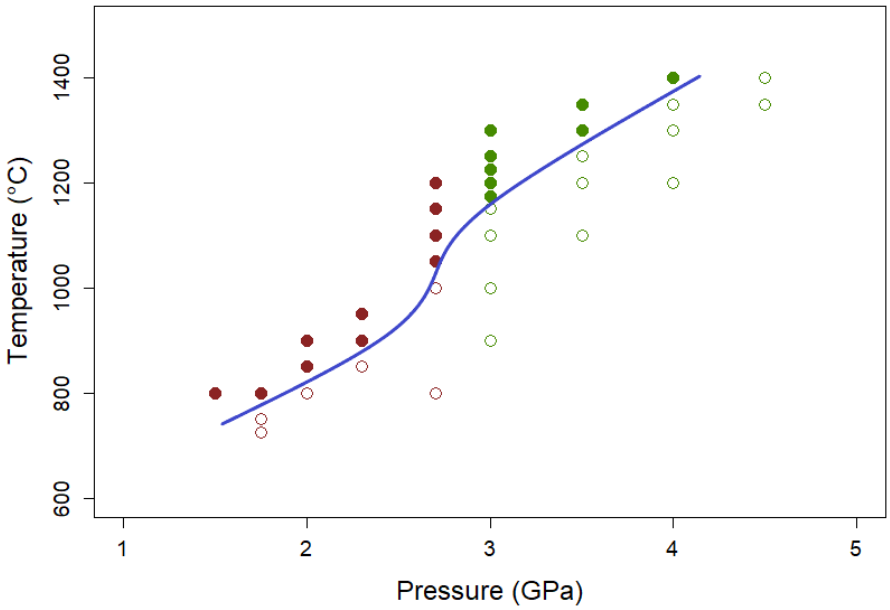

Fig. 3.5-7: The critical curve in the H_2-H_2O system (blue line). Green data points are from the current study, red data points from Bali *et al.* (2013, Nature 495: 220-222). Closed symbols indicate the presence of a single fluid, while open symbols show that two separate fluid phases coexisted.

f. *Nitrogen partitioning between upper mantle minerals and basaltic melts (L. Cialdella, M. Wiedenbeck/Potsdam and H. Keppler)*

Nitrogen is one of the main constituents of the solar system and the most abundant element in Earth's atmosphere. It is continuously exchanged between the Earth's mantle and near-surface reservoirs. Fluctuations in the nitrogen partial pressure of the atmosphere may have strongly influenced the climate and the habitability of our planet. These processes, however, are difficult to quantify since the amount of nitrogen that might be retained in the solid Earth is not well

known. While the atmosphere has been traditionally considered to be the main nitrogen reservoir on Earth, already a concentration of 1 ppm of N in the mantle would be equal to the present-day atmospheric mass of nitrogen. Previous studies showed that nitrogen solubility in melts and minerals increases with pressure and toward reducing conditions. However, less is known on how efficiently nitrogen can be transferred from the mantle to the surface. The release of volatile elements from the solid Earth is essentially driven by magmatism, which involves the partitioning of volatiles between solid, melt and gaseous phases. Therefore, to better constrain the amount of nitrogen presently stored in the deep Earth and to estimate the nitrogen budget retained in the mantle after magma ocean crystallization, it is essential to measure how nitrogen partitions between solid and liquid phases.

We performed systematic mineral/basalt partitioning experiments for different conditions of pressure, temperature and oxygen fugacity. By means of a piston cylinder press, the samples were compressed to 1-3 GPa and shortly heated beyond the liquidus, then slowly cooled over 1 or 2 days to a temperature between the solidus and the liquidus, where they were kept for a few more days. The starting materials were MORB glasses, in some cases enriched with 30 wt. % enstatite, forsterite, or pyrope powders. As a result, plagioclase, olivine, orthopyroxenes, clinopyroxenes, and garnet of different compositions were crystallized from the melt, sometimes in mm-sized crystals (Fig. 3.5-8). Oxidizing conditions above the Ni-NiO buffer were achieved through the high initial Fe^{3+}/Fe^{2+} ratio of the basaltic starting material enclosed in Pt-Rh capsules together with $Ag^{15}N_3$ as nitrogen source. More reducing conditions, close to the Co-CoO buffer, were obtained using cobalt capsules, together with a small amount of CoO, water and $^{15}NH_4{}^{15}NO_3$ as nitrogen source. To reach oxygen fugacities near the the Fe-FeO buffer, iron capsules were employed, together with water and $^{15}NH_4{}^{15}NO_3$. We used ~ 99 % enriched ^{15}N components to avoid analytical interferences due to air contamination. The samples were analyzed by SIMS (secondary ion mass spectrometry) at GFZ Potsdam.

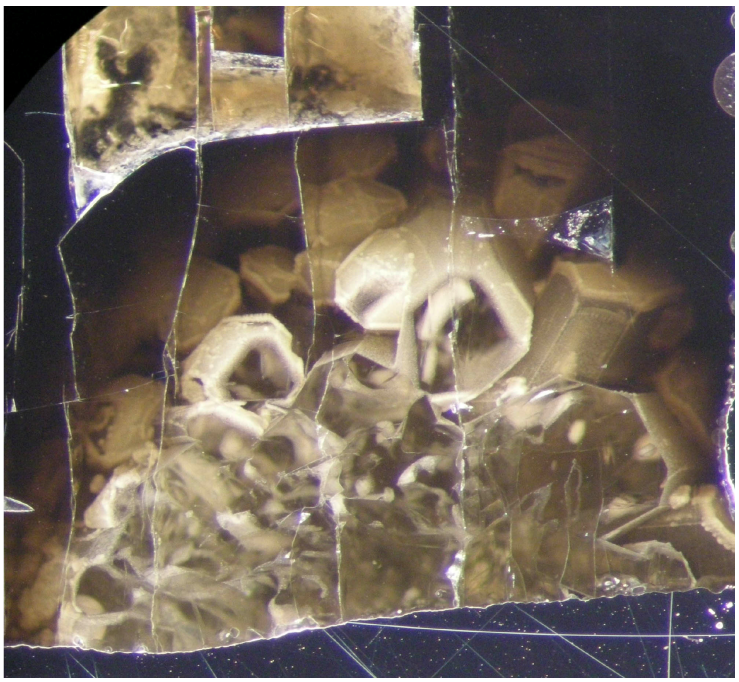

Fig. 3.5-8: Large crystals of orthopyroxene coexisting with residual MORB melt from a piston cylinder experiment. Width about 5 mm.

Preliminary results for the high oxygen fugacity series yielded mineral/basalt partitioning coefficients in the order of 10^{-3} for all the major upper mantle minerals (Fig. 3.5-9). At oxidized conditions, nitrogen is present mostly as N_2 and because of its strong covalent bond, it likely behaves like an inert molecule occupying the interstitial sites of the silicate structures. Accordingly, its geochemistry follows similar patterns as for the noble gases. Consistently, we obtained partitioning coefficients comparable to or slightly higher than those of argon, indicating a small fractionation between these elements in the shallow upper mantle.

At lower oxygen fugacity, nitrogen may occur in the N^{3-} oxidation state and its solubility both in minerals and melts substantially increases due to the possible chemical interactions. This may lead to an increase in the solid/melt partitioning coefficients by at least one order of magnitude, which may provide new constraints on the amount of nitrogen retained in the more reduced zones of the upper mantle after the solidification of the magma ocean.

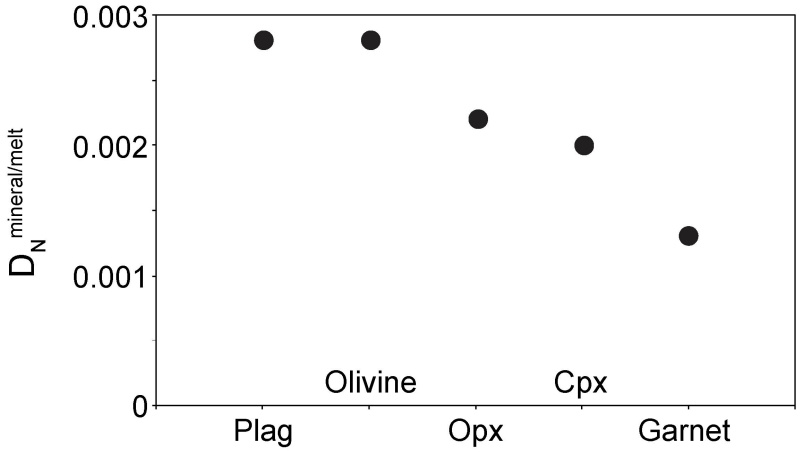

Fig. 3.5-9: Mineral/melt partition coefficients of nitrogen under oxidizing conditions. Error bars are not shown, but may be up to 50 % of the values given.

g. *Chemical and physical effects on the viscosity of volcanic melts (D. Di Genova)*

Volcanoes are important messengers from the deep Earth. They constantly shape our planet and can impact our society, economy and even the global climate. Volcanoes erupt a multiphase high-temperature suspension (melt + crystals + gas bubbles) that is known as magma. The shear viscosity (η) of a magma regulates its transport to the Earth's surface and influences the style (effusive or explosive) of volcanic eruptions. The eruptive style is primarily controlled by the degree of phase separation between the carrying phase (melt + crystals) and exsolved gas bubbles.

Effusive eruptions are fed by a relatively low-viscosity magma, where the gas bubbles efficiently separate from the carrying-phase. By contrast, explosive eruptions occur when the

phase separation does not occur due to the high viscosity of the carrying phase. While the slow effusion of lava flow allows for timely emergency response, violent, sustained volcanic explosions can eject ash and gas over several kilometres on timescales of minutes to hours or days. These aspects make volcanoes potentially dangerous, especially in urbanized and touristic areas. Therefore, one of the tasks of the scientific community is to provide civil protection agencies and policymakers with volcanic scenarios, and their probabilities to occur.

Numerical models of volcanic eruptions enable the forecasting of eruption evolution and so they are central to the planning of emergency response and evacuation. These models are primarily fed by viscosity measurements of volcanic melts as a function of chemical composition (X) and temperature (T). The combined effect of X and T can indeed change the viscosity of melts up to 12 orders of magnitude. Once the X and T contributions are characterized, one can consider the physical effect of crystal (ϕ_c) and bubble (ϕ_b) volume fraction on magma viscosity, which is limited to less than ~ 3 orders of magnitude.

Of particular interest here is recent evidence that volcanic melts may contain iron-bearing nanocrystals. The formation of these nanocrystals is suspected to increase the viscosity of volcanic melts through complex chemical and physical mechanisms, including variation of the chemistry of the liquid phase, the formation of chemical shells around the nanocrystals (Fig. 3.5-10), and aggregate formation. Furthermore, the formation of nanocrystals can also trigger the nucleation of bubbles, which is one of the engines of explosive eruptions, causing dramatic acceleration of the magma in volcanic conduits. Therefore, new studies on the effect of nanocrystals on the viscosity and degassing dynamics of magmas are urgent. However, the fundamental and preparatory steps for the development of these studies are 1) the possibility to produce high-quality data for the viscosity of hydrous melts and 2) the preparation and the careful chemical and textural (nanoscale) characterization of samples used for viscosity measurements.

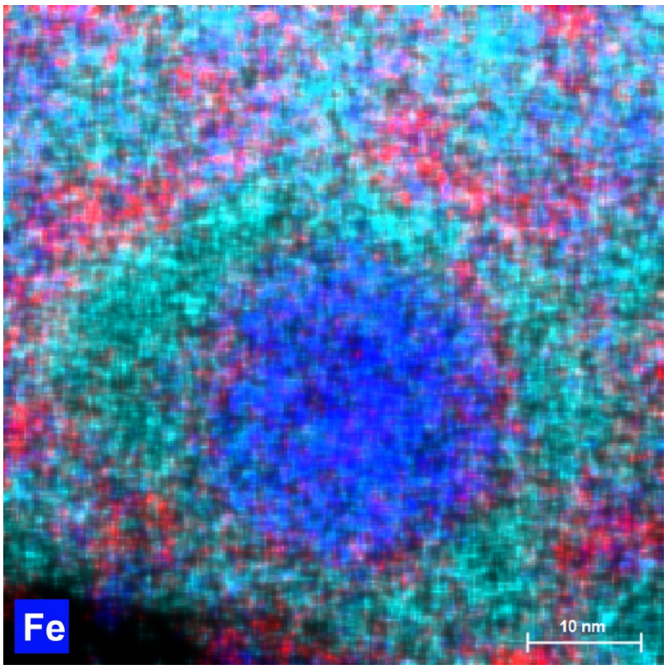

Fig. 3.5-10: A TEM-EDS map of a nanocrystal (ca 25 nm in diameter) in a hydrous basaltic glass. The nanocrystal is enriched in iron (Fe).

Here, we measure the HT-HP viscosity of silicate melts at eruptive conditions using a TZM pressure vessel and the so-called falling sphere method based on Stokes' law. This method, however, requires careful calibration against standard silicate melts, for which the viscosity is independently known. This is a key step, since falling sphere viscosity data are often associated with large uncertainties. These uncertainties preclude the possibility of identifying and separating the different chemical and physical contributions to the melt viscosity. We used a standard silicate melt DGG-1 (Fig. 3.5-11) and demonstrated that after correction for the experimental time, we can accurately measure the standard viscosity (log η = 2.36 Pa s at T = 1125 °C). The correction takes into account the time required to achieve thermal equilibrium, once the sample has been placed in the hot zone of the TZM.

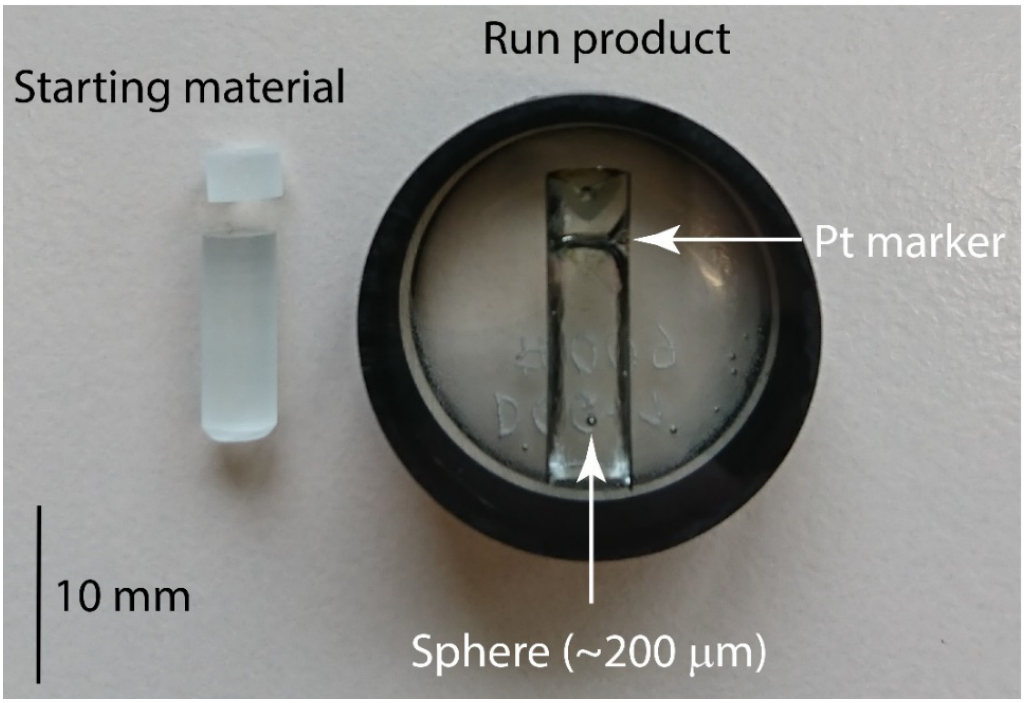

Fig. 3.5-11: Standard glass (left) used for the falling sphere experiments and (right) polished section after the experiment. The falling distance of the sphere is ~ 10 mm. Before running the experiment, the sphere was placed together with a Pt marker between the two cylinders. This allowed the accurate measurement of the falling distance and thus the calculation of the melt viscosity.

Currently, we are synthesizing water-bearing basaltic glasses by using the piston-cylinder apparatus and an internally-heated pressure vessel. The samples are initially characterized by Fourier-transform infrared and Raman spectroscopy to retrieve the amount of water dissolved in all glasses. The inspection of Raman spectra allows to infer the presence of nanocrystals in some samples. These samples will be characterized at the nanoscale by transmission electron microscope. Finally, all samples will be used to carry out high-pressure viscosity measurements as a function of temperature and water content. The obtained data will be used to develop a state-of-the-art viscosity model of basalts.

h. *A quasi-physical two-component, temperature-dependent viscosity model for volcanic melts (D. Langhammer, D. Di Genova and G. Steinle-Neumann)*

The eruptive style of volcanos is largely dictated by shear viscosity (η) and the concentration of volatiles in the melt. Water is the most abundant volatile in magmas, which in turn strongly influences η. In standard laboratory measurements of η, the volcanologically-relevant high-temperature (T) region becomes difficult to access when water is added to the melt. For numerical modelling of volcanic eruptions, a reliable description of η as a function of T and H_2O content is required. Here we introduce a physically motivated two-component model for silicate melt η, in contrast to previous models that are mostly empirical. It is based on the work of Mauro *et al.* (PNAS, *106*, 19780, 2009) (MYEGA model) for anhydrous isochemical compositions and on Schneider *et al.* (Polymer, *38*, 1323, 1997) for a formulation of water-dependence. The model equations are expressed by six parameters: (i) three for the viscosity of the anhydrous composition (η_d), *i.e.*, the glass-transition temperature ($T_{g,d}$) where the viscosity is 10^{12} Pa s, the steepness factor (the so-called melt fragility) of η_d at $T_{g,d}$ (m_d) that describes the rate of viscosity change with temperature at T_g, and the viscosity at infinite T ($\log \eta_\infty$); (ii) the dependence of the glass-transition temperature (with the endmember $T_{g,H2O}$=136 K) and steepness factor on H_2O content is described by three additional empirical parameters. Given a set of anhydrous and hydrous viscosity measurements for a given magma, the anhydrous data is used to fit parameter set (i) first, as this usually presents the most comprehensive and accurate dataset. Then, the three parameters for (ii) are constrained using the measurements of hydrous samples at low T, where volatiles exsolution is virtually suppressed within the experimental timescale.

Figure 3.5-12 shows η measurements by Robert *et al.* (Chem. Geol., *346*, 135, 2013) (circles) for basaltic andesite with varying water contents (colors). The anhydrous measurements (black) are described with similar quality by both the model provided with the data and by our fit, which is expected since these data cover a large η-T range, constraining the fit well. However, significant deviations in the description of the hydrous data (four different sets with an H_2O content of up to 12 mol. %) between the original global empirical model and our fit are apparent: Our physically motivated model describes the experimental measurements better, with a root-mean-square (RMS) error of 0.09 log units compared to 0.24 log units, and shows a different T-dependence of η that becomes increasingly significant with H_2O content.

Fitting η for 25 different data sets, which included both hydrous and anhydrous measurements with a total of 1188 data points, reveals that our model performs comparable to or better than individually formulated empirical models from the respective studies with a RMS error of 0.17 log units, while retaining the same underlying physical basis (Fig. 3.5-13).

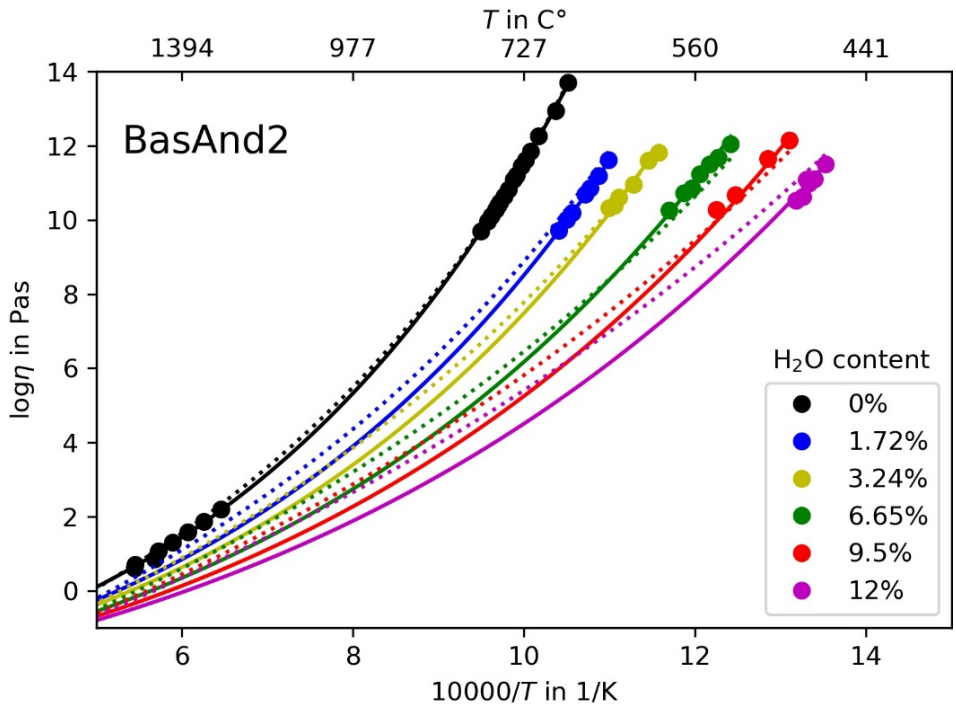

Fig. 3.5-12: Viscosity measurements (circles) for basaltic andesite by Robert *et al.* (Chem. Geol., *346*, 135, 2013) with varying H_2O content (given in mol. %, different colors) and two H_2O-dependent global models describing the data: dotted lines show the empirical model used by Robert *et al.*, the solid lines our newly developed model.

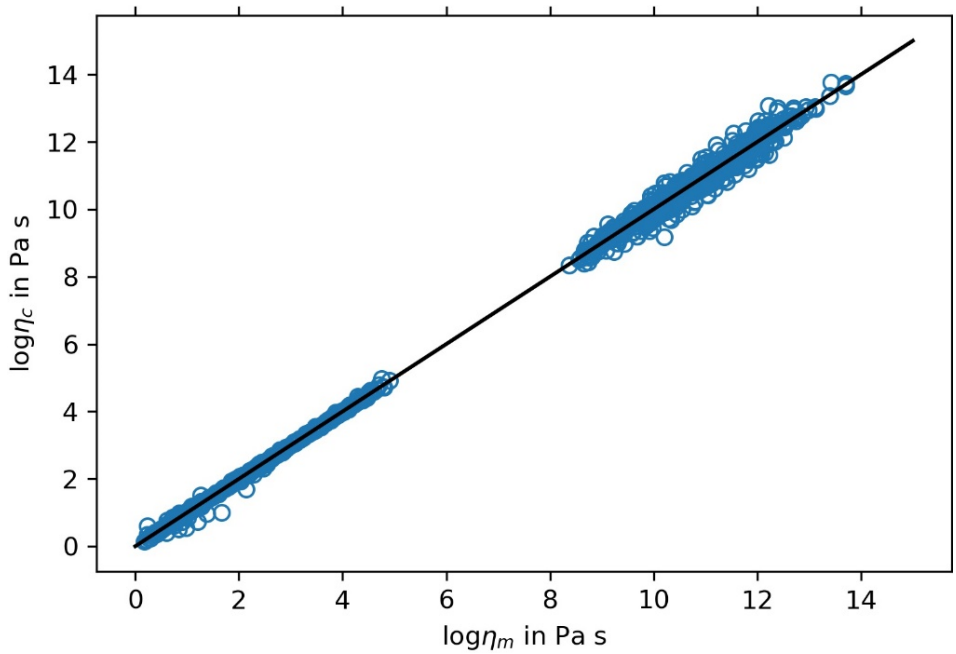

Fig. 3.5-13: Comparison of measured viscosity (η_m) in 25 different data sets with a total of 1188 data points, containing both anhydrous and hydrous data, with the fit using our model (η_c); the black line indicates a 1:1 correspondence.

i. *The viscosity of peridotite liquid to lower mantle conditions (L. Xie, A. Yoneda/Osaka, T. Katsura, D. Andrault/Clermont-Ferrand, Y. Tange/Sayo and Y. Higo/Sayo)*

Owing to the massive energy release during the Moon-forming giant impact, a deep magma ocean formed on the early Earth. Viscosity is a parameter that affects many processes such as convection, the settling of iron droplets, and crystallization in the magma ocean. *In situ* falling sphere viscometry is the most accurate method to measure viscosity at high pressures. Because of the lack of appropriate heating elements and of a suitable camera in previous studies, the viscosity measurements of peridotite liquid were limited to 13 GPa and had relatively large errors. With the application of boron-doped diamond heaters and an ultrafast camera, the pressure range of *in situ* falling sphere viscometry was recently extended to 30 GPa.

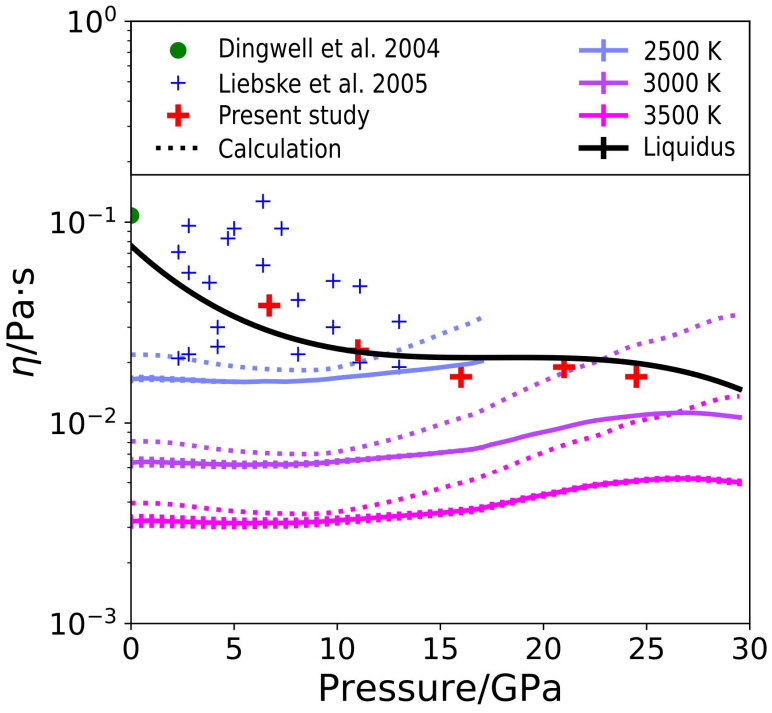

Fig. 3.5-14: Viscosity of peridotite liquid under pressure. The red crosses denote the present experimental data, at temperatures just above the liquidus. The blue, purple, magenta, and black solid curves denote viscosities, which are calculated using the Arrhenius equation, at temperatures of 2500, 3000, 3500 K, and along liquidus, respectively, with one standard deviation. The blue, violet, and magenta dotted curves are viscosities, which are calculated from the endmember viscosities (Xie *et al.*, 2020, *Nat. Commun. 11*) at temperatures of 2500, 3000, and 3500 K, respectively.

In this study, we measured the viscosity of peridotite liquid to lower-mantle conditions. The viscosity decreases from 38 (2) mPa s at 7 GPa to 17 (1) mPa s at 16 GPa, slightly increases to 20 (1) mPa s at 20 GPa, and finally decreases to 17 (1) mPa s at 24.5 GPa (Fig. 3.5-14). We then modeled the peridotite viscosity using the Arrhenius equation as a function of pressure and temperature normalized by the liquidus temperature. The viscosity of peridotite liquid shows a

positive, but weak pressure dependence up to 30 GPa (Fig. 3.5-14, solid curves). More importantly, the directly measured peridotite viscosity is lower than that calculated from the endmember viscosity (dotted curves), probably due to the neglection of mixing entropy according to Adam-Gibbs theory. The low viscosity observed here favors fractional solidification at the top of the lower mantle during magma ocean crystallization, which may have helped to stablish a bridgmanite-enriched layer there.

j. *Compositional effects on the material properties of liquid iron alloys (E. Posner and G. Steinle-Neumann)*

Although nickel is the second most abundant element (5 % - 25 %) in iron meteorites, its presence has been often previously assumed to have a negligible influence on the material properties of liquid iron and has therefore been predominantly excluded from experiments, simulations, and models in geoscience literature involving planetary core liquid analogues. However, recent experimental studies provide strong evidence that the inclusion of even small amounts of nickel may affect the geochemical equilibrium and transport properties of alloying elements in liquid iron and therefore requires further study. For example, nickel has been shown to reduce the solubility of several elements (*e.g.*, C, Re, Ir) in liquid iron alloys, while enhancing the solubility of others (*e.g.*, S, Sn), stabilize the fcc phase over the hcp phase at high pressure, and close the metal-sulfide miscibility gap. A combination of recent experimental and theoretical studies in liquid Fe–C and Fe–Ni–C compositions further show that the diffusion coefficient of carbon is 3-4 times faster in Ni-free alloys (Fig. 3.5-15); however, the mechanism by which nickel affects the diffusion of carbon and possibly other alloying elements remains unknown. To address these questions, we are presently undertaking a detailed investigation of the atomic-scale mechanisms by which nickel influences the material properties of liquid iron alloys relative to Ni-free compositions.

Concentration in the alloy can also strongly influence material properties. For example, as also shown in Figure 3.5-15, the reported activation volume (ΔV) of carbon diffusion in liquid Fe_3C (*i.e.*, 7 wt. % C) and Fe–9 wt. % Ni–5 wt. % C ($\Delta V \sim 1.2$ cm^3/mol) is significantly higher than in binary iron alloys with less than 2.5 wt. % C ($\Delta V \sim 0$), which leads to substantial differences upon extrapolation of data to higher pressure. This is likely because increasing carbon content reduces the density of solid and liquid iron alloys, which reflects differences in the type of atomic packing of both iron and carbon. Pure liquid iron has been shown to transform from a bcc-like structure to a close-packed-like structure near the γ-δ-liquid triple point, which changes the relative size of tetrahedral and octahedral voids. This insight has been used to explain a change in diffusion mechanism and negligible ΔV of interstitial oxygen in dilute $Fe_{0.96}O_{0.04}$ and is also likely applicable for carbon in low-C alloys. In contrast, Fe_3C is already close-packed at ambient pressure, thus a similar change in carbon diffusion mechanism is not likely in liquid Fe_3C. The effect of Ni on ΔV of carbon diffusion remains an open question. The overarching implications of this work are that the application of diffusion and geochemical equilibrium data

from Ni-free liquid compositions and/or liquids with carbon contents above or below a certain value will likely result in considerable errors with regards to the behavior of planetary core analogues and should therefore be used with caution.

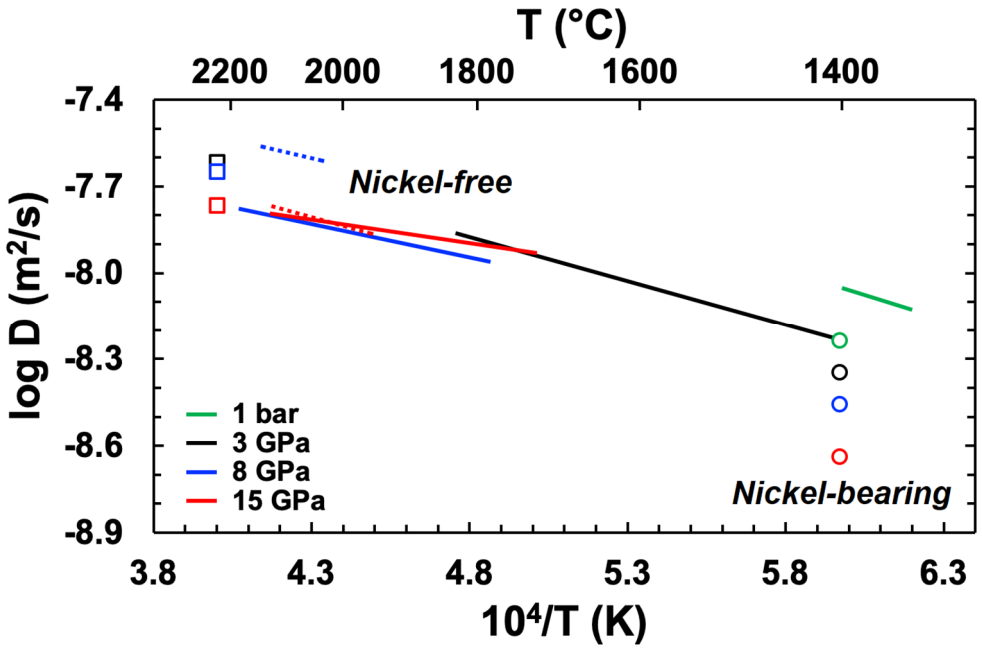

Fig. 3.5-15: Carbon diffusivity in nickel-free (curves and squares) and nickel-bearing liquid iron alloys (circles). The nickel-bearing results are slower than the nickel-free results by a factor of 3-4 with a substantially stronger pressure dependence. The dotted curves represent carbon diffusion in liquid Fe–7 wt. % C, and also show a substantially stronger pressure dependence than in liquid Fe–2.5 wt. % C (solid curves) and Fe–1 wt. % C (squares).

3.6 Rheology and Metamorphism

Rheology describes quantitatively how materials deform and flow in response to non-hydrostatic stress whereas metamorphism is the process by which the mineralogy and texture of rocks change in response to changes in pressure and temperature in the Earth's interior. Rheology and metamorphism are strongly linked and both can involve a similar range of geological processes and rock properties. For example, solid-state diffusion can control the viscous flow of rocks at high temperature and is also a major controlling factor during metamorphism. Rock textures, such as grain size and its evolution with time, are important for both rheology and metamorphism.

Studying the rheology of Earth's deep mantle experimentally is essential for understanding mantle convection and other geodynamic processes. However, such studies are difficult because both differential stress and strain rate need to be determined as a function of temperature and pressure. In addition, experimental strain rates are orders of magnitude faster that mantle strain rates which means that large extrapolations of results are necessary, the reliability of which is often uncertain. An indirect approach to this problem is to study rates of diffusion in mantle minerals at high pressures and temperatures because this process is important in controlling rheology. Grain size evolution at high temperature is also an important parameter that can affect rheology and its evolution with time can also be studied experimentally.

Geodynamic modelling is used to understand a large range of processes in the Earth including mantle convection, plate tectonics, fault generation and deep earthquakes. The results of two such studies are presented below.

The first contribution presents the results of a study of interdiffusion between Al and Si+Mg in Fe-free majorite garnet (an important mineral in Earth's mantle in the depth range ~ 550-900 km) and pyrope garnet. The diffusion experiment was performed at 18.5 GPa and 1750 °C for 300 minutes on an iron-free system and the extent of diffusion was studied by transmission electron microscopy. Both grain boundary and volume diffusion were observed and the extent of volume diffusion is similar to that observed in a previous study of Fe-bearing majorite. The rate of diffusion, which is extremely slow, is also similar to the rates of Si and Mg self-diffusion in bridgmanite, the most abundant mineral in Earth's lower mantle.

The kinetics of grain growth of polycrystalline olivine at high pressure is the subject of the second contribution. The rate of grain growth has been studied at pressures up to 12 GPa, in contrast to previous studies which were performed at relatively low pressures (up to 1.2 GPa). It is found that grain growth becomes significantly slower as pressure increases. This has implications for deformation mechanisms and rheology of the upper mantle and may mean that a transition from dislocation creep to diffusion creep occurs at a shallower depth than previously believed.

The third and fourth contributions of this section are concerned with geodynamic modelling. The first of these investigates the causes of slab detachment, whereby a negatively-buoyant slab detaches itself from subducting lithosphere and sinks into the mantle. Three possible mechanisms are investigated: structural weakening due to necking, material weakening due to grain size reduction using a two-phase grain damage model, and thermal weakening due to shear heating. It is concluded that grain damage is the initial cause of slab detachment but with increasing time thermal weakening becomes more important.

Oceanic transform faults are extremely prominent strike-slip faults that offset mid-oceanic ridges. The second geodynamics contribution investigates the mechanism by which such transform faults are initiated. Results show that grain size reduction is the main cause and that the life time of such faults is controlled by grain growth kinetics.

The final contribution of this section is concerned with quantifying the size of antiphase domains in omphacites from eclogites. Such domains form during metamorphism as the result of cation ordering. The size of antiphase domains can depend on peak temperature, the duration of peak metamorphism and the cooling rate and can therefore provide information about the metamorphic histories of high-pressure rocks. The present study has investigated the size distribution of antiphase domains which shows that the average size may not be the most appropriate parameter by which to characterize such features.

a. *Al, Si interdiffusion in iron-free majoritic garnet: Scanning transmission electron microscopy of a polycrystalline diffusion couple (N. Miyajima)*

Atomic diffusion by vacancy-controlled mechanisms in minerals at high pressure is important for the rheology of the Earth's mantle. Because both diffusion and rheology are controlled by the migration of two defects (line and point defects) at high temperature, the post-mortem examination by analytical transmission electron microscope (ATEM) is indispensable for evaluating the role of these defects. Majoritic garnet (Maj) and bridgmanite are major constituents of the mantle transition zone and the lower mantle, respectively. Differences between the behaviour of defects in these mantle minerals are very important for understanding changes in transport processes, such as viscosity and chemical diffusion, across the boundary between the upper and lower mantle. In particular, such changes are important for understanding the preservation of chemical heterogeneities in the Earth's deep interior.

Here I report on Al ↔ Si + Mg interdiffusion in an iron-free majoritic garnet, and compare the results to those of previous studies in which iron and the other elements such as calcium and chromium were present in the diffusion system (*Nishi et al., Earth. Planet. Sci. Lett., 361, 44, 2013; van Mierlo et al., Nat. Geosci., 6, 400, 2013*). In the present study, the diffusion couples in multianvil experiments consisted of pre-synthesized polycrystalline $Mg_3Al_2Si_3O_{12}$ pyrope (Prp) and majoritic garnet ($Maj_{76}Prp_{26}$). The study of 2Al = Mg + Si interdiffusion between Maj and Prp has been performed at 18.5 GPa and 1750 °C for 300 minutes using a Kawai-type high-

pressure multianvil apparatus. The aluminium (Al) diffusion profiles were measured across the diffusion couple interface by a scanning transmission electron microscopy (STEM) equipped with energy-dispersive X-ray spectrometer (EDXS).

The effects of grain-boundary diffusion were visualized in an EDXS chemical map of Al (Fig. 3.6-1). Excluding the effects of grain boundary diffusion from the profile measurements, the diffusion coefficient for interdiffusion (volume diffusion) was determined to be $D_{Al\text{-}Si} = 6.2(4) \times 10^{-19}$ (m^2/s) at 18.5 GPa and 1750 °C. This result is almost identical to those of *van Mierlo et al., ibid* but one order of magnitude greaer than that of *Nishi et al., ibid.* under similar pressure and temperature conditions. The diffusion coefficient at 1750 °C is also comparable to Mg and Si self-diffusion coefficients in bridgmanite under conditions of the uppermost part of Earth's lower mantle.

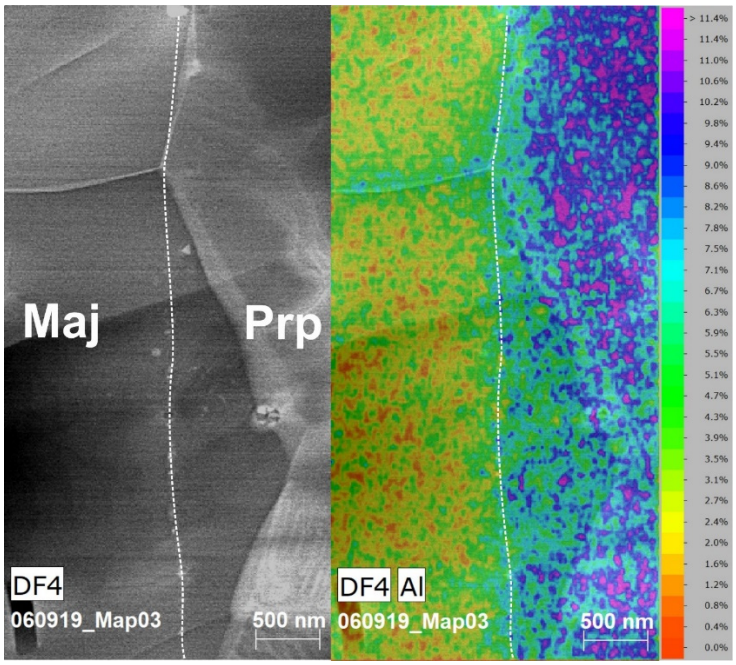

Fig. 3.6-1: Grain boundary diffusion of aluminium (Al) across the interface between polycrystalline majorite (Maj) and pyrope (Prp). The dashed white lines show the location of the diffusion interface. Left: Dark-field scanning TEM image of the diffusion interface. Right: Quantitative EDXS map of the same area showing Al concentrations in atomic weight percent.

b. *Pressure dependence of the kinetics of olivine grain growth at upper mantle conditions (F. Ferreira, M. Thielmann and K. Marquardt/London)*

The grain size of olivine influences several properties of the Earth's upper mantle. However, grain growth, one of the main processes that control grain size and its evolution with time, is still poorly constrained for olivine at upper mantle conditions. Experimental data on grain growth kinetics of olivine are to date restricted to pressures of up to only 1.2 GPa

(corresponding to depths of ≤ 50 km). To evaluate the effects of pressure on grain growth of olivine, we performed annealing experiments at pressures ranging from 1 to 12 GPa and temperatures ranging from 1050 ºC to 1520 ºC, using piston cylinder and multianvil apparatus.

We used EBSD analysis to determine grain-size distributions after various experimental times. Grain size data were fitted with a log-normal distribution and the modes of the resulting distributions (Fig. 3.6-2) were used for further calculations. To extract grain-growth parameters from these distributions, we fitted a normal grain-growth equation to the experimentally determined mean grain sizes.

As can be seen in Figure 3.6-2, increasing pressure results in significantly smaller grain sizes after a given time. The best fit to the data requires an activation volume of 4.3 x 10^{-6} m^3/mol. This value is similar to previously reported activation volumes for silicon grain-boundary diffusion at high pressures. This indicates that grain growth of olivine in the upper mantle may also be controlled by silicon grain-boundary diffusion.

With increasing depths in the Earth's upper mantle, the reduction of grain growth rates due to increasing pressure may offset the effect of increasing temperature. This would result in a smaller average grain size and thus promote a transition from grain size insensitive dislocation creep to grain size sensitive diffusion creep at shallower depths than previously expected.

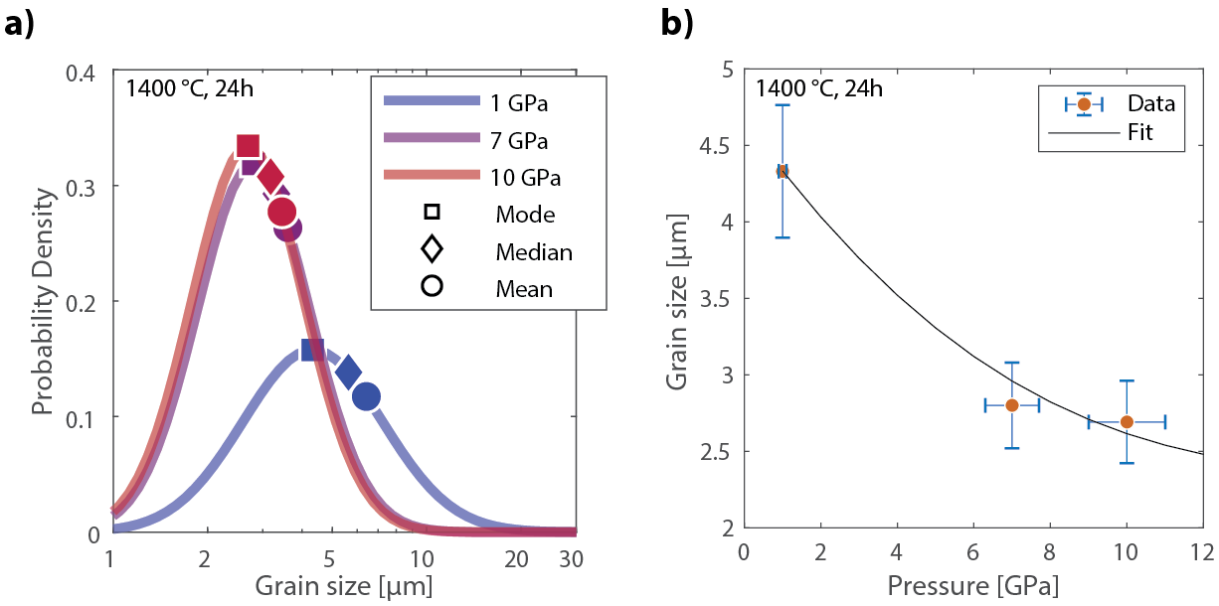

Fig. 3.6-2: The effect of pressure on grain growth of polycrystalline olivine aggregates under upper mantle conditions. (a) Log-normal fits to three different experiments, performed at 1, 7 and 10 GPa, after annealing for 24 h at 1400 °C. Symbols indicate the computed mode, median and mean of each distribution fit. (b) Fit to the experimental data from the annealing experiments shown in (a). The data points correspond to the mode of the grain size distribution of each experiment. Aggregates also contain 13 vol. % of pyroxene.

c. *Contributions of grain damage, thermal weakening, and necking to slab detachment (M. Thielmann and S. Schmalholz/Lausanne)*

The process of the detachment of negatively buoyant subducting lithosphere at convergent plate margins - also termed *slab detachment* - has become a widely applied concept in geodynamics. It has been used to explain numerous phenomena, ranging from rapid topographic uplift to seismicity patterns. However, despite extensive research, the processes that control slab detachment are still insufficiently understood.

In this study, we investigate the impact of three coupled rheological weakening mechanisms on the viscous detachment of a stalled lithospheric slab: structural weakening due to necking, material weakening due to grain size reduction, using a two-phase grain damage model, and thermal weakening due to shear heating (thermal damage) (Fig. 3.6-3). To understand and

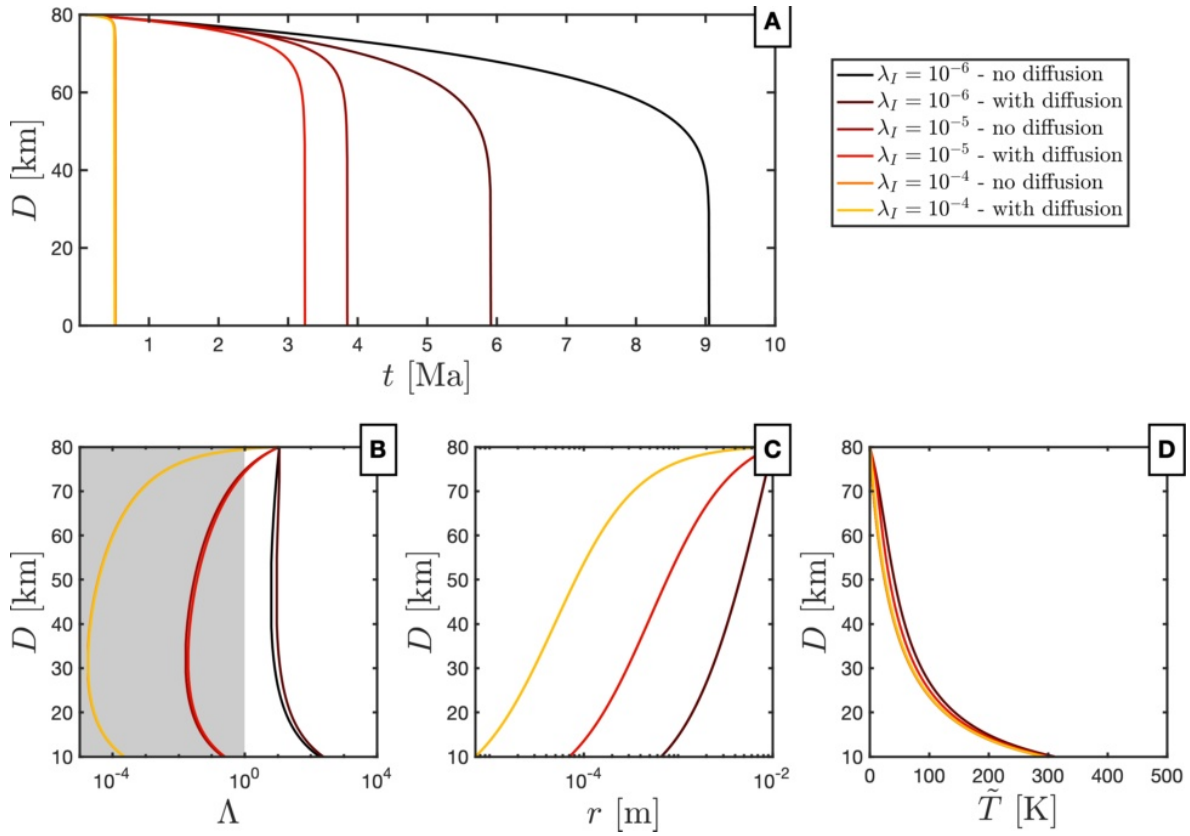

Fig. 3.6-3: Six examples (with and without thermal diffusion) of simulations with a slab temperature of 1,100 K, a slab thickness of 80 km and an initial grain interface curvature (a measure of the grain size) of 1 cm are shown to illustrate the impact of thermal diffusion and the interface partitioning factor λ_I, which controls the fraction of deformational work that is used for grain damage. (A) Evolution of neck thickness D vs. time. (B) Relationship between neck thickness D and the ratio of dislocation creep strain rate to diffusion creep strain rate Λ (with values smaller than 1 indicating diffusion creep dominated deformation. (C) Relationship between interface curvature r and D. (D) Relationship between temperature increase T and neck thickness D. Some lines in the respective plots are invisible because they lie on top of each other.

quantify the coupling of these three nonlinear weakening processes, we derive a mathematical model, which consists of three coupled nonlinear ordinary differential equations describing the evolution of slab thickness, grain size and temperature. With dimensional analysis, we determine the dimensionless parameters which control the relative importance of the three weakening processes and the two creep mechanisms. In addition, we derive several analytical solutions for end-member scenarios that predict the detachment time, that is the duration of the slab detachment process until the slab thickness becomes zero. The combination of dimensionless parameters together with analytical solutions allows us to understand the fundamental feedbacks between the three investigated weakening mechanisms.

These analytical solutions are then tested against numerical solutions for intermediate cases. In addition, we use numerical solutions of the system of equations to systematically explore the parameter space with a Monte Carlo approach. The numerical approach shows that the analytical solutions never deviate by more than 50 % from the numerical ones, even for scenarios where all three weakening and both creep mechanisms are important. When both grain and thermal damage are important, the two damage processes generate a positive feedback loop resulting in the fastest detachment times.

For Earth-like conditions, we find that the onset of slab detachment is controlled by grain damage and that, during the later stages of slab detachment, thermal weakening becomes increasingly important and can become the dominating weakening process.

d. *Can grain size reduction initiate transform faults? Insights from a 3-D numerical study (J. Schierjott/Zurich, M. Thielmann, A. Rozel/Zurich, G.J. Golabek and T. Gerya/Zurich)*

Oceanic transform faults are one of the most striking features at mid-oceanic ridges. At the same time, they remain enigmatic because mechanical models typically struggle to model their formation as well as the strike-slip movement along them. It has been shown that a strong strain weakening rheology is required to allow the formation and persistence of transform faults. However, the underlying physical processes resulting in strain weakening are still unknown.

Given that field observations of transform faults show that they exhibit a strongly reduced grain size compared to the surrounding rock, we here use 3-D thermomechanical visco-plastic numerical models to study the effect of grain size reduction processes on transform fault initiation. These models show that grain size reduction indeed provides sufficient ductile weakening to initiate a transform fault (Fig. 3.6-4). These faults remain stable for up to 2 Myrs when no other weakening mechanisms are considered. The stability and longevity of these transform faults depends strongly on the grain damage formulation and grain growth kinetics, thus highlighting the importance of improving experimental investigations of grain damage and the kinetics of grain growth.

Numerical model results also show that transform faults initiate in the brittle crust close to the surface and propagate downward, thus indicating a top-down controlled formation process. This has important implications not only for transform fault formation, but potentially also for the seismic cycle at transform faults, as deformation of the brittle near-surface layer may be the controlling factor for fault deformation.

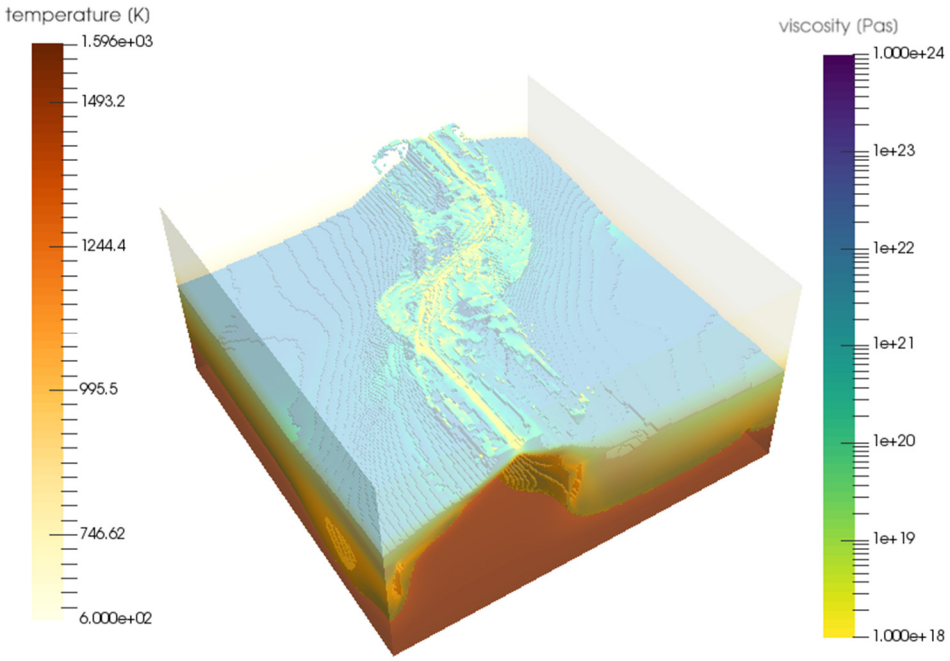

Fig. 3.6-4: Formation of a transform fault formation that offsets a mid-oceanic ridge in a 3D model. Shown is the temperature field (in brownish colors) overlain by the viscosity field. For visibility purposes, only the viscosity structure of the lithosphere is shown. The mid-oceanic ridge and the nascent transform fault that offsets it can be seen as a low-viscosity zone close to the surface.

e. *Revising estimates of antiphase domain size in eclogite-facies omphacites (R. Fukushima and T. Tsujimori/Sendai, N. Miyajima)*

Omphacite, an important clinopyroxene whose chemical compositions are close to $Ca_{0.5}Na_{0.5}[Mg,Fe^{2+}]_{0.5}Al_{0.5}Si_2O_6$, is one of the main minerals occurring in eclogites. It is thus ubiquitous in high-pressure (H*P*) and ultrahigh-pressure (UH*P*) basic metamorphic rocks. Omphacites at higher temperatures have the cation-disordered structure (*C*2/*c*), whereas those at lower temperatures, especially in blueschists and most orogenic eclogites, can have the cation-ordered structure (*P*2/*n)*. Since omphacite can nucleate with the *C*2/*c* structure as a metastable state at low temperature (*T)*, its cation ordering processes can occur not only with cooling but also during prograde metamorphism.

By observing low-*T* omphacites with transmission electron microscopy (TEM), we can understand how cation ordering occurs; the process generates bubble-like or columnar

microstructures called 'antiphase domains' (APDs). On the basis of the dependency of the size of APDs on annealing time and temperature, Carpenter (*Contrib. Mineral. Petrol*., 78, 441, 1981) proposed geothermometry/geospeedometry determinations based on the average size of equiaxed APDs in omphacite, and showed their potential for determining the kinetics of eclogitization.

However, there are two major problems in applying analytical methods to natural low-*T* omphacites: 1) omphacite can lose its APD structures when it recrystallizes, and 2) it is not certain whether the 'average' APD size is truly appropriate for understanding the timescales of metamorphic events. Therefore, we propose a new image-analytical method to elucidate the APD size distributions, especially in order to resolve the second problem.

We binarized acquired digital TEM images using the Trainable Weka Segmentation method bundled in the image processing package Fiji, which is a modified version of the open source, Java-based image processing program Image J. After excluding the noise and APDs with abnormal shapes by setting thresholds of their circularities, we calculated their size distributions. Our result shows that all of the obtained size-distributions are non-Gaussian (Fig. 3.6-5). This creates controversy concerning the 'average' APD-size analyses because the mean value is significantly larger than the major mode, by no less than 38 nm for one of our samples (Fig. 3.6-5b). Besides, since they seem to be slightly multi-modal size distributions, we might have to consider the complicated histories of multiple cation ordering events. Although the explicit relationships between the non-Gaussian size distributions and their growth kinetics remain to be resolved, further analyses of APD sizes will facilitate discussion about the timescales of low-*T* metamorphic processes in subduction zones.

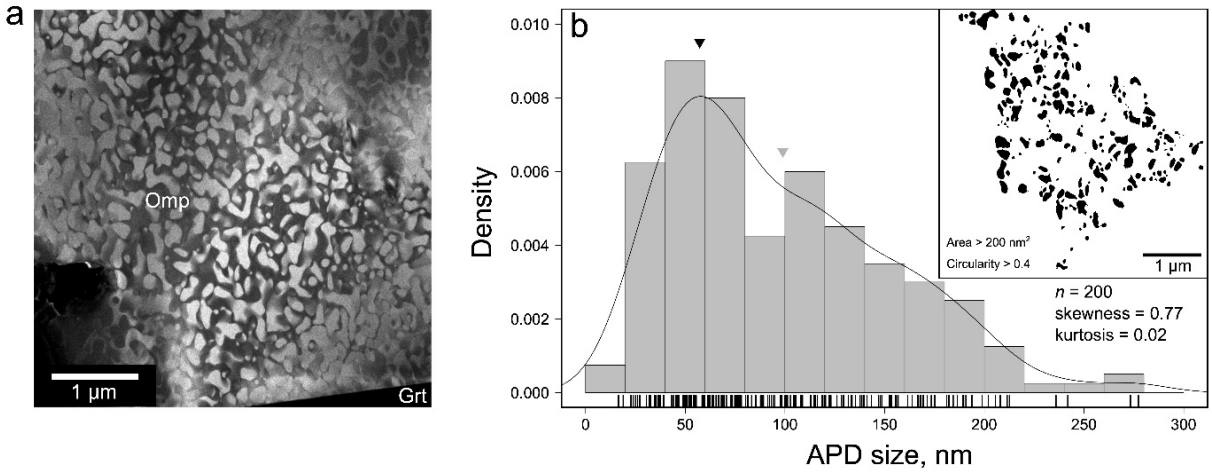

Fig. 3.6-5: An example of equiaxed antiphase domains in omphacite obtained from a low-*T* eclogite from Syros. Greece. a) Dark-field TEM image (g = 050) that includes a garnet–omphacite phase boundary; b) histogram of the measured APD sizes. As an inset, we show binarized dark-field images from which noise and highly distorted APDs are excluded. Results of the kernel density estimates are also shown (band width = 17.07 nm). The black and gray triangles indicate its mode (~ 60 nm) and mean (~ 98 nm), respectively. In (a), Omp = omphacite, Grt = garnet.

3.7 Material Science

Research in the field of material chemistry and physics at the Bayerisches Geoinstitut benefits from a unique combination of high-pressure equipment, an increasing possibility of *in situ* characterization of samples, and expertise in computational solid-state physics. In this year's Annual Report, we present results of studies of various classes of solids: elemental nitrogen and transition metal-based nitrides, carbides, and hydrides. *In situ* high-pressure single-crystal X-ray diffraction in the diamond anvil cell – developed over the past couple of years at important synchrotron facilities with researchers from Bayerisches Geoinstitut contributing significantly – plays a central role in the contributions to this section.

Nitride solids – and underlying elemental nitrogen – continue to receive significant attention in research at high pressure as – with the very adaptive N-N bond – they show great potential as high energy density materials and therefore as environmentally friendly propellants and explosives. The first contribution in this section shows that elemental nitrogen adopts the black phosphorous phase above 100 GPa, a polymorph that had been expected to be stable based on systematic considerations for the nitrogen group elements, but previously not observed. In the second contribution, X-ray diffraction and *ab initio* simulations illustrate the flexibility of N_2 anions in Y_5N_{14} at 50 GPa, with two differently charged dimers – $[N{=}N]^{2-}$ and $[N{\equiv}N]^{3-}$– observed, the latter exhibiting a significantly longer N-N bond.

Yttrium is also the basis of a high-pressure carbide Y_4C_5 that is investigated in the third contribution, with carbides playing an important role as highly refractory and hard materials. Similar to Y_5N_{14}, yttrium carbide Y_4C_5 synthesized and characterized at 44 GPa, is remarkable in its structure, with carbon appearing both as dimers C_2 and trimers C_3, and C-C distances in-between characteristic double- and single-bond lengths. Analyzing the charge density obtained with density functional theory-based calculations reveals a metallic state, and formal charges of $[C_2]^{5-}$ and $[C_3]^{6-}$.

In addition to X-ray diffraction and *ab initio* simulations, the final contribution in this section also uses proton nuclear magnetic resonance (NMR) spectroscopy to characterize the hydrogen environment in iron und copper hydrides. In metallic FeH and Cu_2H, the NMR data show a deviation from an expected free-electron gas like behaviour over a limited pressure range, which – based on the computed electron density – can be interpreted as interactions forming on the hydrogen sublattice and contributing to metallic conduction. The characteristic H-H distances at which this phenomenon occurs are significantly larger than what have been previously assumed. As hydrogen contributions are expected to play a critical role in the high-temperature superconductivity of metal hydrides at high pressure, this is a significant finding that requires further analysis with additional experimental and more advanced theoretical methods.

a. *A high-pressure polymeric nitrogen allotrope with the black phosphorus structure (D. Laniel/Bayreuth, B. Winkler/Frankfurt, M., T. Fedotenko/Bayreuth, A. Pakhomova/Hamburg, S. Chariton/Chicago, V. Milman/Cambridge, V. Prakapenka/Chicago, L.S. Dubrovinsky and N.A. Dubrovinskaia/Bayreuth)*

Polymeric nitrogen phases are obtained through the compression of molecular nitrogen above 110 GPa and are of great interest as prototypes for the design of novel high energy density materials. Their potential technological relevance has led to intensive theoretical studies and numerous crystal structure predictions. Among these, the layered polymeric structure of black phosphorus – the thermodynamically stable form of phosphorus at ambient conditions – has been suggested as a potential candidate for polymeric nitrogen. This structural prediction was partially inspired by the commonly accepted paradigm that elements of the same column in the periodic table adopt the structure of the elements below them, but at higher pressure. This empirical model of the structural behaviour of elements under pressure has been shown to generally hold for the nitrogen family group elements (pnictogens), with a notable exception for nitrogen itself.

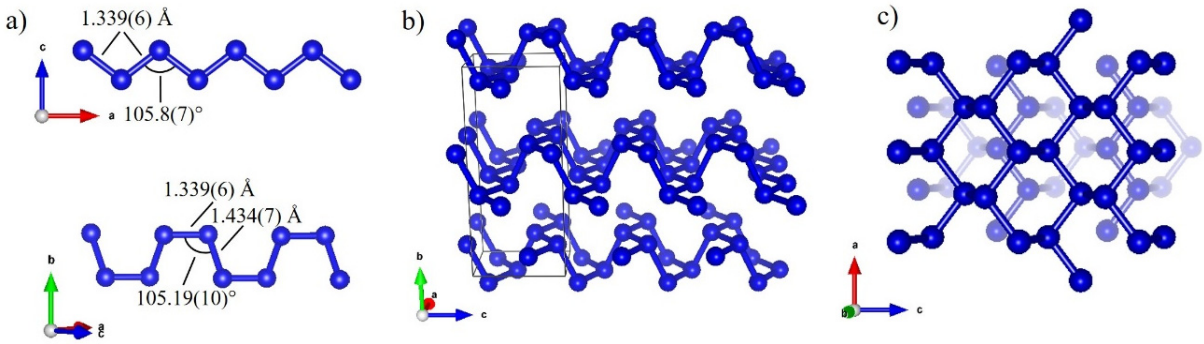

Fig. 3.7-1: a) The zigzag (ZZ) and armchair (AC) arrangements forming the bp-N layers. b) The crystal structure of bp-N, where the ZZ and AC chains are visible. c) Two superimposed layers of the bp-N structure, highlighting the puckered honeycomb arrangement of fused N_6 hexagons.

To uncover novel polymeric nitrogen phases, we performed high-pressure and high-temperature experiments on nitrogen up to 140 GPa and ~ 4000 K. The samples were characterized *in situ* by Raman spectroscopy and by synchrotron single-crystal X-ray diffraction measurements at the Advanced Photon Source (APS) and the Deutsches Elektronen-Synchrotron (DESY). These measurements suggested the synthesis of a new phase of polymeric nitrogen. Single crystal X-ray diffraction data enabled a full structural solution of the produced solid (Fig. 3.7-1), which was unambiguously found to be isostructural to black phosphorus – and hence coined as black phosphorus-type polymeric nitrogen (bp-N). The highly anisotropic bp-N is expected to exceed the exotic thermal, electronic, and optical properties found in black phosphorus, due to the geometry of its zigzag and armchair chains. DFT calculations found bp-

N to have a wide bandgap of about 2.2 eV – making it the sole known semiconducting phase of nitrogen.

The structural identification of this polymeric nitrogen phase reconciles the systematic trend in high-pressure phase relations for the pnictogen elements mentioned above, with nitrogen and phosphorus having the same 2D layered orthorhombic crystal structure. This study also allowed a better understanding of the behaviour of homoatomic polymeric solids under pressure and resolves previous inconsistencies in the density evolution of polymeric nitrogen phases. Further investigations into the electronic, optical and thermal properties of bp-N are expected.

b. *High-pressure synthesis of novel yttrium nitride, Y_5N_{14}, at 50 GPa (A. Aslandukov/Bayreuth, A. Aslandukova, D. Laniel/Bayreuth, T. Fedotenko/Bayreuth, L. Yuan, G. Steinle-Neumann, L.S. Dubrovinsky, N.A. Dubrovinskaia/Bayreuth and K. Glazyrin/Hamburg)*

Homonuclear dinitrogen anions are common intermediates in biological and organometallic synthetic chemistry, and play an important role in nitrogen reduction to ammonia. In extended solid-state compounds, nitrogen is typically present in the form of a nitride anion N^{3-} and does not form catenated polyanions (with the exception of azides). The first alkali and alkaline-earth diazenides Li_2N_2, CaN_2, SrN_2, and BaN_2 containing $[N_2]^{2-}$ anions were synthesized at high pressure only at the beginning of the XXI century; in 2013, LaN_2 dinitride with $[N_2]^{3-}$ anions was synthesized by shock compression. Diamond anvil cell techniques subsequently succedded in the synthesis of a series of transition-metal dinitride compounds MN_2 (M = Ti, Cr, Fe, Co, Ni, Cu, Ru, Rh, Pd, Re, Os, Ir, Pt) at pressures of 30-70 GPa. In MN_2 compounds, metals usually possess their common oxidation states, and the dinitrogen anion formally accommodates 1 to 4 electrons. The degree of charge transfer from the metal to the nitrogen dimers significantly affects the properties of the materials, with $M^{IV}N_2$ (M = Pt, Ir, Os, Ti) pernitrides, containing $[N_2]^{4-}$ units, being much less compressible than $M^{III}N_2$ (M = Cr, Fe, Co, Ni, Ru, Rh) with $[N_2]^{3-}$ units, for example.

In the current study we compressed yttrium and molecular nitrogen to 50 GPa and laser heated to above 2000 K. Under these conditions, synchrotron single-crystal X-ray diffraction from multigrain samples revealed the formation of a new tetragonal yttrium nitride phase with the unusual Y_5N_{14} composition (Fig. 3.7-2). All nitrogen atoms form dimers, but strikingly there are three different types of nitrogen dimers in the structure with bond lengths of 1.24 Å, 1.28 Å and 1.36 Å (Fig. 3.7-2) that correlate with the multiplicity of the dimer bond type and charge state: There are six $[N{=}N]^{2-}$ dimers (N01-N01 and N03-N03 in Fig. 3.7-2b) and one $[N\dddot{=}N]^{3-}$ dimer (N02-N02 in Fig. 3.7-2b) per Y_5N_{14} formula unit, which corresponds to Y^{3+} oxidation state for all yttrium atoms. *Ab initio* calculations confirm that this structure is dynamically stable at such pressure (Fig. 3.7-3). Although $[N_2]^{2-}$ and $[N_2]^{3-}$ ions are known in the structures of other dinitrides, Y_5N_{14} is the first example of the presence of two different types of charged nitrogen dimers in the same structure, which suggests that complex chemical processes operate in dense dinitrides formation under high pressure.

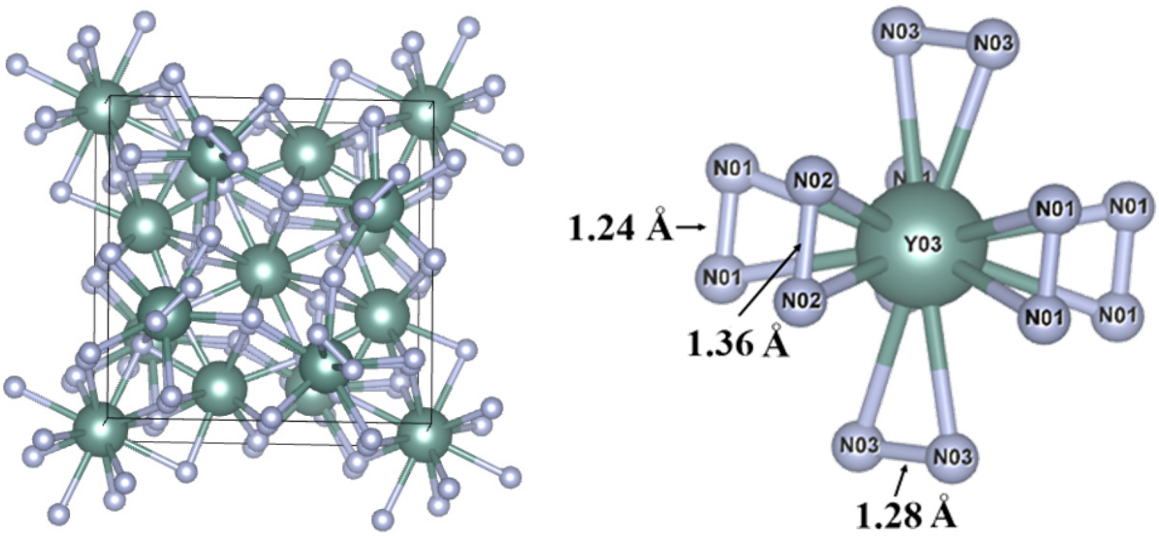

Fig. 3.7-2: (left) Structure of the novel Y_5N_{14} phase and (right) different dinitrogen anions in the Y coordination environment.

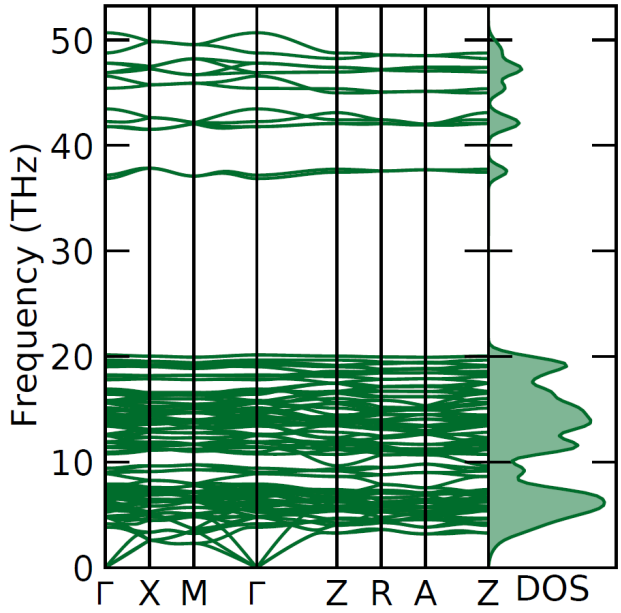

Fig. 3.7-3: Computed phonon dispersion of Y_5N_{14} at 50 GPa along the high-symmetry directions in Brillouin zone and the phonon density of state (right).

c. *Novel high-pressure yttrium carbide, HP-Y_4C_5 (A. Aslandukova, L. Yuan, D. Laniel/ Bayreuth, A. Aslandukov/Bayreuth, S. Khandarkhaeva, T. Fedotenko/Bayreuth, G. Steinle-Neumann, N.A. Dubrovinskaia/Bayreuth, L.S. Dubrovinsky and K. Glazyrin/Hamburg)*

Transition-metal carbides exhibit high melting points, high hardness, and metallic conductivity that make these materials attractive candidates for different technological applications and for material science studies. Carbon has the capability of forming various bonding states, affecting the structures and properties of transition metal carbides. High pressure can alter their bonding patterns, leading to new compounds with unusual bonding states and properties.

The yttrium carbide family shows a large variety of possible phases at ambient pressure with different stoichiometry (*e.g.*, Y_2C, Y_4C_5, Y_3C_4, Y_2C_3, Y_4C_7, YC_2). Here, we report results on the synthesis and characterization of a previously unknown high-pressure yttrium carbide, HP-Y_4C_5, which displays very unusual crystal chemistry. The HP-Y_4C_5 phase was synthesized by chemical reaction of pure metallic yttrium and paraffin oil at $P \sim 44$ GPa and $T \sim 1500$ K in a laser-heated diamond anvil cell, and was characterized by synchrotron single-crystal X-ray diffraction and Raman spectroscopy. On decompression, diffraction lines of HP-Y_4C_5 were traced to 16(2) GPa, and the characteristic Raman modes of the phase were observed to ~ 2 GPa.

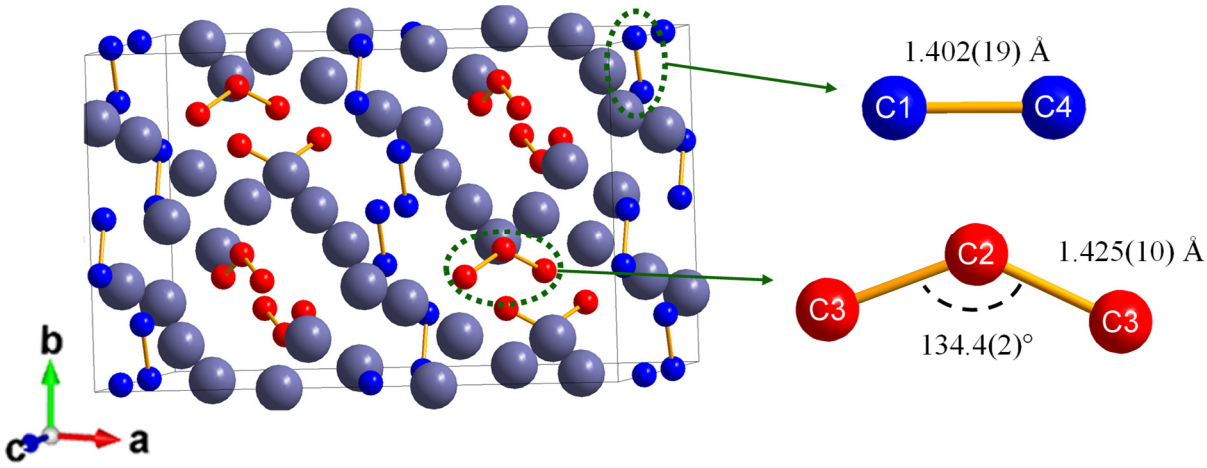

Fig. 3.7-4: Crystal structure of Y_4C_5 at 44 GPa. The grey, blue and red spheres represent yttrium and carbon atoms in dimers and trimers, respectively. The $[C_2]^{5-}$ and $[C_3]^{6-}$ species with their bond lengths and angles are indicated on the right side.

The HP-Y_4C_5 phase crystallizes in the orthorhombic system (space group *Cmce, Z* = 16) with the unit cell parameters a = 12.1834(8) Å, b = 7.6592(4) Å and c = 8.8584(11) Å at 44 GPa (Fig. 3.7-4). Notable structural elements of HP-Y_4C_5 are $[C_2]$ dumbbells and $[C_3]$ trimers. While the first coordination sphere Y-C distances (2.24-2.69 Å) are typical for yttrium carbides – accounting for high-pressure conditions – C-C distances in the $[C_2]$ dimers (1.40(2) Å) and the $[C_3]$ trimers (1.43(1) Å) are unusual: they are significantly larger than expected for double-bonded carbon atoms (~ 1.33 Å) and much shorter than for single-bonded (~ 1.54 Å). Taking into account the unique bent nature of the trimers $[C_3]$, it is hard to evaluate the nature of the bonding of the carbon atoms in HP-Y_4C_5 empirically, without involving theoretical calculations.

Full relaxation of the structural model (at a volume corresponding to about 44 GPa) using the *ab initio* VASP program resulted in the unit cell parameters and atomic coordinates that perfectly agree with the experiment. Phonon dispersion calculations show that HP-Y_4C_5 is dynamically stable at 44 GPa. The electron localization function (ELF) demonstrates strong covalent bonding between carbon atoms within the carbon dumbbells and trimers, and covalent bonds between Y and C (Fig. 3.7-5). According to our analysis of the charge distribution in the ionic approximation, the HP-Y_4C_5 phase contains the anions $[C_2]^{5-}$ and $[C_3]^{6-}$, with a bond order

of 1.5 in both cases. The calculated electronic density of states shows that yttrium carbide HP-Y_4C_5 is metallic and that the main contribution at the Fermi level comes from Y *4d* and C *2p* states (Fig. 3.7-5).

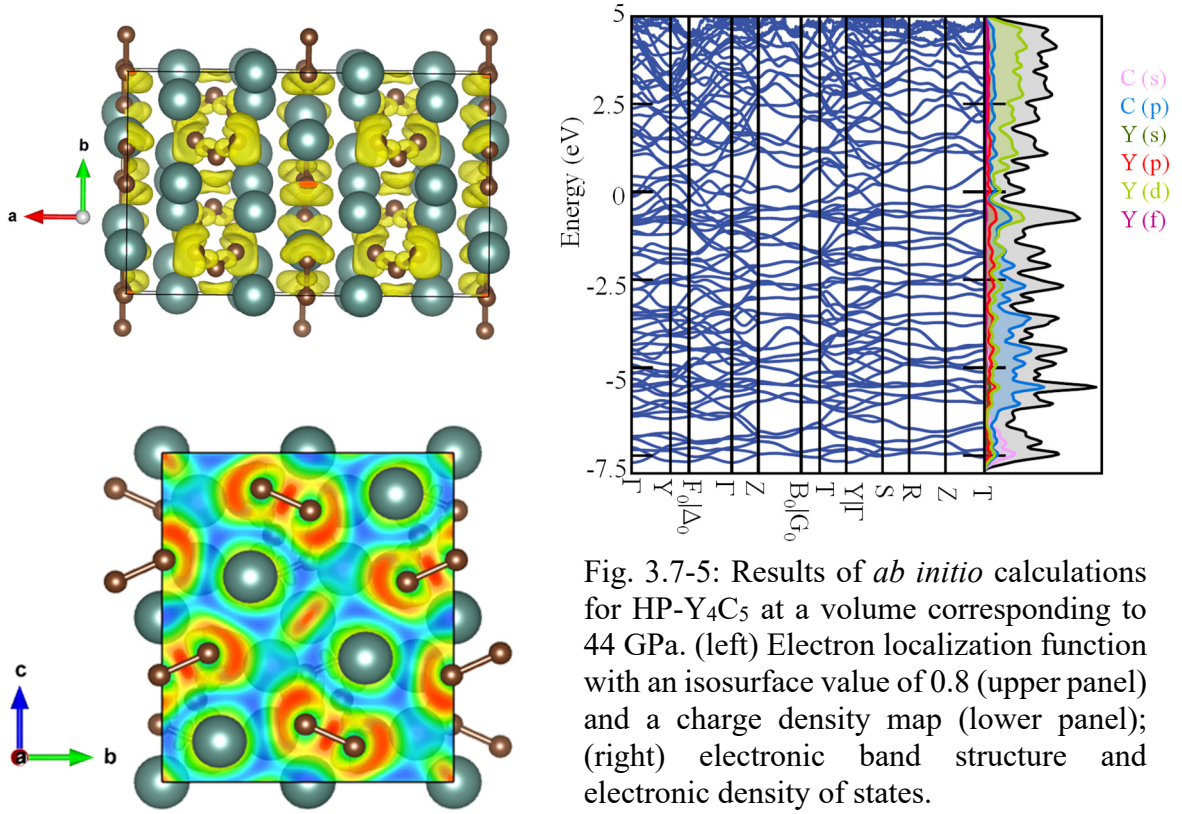

Fig. 3.7-5: Results of *ab initio* calculations for HP-Y_4C_5 at a volume corresponding to 44 GPa. (left) Electron localization function with an isosurface value of 0.8 (upper panel) and a charge density map (lower panel); (right) electronic band structure and electronic density of states.

d. *Synthesis and investigation of high-pressure metal hydrides by in situ Nuclear Magnetic Resonance spectroscopy (T. Meier, F. Trybel, G. Criniti, D. Laniel/Bayreuth, S. Khandarkhaeva, E. Koemets, T. Fedotenko/Bayreuth, K. Glazyrin/Hamburg, M. Hanfland/ Grenoble, M. Bykov/Washington D.C., G. Steinle-Neumann, N.A. Dubrovinskaia/Bayreuth and L.S. Dubrovinsky)*

Hydrogen rich metal hydrides are believed to yield the key for our understanding of high-temperature superconductivity, with the prospect of stabilizing superconducting quantum condensates at room temperature at megabar pressures. Experimental difficulties associated with electronic transport measurements and sample synthesis as well as the inability of complementary structural methods like X-ray diffraction to fully solve the arrangement of hydrogen atoms, hinder an in-depth investigation of these new class of superconductors.

We are able to show that *in situ* high-pressure nuclear magnetic resonance (NMR) spectroscopy in diamond anvil cells is a promising route towards understanding the electronic properties of the hydrogen sublattices in metal hydrides. In particular, we present an ^{1}H-NMR study of cubic FeH up to 202 GPa, in which we observe a distinct deviation from ideal metallic behaviour in the range 64-110 GPa, suggesting pressure-induced H-H interactions (Fig. 3.7-6).

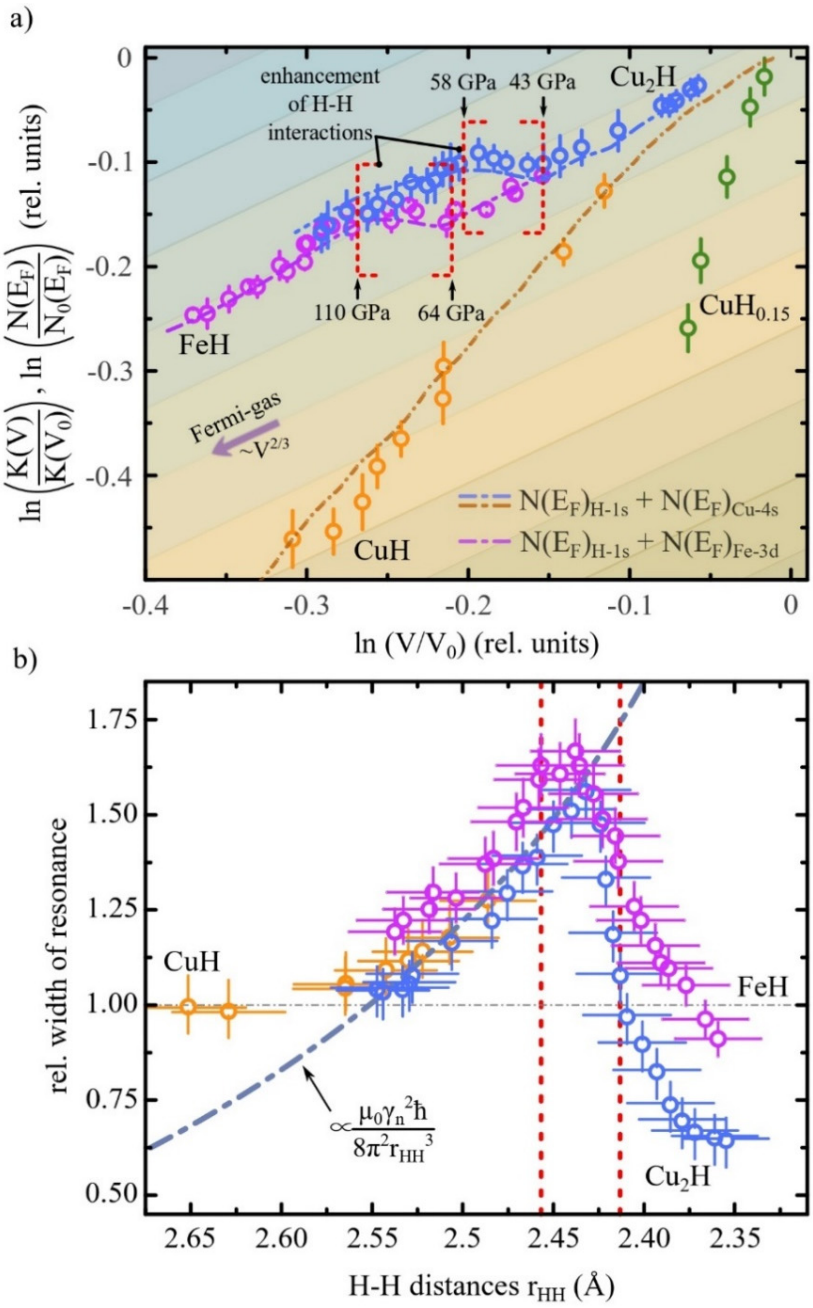

Fig. 3.7-6: Comparison of experimental NMR data and DFT-based electronic structure calculations. a) Double logarithmic power plot of relative changes in the NMR Knight shift K_H and the electron density-of-states at the Fermi energy $N(E_F)$ as a function of compression. Experimental data (blue, magenta, orange and green) are normalized to K_H at the reference volume from the respective equation-of-state ($CuH_{0.15}$) and DFT computations from this study (CuH and Cu_2H); the blue, magenta and orange dashed lines (splines through computed values) show the respective volume dependence of $N(E_F)$. Diagonal color stripes are guides to the eye representing a $\propto V^{2/3}$ scaling for free-electron Fermi-gas-like behaviour. Black arrows denote respective pressures points. b) Relative FWHM line-widths of ^{1}H-NMR spectra as a function of the H-H distance r_{HH} for CuH, Cu_2H, and FeH. The dotted blue line depicts the theoretical line-width dependence for pure dipolar broadening and vertical red dashed lines show the r_{HH}-range corresponding to the pressure intervals marked in panel (a).

Accompanying *ab initio* calculations support these findings, as they reveal the formation of an intercalating sublattice of electron density, which enhances the hydrogen contribution to the electronic density of states at the Fermi level. The pressure-induced H-H interactions occur in metal hydrides at much lower compressions and larger H-H distances than previously thought (Fig. 3.7-6b).

In addition, we have investigated the atomic and electronic structures of Cu_2H and CuH by high-pressure NMR spectroscopy up to 96 GPa, X-ray diffraction up to 160 GPa and density functional theory-based calculations. Metallic Cu_2H is synthesized at 40 GPa, and semi-metallic CuH at 90 GPa, found stable up to 160 GPa. For Cu_2H, experiments and computations show an anomalous increase in the electronic density of state at the Fermi level for the hydrogen 1s states and the formation of a hydrogen network in the pressure range 43-58 GPa (Fig. 3.7-6a), together with high ^1H mobility of ~ 10^{-7} cm^2/s. A comparison of these observations with results on FeH suggests that they could be common features in metal hydrides. Combining our findings for FeH and Cu_2H, we suggest that H-H interactions could be common features in metal hydride systems.

3.8 Methodological Developments

Development of novel experimental, analytical and numerical techniques and the exploration of their potential are exciting scientific challenges, by which unexpected pioneering results can be produced. Such innovative efforts are therefore necessary to achieve fundamental breakthroughs in the next scientific stages and to stand at the forefront in a scientific discipline. Efforts and resources have been invested for a number of time-consuming developments in the Bayerisches Geoinstitut. The following nine challenges are reported in methodological developments this year, which consist of five projects involving the multianvil apparatus, one in the piston-cylinder apparatus, one in the diamond anvil cell, and one involving numerical modelling, as summarized below.

In any high-pressure experiment, researchers wish to expand the ranges of achievable pressures of their apparatus. Ishii *et al*. report in the first section that the pressure limit of multianvil presses with carbide anvils was increased to 52 GPa at a high temperature of 2000 K. Using this technology, they investigated phase relations in a basaltic system at depths down to 1300 km of the Earth's mantle.

Mafic and ultramafic melts play important roles in various geochemical processes in the mantle. Knowledge of melt properties is useful for the investigation of mantle geochemistry. Although post-experiment analysis of quenched melts renders it possible to obtain a variety of melt properties, ultramafic melts are difficult to quench at high pressures owing to limited cooling rates in high-pressure apparatus. Bondar *et al*. increased the cooling rate of multianvil presses by one order of magnitude by developing a rapid-quench technique, and successfully quenched hydrous ultramafic melts to glasses for the first time.

High pressures in terrestrial planets are associated with high temperatures, but that is not the case for the mantles of gas giants and their icy satellites. A development that enables high-pressure cryo-experiments in the multianvil press is described by Howard and Walte. This system is already in place for cryo-recovery experiments, and in the future will be used for *in situ* neutron-beam experiments to study icy solar-system bodies.

Knowledge of rheological properties is essential for understanding mantle dynamics. The six-ram multianvil press allows tri-axial deformation of mineral and rock samples under upper-mantle pressures. Although deviatoric stresses on the samples can be obtained by means of X-ray stress analysis using synchrotron radiation, availability of synchrotron beams is limited. Dolinschi and Frost are developing a technique to measure sample stresses *in situ* using piezoelectric crystals. The fourth contribution reports their current results of this *in situ* stress measurement at ambient temperature.

Measurement of ultrasound velocities of mantle minerals to determine their equations of state is one of the major tasks in experimental geoscience. Although the velocities of minerals have

to be measured as a function of pressure and temperature, pressure uncertainties are significant in in-house experiments, because sample pressures are estimated using a calibration curve determined in separate experiments. Neri *et al*. attempted to determine the sample pressure by measuring sound velocities of garnet single crystals, whose velocities are well calibrated, as a standard material, and report current results of this attempt in the fifth contribution.

The piston cylinder is one of the most popular high-pressure apparatus. The mechanism of the uniaxial compression of the piston cylinder apparatus, however, often produces heterogeneous sample-temperature fields due to deformation of the heater. In order to suppress this problem, a new assembly, which is mainly composed of NaCl, has been developed. Audetat *et al*. examined temperature distributions in various piston-cylinder assemblies with NaCl pressure media by mapping the CaO and TiO_2 contents in albite melt coexisting with titanite in the sample chambers.

Nuclear magnetic resonance (NMR) spectroscopy is a powerful method to investigate spin states of transition metals. Meier and his colleagues have been applying this technique to the high-pressure environment in diamond anvil cells. In the last year, they pursued high-resolution spin decoupling techniques in paramagnetic resonance using δ-(Al,Fe)OOH as a test sample of high-pressure minerals.

The final contribution focusses on development of numerical modelling. In general, the regime of plate tectonics was not well reproduced by numerical simulation. Marzotto *et al*. examined the effects of grid resolution and a yield-stress limiter on the simulation of plate tectonics. They showed that high grid resolutions are necessary to simulate the lithosphere structure.

a. *Simultaneous pressure-temperature generation techniques to 53 GPa and 2000 K by multianvil press with tungsten carbide anvils, and its application to phase relations of basaltic crust (T. Ishii, N. Miyajima, G. Criniti and T. Katsura)*

Recent seismological studies observed stagnation of subducted slabs between 660 and 1000 km depth and small scale (~ 10 km) scattering around 860-1800 km depths. These observations have been supported by recent geodynamic modelling, indicating that basaltic fragments from the top parts of subducted slabs are accumulated in the mid-mantle. Although the density of basalt is critical for such modelling, poor knowledge of phase relations in basaltic systems prevents evaluation of the density. Laser-heated diamond anvil cell (LHDAC) experiments have covered a range of mid-mantle conditions, but the laser heating resulted in phase disequilibrium due to inhomogeneous laser absorption among phases having different iron contents. Although large-volume multianvil press (MAP) experiments can achieve phase equilibrium because of their homogeneous P-T distributions, the pressure range did not cover mid-mantle conditions so far.

We 7 have developed a pressure-temperature generation technique using the multianvil press (IRIS-15 at BGI) with tapered ultra-hard tungsten carbide anvils (TJS01, produced by Fuji Die Co. Ltd.). We used $65MgSiO_3$-$35Al_2O_3$ akimotoite as a pressure calibrant and adopted a relationship between alumina content in bridgmanite and pressure to calibratable generated pressure. Based on the chemical analysis of the recovered bridgmanite, we have demonstrated pressure generation up to 53 GPa at 2000 K (Fig. 3.8-1), corresponding to a 1300-km depth in the Earth's mantle. Using this technology, phase relations in the MORB system were determined at pressures of 27-53 GPa and a temperature of 2000 K. The starting material was a fine-grained oxide mixture with a bulk composition matching that of normal MORB. Phase identification

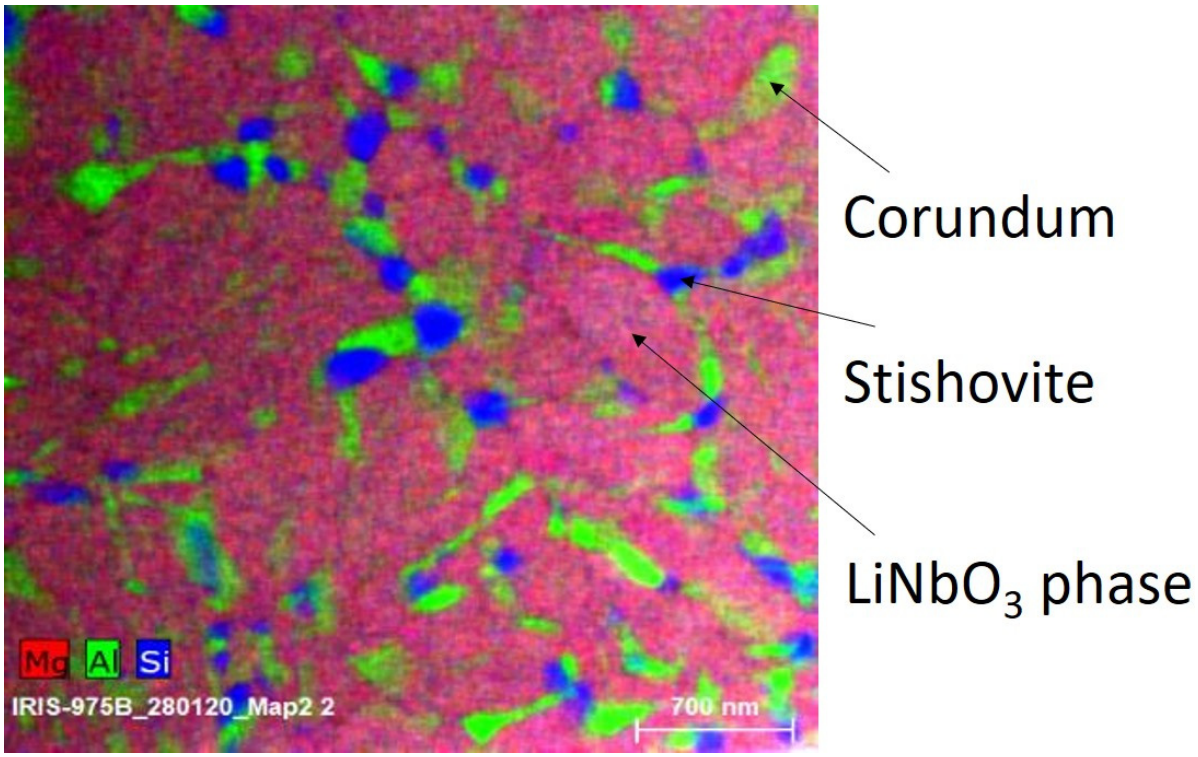

Fig. 3.8-1: A compositional map by TEM-EDS of the pressure calibrant. The alumina content of the recovered $MgSiO_3$-Al_2O_3 bridgmanite (lithium niobate phase) was estimated to be 30.3(7) mol. %, corresponding to 52.7(9) GPa.

and compositional analysis of run products were conducted using a TEM with an EDX system in combination with a FIB micro-sampling technique. We have identified the mineral assemblage of bridgmanite, stishovite, $CaSiO_3$ perovskite, Al-rich calcium-ferrite phase, and a new aluminous (hexagonal) phase at all the investigated pressures. We found a significant compositional change in bridgmanite at pressures of 40-45 GPa, which was not shown by the previous LHDAC studies. In addition, bridgmanite has only 20-25 % ferric iron in the investigated pressure range (Fig. 3.8-2), which is much less than peridotitic bridgmanite. Basaltic crust has higher density than the preliminary reference Earth model in the investigated pressure range.

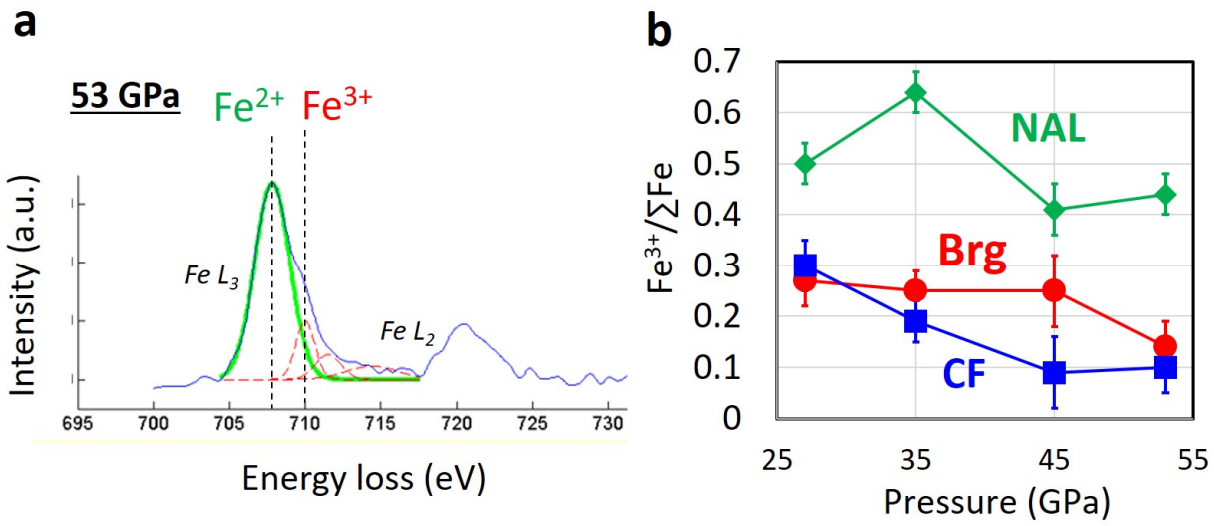

Fig. 3.8-2: (a) An electron energy loss spectrum (Fe L-edge ELNES) of bridgmanite synthesized at 53 GPa and 2000 K. (b) Ferric iron contents in bridgmanite (Brg), calcium ferrite phase (CF) and new aluminous phase (NAL).

b. *Synthesis of high-pressure peridotite glasses using a rapid-quench multianvil technique (D. Bondar, H. Fei, A.C. Withers, N. Miyajima, T. Ishii, A. Chanyshev and T. Katsura)*

The bulk silicate Earth is considered to have A composition similar to peridotite. This idea is supported by compositions of mantle xenoliths and estimated source materials of mid-oceanic basalts. Since melts resulting from partial melting of peridotite become ultramafic with increasing pressure, and the whole mantle was considered to be melted in an early history of the Earth, properties of ultramafic melts are vital for understanding the deep structure and early evolution of the Earth's mantle. For example, partition coefficients of volatiles between melts and minerals are significant, because volatiles affect physical properties of mantle minerals and rocks, and early evolution of the atmosphere should have been controlled by the interaction with the Earth's interior. The density and viscosity of melts are essential to investigate thermal evolution of the Earth's magma ocean. The sound velocity is useful to assess the melt distribution in the mantle by seismic studies.

Ultramafic melts are, however, difficult to quench: they normally crystallize to form fine-grained aggregates. This difficulty tremendously increases with increasing pressure and volatile content. As a result, all information about the structure and properties is lost upon quenching, and some components could be exsolved or segregated. In addition, such crystalline aggregates are unsuitable for precise bulk analysis. The unquenchability of ultramafic melts at high pressures and with volatiles is a serious limitation of research.

The reason for that peridotite melts crystallize upon quenching in conventional experiments lies in the insufficient cooling rates, which are about 130 °C/s and 650 °C/s in regular piston-cylinder and multianvil apparatuses, respectively. These low cooling rates are caused by large

heater sizes and ZrO_2 thermal insulation, which are placed into the standard assemblies to provide maximum sample volumes and heating efficiencies.

In order to overcome these limitations, and to be able to quench various (up to 40 wt. % of MgO) ultramafic glasses, including hydrous ones, at high pressures, we have developed a rapid-quench multianvil technique. This technique includes a low thermal-inertia assembly design and an external cooling system in combination with 15-MN DIA-type multianvil press (IRIS-15) installed in Bayerisches Geoinstitut. In contrast to regular multianvil assemblies, the low thermal-inertia assembly is designed to remove heat from the sample as fast as possible by replacing the ZrO_2 thermal insulator by highly thermally conductive and refractory metal, namely tungsten, and to decrease the amount of heat production by reducing the heater size. The external cooling system circulates 1:1 mixture of water and ethylene glycol between first- and second-stage anvils at -25 °C to allow effective heat removal.

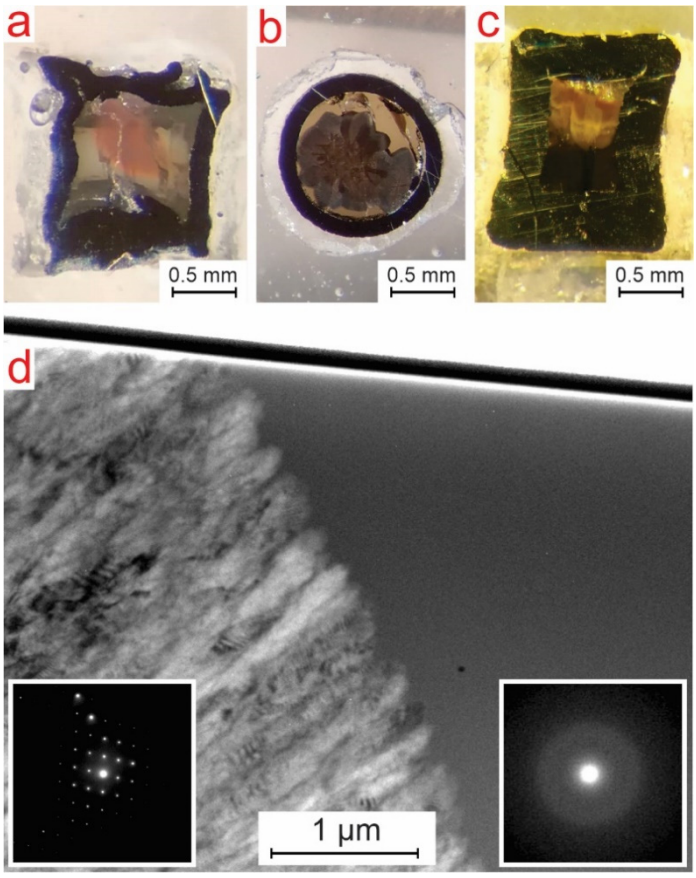

Fig. 3.8-3: (a-c) Optical images of hydrous peridotite glasses (0.2, 2 and 4 wt. % H_2O respectively) obtained at 1 GPa, (d) Transmission electron microscopy micrograph from sample (a) with inserts of electron diffraction patterns of corresponding regions.

Our technique produces a very high cooling rate of 7330 °C/s. Due to the high heat release, on the other hand, the heating efficiency was found very low: it requires 80 % higher electric power to heat the sample, even though the volume in the furnace is only 15 % of that in the standard assembly. Since the design of the rapid-quench cell differs dramatically from the standard multianvil assemblies, pressure calibration at high temperature was performed. The temperature homogeneity in the sample chambers is found to be similar between the present and standard

assemblage: the two-pyroxene thermometry indicated the temperature difference less than 90 °C within the sample capsule (h = 1 mm, d = 1 mm). Heating demonstrated good sustainability as well: a temperature of about 1450 °C was kept for 24 hours in a test run.

Thanks to these efforts, we have succeeded in quenching high-pressure peridotite glasses of KLB-1 like composition with various water contents (0.2-4 wt. %) for the very first time, as far as we are aware (Fig. 3.8-3). The experimental charges contain regions of glass and quench crystals, and both regions have the same composition as starting material. These features are similar among the experiments. In order to confirm homogeneity and absence of micro- and nanolites, the obtained glasses were investigated using scanning and transmission electron microscopies and electron microprobe. Water contents were estimated using Fourier-transform infrared spectroscopy. Future investigation of properties of such glasses should provide insights on the evolution of the Earth's mantle.

c. *A novel cooling system for the three-axis multianvil press SAPHiR at the FRM II (C. Howard and N. Walte/Garching)*

Multianvil presses are typically used to study the physical properties and phase equilibria of rocks and minerals under the conditions of the Earth's mantle. However, although these instruments are capable of reaching a few thousand degrees up to several tens of GPa, there a very few examples of cooling systems for multianvil presses, owing to their high thermal mass. The advantage of being able to perform high-pressure experiments below room temperature allows for study of the mantles of icy moons and the ice giants of the solar system. Additionally, rapid cooling enables high-pressure phases to be recovered to ambient pressure at liquid nitrogen temperatures, where samples can be characterised in other instruments.

Since the new cooling system has been developed for use with the six-ram press SAPHiR at the FRM II (see previous annual reports), samples can now also be deformed at high pressure below room temperature to study their rheological properties. This is important for studying the mantle dynamics and convective heat transfer of icy moons and ice giants of the solar system, much like the importance of deformation in the Earth's mantle. There are few examples of other instruments that are capable of controlled deformation, with these having limitations in either low maximum pressure or small sample volume. Since SAPHiR is to be used in neutron scattering experiments, large sample sizes are required over a large pressure range due to the limited intensity of neutron sources, therefore this cooling system combined with this instrument provides a good compromise between sample volume and maximum pressure.

Two systems have been developed to cool samples below room temperature at high pressure (Fig. 3.8-4). Both systems are based on the 6-6 geometry of the press, where the press force is transferred from six primary anvils to smaller secondary anvils that can be thermally isolated and follow the same principle: the secondary anvils are enclosed by partially hollow rings or sleeves that remove heat by a liquid cryogen. The first design is used with the standard

secondary anvils of SAPHiR that have varying truncation and are composed of a central cylinder of Ni-bound tungsten carbide, which is shrunk into a steel jacket. Narrow cooling rings are attached around the bottom of each of the six secondary anvils. The original design used a copper ring inside an aluminium ring; however, there were leaks at the contact between the two metals. An updated design is constructed of 3-D printed aluminium, with a small section cut to allow the ring to be placed around the secondary anvils. To maintain a good thermal contact, the rings are tightened with a screw. Each ring contains two ports, one for incoming and one for outgoing cryogen.

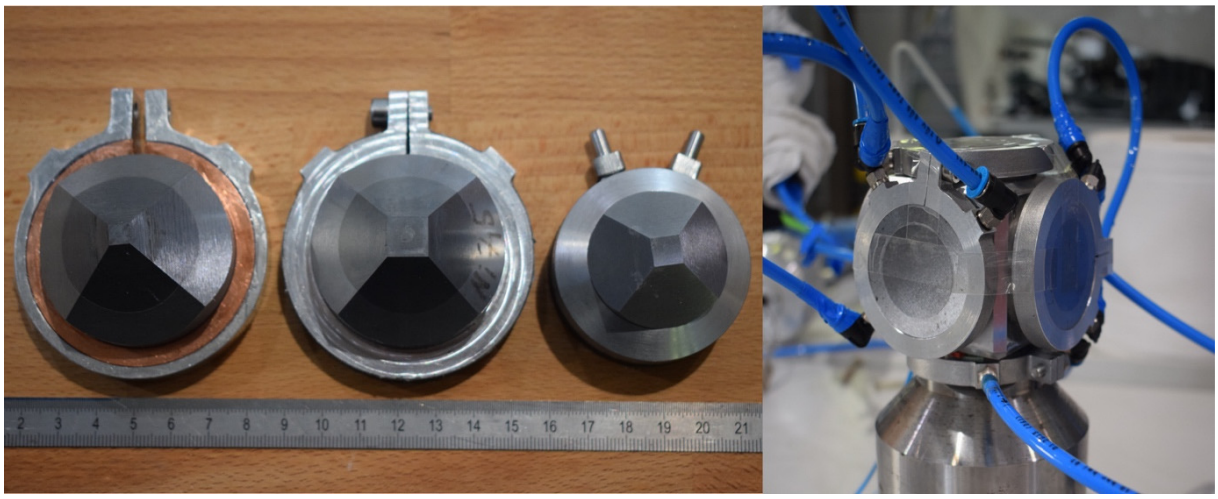

Fig. 3.8-4: (*left*) Three designs of the cooling system, from the original on the left to the newest design on the right, with the performance improving with each new design. (*right*) The cryo-rings fitted around each of the secondary anvils mounted in the anvil guide frame, connected together in series.

In order to further improve the cooling capability of the cryo-system, the second design has been developed that replaces the standard steel jackets surrounding the cylindrical anvil cores. The new cryo-jackets, also constructed from aluminium, contain an internal cavity for cryogen flow to directly cool the anvil core that is in contact with the cubic pressure medium containing the sample. As with the standard steel jackets, they are shrink-fitted to the WC anvil cores, having the additional benefits of ensuring good thermal contact and fixing the jacket in place. The cryo-jacket is slightly reduced in height compared to the standard steel jackets, so that the base of the anvil core protrudes from the jacket by ~ 0.5 mm to ensure minimal thermal contact of the cryo-jacket with the primary anvils.

To assess the performance of the new cooling system, tests were carried out at various pressures on SAPHiR. The current lowest temperature of the cooling rings is ~ 120 K, achieved within 40 minutes of the start of cooling, with an average cooling rate of ~ 2 K min^{-1}. The cryo-jackets have an improved performance, with the lowest temperature of ~ 83 K, which is reached within 10 minutes of initiating the flow of nitrogen, having an average cooling rate of ~ -20 K min^{-1}. However, although the cryo-jackets are capable of colder temperatures with increased cooling

rates than the cryo-rings, the lack of steel mantles lowers the lateral support of the WC cores, which reduces the maximum press load that can be sustained by the secondary anvils. Hence, the cryo-rings may be able to achieve higher maximum pressure at a given truncation.

The new cooling system will allow for *in situ* neutron experiments to be performed at pressures up to 20 GPa at temperatures between 80-300 K. In addition, it is highly portable and can in principle be adapted to any six-ram multianvil press with the 6-6 anvil geometry, such as at instruments at synchrotron or neutron facilities. Until SAPHiR is provided with neutrons (currently planned for 2022), applications of the cooling system are cryo-recovery studies of high-pressure phases, and of the deformation textures of high-pressure phases, that will be measured with the FRM II instruments SPODI (a high-resolution powder diffraction instrument at the FRM II) and STRESSPEC (a powder diffractometer for crystallographic preferred orientation measurements).

d. *Development of a high-pressure assembly for a six-ram large-volume press for piezoelectric measurements and measurement of deformation pressure and strain* in situ *(J.D. Dolinschi and D.J. Frost)*

The six-ram large-volume press available at Bayerisches Geoinstitut is capable of independently advancing all 6 anvils. This allows for deformation and deviatoric stress experiments. To measure the deviatoric stress in a large-volume press experiment, there are two methods traditionally available. The first is to run the experiment in a synchrotron facility and take X-rays of the sample during the experiment; this is a form of *in situ* measurement. The second is to analyse the sample after the experiment and measure properties such as crystal preferred orientation or dislocation densities; this is a form of *ex situ* measurement. In this project, we are developing another method where measurements of deviatoric stress on the sample can be acquired *in situ* without requiring beamtime at a synchrotron facility.

There are some crystals that, due to their crystal symmetry, will develop an electric charge across the crystal in response to mechanical stress, and *vice versa*, on a specific crystal axis. These are known as piezoelectric crystals, with some examples being α-quartz, topaz, and gallium orthophosphate. This project seeks to develop an assembly for the six-ram press that can measure the voltage across the crystal during a deformation experiment. Using this voltage measurement, it is possible to calculate the force on the crystal exerted by the press and ultimately measure the deviatoric stress experienced by the crystal, as shown in Figure 3.8-5. The assembly consists of a sub-millimetre-thick disk of a piezoelectric crystal placed inside a 15 mm edge-cut cube assembly, with copper wires connected to thin copper or gold foil placed on both sides of the crystal disk. The voltage difference across the two sides is then measured during a deformation experiment. During the experiment, the deviatoric pressure on the sample from the deformation can be directly measured. By combining this with the known strain-rate from the deformation, properties such as viscosities of samples at high pressures and high temperatures can be achieved.

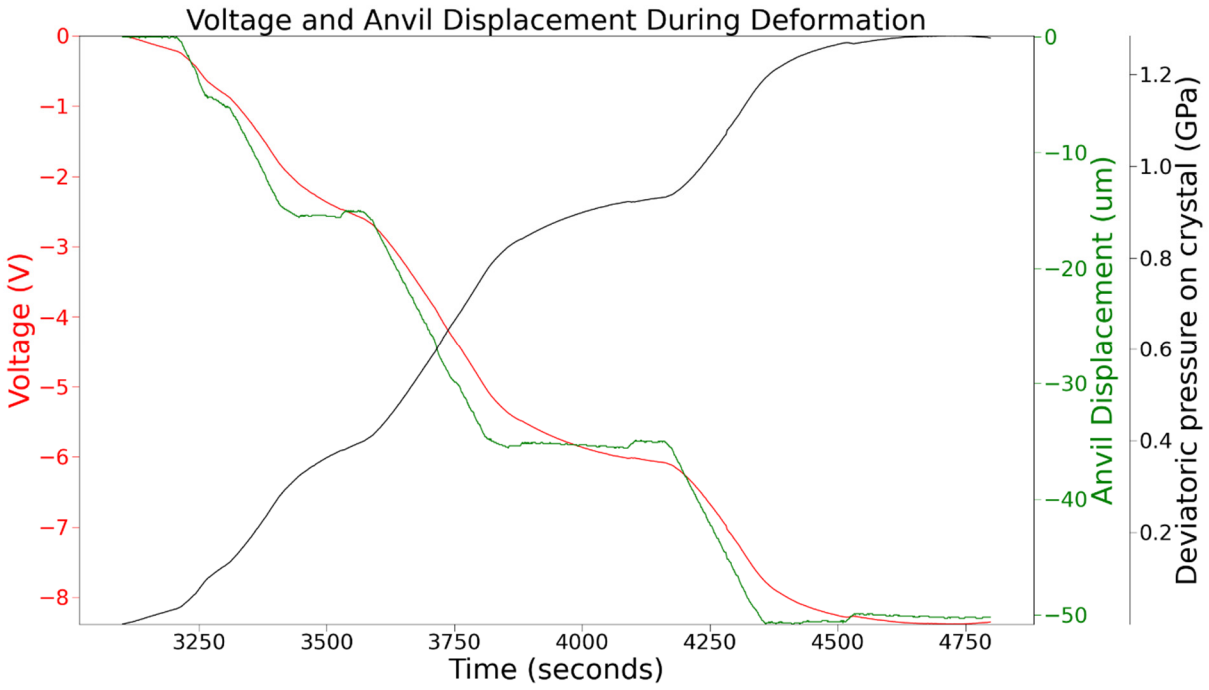

Fig. 3.8-5: Example output from an assembly at 3 GPa. The green line shows the anvil displacement inwards that is causing the deformation of the assembly. The red line is the direct voltage output from the quartz crystal during deformation. The black line is the calculated axial deviatoric stress on the quartz crystal from the deformation. The horizontal axis is seconds passed from the start of the experiment.

A hurdle that must be surpassed is the loss of piezoelectric properties in quartz at high temperatures. Thus, the assembly must either use a different piezoelectric crystal, such as gallium orthophosphate, that exhibits higher thermal stability, or an assembly designed in such a way that it insulates the quartz crystal from high temperatures while still heating the sample itself.

e. *Development of an internal pressure standard for in-house ultrasonic measurements (A. Néri, T. Boffa Ballaran and D.J. Frost)*

Laboratory wave-speed measurements constitute a powerful tool to determine the equations of state of mantle minerals and to better understand the complex structure of the Earth's mantle. Acoustic interferometry methods are usually adapted to large-volume multianvil presses, allowing the probing of conditions up to 3000 K and 25 GPa. This technique uses a piezoelectric crystal (transducer), attached to the back of a tungsten carbide (WC) anvil, that is excited to produce acoustic waves. These waves propagate through the anvil itself and are brought to the sample by an alumina buffer rod (BR). Waves are reflected at the different interfaces encountered, producing echoes that back-propagate to the transducer (Fig. 3.8-6A). The transducer acts not only as an emitter but also as a receiver, generating an electric signal when an echo arrives, which is recorded by an oscilloscope. The time difference between the different

echoes then give the two-way travel time through a given material – for instance, the time difference between echoes E2 and E3 in Figure 3.8-6A gives the two-way travel time through the sample. Velocities are finally calculated knowing the length of the sample, but both a good description of the equation of state of the material under study and an accurate knowledge of pressure and temperature conditions are required since during "in-house" experiments the density of the sample cannot be measured *in situ* as is usually done at synchrotron facilities.

The critical step of the in-house experiments is the pressure determination, as temperature is measured using a thermocouple – knowledge of pressure mostly relies on calibration curves that were collected at room temperature. Ideally, the accurate measurement of pressure could be obtained by measuring the travel time through a reference material inserted in the same assembly as the sample of interest.

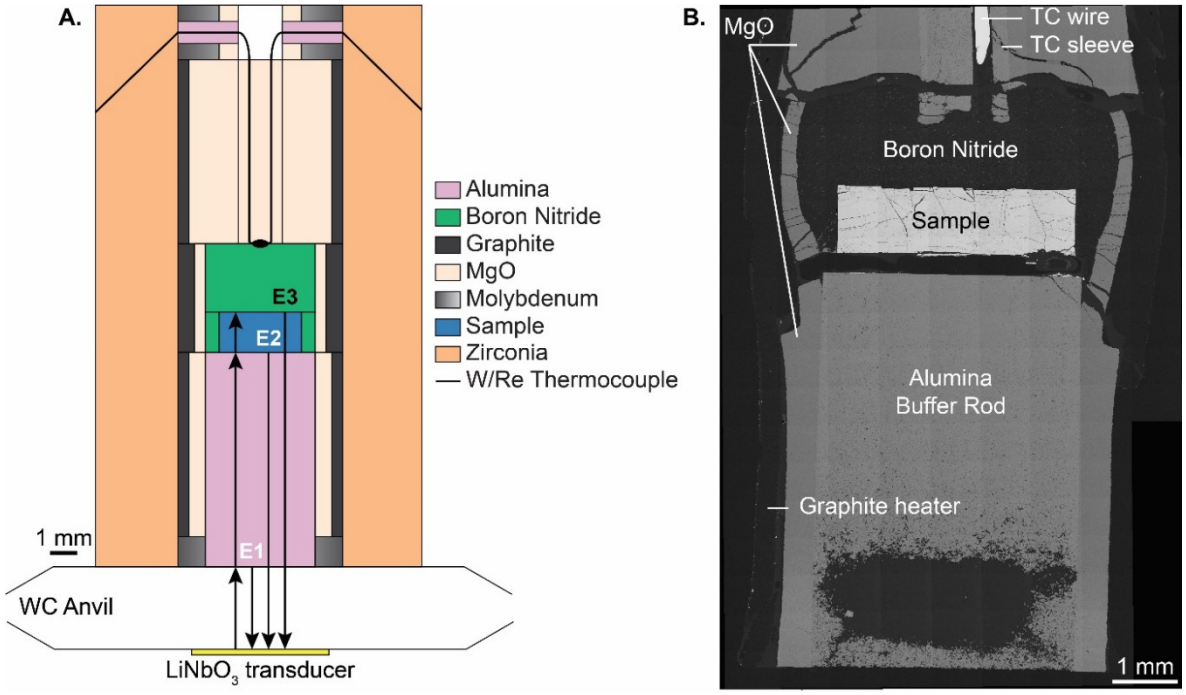

Fig. 3.8-6: (A.) Assembly designed for the ultrasonic experiments. Arrows denote the path of the acoustic waves generated by the transducer; E1 indicates the WC anvil - buffer rod echo, E2 the buffer rod - sample one and E3 the echo on the sample back. (B.) SEM image of a recovered assembly. The surface at the back of the sample shows cracks that may be the result of stress.

In this study, we have chosen to test whether garnet single crystals could be used as internal calibrants, as their equations of state are well known and therefore from the temperature reading of the thermocouple and the travel time measured, it should be possible to recalculate pressure. Preliminary results collected so far during two experiments, indicate that data collected at room temperature are in agreement with previously determined calibration curves. However, upon increasing temperature a pressure drop has been observed, most likely due to stress relaxation.

Further decreasing temperature releases thermal pressure and results in a decrease of the effective pressure. The garnet single crystals used during these preliminary runs seem to have been subjected to significant stresses (recovered samples show some deformation, Fig. 3.8-6B), which artificially increases the error on the determined pressure. As of now, the assembly is being optimised to reduce the stress applied to the sample in order to further reduce the uncertainty on pressure determination. Applications will include determining the seismic signature of melt accumulations in the Earth's upper mantle without the need of synchrotron radiation for volume determinations.

f. *Mapping the temperature distribution within piston cylinder sample capsules (A. Audétat, A. Krupp and R. Putra)*

Rigorous control on pressure and temperature is an essential requirement for the realization of successful high *P-T* experiments. The standard assembly used for piston-cylinder experiments at BGI consists of inner parts made of crushable Al_2O_3, a graphite heater, a Pyrex glass sleeve, and an outer talc sleeve. Although very robust, this assembly has several drawbacks, including a high friction correction of ~ 20 %, and the frequent deformation of the graphite heater due to cracking of the Pyrex glass at the beginning of the experiment. The latter could potentially cause severe temperature gradients. In order to quantify this effect and to test the performance of alternative assemblies consisting solely of MgO parts, graphite, and an outer NaCl sleeve, a method was developed to map the temperature distribution within sample capsules.

For this purpose, Pt capsules were filled with a fine-grained (100-160 µm) mixture of natural, gem-quality titanite and a $Na_2Si_2O_5$-enriched albite glass at a mass ratio of ~ 5:1. During the run titanite dissolves into the albite melt, with the final TiO_2 and CaO content of the melt being a function of temperature (Fig. 3.8-7). By analysing the compositions of many melt pools across the sample capsules, it is thus possible to map the temperature distribution. All experiments were performed at 1250 °C and 2.0 GPa.

The temperature distribution within a sample capsule retrieved from a MgO-NaCl assembly with a straight-walled graphite furnace is shown in Fig. 3.8-8a. An overall temperature variation of ~ 40 °C is recorded in this sample. As expected, there was a thermal high at middle height of the capsule, but contrary to expectation the highest temperatures is not in the centre but rather at the rim. A similar assembly with a stepped graphite heater (Fig. 3.8-8b; 0.3 mm step size) resulted in a distinctly larger thermal gradient (ΔT = 60-80 °C) and a very different temperature distribution, with a thermal low slightly below the centre and thermal maxima in the corners, particularly at the upper left and right. Apparently, the step in the graphite heater was too thick (and potentially also too short). A third assembly with a thinner step of the same length (step size of 0.15 mm) resulted in a much more even temperature distribution (Fig. 3.8-8c). Other runs revealed pronounced thermal maxima next to faults in the graphite furnace, although not all faults seem to have had any effect. In summary, the method is a promising new tool to optimize assembly designs, and the results emphasize the fact that already small variations in furnace thickness and geometry have a large impact on temperature.

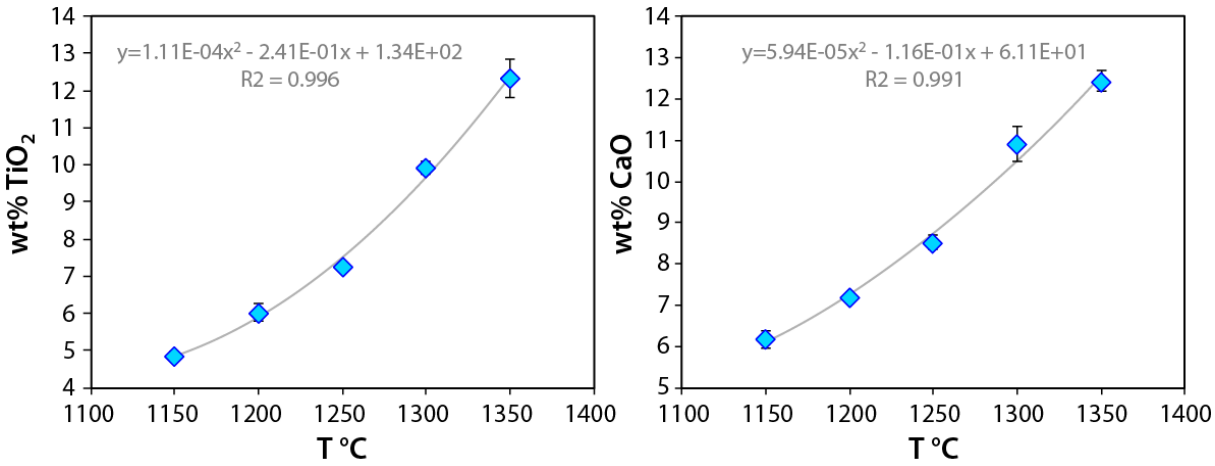

Fig. 3.8-7: TiO_2 and CaO content of the silicate melt as a function of temperature.

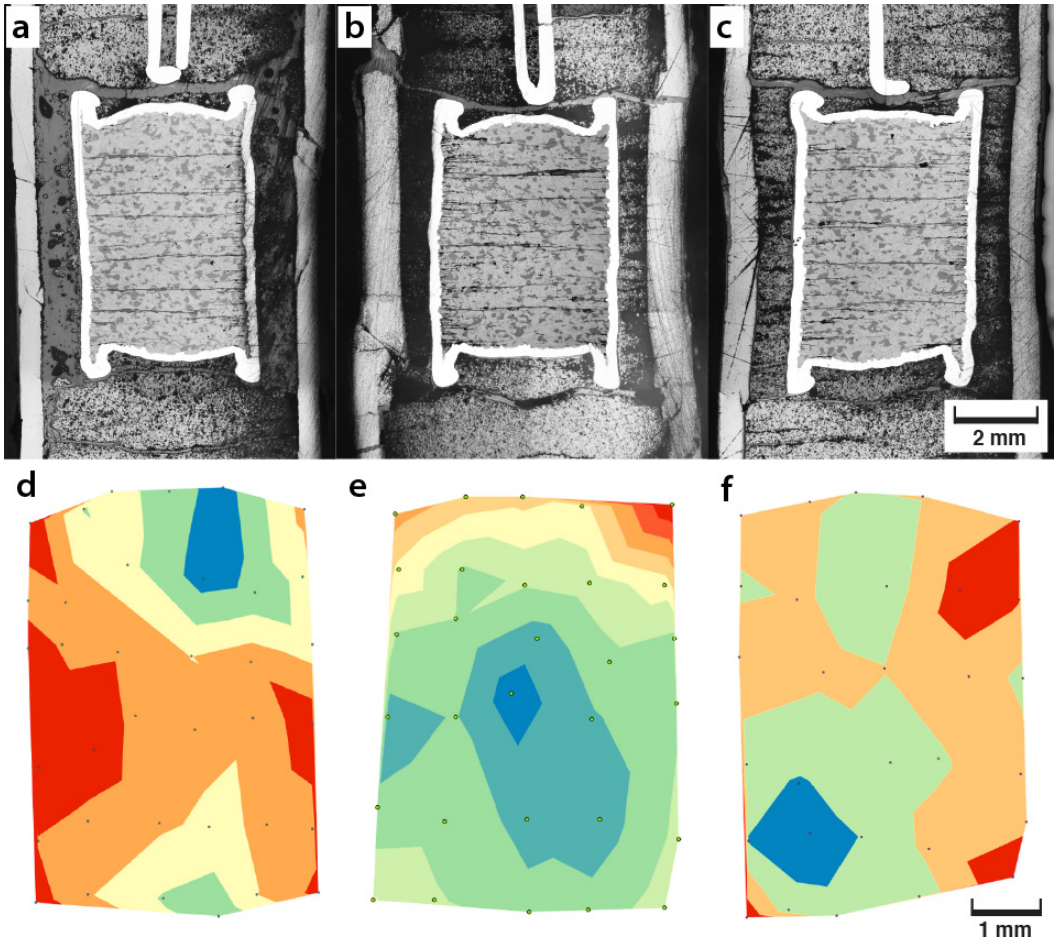

Fig. 3.8-8: (a-c) Reflected-light images of sample capsules within piston cylinder assemblies after experiments. The dark grey patches within the sample capsules are melt pools; the lighter grey rest is titanite. (a) straight-walled graphite furnace; (b) furnace with thick step; (c) furnace with thin step. (d-e) corresponding temperature distribution within the sample capsules. Each colour reflects a 10 °C interval; blue is cold; red is hot; dots represent measuring spots.

g. *High resolution paramagnetic resonance in hydrous minerals under extreme conditions (T. Meier, F. Trybel, S. Khandarkhaeva, D. Simonova, I. Koemets, A. Kurnosov, T. Ishii, N. Dubrovinskaia/Bayreuth and L. Dubrovinsky)*

Iron- and aluminium-bearing oxyhydroxides are considered to be potential transport agents of hydrogen into Earth's mantle region. However, structural complexity, magnetic ordering, as well as the nature of the hydrogen bonding render a deeper investigation of these materials at high-pressure conditions challenging. Here, we present ^{1}H-NMR data on δ-$(Al_{1-x}Fe_x)OOH$ (x = 0, and 0.7) in diamond anvil cells at pressures of up to 70 GPa. Paramagnetic high-resolution two-dimensional Lee-Goldburg (LG) decoupling experiments were used to assign and identify the hydrogen bond manifold in the Fe^{3+} bearing compound, achieving a 1.25 ppm spectral resolution. At low pressures, the $Pnm2_1 \rightarrow Pnnm$ transition was observed in both samples by a sudden change of resonance frequencies as the unimodal hydrogen probability density shifts towards the centre of the H-bond. The paramagnetic shift of δ-$(Al_{0.3}Fe_{0.7})OOH$ was found to collapse at the high spin → low spin transition inferred from complementary diffraction data at p ≈ 42 GPa. Lineshape analysis reveal several maxima of the hydrogen diffusion coefficients ($D_{^1H} \approx 10^{-10}$m^2/s) within the hydrogen bond network. This study demonstrates the potential use of high-resolution spin decoupling techniques in paramagnetic resonance for *in situ* high-pressure experiments in diamond anvil cells on structurally complex systems, and might open up the field of high-pressure NMR crystallography.

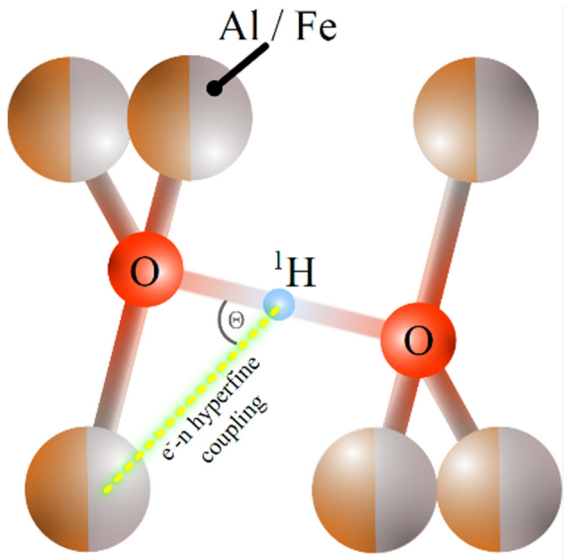

Fig. 3.8-9: Upper: Local structure of the hydrogen atoms serving as the NMR probe. The anion positions are stochastically occupied by aluminium or iron atoms according to the stoichiometry of the sample. The hydrogen spin system is predominantly influenced by the paramagnetic centres of ferric iron in their high pressure, S = 5/2, or their low pressure, S = 1/2, electronic configuration. Lower: 2D-Lee Goldburg decoupling spectrum of δ-$(Al_{0.3}Fe_{0.7})OOH$ at 15.7 GPa.

h. *Effect of grid resolution on tectonic regimes in global-scale convection models (E. Marzotto, M. Thielmann and G.J. Golabek)*

In numerical models, the plate-tectonic regime is achieved by implementing a visco-plastic rheology. Strongly temperature-dependent viscosity generates a rigid lid, whereas the rupture

of the lithosphere is handled by a yield stress limiter (τ_y). Once this value is reached, a low viscosity zone is created and the plate boundaries are finally formed.

By changing τ_y, different tectonic regimes can be reproduced:

1. Dripping (low τ_y): the lithosphere is continuously sinking into the mantle, but lacks rigidity to sustain continuous subduction.
2. Plate-like behaviour (intermediate-low τ_y): a plate boundary is formed and, once subduction starts, the slab is rigid enough to avoid repetitive slab breakoff.
3. Episodic behaviour (intermediate-high τ_y): a long-term stagnant lid stage is followed by episodic overturn events.
4. Stagnant lid behaviour (high τ_y): the elevated strength the lithosphere leads to the formation of one continuous plate.

Each lid behaviour can be distinguished by comparing the evolution profiles of several parameters (Fig. 3.8-11).

Although many studies have tried to implement several sophisticated rheologies to control lithospheric rupture, very few have addressed the effects of numerical parameters on the tectonic regimes. Here we use the code StagYY in a 2D spherical annulus geometry to determine the resolution-dependent tectonic regime for different τ_y. We tested 12 grid resolutions (ranging from 128×32 to 1024×128 nodal points) and 9 different τ_y (ranging from 10 to 90 MPa), keeping all the remaining physical parameters unchanged. We assume isothermal free-slip boundaries, constant radiogenic heating, no melting, endothermic (410) and exothermic (660) phase transitions. Each simulation was run for 15 Gyrs to make sure that steady-state conditions were reached.

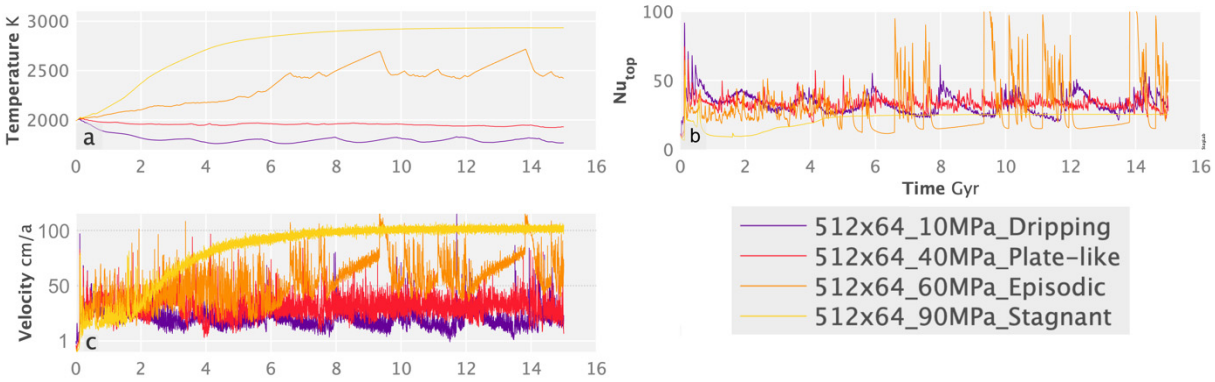

Fig. 3.8-11: Different lid regimes over time: (a) temperature, (b) surface Nusselt number, (c) whole mantle velocity. Dripping (purple), plate-like (red), episodic (orange) and stagnant (yellow).

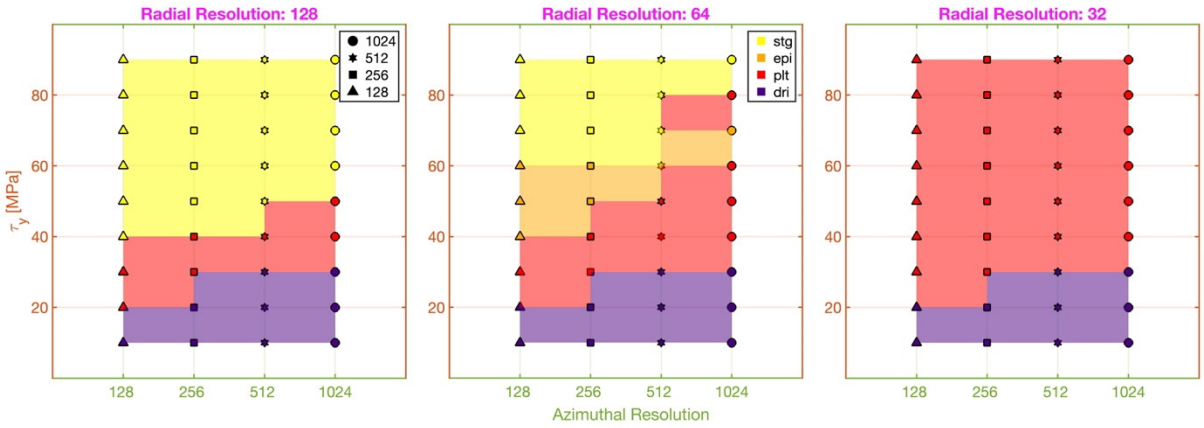

Fig. 3.8-12: Lid regimes obtained for various yield stresses. Each marker represents a simulation. In each box the radial resolution is kept constant (32, 64 and 128 nodes) whereas the azimuthal resolution is changed. The colour code is the same of Fig. 3.8-11.

Our resolution tests showed that the resulting tectonic regime depends on the grid resolution, in particular how well resolved the lithosphere is. Low radial resolutions in the lithosphere (thick cells) favour weak lid regimes (dripping and plate-like), since the temperature, viscosity and stress fields are interpolated from higher depths. Low azimuthal resolutions, on the other hand, favour strong lid regimes (episodic and stagnant) since plate boundaries remain unresolved. In conclusion, only at high grid resolutions (1024×128 and higher) the numerical influence on the observed tectonic regime is low.

4. International Research and Training Group – "Deep Earth Volatile Cycles" (DFG GRK 2156/1)

The International Research and Training Group (IRTG) "Deep Earth Volatile Cycles" is funded by the *Deutsche Forschungsgemeinschaft* (DFG). This graduate school for doctoral studies started in April 2016 for a period of 4.5 years. It is a cooperation between the Bayerisches Geoinstitut (BGI) and the Department of Earth Sciences at Tohoku University, Sendai/Japan. The IRTG is chaired by Dan Frost/Bayreuth and Michihiko Nakamura/Sendai.

The objective of this collaborative research effort is to study the cycling of volatile elements through the deep interior of the Earth. Using mainly experimental and computational methods the group's goal is to quantify how volatile elements such as carbon, hydrogen and nitrogen are transported, stored and expelled from the interior as a result of plate tectonic processes. Doctoral researchers receive training in modern experimental and modelling techniques employed in solid Earth geosciences in a structured learning programme. At the same time, they pursue independent research into geochemical and geophysical aspects of the internal volatile cycle. Doctoral researchers from the BGI spend between 6 to 12 months at Tohoku University as part of a complementary research exchange that sees scientists from Tohoku University spending time at the BGI.

IRTG Activities in 2020:

Participants and lecturers of the DMG short course "*High-Pressure Experimental Techniques and Applications to the Earth's Interior*" at BGI.

High-pressure short course: Thirty-two doctoral and master students took part in a five-day high-pressure short course at Bayerisches Geoinstitut in February before serious travel restrictions due to corona were in place. Participants came to Bayreuth from nine countries and four doctoral IRTG students from Tohoku University joined the course. The program consisted of introductory lectures and practical lab exercises covering high pressure and temperature

experimentation as well as analytical techniques commonly used in the investigation of high pressure samples. Coffee breaks and a Frankonian dinner evening in the center of Bayreuth gave ample chance to foster exchange and collaboration between participants and lecturers.

IRTG equal opportunity work shop: On January 21 a training course was offered at the BGI with the topic: 'Discrimination – hostility – conflict: Strategies to recognize and to fight them'. It was specially geared towards female employees and was attended by nine female master and PhD students as well as scientists. The course gave very valuable advice for identifying and resolving negative influences and conflicts in the scientific work environment and was very much appreciated by the participants.

Common IRTG neutron beam time at JPARC: At the beginning of March a team comprised mainly of IRTG students from the BGI and researchers from Tohoku University, participated in a 7 day neutron diffraction experiment at the PLANET high pressure beamline of the Material and Life science experimental Facility (MLF) at the J-PARC research campus in Japan. The objective of the experiment was to study the solubility hydrogen in iron sulphide at high pressure and temperature and to identify the atomic position where hydrogen exists in the sulphide mineral structure (yearbook contribution 3.3-h). J-PARC is one of the brightest spallation neutron sources in the world. A six-axis multianvil apparatus (ATSUHIME) installed at the beamline allows *in situ* neutron diffraction measurements to be made at simultaneous high pressure and temperature.

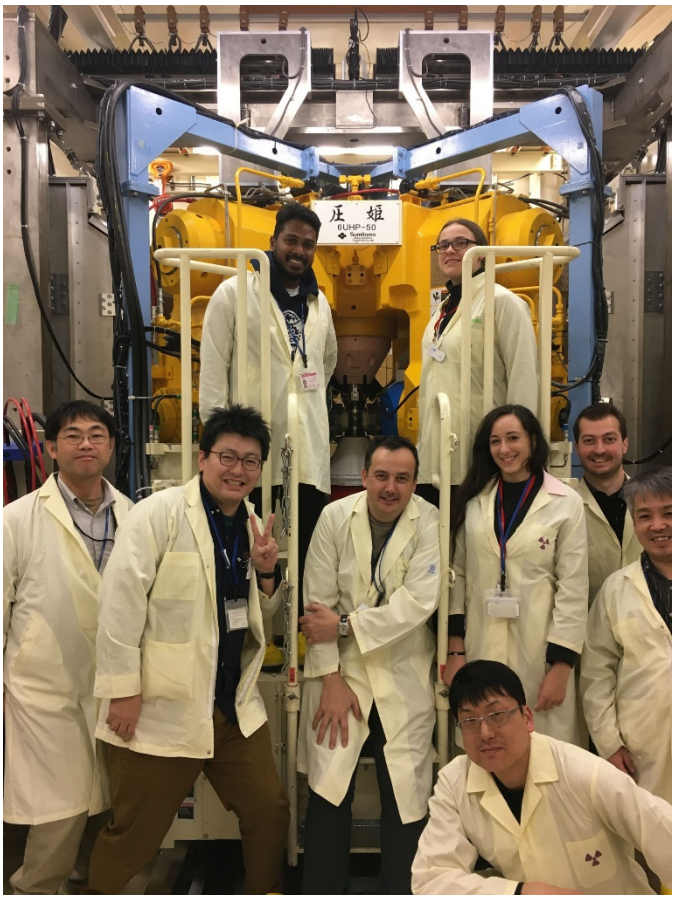

Participants of the beamtime experiment at PLANET beamline (BL 11), J-PARC standing in front of the 6-axis multi-anvil "ATSUHIME" press.

Research visits to BGI/Tohoku University: In the beginning of 2020 the following staff members and PhD students from Tohoku University and BGI visited the partner institution. From March 2020 all other visits to Tohoku University or to BGI had to be postponed due to travel restrictions because of the Corona-pandemic.

Tohoku colleagues visiting BGI in 2020:

Name	**Period**	**Name**	**Period**
Huang, Yongsheng	06.02.-14.03.	Takahashi, Naoko	10.02.-22.02
Nakamura, Michihiko, Prof.	09.02.-12.02.	Ohashi, Tomonori	10.02.-16.03.
Suzuki, Akio, Prof.	09.02.-22.02.	Araya, Naoki	10.02.-18.02.
Ohtani, Eiji, Prof.	10.02.-13.02.	Yutani, Taku	13.02.-19.03.
Ikeda, Osamu	10.02.-22.02.		

BGI colleagues visiting Tohoku in 2020:

Name	**Period**	**Name**	**Period**
Abeykoon, Sumith	01.01.-30.04.	Eberhard, Lisa	06.03.-19.03.
Dominijanni, Serena	11.01.-31.03.	Frost, Dan, Prof.	06.03.-13.03.

5. Publications, Conference Presentations, Seminars

5.1 Publications (published)

Supplement to **2019** (papers published at the end of 2019):

ROTTIER, B.; AUDÉTAT, A.; KODĚRA, P.; LEXA, J. (2019): Origin and evolution of magmas in the porphyry Au-mineralized Javorie Volcano (Central Slovakia): Evidence from thermobarometry, melt inclusions and sulfide inclusions. Journal of Petrology, 60(12), 2449-2482

2020

a) Refereed international journals

ANZOLINI, C.; MARQUARDT, K.; STAGNO, V.; BINDI, L.; FROST, D.J.; PEARSON, D.G.; HARRIS, J.W.; HEMLEY, R.J.; NESTOLA, F. (2020): Evidence for complex iron oxides in the deep mantle from FeNi(Cu) inclusions in superdeep diamond. Proceedings of the National Academy of Sciences of the United States of America 117, 21088-21094, https://doi.org/10.1073/pnas.2004269117

APRILIS, G.; PAKHOMOVA, A.; CHARITON, S.K.; MELAI, C.; BYKOVA, E.; BYKOV, M.; FEDOTENKO, T.; KOEMETS, E.; MCCAMMON, C.; CHUMAKOV, A.; HANFLAND, M.; DUBROVINSKAIA, N.; DUBROVINSKY, L. (2020): The effect of pulsed laser heating on the stability of ferropericlase at high pressures. Minerals 10(6), 542, https://doi.org/10.3390/min10060542

ARMSTRONG, K.; SIERSCH, N.; BOFFA BALLARAN, T.; FROST, D.J.; YU, T.; WANG, Y.B. (2020): Equations of state, phase relations, and oxygen fugacity of the Ru-RuO_2 buffer at high pressures and temperatures. American Mineralogist, 105, 333-343

BHAT, S.; LALE, A.; BERNARD, S.; ZHANG, W.; ISHIKAWA, R.; HASEEN, S.; KROLL, P.; WIEHL, L.; FARLA, R.; KATSURA, T.; IKUHARA, Y.; RIEDEL, R. (2020): Discovery of ternary silicon titanium nitride with spinel-type structure. Scientific Reports 10, 7372, https://doi.org/10.1038/s41598-020-64101-5

BHAT, S.; WIEHL, L.; HASEEN, S.; KROLL, P.; GLAZYRIN, K.; LEIDREITER, P.G.; KOLB, U.; FARLA, R.; TSENG, J.-C.; IONESCU, E.; KATSURA, T.; RIEDEL, R. (2020): A novel high-pressure tin oxynitride Sn_2N_2O. Chemistry – A European Journal 26, 2187-2194, https://doi.org/10.1002/chem.201904529

BINCK, J.; CHARITON, S.; STEKIEL, M.; BAYARJARGAL, L.; MORGENROTH, L.; MILMAN, V.; DUBROVINSKY, L.; WINKLER, B. (2020): High-pressure, high-temperature phase stability of iron-poor dolomite and the structures of dolomite-IIIc and dolomite-V. Physics of the Earth and Planetary Interiors 299, 106403, https://doi.org/10.1016/j.pepi.2019.106403

BONDAR, D.; FEI, H.; WITHERS, A.C.; KATSURA, T. (2020): A rapid-quench technique for multi-anvil high-pressure-temperature experiments. Review of Scientific Instruments 91, 065105, https://doi.org/10.1063/5.0005936

BORISOVA, A.Y.; BINDEMAN, I.N.; TOPLIS, M.J.; ZAGRTDENOV, N.R.; GUIGNARD, J.; SAFONOV, O.G.; BYCHKOV, A.Y.; SHCHEKA, S.; MELNIK, O.E.; MARCHELLI, M.; FEHRENBACH, J. (2020): Zircon survival in shallow asthenosphere and deep lithosphere. American Mineralogist 105, 1662-1671, https://doi.org/10.2138/am-2020-7402

BORISOVA, A.Y.; ZAGRTDENOV, N.R.; TOPLIS, M.J.; CEULENEER, G.; SAFONOV, O.G.; POKROVSKI, G.S.; JOCHUM, K.P.; STOLL, B.; WEIS, U.; SHCHEKA, S.; BYCHKOV, A.Y. (2020): Hydrated peridotite–basaltic melt interaction Part II: Fast assimilation of serpentinized mantle by basaltic magma. Frontiers in Earth Science 8, 84, https://doi.org/10.3389/feart.2020.00084

BYKOV, M.; CHARITON, S.; BYKOVA, E.; KHANDARKHAEVA, S.; FEDOTENKO, T.; PONOMAREVA, A.; TIDHOLM, J.; TASNÁDI, F.; ABRIKOSOV, I.; SEDMAK, P.; PRAKAPENKA, V.; HANFLAND, M.; LIERMANN, H.-P.; MAHMOOD, M.; GONCHAROV, A.; DUBROVINSKAIA, N.; DUBROVINSKY, L. (2020): High-pressure synthesis of metal-inorganic frameworks $Hf_4N_{20}{\cdot}N_2$, $WN_8{\cdot}N_2$, and $Os_5N_{28}{\cdot}3\ N_2$ with polymeric nitrogen linkers. Angewandte Chemie 59(26), 10321-10326, https://doi.org/10.1002/anie.202002487

CHARITON, S.; BYKOV, M.; BYKOVA, E.; KOEMETS, E.; FEDOTENKO, T.; WINKLER, B.; HANFLAND, M.; PRAKAPENKA, V.; GREENBERG, E.; MCCAMMON, C.; DUBROVINSKY, L. (2020): The crystal structures of Fe-bearing $MgCO_3$ sp^2-and sp^3-carbonates at 98 GPa from single-crystal X-ray diffraction using synchrotron radiation. Acta Crystallographica Section E: Crystallographic Communications 76(5), 715-719, https://doi.org/10.1107/S2056989020005411

CHARITON, S.; MCCAMMON, C.; VASIUKOV, D.; STEKIEL, M.; KANTOR, A.; CERANTOLA, V.; KUPENKO, I.; FEDOTENKO, T.; KOEMETS, E.; HANFLAND, M.; CHUMAKOV, A.; DUBROVINSKY, L. (2020): Seismic detectability of carbonates in the deep Earth: A nuclear inelastic scattering study. American Mineralogist 105, 325-332, https://doi.org/10.2138/am-2020-6901

CRAMERI, F.; MAGNI, V.; DOMEIER, M.; SHEPHARD, G.E.; CHOTALIA, K.; COOPER, G.; EAKIN, C.M.; GRIMA, A.G.; GÜRER, D.; KIRÁLY, Á.; MULYUKOVA, E.; PETERS, K.; ROBERT, B.; THIELMANN, M. (2020): A transdisciplinary and community-driven database to unravel subduction zone initiation. Nature Communications 11, 3750, https://doi.org/10.1038/s41467-020-17522-9

DE MIN, A.; VELICOGNA, M.; ZIBERNA, L.; CHIARADIA, M.; ALBERTI, A.; MARZOLI, A. (2020): Triassic magmatism in Southern Alps as an early phase of Pangea Break-up. Geological Magazine, https://doi.org/10.1017/S0016756820000084

DI GENOVA, D.; BROOKER, R.A.; MADER, H.; DREWITT, J.W.E.; LONGO, A.; DEUBENER, J.; NEUVILLE, D.R.; FANARA, S.; SHEBANOVA, O.; ANZELLINI, S.; ARZILLI, F.; BAMBER, E.C.; HENNET, L.; LA SPINA, G.; MIYAJIMA, N. (2020): *In situ* observation of nanolite growth in volcanic melt: A driving force for explosive eruptions. Science Advances 6(39), eabb0413, https://doi.org/10.1126/sciadv.abb0413

DOBSON, K.J.; ALLABAR, A.; BRETAGNE, E.; COUMANS, J.; CASSIDY, M.; CIMARELLI, C.; COATS, R.; CONNOLLEY, T.; COURTOIS, L.; DINGWELL, D.B.; DI GENOVA, D.; FERNANDO, B.; FIFE, J.L.; FYFE, F.; GEHNE, S.; JONES, T.; KENDRICK, J.E.; KINVIG, H.; KOLZENBURG, S.; LAVALLÉE, Y.; LIU, E.; LLEWELLIN, E.W.; SCHLEPÜTZ, C.M.; SELLICK, C.; VASSEUR, J.; VON AULOCK, F.W.; WADSWORTH, F.B.; WIESMAIER, S.; WANELIK, K. (2020): Quantifying microstructural evolution in moving magma. Frontiers in Earth Sciences 8, 1-22, https://doi.org/10.3389/feart.2020.00287

DORFMAN, S.M.; POTAPKIN, V.; LV, M.; GREENBERG, E.; KUPENKO, I.; CHUMAKOV, A.; BI, W.; ALP, E.; LIU, J.; MAGREZ, A.; DUTTON, S.; CAVA, R.; MCCAMMON, C.; GILLET, P. (2020): Effects of composition and pressure on electronic states of iron in bridgmanite. American Mineralogist 105, 1030-1039; https://doi.org/10.2138/am-2020-7309

DU, J.; AUDÉTAT, A. (2020): Early sulfide saturation is not detrimental to porphyry Cu-Au formation. Geology 48, https://doi.org/10.1130/G47169.1

EICHHEIMER, P.; THIELMANN, M.; FUJITA, W.; GOLABEK, G.J.; NAKAMURA, M.; OKUMURA, S.; NAKATANI, T.; KOTTWITZ, M.O. (2020): Combined numerical and experimental study of microstructure and permeability in porous granular media. Solid Earth 11, 1079-1095, https://doi.org/10.5194/se-11-1079-2020

FEDOTENKO, T.; DUBROVINSKY, L.; KHANDARKHAEVA, S.; CHARITON, S.; KOEMETS, E.; KOEMETS, I.; HANFLAND, M.; DUBROVINSKAIA, N. (2020): Synthesis of palladium carbides and palladium hydride in laser heated diamond anvil cells. Journal of Alloys and Compounds 844, 156179, https://doi.org/10.1016/j.jallcom.2020.156179

FEI, H.; DRUZHBIN, D.; KATSURA, T. (2020): The effect of water on ionic conductivity in olivine. Journal of Geophysical Research: Solid Earth 125(3), e2019JB019313, https://doi.org/10.1029/2019JB019313

FEI, H.; LIU, Z.; MCCAMMON, C.A.; KATSURA, T. (2020): Oxygen vacancy substitution linked to ferric iron in bridgmanite at 27 GPa. Geophysical Research Letters 47(6) e2019GL086296, https://doi.org/10.1029/2019GL086296

FEI, H.; KATSURA, T. (2020): Pressure dependence of proton incorporation and water solubility in olivine. Journal of Geophysical Research: Solid Earth 125(2), e2019JB018813, https://doi.org/10.1029/2019JB018813

FEI, H.; KATSURA, T. (2020): High water solubility of ringwoodite at mantle transition zone temperature. Earth and Planetary Science Letters 531, 115987, https://doi.org/10.1016/j.epsl.2019.115987

FUKIMOTO, K.; MIYAHARA, M.; SAKAI, T.; OHFUJI, H.; TOMIOKA, N.; KODAMA, Y.; OHTANI, E.; YAMAGUCHI, A. (2020): Back-transformation mechanisms of ringwoodite and majorite in an ordinary chondrite. Meteoritics & Planetary Science 55(8), 1749-1763, https://doi.org/10.1111/maps.13543

GABORIEAU, M.; LAUBIER, M.; BOLFAN-CASANOVA, N.; MCCAMMON, C.; VANTELON, D.; CHUMAKOV, A.I.; SCHIAVI, F.; NEUVILLE, D.; VENUGOPAL, S. (2020): $Fe^{3+}/\Sigma Fe$ of olivine-hosted melt inclusions inferred from Mössbauer and XANES spectroscopy. Chemical Geology 547, 119646, https://doi.org/10.1016/j.chemgeo.2020.119646

GATTACCECA, J.; MCCUBBIN, F.; BOUVIER, A.; GROSSMAN, J. (2020): The Meteoritical Bulletin, No. 107 Meteoritics & Planetary Science, 55(2), 460-462, https://doi.org/10.1111/maps.13440

GATTACCECA, J.; MCCUBBIN, F.; BOUVIER, A.; GROSSMAN, J. (2020): The Meteoritical Bulletin, No. 108. Meteoritics & Planetary Science, 55(5), 1146-1150, https://doi.org/10.1111/maps.13493

GILLMANN, C.; GOLABEK, G.J.; RAYMOND, S.; TACKLEY, P.J.; SCHÖNBÄCHLER, M.; DEHANT, V.; DEBAILLE, V. (2020): Dry late accretion inferred from Venus's coupled atmosphere and internal evolution. Nature Geoscience 13, 265-269, https://doi.org/10.1038/s41561-020-0561-x

GLAZYRIN, K.; KHANDARKHAEVA, S.; DUBROVINSKY, L.; SPRUNG, M. (2020): Revisiting spin-state crossover in (MgFe) O by means of high-resolution x-ray diffraction from a single crystal. Physical Review B 101, 184203, https://doi.org/10.1103/PhysRevB.101.184203

GORELOVA, L.A.; PAKHOMOVA, A.S.; KRZHIZHANOVSKAYA, M.G.; WINKLER, B.; KRIVOVICHEV, S.V.; DUBROVINSKY, L. (2020): Pressure-induced phase transitions in danburitet-type borosilicates. The Journal of Physical Chemistry C 124, 26048-26061, https://doi.org/10.1021/acs.jpcc.0c08616

GORELOVA, L.A.; PAKHOMOVA, A.; KRIVOVICHEV, S.V.; KASATKIN, A.V.; DUBROVINSKY, L. (2020): Compressibility of hingganite-(Y): high-pressure single crystal X-ray diffraction study. Physics and Chemistry of Minerals 47, 22, https://doi.org/10.1007/s00269-020-01090-x

GRUENINGER, H.; ZHAODONG, L.; BRAUCKMANN, J.O.; HONGZHAN, F.; BOFFA BALLARAN, T.; MARTIN, T.; SIEGEL, R.; KENTGENS, A.P.M.; FROST, D.J.; SENKER, J. (2020): Hydroxyl defects and oxide vacancies within ringwoodite-toward understanding the defect chemistry of spinel-type oxides. Journal of Physical Chemistry C 124, 12001-12009

GUO, H.; LI, W.-Y.; NAN, X.; HUANG, F. (2020): Experimental evidence for light Ba isotopes favouring aqueous fluids over silicate melts. Geochemical Perspective Letters 16, 6-11, https://doi.org/10.7185/geochemlet.2036

HECK, P.R.; GREER, J.; BOESENBERG, J.S.; BOUVIER, A.; CAFFEE, M.W.; CASSATA, W.S.; CORRIGAN C.; DAVIS, A.M.; DAVIS, D.W.; FRIES, M.; HANKEY, M.; JENNISKENS, P.; SCHMITT-KOPPLIN, P.; SHEU, S.; TRAPPITSCH, R.; VELBEL, M.; WELLER, B.; WELTEN, K.; YIN, Q.-Z.; SANBORN, M.E.; ZIEGLER, K.; ROWLAND, D.; VEROSUB, K.L.; ZHOU, Q.; LIU, Y.; TANG, G.; LI, Q.; LI, X.; ZAJACZ, Z. (2020): The fall, recovery and classification of the Hamburg, Michigan H4 chondrite. Meteoritics & Planetary Science 55(11), 2341-2359, https://doi.org/10.1111/maps.13584

HIRAO, N.; KAWAGUCHI-IMADA, S.; HIROSE, K.; SHIMIZU, K.; OHTANI, E.; OHISHI, Y. (2020): New developments in high-pressure X-ray diffraction beamline for diamond anvil cell at SPring-8. Matter and Radiation at Extremes 5, 018403, https://doi.org/10.1063/1.5126038

HSIEH, W.P.; ISHII, T.; CHAO, K.H.; TSUCHIYA, J.; DESCHAMPS, F.; OHTANI, E. (2020): Spin transition of iron in δ-(Al, Fe) OOH induces thermal anomalies in Earth's lower mantle. Geophysical Research Letters 47(4), e2020GL087036, https://doi.org/10.1029/2020GL087036

HUANG, Y.; NAKATANI, T.; NAKAMURA, M.; MCCAMMON, C. (2020): Experimental constraint on grain-scale fluid connectivity in subduction zones. Earth and Planetary Science Letters 105, 116610, https://doi.org/10.1016/j.epsl.2020.116610

HUECK, M.; WEMMER, K.; BASEI, M.A.S.; PHILIPP, R.P.; ORIOLO, S.; HEIDELBACH, F.; OYHANTÇABAL, P.; SIEGESMUND, S. (2020): Dating recurrent shear zone activity and the transition from ductile to brittle deformation: White mica geochronology applied to the Neoproterozoic Dom Feliciano Belt in South Brazil. Journal of Structural Geology 141, 104199, https://doi.org/10.1016/j.jsg.2020.104199

ISHII, T.; MIYAJIMA, N.; SINMYO, R.; KOJITANI, H.; MORI, D.; INAGUMA, Y.; AKAOGI, M. (2020): Discovery of new-structured post-spinel $MgFe_2O_4$: Crystal structure and high-pressure phase relations. Geophysical Research Letters, 47(6), e2020GL087490, https://doi.org/10.1029/2020GL087490

ISKRINA, A.V.; SPIVAK, A.V.; BOBROV, A.V.; EREMIN, N.N.; MARCHENKO, E.I.; DUBROVINSKY, L. (2020): Synthesis and crystal structures of new high-pressure phases $CaAl_2O_4$ and $Ca_2Al_6O_{11}$. Lithos 374-375, 105689, https://doi.org/10.1016/j.lithos.2020.105689

ISRAEL, C.; BOYET, M.; DOUCELANCE, R.; BONNAND, P.; FROSSARD, P.; AUCLAIR, D.; BOUVIER, A. (2020): Formation of the Ce-Nd mantle array: Crustal extraction vs. recycling by subduction. Earth and Planetary Science Letters 530, 115941, https://doi.org/10.1016/j.epsl.2019.115941

JENNINGS, E.S.; JACOBSON, S.A.; RUBIE, D.C.; NAKAJIMA, Y.; VOGEL, A.K.; ROSE-WESTON, L.A.; FROST, D.J. (2020): Metal-silicate partitioning of W and Mo and the role of carbon in controlling their abundances in the Bulk Silicate Earth. Geochimica et Cosmochimica Acta 293, 40-69, https://doi.org/10.1016/j.gca.2020.09.035

JOURNAUX, B.; BROWN, J.M.; PAKHOMOVA, A.; COLLINGS, I.E.; PETITGIRARD, S.; ESPINOZA, P.; BOFFA BALLARAN, T.; VANCE, S.D.; OTT, J.; COVA, F.; GARBARINO, G.; HANFLAND, M. (2020): Holistic approach for studying planetary hydrospheres: Gibbs representation of ices thermodynamics, elasticity, and the water phase diagram to 2,300 MPa. Journal of Geophysical Research – Planets 125, e2019JE006176, https://doi.org/10.1029/2019JE006176

KATSURA, T.; FEI, H. (2020): Asthenosphere dynamics based on the H_2O dependence of element diffusivity in olivine. National Science Review, nwaa278, https://doi.org/10.1093/nsr/nwaa278

KIM, H.-I.; LEE, S.; KIM, E.J.; LEE, S.K. (2020): Structure and disorder in Pb-Na metasilicate ($PbO:Na_2O:2SiO_2$) glasses: A view from high-resolution ^{17}O solid-state NMR. Journal of the American Ceramic Society 104(3), 1318-1330, https://doi.org/10.1111/jace.17536

KLUMBACH, S.; KEPPLER, H. (2020): Electrical conductivity of HCl-bearing aqueous fluids to 700 °C and 1 GPa. Contributions to Mineralogy and Petrology 175, 114, https://doi.org/10.1007/s00410-020-01754-5

KOEMETS, E.; YUAN, L.; BYKOVA, E.; GLAZYRIN, K.; OHTANI, E.; DUBROVINSKY, L. (2020): Interaction between FeOOH and NaCl at extreme conditions: synthesis of novel $Na_2FeCl_4OH_X$ compound. Minerals 10(1), 51, https://doi.org/10.3390/min10010051

KOEMETS, I.; SATTA, N.; MARQUARDT, H.; KISEEVA, E.S.; KURNOSOV, A.; STACHEL, T.; HARRIS, J.W.; DUBROVINSKY, L. (2020): Elastic properties of majoritic garnet inclusions in diamonds and the seismic signature of pyroxenites in the Earth's upper mantle. American Mineralogist 105, 984-991, https://doi.org/10.2138/am-2020-7136CCBY

KONYASHIN, I.; FROST, D.J.; SIDORENKO, D.; OREKHOV, A.; OBRAZTSOVA, E.A.; SVIRIDOVA, T.A. (2020): Nanocrystals of face-centred cubic carbon, i-carbon and diamond obtained by direct conversion of graphite at high temperatures and static ultra-high pressures. Diamond and Related Materials 109, 108017, https://doi.org/10.1016/j.diamond.2020.108017

KUDRYAVTSEV, D.A.; FEDOTENKO, T.M.; KOEMETS, E.; KHANDARKHAEVA, S.; KUTCHEROV, V.; DUBROVINSKY, L. (2020): Raman spectroscopy study on chemical transformations of propane at high temperatures and high pressures. Scientific Reports 10, 1483, https://doi.org/10.1038/s41598-020-58520-7

LANIEL, D.; WINKLER, B.; BYKOVA, E.; FEDOTENKO, T.; CHARITON, S.; MILMAN, V.; BYKOV, M.; PRAKAPENKA, V.; DUBROVINSKY, L.; DUBROVINSKAIA, N. (2020): Novel sulfur hydrides synthesized at extreme conditions. Phys Rev B 102, 134109, https://doi.org/10.1103/PhysRevB.102.134109

LANIEL, D.; WINKLER, B.; FEDOTENKO, T.; PAKHOMOVA, A.; CHARITON, S.; MILMAN, V.; PRAKAPENKA, V.; DUBROVINSKY, L.; DUBROVINSKAIA, N. (2020): High-pressure polymeric nitrogen allotrope with the black phosphorus structure. Physical Review Letters 124, 216001, https://doi.org/10.1103/PhysRevLett.124.216001

LIU, H.; YANG, X. (2020): Solubility of hydroxyl groups in pyroxenes: Effect of oxygen fugacity at 0.2-3 GPa and 800-1200 °C. Geochimica et Cosmochimica Acta 286, 355-379

LIU, X.; SUI, Z.; FEI, H.; YAN, W.; MA, Y.; YE, Y. (2020): IR features of hydrous Mg_2SiO_4-ringwoodite, unannealed and annealed at 200-600 °C and 1 atm, with implications to hydrogen defects and water-coupled cation disorder. Minerals 10(6), 499, https://doi.org/10.3390/min10060499

LIU, Z.; MCCAMMON, C.; WANG, B.; DUBROVINSKY, L.; ISHII, T.; BONDAR, D.; NAKAJIMA, A.; TANGE, Y.; HIGO, Y.; CUI, T.; LIU, B.; KATSURA, T. (2020): Stability and solubility of the $FeAlO_3$ component in bridgmanite at uppermost lower mantle conditions. Journal of Geophysical Research: Solid Earth 125(2), e2019JB018447, https://doi.org/10.1029/2019JB018447

MARZOTTO, E.; HSIEH, W.-P.; ISHII, T.; CHAO, K.-H.; GOLABEK, G.J.; THIELMANN, M.; OHTANI, E. (2020): Effect of water on lattice thermal conductivity and its implications for the thermal evolution of descending slabs. Geophysical Research Letters 47(13), e2020GL087607, https://doi.org/10.1029/2020GL087607

MASHINO, I.; MURAKAMI, M.; MIYAJIMA, N.; PETITGIRARD, S. (2020): Experimental evidence for silica-enriched Earth's lower mantle with ferrous iron dominant bridgmanite. Proc Natl Acad Sci U S A, 117(45), 27899-27905, https://doi.org/10.1073/pnas.1917096117

MATJUSCHKIN, V.; WOODLAND, A.B.; FROST, D.J.; YAXLEY, G.M. (2020): Reduced methane-bearing fluids as a source for diamond. Scientific Reports 10, 6961, https://doi.org/10.1038/s41598-020-63518-2

MCCAMMON, C.; BUREAU, H.; CLEAVES, H.J.; COTTRELL, E.; DORFMAN, S.M.; KELLOGG, L.H.; LI, J.; MIKHAIL, S.; MOUSSALLAM, Y.; SANLOUP, C.; THOMSON, A.; BROVARONE, A.V. (2020): Deep Earth carbon reactions through time and space. American Mineralogist 105, 22-27, https://doi.org/10.2138/am-2020-6888CCBY

MEIER, T.; TRYBEL, F.; CRINITI, G.; LANIEL, D.; KHANDARKHAEVA, S.; KOEMETS, E.; FEDOTENKO, T.; GLAZYRIN, K.; HANFLAND, M.; BYKOV, M.; STEINLE-NEUMANN, G.; DUBROVINSKAIA, N.; DUBROVINSKY, L. (2020): Proton mobility in metallic copper hydride from high-pressure nuclear magnetic resonance. Physical Review B 102, 165109, https://doi.org/10.1103/PhysRevB.102.165109

MEIER, T.; LANIEL, D.; PENA-ALVAREZ, M.; TRYBEL, F.; KHANDARKHAEVA, S.; KRUPP, A.; JACOBS, J.; DUBROVINSKAIA, N.; DUBROVINSKY, L. (2020): Nuclear spin coupling crossover in dense molecular hydrogen. Nature Communications 11, 6334, https://doi.org/10.1038/s41467-020-19927-y

MENDEZ, A.S.J.; MARQUARDT, H.; HUSBAND, R.J.; SCHWARK, I.; MAINBERGER, J.; GLAZYRIN, K.; KURNOSOV, A.; OTZEN, C.; SATTA, N.; BEDNARCIK, J.; LIERMANN, H.P. (2020): A resistively-heated dynamic diamond anvil cell (RHdDAC) for fast compression X-ray diffraction experiments at high temperatures. Review of Scientific Instruments 91, 073906, https://doi.org/10.1063/5.0007557

MEZGER, K.; SCHÖNBÄCHLER, M.; BOUVIER, A. (2020): Accretion of the Earth – missing components? Space Sciences Revies 216, 27, https://doi.org/10.1007/s11214-020-00649-y

MILLOT, M.; ZHANG, S.; FRATANDUONO, D.; COPPARI, F.; HAMEL, S.; MILITZER, B.; SIMONOVA, D.; SHCHEKA, S.; DUBROVINSKAIA, N.; DUBROVINSKY, L.; EGGERT, J.H. (2020): Recreating giants impacts in the laboratory: Shock compression of bridgmanite to 14 mbar. Geophysical Research Letters 47(4), e2019GL085476, https://doi.org/10.1029/2019GL085476

MORBIDELLI, A.; LIBOUREL, G.; PALME, H.; JACOBSON, S.; RUBIE, D. (2020): Sub-solar Al/Si and Mg/Si ratios of the enstatite chondrites reveal planetesimal formation during early condensation in the protoplanetary disk. Earth and Planetary Science Letters 538, 116220, https://doi.org/10.1016/j.epsl.2020.116220

MOROZOVA, N.V.; KOROBEINIKOV, I.V.; ABROSIMOV, N.V.; OVSYANNIKOV, S.V. (2020): Controlling the thermoelectric power of silicon-germanium alloys in different crystalline phases by applying high pressure. CrystEngComm 22, 5416-5435, https://doi.org/10.1039/D0CE00672F

MOROZOVA, N.V.; KOROBEINIKOV, I.V.; KUROCHKA, K.V.; OVSYANNIKOV, S.V. (2020): Colossal variations in the thermopower and *n-p* conductivity switching in topological tellurides under pressure. Journal of Applied Physics 128, 245902, https://doi.org/10.1063/5.0031818

NISHIDA, K.; XIE, L.; KIM, E.J.; KATSURA, T. (2020): A strip-type boron-doped diamond heater synthesized by chemical vapor deposition for large volume presses. Review of Scientific Instruments 91, 095108, https://doi.org/10.1063/5.0011742

OHTANI, E. (2020): The role of water in the Earth's mantle. National Science Review 7, 224-232, https://doi.org/10.1093/nsr/nwz071

OVSYANNIKOV, S.V.; BYKOV, M.; MEDVEDEV, S.A.; NAUMOV, P.G.; JESCHE, A.; TSIRLIN, A.A.; BYKOVA, E.; CHUVASHOVA, I.; KARKIN, A.A.; MCCAMMON, C.; DYADKIN, V.; CHERNYSHOV, D.; DUBROVINSKY, L.S. (2020): A room-temperature Verwey-type transition in iron oxide, Fe_5O_6. Angewandte Chemie International Edition 59(14), 5632-5636, https://doi.org/10.1002/anie.201914988

PAKHOMOVA, A.; SIMONOVA, D.; KOEMETS, I.; KOEMETS, E.; APRILIS, G.; BYKOV, M.; GORELOVA, L.; FEDOTENKO, T.; PRAKAPENKA, V.; DUBROVINSKY, L. (2020): Polymorphism of feldspars above 10 GPa. Nature Communications 11, 2721, https://doi.org/10.1038/s41467-020-16547-4

PAPA, S.; PENNACCHIONI, G.; MENEGON, L.; THIELMANN, M. (2020): High-stress creep preceding coseismic rupturing in amphibolite-facies ultramylonites. Earth and Planetary Science Letters 541, 116260, https://doi.org/10.1016/j.epsl.2020.116260

PARMENTER, S.; IVANIC, T.J.; KORHONEN, F.J.; BOUVIER, A.; YAKYMCHUK C. (2020): Metamorphism of the Mougooderra Formation: Implications for Neoarchean tectonics in the western Youanmi Terrane, Yilgarn Craton. Precambrian Research 350, 105862, https://doi.org/10.1016/j.precamres.2020.105862

PUREVJAV, N.; OKUCHI, T.; HOFFMANN, C. (2020): Strong hydrogen bonding in a dense hydrous magnesium silicate discovered by neutron Laue diffraction. International Union of Crystallography Journal 7(3), 370-374, https://doi.org/10.1107/S2052252520003036

ROTTIER, B.; AUDÉTAT, A.; KODERA, P.; LEXA, J. (2020): Origin and evolution of magmas in the porphyry Au-mineralized Javorie volcano (Central Slovakia): Evidence from thermobarometry, melt inclusions, and sulfide inclusions. Journal of Petrology 60, 2449-2482, https://doi.org/10.1093/petrology/egaa014

ROTTIER, B.; AUDÉTAT, A.; KODĚRA, P.; LEXA, J. (2020): Magmatic evolution of the mineralized Štiavnica Volcano (Central Slovakia): Evidence from thermobarometry, melt inclusions, and sulfide inclusions. Journal of Volcanology and Geothermal Research 401, 106967, https://doi.org/10.1016/j.jvolgeores.2020.106967

SCHIERJOTT, J.C.; THIELMANN, M.; ROZEL, A.B.; GOLABEK, G.J.; GERYA, T.V. (2020): Can grain size reduction initiate transform faults? – Insights from a 3D numerical study. Tectonics 39(10), e2019TC005793, https://doi.org/10.1029/2019TC005793

SEMERIKOVA, A.; CHANYSHEV, A.D.; GLAZYRIN, K.; PAKHOMOVA, A.; KURNOSOV, A.; LITASOV, K.; DUBROVINSKY, L.; RASHCHENKO, S. (2020): Face-centered cubic platinum hydride and phase diagram of PtH. European Journal of Inorganic Chemistry 48, 4532-4538, https://doi.org/10.1002/ejic.202000849

SEROVAISKII, A.; DUBROVINKY, L.; KUTCHEROV, V. (2020): Stability of a petroleum-like hydrocarbon mixture at thermobaric conditions that correspond to depths of 50 km. Minerals 10(4), 355, https://doi.org/10.3390/min10040355

SIMONOVA, D.; BYKOVA, E.; BYKOV, M.; KAWAZOE, T.; SIMONOV, A.; DUBROVINSKAIA, N.; DUBROVINSKY, L. (2020): Structural study of δ-AlOOH up to 29 GPa. Minerals 10, 1055-1061, https://doi.org/10.3390/min10121055

SPIEKERMANN, G.; KUPENKO, I.; PETITGIRARD, S.; HARDER, S.; NYROW, A.; WEIS, C.; ALBERS, C.; BIEDERMANN, N.; LIBON, L.; SAHLE, C.; CERANTOLA, V.; GLAZYRIN, K.; KONÔPKOVÁ, Z.; SINMYO, R.; MORGENROTH, W.; SERGUEEV, I.; YAVAS, H.; DUBROVINSKY, L.; TOLAN, M.; STERNEMANN, C.; WILKE, M. (2020): A portable on-axis laser-heating system for near-90° X-ray spectroscopy: application to ferropericlase and iron silicide. Journal of Synchrotron Radiation 27, 414-424, https://doi.org/10.1107/S1600577519017041

TAKAHASHI, S.; OHTANI, E.; SAKAI, T.; KAMADA, S.; OZAWA, S.; SAKAMAKI, T.; MIYAHARA, M.; ITO, Y.; HIRAO, N.; OHISHI, Y. (2020): Phase and melting relations of Fe_3C to 300 GPa and carbon in the core. – In: C.E. MANNING; LIN, J.-F.; MAO, W. (Eds.): Carbon in Earth's interior. AGU Monograph Volume, Chapter 3, 25-36

TANAKA, R.; SAKAMAKI, T.; OHTANI, E.; FUKUI, H.; KAMADA, S.; SUZUKI, A.; TSUTSUI, S.; UCHIYAMA, H.; BARON, A.Q.R. (2020): The sound velocity of wüstite at high pressures: implications for low-velocity anomalies at the base of the lower mantle. Progress in Earth and Planetary Science 7, 23, https://doi.org/10.1186/s40645-020-00333-3

THIELMANN, M.; GOLABEK, G.J.; MARQUARDT, H. (2020): Ferropericlase control of lower mantle rheology: Impact of phase morphology. Geochem. Geophys. Geosyst. 21(2), e2019GC008688, https://doi.org/10.1029/2019GC008688

THIELMANN, M.; SCHMALHOLZ, S.M. (2020): Contributions of grain damage, thermal weakening, and necking to slab detachment. Frontiers in Earth Science 8, 254, https://doi.org/10.3389/feart.2020.00254

VOGEL, S.; BYKOV, M.; BYKOVA, E.; WENDL, S.; KLOß, S.; PAKHOMOVA, A.; DUBROVINSKAIA, N.; DUBROVINSKY, L.; SCHNICK, W. (2020): Nitride Spinel: An ultraincompressible high-pressure form of BeP_2N_4. Angewandte Chemie International Edition 59(7), 2730-2734, https://dx.doi.org/10.1002%2Fanie.201910998

WALTE, N.P.; SOLFERINO, G.F.D.; GOLABEK, G.J.; SILVA SOUZA, D.; BOUVIER, A.: (2020): Two-stage formation of pallasites and the evolution of their parent body revealed by deformation experiments. Earth & Planetary Science Letters, 546, 116419, https://doi.org/10.1016/j.epsl.2020.116419

WITTKOP, C.; BARTLEY, J.K.; KRUEGER, R.; BOUVIER, A.; GEORG, R.B.; KNAEBLE, A.R.; ST. CLAIR, K.; PIPER, C. (2020): Influence of provenance and depositional process on the geochemistry and radiogenic (Hf, Nd, and Sr) isotopic composition of Pleistocene glacial tills, Minnesota USA. Chemical Geology 532, 119390, https://doi.org/10.1016/j.chemgeo.2019.119390

XIE, L.; YONEDA, A.; LIU, Z.; NISHIDA, K.; KATSURA, T. (2020): Boron-doped diamond synthesized by chemical vapor deposition as a heating element in a multi-anvil apparatus. High Pressure Research 40, 369-378, https://doi.org/10.1080/08957959.2020.1789618

XIE, L.; YONEDA, A.; XU, F.; HIGO, Y.; WANG, C.; TANGE, Y.; KING, A.; ANTONANGELI, D.; MORARD, G.; GUIGNOT, N. (2020): Boron-MgO composite as a X-ray transparent pressure medium in the Kawai high pressure apparatus. Review of Scientific Instruments 91, 043903, https://doi.org/10.1063/1.5137740

XIE, L.; YONEDA, A.; MANTHILAKE, G.; YAMAZAKI, D.; HIGO, Y.; TANGE, Y.; GUIGNOT, N.; ANDRAULT, D. (2020): Formation of bridgmanite-enriched layer at the top lower-mantle during Magma Ocean solidification. Nature Communications 11, 548, https://doi.org/10.1038/s41467-019-14071-8

XU, F.; XIE, L.; YONEDA, A.; GUIGNOT, N.; KING, A.; MORARD, G.; ANTONANGELI, D. (2020): TiC-MgO composite: an X-ray transparent and machinable heating element in a multi-anvil high pressure apparatus. High Pressure Research 40(2), 257-266, https://doi.org/10.1080/08957959.2020.1747452

YUAN, L.; STEINLE-NEUMANN, G. (2020): Strong sequestration of hydrogen into the Earth's core during planetary differentiation. Geophysical Research Letters 47, e2020GL088303, https://doi.org/10.1029/2020GL088303

YUAN, L.; STEINLE-NEUMANN, G.; SUZUKI, A. (2020): Structure and density of H_2O-rich Mg_2SiO_4 melts at high pressure from *ab initio* simulations. Journal of Geophysical Research 125, e2020JB020365, https://doi.org/10.1029/2020JB020365

YUSENKO, K.V.; MARTYNOVA, S.; KHANDARKHAEVA, S.; FEDOTENKO, T.; GLAZYRIN, K.; KOEMETS, E.; BYKOV, M.; HANFLAND, M.; SIEMENSMEYER, K.; SMEKHOVA, A.; GROMILOV, S.A.; DUBROVINSKY, L. (2020): High compressibility of synthetic analogous of binary iridium–ruthenium and ternary iridium–osmium–ruthenium minerals. Materialia 14, 100920, https://doi.org/10.1016/j.mtla.2020.100920

YUSENKO, K.; SPEKTOR, K.; KHANDARKHAEVA, S.; FEDOTENKO, T.; PAKHOMOVA, A.; KUPENKO, I.; ROHRBACH, A.; KLEMME, S.; CRICHTON, W.A.; DYACHKOVA, T.; TYUTYUNNIK, A.; ZAINULIN, Y.; DUBROVINSKY, L.; GROMILOV S. (2020): Decomposition of single-source precursors under high-temperature high-pressure to access osmium–platinum refractory alloys. Journal of Alloys and Compounds 813, 152121, https://doi.org/10.1016/j.jallcom.2019.152121

YUSENKO, K.; KHANDARKHAEVA, S.; BYKOV, M.; FEDOTENKO, T.; HANFLAND, M.; SUKHIKH, A.; GROMILOV, S.; DUBROVINSKY, L. (2020): Face-centered cubic refractory alloys prepared from single-source precursors. Materials 13(6), 1418, https://doi.org/10.3390/ma13061418

ZEDGENIZOV, D.; KAGI, H.; OHTANI, E.; TSUJIMORI, T.; KOMATSU, K. (2020): Retrograde phases of former bridgmanite inclusions in superdeep diamonds. Lithos 370-371, 105659, https://doi.org/10.1016/j.lithos.2020.105659

5.2 Publications (submitted, in press)

ADAMS, D.J.; WANG, L.; STEINLE-NEUMANN, G.; PASSERONE, D.; CHURAKOV, S.V.: Anharmonic effects on the dynamics of solid aluminium from ab-initio simulations. Journal of Physics: Condensed Matter (in press), https://doi.org/10.1088/1361-648X/abc972

AUDÉTAT, A.; EDMONDS, M.: Magmatic-hydrothermal fluids. – In: STEELE-MACINNIS, M.; MANNING, C.E. (Eds.): Hydrothermal fluids, Elements (in press)

AUDÉTAT, A.: Comment on Zhang et al.: "Ti-in-quartz thermobarometry and TiO_2 solubility in rhyolitic melts: New experiments and parametrization". Earth and Planetary Science Letters (submitted)

AUDÉTAT, A.: A plea for more skepticism towards fluid inclusions (II): Brine inclusions that homogenize via halite dissolution are commonly the result of postentrapment modifications. Economic Geology (submitted)

BEYER, C.; MYHILL, R.; MARQUARDT, K.; MCCAMMON, C.: A reversed redox gradient in Earth's mantle transition zone. Earth and Planetary Science Letters (submitted)

BLANCHARD, I.; ABEYKOON, S.; RUBIE, D.C.; FROST, D.J.: Sulfur content at sulfide saturation of peridotitic melt at upper mantle conditions. Mineralogical Magazine (in press), https://doi.org/10.2138/am-2021-7649

BLANCHARD, I.; JENNINGS, E.S.; FRANCHI, I.A.; ZHAO, X.; PETITGIRARD, S.; MIYAJIMA, N.; JACOBSON, S.A.; RUBIE, D.C.: The fate of carbon during Earth's core-mantle differentiation. Earth and Planetary Science Letters (submitted)

BLUNDY, J.; MELEKHOVA, E.; ZIBERNA, L.; HUMPHREYS, M.; CERANTOLO, V.; BROOKER, R.; MCCAMMON, C.; PICHAVANT, M.; ULMER, P.: Effect of redox on Fe-Mg-Mn exchange between olivine and melt and an oxybarometer for basalts. Contributions to Mineralogy and Petrology (submitted)

CAMBIONI, S.; JACOBSON, S.; EMSENHUBER, A.; ASPHAUG, E.; RUBIE, D.; GABRIEL, T.; SCHWARTZ, S.; FURFARO, R.: Realistic on-the-fly outcomes of planetary collisions. III. The effect of inefficient accretion on planetary differentiation. Planetary Science Journal (submitted)

CASSETTA, M.; DI GENOVA, D.; GIAROLA, M.; ZANATTA, M.; MARIOTTO, G.: Elastic properties of calcalkaline rhyolite glasses. Scientific Reports (submitted)

CHANG, J.; AUDÉTAT, A.: LA-ICP-MS analysis of crystallized melt inclusions in olivine, plagioclase, apatite and pyroxene: Quantification strategies and effects of post-entrapment modifications. Journal of Petrology (in press)

CHANG, J.; AUDÉTAT, A.; LI, J.-W.: Petrogenesis of hornblendites and related intermediate to felsic rocks in the Early Cretaceous Laiyuan complex, North China Craton: The role of *in situ* reaction-replacement amphibole crystallization. Journal of Petrology (submitted)

CHANG, J.; AUDÉTAT, A.; LI, J.-W.: Tectono-magmatic controls on decratonic gold deposits. Economic Geology (submitted)

CHRISTOFFERSEN, P.A.; WANG, S.-J.; WASYLENKI, L.; GEORG, R.B.; OSINSKI, G.R.; BOUVIER, A.: Stable Cu, Fe, and Ni isotopic systematics of the Offset Dikes and associated rocks at the Sudbury impact structure. Chemical Geology (submitted)

CRINITI, G.; KURNOSOV, A.; BOFFA BALLARAN, T.; FROST, D.J.: Single-crystal elasticity of $MgSiO_3$ bridgmanite to mid-lower mantle pressure. Journal of Geophysical Research: Solid Earth (submitted)

DOMINIJANNI, S.; MCCAMMON, C.A.; OHTANI, E.; IKUTA, D.; SAKAMAKI, T.; ISHII, T.; CRINITI, G.; DUBROVINSKY, L.S.; KHANDARKHAEVA, S.; FEDOTENKO, T.; GLAZYRIN, K.; UCHIYAMA, H.; FUKUI, H.; BARON, A.Q.R.: Sound velocity measurements of B2-Fe-Ni-Si alloy under high pressure by inelastic X-ray scattering: Implications for the composition of Earth's core. Geophysical Research Letter (submitted)

FEI, H.: Water content of the dehydration melting layer in the topmost lower mantle. Geophysical Research Letters (in press)

FEI, H.; LIU, Z.; HUANG, R.; KAMADA, S.; HIRAO, N.; KAWAGUCHI, S.; MCCAMMON, C.; KATSURA, T.: Pressure destabilizes oxygen vacancies in lower mantle bridgmanite. Earth and Planetary Science Letters (submitted)

FEI, Y.; WALTER, M.; BADRO, J.; HIROSE, K.; CAMPBELL, I.; OHTANI, E.: Experimental petrology and geochemistry by the laser-heated diamond anvil cell. Cambridge University Press (submitted)

FROSSARD, P.; GUO, Z.; SPENCER, M.; BOYET, M.; BOUVIER, A.: Temporal evolution of Nd nucleosynthetic anomalies in achondrites: a possible link with chondrule formation. Earth and Planetary Science Letters (submitted)

FUKUSHIMA, R.; TSUJIMORI, T.; MIYAJIMA, N. (2020): Various antiphase domains in garnet-hosted omphacite in low temperature eclogite: A FIB–TEM study on heterogeneous ordering processes. American Mineralogist (accepted)

GOLABEK, G.J.; JUTZI, M.: Modification of icy planetesimals by early thermal evolution and collisions: Constraints for formation time and initial size of comets and small KBOs. Icarus (submitted)

HUANG, R.; BOFFA BALLARAN, T.; MCCAMMON, C.; MIYAJIMA, N.; FROST, D.: The composition of bridgmanite in the Earth's lower mantle. Geochimica et Cosmochimica Acta (submitted)

IKUTA, D.; HIRAO, N.; OHTANI, E.: Earth's inner core may contain a teo phase mixture of Fe-Ni-Si alloy. Science Advances (submitted)

IKUTA, D.; OHTANI, E.; SAKAMAKI, T.; FUKUI, H.; ISHIKAWA, D.; BARON, A.Q.R.: Large density deficit of Earth's core revealed by a multi-megabar primary pressure scale. Nature (submitted)

ISHII, T.; CRINITI, G.; BYKOVA, E.; DUBROVINSKY, L.; KATSURA, T.; ARII, H.; KOJITANI, H.; AKAOGI, M.: High-pressure syntheses and crystal structure analyses of a new low-density $CaFe_2O_4$- related and $CaTi_2O_4$-type $MgAl_2O_4$ phases. American Mineralogist (in press)

ISHII, T.; OHTANI, E.: Dry metastable olivine and slab deformation in a wet subducting slab. Nature Geoscience (submitted)

ISHII, T.; FROST, D.J.; CHANYSHEV, A.; NISHIDA, K.; KIM, E.J.; WANG, B.; BAN, R.; XU, J.; LIU, J.; SU, X.; HIGO, Y.; TANGE, Y.; KATSURA, T.: Consequences of a curved post-garnet boundary for mantle convection. Nature (submitted)

KAMADA, S.; SAKAMAKI, T.; OHTANI, E.: Elasticity at high pressure. Cambridge University Press (submitted)

KATSURA, T.; TANGE, Y.: A plain derivation of Birch-Murnaghan equations of state, and comparison with other equations of state. The Review of High Pressure Science and Technology (in press)

KOEMETS, E.; BYKOV, M.; BYKOVA, E.; CHARITON, S.; APRILIS, G.; FEDOTENKO, T.; CLÉMENT, S.; ROUQUETTE, J.; HAINES, J.; CERANTOLA, V.; GLAZYRIN, K.; ABAKUMOV, A.; ISMAILOVA, L.; MCCAMMON, C.; PRAKAPENKA, V.B.; HANFLAND, M.; LIERMANN, H.-P.; SVITLYK, V.; ROSA, A.; IRIFUNE, T.; LEONOV, I.; PONOMAREVA, A.V.; ABRIKOSOV, I.A.; DUBROVINSKAIA, N.; DUBROVINSKY, L.: Revealing the complex nature of structure and bonding of binary high-pressure compound FeO_2. Physical Review Letters (submitted)

KOEMETS, E.; FEDOTENKO, T.; KHANDARKHAEVA, S.; BYKOV, M.; BYKOVA, E.; THIELMANN, M.; CHARITON, S.; APRILIS, G.; KOEMETS, I.; LIERMANN, H.-P.; HANFLAND, M.; OHTANI, E.; DUBROVINSKAIA, N.; MCCAMMON, C.; DUBROVINSKY, L.: Role of FeOOH in oxygen recycling in early Earth history. Science Advances (submitted)

LA SPINA, G.; ARZILLI, F.; LLEWELLIN, E.W.; BURTON, M.; CLARKE, A.B.: DE' MICHIELI VITTURI, M.; POLACCI, M.; HARTLEY, M.; DI GENOVA, D.; MADER, H.M.: Explosivity of basaltic lava fountains is controlled by magma rheology, ascent rate and outgassing. Earth and Planetary Science Letters (in press)

LI, Y.; AUDÉTAT, A.; LIU, Z.; WANG, F.: Chalcophile element partitioning between Cu-rich sulfide phases and silicate melt and implications for the formation of Earth's continental crust. Geochimica et Cosmochimica Acta (submitted)

LICHTENBERG, T.; DRĄŻKOWSKA, J.; SCHÖNBÄCHLER, M.; GOLABEK, G.J.; HANDS, T.: Bifurcation of planetary building blocks during Solar System formation. Science (submitted)

LIU, Z.; LIU, R.; SHANG, Y.; SHEN, F.; CHEN, L.; HOU, X.; YAO, M.; CUI, T.; LIU, B.; KATSURA, T.: Aluminum solubility in bridgmanite up to 3000 K at the top lower mantle. Geoscience Frontier (in press), https://doi.org/10.1016/j.gsf.2020.04.009

MAH, J.; BRASSER, R.; WOO, J.M.Y.; MOJZSIS, S.J.; BOUVIER, A.: Evidence for an incipient isotopic gradient in the inner region of the solar protoplanetary disc. Icarus (submitted)

MANTHILAKE, G.; MOOKHERJEE, M.; MIYAJIMA, N. (2020): Carbon bearing aqueous fluids in the slab: Insights on the deep carbon cycle. Scientific Reports (submitted)

MCCAMMON, C.: Mössbauer spectroscopy with high spatial resolution: Spotlight on geoscience. – In: YOSHIDA, Y.; LANGOUCHE, G. (Eds.): Modern Mössbauer Spectroscopy: New Challenges Based on Cutting-Edge Techniques, Springer (in press)

MÉNDEZ, A.S.J.; TRYBEL, F.; HUSBAND, R.; STEINLE-NEUMANN, G.; LIERMANN, H.-P.; MARQUARDT, H.: Bulk modulus of H_2O across the ice VII – ice X transition measured by time-resolved X-ray diffraction in dynamic Diamond Anvil Cell experiments. Physical Review B (submitted)

MURAKAMI, M.; GONCHAROV, A.F.; MIYAJIMA, N.; YAMAZAKI, D.; HOLTGREWE, N.: Highly transparent Earth's lowermost mantle: Implications for thermal evolution of the Earth. Science Advances (submitted)

NAKAJIMA, M.; GOLABEK, G.J.; WÜNNEMANN, K.; RUBIE, D.C.; BURGER, C.; MANSKE, L.; MELOSH, H.J.; NIMMO, F.; JACOBSON, S.A.; SCOTT, D.; HULL, S.D.: Scaling laws for the geometry of an impact-induced magma ocean. Earth and Planetary Science Letters (submitted)

OHTANI, E.: Hydration and dehydration in the deep interiors of the Earth and planets. Annual Review of Earth and Planetary Sciences (submitted)

PATRICK, M.; INDARES, A.; MCCAMMON, C.: The influence of ferric iron on phase stability in midpressure anatectic aluminous gneisses. Canadian Mineralogist (submitted)

PEIFFER, S.; KAPPLER, A.; HADERLEIN, S.; SCHMIDT, C.; BYRNE, J.; KLEINDIENST, S.; VOGT, C.; RICHNOW, H.; OBST, M.; ANGENENT, L.; BRYCE, C.; MCCAMMON, C.; PLANER-FRIEDRICH, B.: The role of redox-active metastable phases in how ecosystems respond to hydrological perturbations. Nature Geoscience (submitted)

PISTONE, M.; ZIBERNA, L.; HETÉNYI, G.; SCARPONI, M.; ZANETTI, A.; MÜNTENER, O.: Joint geophysical-petrological modeling on the Ivrea geophysical body (Val Sesia, Italy): Constraints on the continental lower crust. Geochemistry, Geophysics, Geosystems (accepted)

REBAZA, A.M.; POSNER, E.S.; THIELMANN, M.; RUBIE, D.C.; STEINLE-NEUMANN, G.: Experimental determination of carbon diffusion in liquid iron at high pressure. American Mineralogist (in press), https://doi.org/10.2138/am-2021-7644

REYNARD, B.; FELLAH, C.; MCCAMMON, C.: Iron oxidation state in serpentines and chlorites: Overestimation by X-ray Absorption Near Edge Structure (XANES) compared to Mössbauer spectroscopy. American Mineralogist (submitted)

ROBINSON, P.; MCENROE, S.; HARRISON, R.; FABIAN, K.; HEIDELBACH, F.; JACKSON, M.: Lamellar magnetism and exchange bias in billion-year-old metamorphic titanohematite with nanoscale ilmenite exsolution lamellae: III. Atomic-magnetic basis for experimental results. Geophysical Journal International (submitted)

RUSTIONI, G; AUDETAT, A.; KEPPLER; H.: A systematic assessment of the diamond trap method for measuring fluid compositions in high-pressure experiments. American Mineralogist (in press)

RUSTIONI, G; AUDETAT, A.; KEPPLER; H.: The composition of subduction zone fluids and the origin of the trace element enrichment in arc magmas. Contributions to Mineralogy and Petrology (submitted)

SAKAMAKI, T.; OHTANI, E.: High pressure melt. Review in Mineralogy and Geochemistry (submitted)

SAWA, S.; MIYAJIMA, N.; MUTO, J.; NAGAHAMA, H.: Strain-induced partial serpentinization of germanate olivine with a small amount of water. American Mineralogist (accepted)

SCHRÖDER, C.; WAN, M.; BUTLER, I.B.; TAIT, A.; PEIFFER, S.; MCCAMMON, C.A.: Identification of mackinawite and constraints on its electronic configuration using Mössbauer spectroscopy. Minerals (submitted)

STABILE, P.; SICOLA, S.; GIULI, G.; PARIS, E.; CARROLL, M.R.; DEUBENER, J.; DI GENOVA, D.: The effect of iron and alkali on the nanocrystal-free viscosity of volcanic melts: A combined Raman spectroscopy and DSC study. Chemical Geology (in press)

STROHM, C.; APRILIS, G.; KUPENKO, I.; VASIUKOV, D.M.; CERANTOLA, V.; CHUMAKOV, A.; RÜFFER, R.; MCCAMMON, C.; DUBROVINSKY, L.: Fully time resolved synchrotron Mössbauer spectroscopy for pulsed laser heating experiments in diamond anvil cells. Journal of Synchrotron Radiation (submitted)

TOMIOKA, N.; BINDI, L.; OKUCHI, T.; MIYAHARA, M.; IITAKA, T.; LI, Z.: KAWATSU, T.; XIE, X.; PUREVJAV, N.; TANI, R.; KODAMA, Y.: Poirierite, a dense metastable polymorph of magnesium iron silicate in shocked meteorites. Communications Earth & Environment (accepted)

TRYBEL, F.; COSACCHI, M.; MEIER, T.; AXT, V.M.; STEINLE-NEUMANN, G.: Proton dynamics in high-pressure ice-VII from density functional theory. Physical Review B (in press)

YUAN, L.; STEINLE-NEUMANN, G.: The helium elemental and isotopic compositions of the Earth's core based on *ab initio* simulations. Journal of Geophysical Research (submitted)

ZHANG, B.; LIN, Y.; MOSER, D.E.; HAO J.; LIU, Y.; ZHANG, J.; BARKER, I.R.; LI, Q.; SHIEH, S.R.; BOUVIER, A.: Radiogenic Pb remobilization induced by shock-related deformation in early lunar zircons of the Apollo 17 Civet Cat norite. Geochimica et Cosmochimica Acta (submitted)

ZHANG, B.; LIN, Y.; MOSER, D.E.; HAO, J.; LIU, Y.; ZHANG, J.; BARKER, I.R.; LI, Q.; SHIEH, S.R.; BOUVIER, A.: Timing of the lunar Mg-suite magmatism constrained by SIMS U-Pb dating of Apollo Norite 78238. Earth and Planetary Science Letters (submitted)

ZHANG, D.; AUDÉTAT, A.: A plea for more skepticism towards fluid inclusions (I): Postentrapment changes in fluid density and fluid salinity are very common! Economic Geology (submitted)

ZHU, M.-H.; MORBIDELLI, A.; NEUMANN, W.; YIN, Q.-Z.; DAY, J.M.D.; RUBIE, D.C.; ARCHER, G.J.; ARTEMIEVA, N.; BECKER, H.; WÜNNEMANN K.: Vesta reveals common feedstocks of late accretion for the terrestrial planets. Nature Astronomy (submitted)

5.3 Presentations at scientific institutions and at congresses

ABEYKOON, S.; FROST, D.J.; LAURENZ, V.; MIYAJIMA, N.: 04.-08.05.2020, EGU General Assembly 2020, online: "The oxygen content of sulphide inclusions in diamonds and its use as a mantle geothermometer", EGU2020-22685

ARZILLI, F.; LA SPINA, G.; BURTON, M.; POLACCI, M.; LE GALL, N.; HARTLEY, M.; DI GENOVA, D.; CAI, B.; VO, N.; BAMBER, E.; NONNI, S.; ATWOOD, R.C.; LLEWELLIN, E.; LEE, P.: 01.-17.12.2020, AGU Fall Meeting 2020, virtual meeting: "Highly explosive basaltic eruptions: magma fragmentation induced by rapid crystallisation"

BILLEN, M.I.; FILDES, R.A.; THIELMANN, M.: 01.-17.12.2020, AGU Fall Meeting 2020, virtual meeting: "Spatial distribution of deep earthquakes tied to strain-rate variations in slabs"

BONDAR, D.; FEI, H.; WITHERS, A.C.; KATSURA, T.: 01.-17.12.2020, AGU Fall Meeting 2020, virtual meeting: "Rapid-quench multi-anvil technique and its application to water partitioning study"

BOUVIER, A.: 12.05.2020, CRC 235-Emergence of Life series, Ludwig-Maximilians-Universität, München, Germany: "Making Earth, a recipe from meteorites"

CAMBIONI, S.; JACOBSON, S.A.; EMSENHUBER, A.; ASPHAUG, E.; RUBIE, D.C.; GABRIEL, T.S.J.; SCHWARTZ, S.R.; FURFARO, R.: 21.09.-09.10.2020, Europlanet Science Congress 2020, virtual meeting: "The effect of inefficient accretion on planetary differentiation"

CHANYSHEV, A.; ISHII, T.; JEONG KIM, E.; BHAT, S.; BONDAR, D.; FARLA, R.; KATSURA, T.: 17.-18.09.2020, International Workshop on 'Development of multi-anvil technology, and its applications to lower-mantel research and material sciences', Bayerisches Geoinstitut, Bayreuth, Germany, virtual: "Precise determination of akimotoite-bridgmanite ($MgSiO_3$) phase transition boundary at 1250-2085 K in a multi-anvil press with *in situ* X-ray diffraction"

CHANYSHEV, A.; ISHII, T.; BONDAR, D.; BHAT, S.; KIM, E.J.; FARLA, R.J.; LIU, Z.; WANG, L.; NAKAJIMA, A.; YANG, B.; TANG, H.; CHEN, Z.; HIGO, Y.; TANGE, Y.; KATSURA, T.: 01.-17.12.2020, AGU Fall Meeting 2020, virtual meeting: "Reconciliation of the negative pressure dependence of the 660-km discontinuity depth with the bridgmanite forming reactions in MgO-SiO_2 systems"

CHOTALIA, K.; COOPER, G.; CRAMERI, F.; DOMEIER, M.; EAKIN, C.; GRIMA, A.G.; GÜRER, D.; KIRÁLY, Á.; MAGNI, V.; MULYUKOVA, E.; PETERS, K.; ROBERT, B.; SHEPHARD, G.; THIELMANN, M.: 04.-08.05.2020, EGU General Assembly 2020, online: "The trans-disciplinary and community-driven subduction zone initiation (SZI) database", EGU2020-15910

CZEKAY, L.; MIYAJIMA, N.; MCCAMMON, C.A.; FROST, D.J.: 30.11.-02.12.2020, DMG Virtual Poster Session 2020, online: "Aluminous bridgmanite for Al, Si interdiffusion experiments by using a multianvil press. TEM-EDS evaluations"

DOMINIJANNI, S.; MCCAMMON, C.A.; OHTANI, E.; IKUTA, D.; SAKAMAKI, T.; ISHII, T.; CRINITI, G.; DUBROVINSKY, L.S.; KHANDARKHAEVA, S.; FEDOTENKO, T.; GLAZYRIN, K.; UCHIYAMA, H.; FUKUI, H.; BARON, A.Q.R.: 01.-03.03.2020, EMPG XVII 2020 – 17th International Symposium on Experimental Mineralogy, Petrology and Geochemistry, virtual meeting: "Sound velocity measurements of B2-Fe-Ni-Si alloy under high pressure by inelastic X-ray scattering: Implications for the composition of Earth's core"

DOMINIJANNI, S.; MCCAMMON, C.; OHTANI, E.; IKUTA, D.; SAKAMAKI, T.; ISHII, T.: 04.-08.05.2020, EGU General Assembly 2020, online: "Composition of the Earth's inner core from high pressure sound velocity measurements of Fe-Ni-Si alloys", EGU2020-12120

DOMINIJANNI, S.; OHTANI, E.; IKUTA, D.; SAKAMAKI, T.; FUKUI, H.; MCCAMMON, C.; DUBROVINSKY, L.; UCHIYAMA, H.; BARON, A.Q.R.: 12.-16.07.2020, JpGU – AGU Joint Meeting 2020, virtual meeting: "Sound velocity of B2-FeNiSi alloy at high pressure determined with inelastic X-ray scattering: Implications for the composition of the Earth's inner core"

EICHHEIMER, P.; THIELMANN, M.; FUJITA, W.; GOLABEK, G.J.; NAKAMURA, M.; OKUMURA, S.; NAKATANI, T.; KOTTWITZ, M.O.: 04.-08.05.2020, EGU General Assembly 2020, online: "Combined numerical and experimental study of microstructure and permeability in porous granular media", EGU2020-2992

FERREIRA, F.; THIELMANN, M.; MARQUARDT, K.: 04.-08.05.2020, EGU General Assembly 2020, online: "Pressure dependence of olivine grain growth at upper mantle conditions", EGU2020-18346

FILDES, R.A.; BILLEN, M.I.; THIELMANN, M.: 01.-17.12.2020, AGU Fall Meeting 2020, virtual meeting: "Investigating thermal shear instability as a viable failure mechanism for deep earthquakes in high strain-rate regions of subducting slabs"

FROSSARD, P.; BOYET, M.; BOUVIER, A.; HAMMOUDA, T.; BONNAND, P.: 21.-26.06.2020, Goldschmidt Virtual 2020, Honolulu, USA: "Deciphering Nd and Sm isotope composition in chondrites"

FROST, D.; EBERHARD, L.; MELAI, C.; BOFFA BALLARAN, T.; MCCAMMON, C.: 21.-26.06.2020, Goldschmidt Virtual 2020, Honolulu, USA (*keynote*): "The redox state of subduction zones and the implications for the speciation of volatiles"

FROST, D.; HUANG, R.; BOFFA BALLARAN, T.; MCCAMMON, C.: 08.10.2020, Earth and Planets Laboratory, Carnegie Institution for Science, Washington D.C., USA, virtual: "The redox state of the lower mantle"

FUKUSHIMA, R.; TSUJIMORI, T.; MIYAJIMA, N.; AOKI, K.: 12.-16.07.2020, JpGU – AGU Joint Meeting 2020, virtual meeting: "An integrated study of prograde-zoned garnets in low-temperature eclogites: Reappraisal of omphacite antiphase domain geospeedometry and new insights in fluid-induced metamorphic crystal growths"

GOLABEK, G.J.; GÜLCHER, A.J.P.; THIELMANN, M.; TACKLEY, P.J.; BALLMER, M.D.: 04.-08.05.2020, EGU General Assembly 2020, online: "Strain-weakening rheology in Earth's lower mantle: A multi-scale numerical endeavour", EGU2020-11689

GOLABEK, G.; LICHTENBERG, T.; BURN, R.; MEYER, M.; ALIBERT, Y.; GERYA, T.; MORDASINI, C.: 01.06.2020, University of Glasgow, U.K.: "A water budget dichotomy of rocky protoplanets from ^{26}Al-heating"

GOLABEK, G.; LICHTENBERG, T.; BURN, R.; MEYER, M.; ALIBERT, Y.; GERYA, T.; MORDASINI, C.: 03.09.2020, Universität Frankfurt/M., Germany: "A water budget dichotomy of rocky protoplanets from ^{26}Al-heating"

GOLABEK, G.; GÜLCHER, A.J.P.; THIELMANN, M.; BALLMER, M.; TACKLEY, P.J.: 01.-17.12.2020, AGU Fall Meeting 2020, virtual meeting: "Strain-weakening rheology in Earth's lower mantle and its control on mantle convection and tectonics"

HOWARD, C.: 08.-09.12.2020, MLZ User Meeting 2020, virtual: "Cool Pressure: Implementing cryogenic temperatures at the high-pressure instrument SAPHiR"

HUANG, Y.; NAKATANI, T.; NAKAMURA, M.; MCCAMMON, C.: 12.-16.07.2020, JpGU – AGU Joint Meeting 2020, virtual meeting: "Experimental constraint on the fluid connectivity in an olivine–H_2O–CO_2–NaCl system in subduction zones"

IKUTA, D.; OHTANI, E.; FUKUI, H.; UCHIYAMA, Y.; TSUTSUI, T.; BARON, A.Q.R.: 12.-16.07.2020, JpGU – AGU Joint Meeting 2020, virtual meeting: "Sound velocity measurements of Fe-Ni-Si alloys at high pressure and high temperature"

ISHII, T.; OHTANI, E.: 02.-04.12.2020, The 61st High Pressure Conference of Japan, online: "Water partitioning between olivine and its polymorphs and hydrous phases under water-undersaturated conditions", Session number: 2A09

ISHII, T.; MIYAJIMA, N.; KATSURA, T.: 01.-17.12.2020, AGU Fall Meeting 2020, virtual meeting: "Phase relations of basaltic crust determined by simultaneous pressure-temperature generation techniques to 52 GPa and 2000 K using a multi-anvil press with tungsten carbide anvils" Abstract DI005-0015

JUTZI, M.; GOLABEK, G.: 04.-08.05.2020, EGU General Assembly 2020, online: "Modification of cometesimal interiors by early thermal evolution and collisions", EGU2020-5144

KATSURA, T.: 29.-31.01.2020, DESY Photon Science Users' Meeting, SATELLITE WORKSHOP 'High-pressure Science in the Large Volume Press at P61B', DESY Hamburg, Germany: "*In situ* X-ray observation in a large-volume press with high flux X-rays under ultra-high-pressure and ultra-high-temperature conditions"

KATSURA, T.; ISHII, T.; MIYAJIMA, N.; PETITGIRARD, S.: 17.-18.09.2020, International Workshop on 'Development of multi-anvil technology, and its applications to lower-mantel research and material sciences', Bayerisches Geoinstitut, Bayreuth, Germany, virtual: "No hydrous phases in the lower mantle: Reductive breakdown of phase Egg by formation of Fe, Al-bearing bridgmanite"

KATSURA, T.: 05.-06.11.2020: Satellite Workshop on Scientific Instrument Proposals for Extreme Pressures and Temperatures Research at PETRA IV, virtual: "Towards advanced *in situ* X-ray diffraction experiments by combination of a multi-anvil press and high-density monochromatic X-ray beams"

KATSURA, T.: 18.11.2020, 25.11.2020, 02.12.2020, 09.12.2020, 16.12.2020, 23.12.2020, Graduate School of Science, Tohoku University (invited lecture): "Physics and Chemistry in the Earth's Interior"

KATSURA, T.; ISHII, T.; FROST, D.J.; CHANYSHEV, A.; NISHIDA, K.; KIM, E.J.; WANG, B.; BAN, R.; XU, J.; LIU, J.; SU, X.; HIGO, Y.; TANGE, Y.: 01.-17.12.2020, AGU Fall Meeting 2020, virtual meeting: "A non-linear Clapeyron slope of the post-garnet transition determined by advanced multianvil and *in situ* X-ray observation technologies, and its multiple effects on mantle dynamics in various tectonic settings"

KATSURA, T.: 11.12.2020, Tips for ERC Advanced Grant Application for Japanese Scientists, The EUROPEAN RESEARCH COUNCIL (ERC) with EURAXESS Japan, virtual: "Advancing your research career in Europe"

KEPPLER, H.: 22.09.2020, MLZ meeting, Garching, Germany: "The instrument SAPHiR"

KIM, E.J.; FEI, H.; NISHIDA, K.; KATSURA, T.: 17.-18.09.2020, International Workshop on 'Development of multi-anvil technology, and its applications to lower-mantel research and material sciences', Bayerisches Geoinstitut, Bayreuth, Germany, virtual: "Chemistry of Fe^{2+}-rich bridgmanite, periclase and CF-structure $MgAl_2O_4$ at 27 GPa: Preliminary results"

LA SPINA, G.; ARZILLI, F.; LLEWELLIN, E.; BURTON, M.; CLARKE, A.B.; DE' MICHIELI VITTURI, M.; POLACCI, M.; DI GENOVA, D.; HARTLEY, M.: 01.-17.12.2020, AGU Fall Meeting 2020, virtual meeting: "Role of rheology, ascent rate and outgassing on fragmentation: implications for basaltic lava fountains", Abstract 783690

LANGHAMMER, D.; DI GENOVA, D.; STEINLE-NEUMANN, G.: 20.-23.10.2020, 732. WE-Heraeus-Seminar on 'Matter under Extreme Conditions', virtual: "A two component model for silicate melt viscosity"

LIBON, L.; SPIEKERMANN, G.; SIEBER, M.; KAA, J.; APPEL, K.; DOMINIJANNI, S.; MORGENROTH, W.; ALBERS, C.; BIEDERMANN, N.; MCCAMMON, C.; RODDATIS, V.; HENNET, L.; WILKE, M.: 30.11.-02.12.2020, DMG Virtual Poster Session 2020, online: "Experimental investigation of the phase stability in the bridgmanite-magnesite system"

MARZOTTO, E.; THIELMANN, M.; GOLABEK, G.J.: 04.-08.05.2020, EGU General Assembly 2020, online: "Effect of grid resolution on tectonic regimes in global-scale convection models", EGU2020-4483

MARZOTTO, E.; HSIEH, W.P.; ISHII, T.; CHAO, K.H.; GOLABEK, G.J.; THIELMANN, M.; OHTANI, E.: 03.09.2020, Harro Schmeling Symposium, Frankfurt/M., Germany: "Effect of water on lattice thermal conductivity of ringwoodite and its implications for the thermal evolution of descending slabs"

MCCAMMON, C.; WEI, Q.; GILDER, S.: 04.-08.05.2020, EGU General Assembly 2020, online: "Magnetic properties of synthetic taenite at high pressure", EGU2020-5047

MCCAMMON, C.; WEI, Q.; GILDER, S.: 21.-26.06.2020, Goldschmidt Virtual 2020, Honolulu, USA: "Magnetism in iron-nickel alloys"

MCCAMMON, C.A.; DOMINIJANNI, S.; DUBROVINSKY, L.; MIYAJIMA, N.; KOEMETS, E.; FROST, D.J.: 12.-16.07.2020, JpGU – AGU Joint Meeting 2020, virtual meeting: "Developing a laboratory technique to probe volatile transport in the deep mantle"

MCCAMMON, C.: 08.09.2020, 5th Meeting of FOR2125/2, Frankfurt/M,. Germany: "Oxygen fugacity meets carbonates: Update from project 6"

MCCAMMON, C.: 19.10.2020, EGU Webinar 'Funding opportunities: European Research Council grants', online: "Perspectives from a former PE10 panel chair"

MCCAMMON, C.: 26.11.2020, EURAXESS Webinar 'Applying for an ERC grant', online: "Advice from an evaluator's perspective"

MCCAMMON, C.; SZLACHTA, V.; BYRNE, J.M.: 01.-17.12.2020, AGU Fall Meeting 2020, virtual meeting: "What can really old red and white rocks tell us about breathing air on our world a long time ago?"

MEIER, T.; TRYBEL, F.; CRINITI, G.; LANIEL, D.; KHANDARKHAEVA, S.; KOEMETS, E.; FEDOTENKO, T.; GLAZYRIN, K.; HANFLAND, M.; BYKOV, M.; STEINLE-NEUMANN, G.; DUBROVINSKAIA, N.; DUBROVINSKY, L.: 06.-11.09.2020, 58th European High Pressure Research Group International Conference, Teneriffe, Spain: "Electronic properties of hydrogen sublattices in transition metal hydrides"

MEIER, T.; TRYBEL, F.; KHANDARKHAEVA, S.; SIMONOVA, D.; KOEMETS, J.; KURNOSOV, A.; ISHII, I.; DUBROVINSKAIA, N.; DUBROVINSKY, L.: 17.-18.09.2020, International Workshop on 'Development of multi-anvil technology, and its applications to lower-mantel research and material sciences', Bayerisches Geoinstitut, Bayreuth, Germany, virtual: "Killing three birds with one stone: Structural symmetrisation, hydrogen mobility and electron spin transition in (Al,Fe)OOH observed with nuclear magnetic resonance spectroscopy"

MELAI, C.; FROST, D.; BALLARAN, T.B.; MCCAMMON, C.; MARQUARDT, K.: 12.-16.07.2020, JpGU – AGU Joint Meeting 2020, virtual meeting: "The conditions of sub-lithospheric diamond formation constrained from ferric iron-rich exsolution in ferropericlase inclusions in diamond"

MIYAJIMA, N.; BUCHEN, J.; KAWAZOE, T.: 12.-16.07.2020, JpGU – AGU Joint Meeting 2020, virtual meeting: "Twinning in wadsleyite"

MIYAJIMA, N.: 01.-03.03.2020, EMPG XVII 2020 – 17th International Symposium on Experimental Mineralogy, Petrology and Geochemistry, virtual meeting: "Al, Si interdiffusion in iron-free majoritic garnet: TEM of a polycrystalline diffusion couple"

NATHAN, G.; JACOBSON, S.A.; RUBIE, D.C.: 01.-17.12.2020, AGU Fall Meeting 2020, virtual meeting: "Isotopic fractionation during multi-stage core formation", Abstract 716560

OHTANI, E.; HSIEH, W.-P.; ISHII, T.; OHIRA, I.: 12.-16.07.2020, JpGU – AGU Joint Meeting 2020, virtual meeting: "Effect of spin transition of iron in physical properties of hydrous phase δ-(Al,Fe)OOH under the lower mantle conditions"

OVSYANNIKOV, S.: 31.08.-04.09.2021, IUCr/DGK Summer School 2020 'Introduction to Novel Methods of Atomic and Electronic Structure Studies at High Pressures', Bayreuth, Germany: "Using a single-crystal X-ray diffraction in materials science"

POSNER, E.S.; STEINLE-NEUMANN.: 20.-23.10.2020, 732. WE-Heraeus-Seminar on 'Matter under Extreme Conditions', virtual: "Atomic-scale insight into the material properties of liquid iron alloys as a function of pressure, temperature, and composition"

PUREVJAV, N.; TOMIOKA, N.; YAMASHITA, S.; LIN, J.-F.; SHINODA, K.; KOBAYASHI, S.; SHIMIZU, K.; HOFFMANN, C.; ITO, M.; FU, S.; GU, J.; BI, W.; OKUCHI, T.: 02.-04.12.2020, The 61st High Pressure Conference of Japan, online: "Hydrogen incorporation mechanism in bridgmanite"

SATTA, N.: 01.-17.12.2020, AGU Fall Meeting 2020, virtual meeting: "Elastic softening driven by hydrogen disorder in δ-(Al,Fe)OOH"

SAWA, S.; MIYAJIMA, N.; MUTO, J.; NAGAHAMA, H.: 02.-04.12.2020, The 61st High Pressure Conference of Japan, online: "Strain-induced partial serpentinization of germanate olivine under unsaturated, limited amount of water"

STEINLE-NEUMANN, G.; POSNER, E.S.: 12.-16.07.2020, JpGU – AGU Joint Meeting 2020, virtual meeting: "Mass transport and structural properties of liquid iron alloys at high pressure from *ab-initio* simulations", Abstract SIT31-09

STEINLE-NEUMANN, G.; YUAN, L.; SUZUKI, A.: 12.-16.07.2020, JpGU – AGU Joint Meeting 2020, virtual meeting: "Structure and density of H_2O-rich Mg_2SiO_4 melts at high pressure from *ab initio* simulations", Abstract SIT24-P02

STEINLE-NEUMANN, G.; TRYBEL, F.; LANGHAMMER, D.: 20.-23.10.2020, 732. WE-Heraeus-Seminar on 'Matter under Extreme Conditions', virtual: "Phase transitions in silicates at conditions of super-Earth interiors"

THIELMANN, M.; GOLABEK, G.; MARQUARDT, H.: 28.04.2020, Structural Geology Seminar, University of Vienna, Austria (online): "From morphology to rheology: Impact of weak phase alignment on effective rock viscosity"

THIELMANN, M.; DURETZ, T.: 04.-08.05.2020, EGU General Assembly 2020, online: "Going from stable creep to aseismic slow slip events in the ductile realm", EGU2020-18554

THIELMANN, M.; DURETZ, T.: 09.07.2020, Endogenous Geology Seminar, LMU München, Germany (online): "Fast ductile shear zone formation due to microstructural and thermal damage"

THIELMANN, M.; GOLABEK, G.; MARQUARDT, H.: 01.-17.12.2020, AGU Fall Meeting 2020, virtual meeting: "Ferropericlase control of lower mantle rheology: Impact of phase morphology"

WITTKOP, C.; BARTLEY, J.K.; KRUEGER, R.; BOUVIER, A.; GEORG, R.B.; KNAEBLE, A.R.; ST. CLAIR, K.; PIPER, C. BRECKENRIDGE, A.: 17.-19.05.2020, 54th Annual Meeting of the Geological Society of America, North-Central Section, virtual meeting: "Geochemical and isotopic tools for Pleistocene sediment provenance in the North American Midcontinent, North-Central", virtual poster, 31-11

YAMASHITA, K.; KUBO, T.; TANGE, Y.; HIGO, Y.; MIYAJIMA, N.: 12.-16.07.2020, JpGU – AGU Joint Meeting 2020, virtual meeting: "Mechanisms of the post-perovskite transformation in $NaNiF_3$ and implications for seismic anisotropy in the D" region"

YAO, J.; STEINLE-NEUMANN, G.; FROST, D.J.: 20.-23.10.2020, 732. WE-Heraeus-Seminar on 'Matter under Extreme Conditions', virtual: "Melting phase relations in $MgSiO_3$-SiO_2 system at 24 GPa: implications for melting in Earth's lower mantle"

YUAN, L.; STEINLE-NEUMANN, G.: 20.-23.10.2020, 732. WE-Heraeus-Seminar on 'Matter under Extreme Conditions', virtual: "Hydrogen in the Earth's core"

YUTANI, T.; CONDAMINE, P.; HIRANO, N.; MCCAMMON, C.; FROST, D.: 21.-26.06.2020, Goldschmidt Virtual 2020, Honolulu, USA: "An experimental approach to a multiple saturation point of a "direct ascent" petit-spot basalt"

5.4 Lectures and seminars at Bayerisches Geoinstitut

ADELEKE, Adebayo, University of Saskatchewan, Department of Physics and Engineering Physics, Saskatoon, Canada (online): "Structures, structural transformation and properties of selected elemental and extended solids", 01.10.2020

BINDI, Luca, Università degli Studi di Firenze, Dipartimento di Scienze della Terra, Firenze, Italy (online): "Once upon a time in Kamchatka: the discovery of the first natural quasicrystal", 22.10.2020

BUITER, Susanne, RWTH Aachen, Fachgruppe für Geowissenschaften und Geographie, Aachen, Germany (online): "How mountains become rifts: Numerical experiments investigating the impact of collisional inheritance on rifted margin architecture", 26.11.2020

DI GENOVA, Danilo, Bayerisches Geoinstitut, Bayreuth, Germany (online): "The impact of nanocrystal formation on magma viscosity and degassing: Implications for the style of volcanic eruptions", 23.07.2020

GERYA, Taras, ETH Zurich, Institute of Geophysics, Zurich, Switzerland (online): "Biogeodynamics: Influence of plate tectonics on life evolution and biodiversity", 16.07.2020

HUANG, Shengxuan, Peking University, School of Earth and Space Sciences, Beijing, P.R. China (online): "Iron carbonitrides and oxides at extreme conditions: Implications for Earth's and planetary deep interiors", 19.11.2020

KELLER, Tobias, University of Glasgow, School of Geographical and Earth Sciences, Glasgow, U.K. (online): "A little goes a long way: the role of volatiles in volcanism", 08.06.2020

KUBIK, Edith, Institut de Physique du Globe de Paris, France (online): "Investigating the Earth's volatile delivery with siderophile and volatile elements", 26.10.2020

MARZOTTO, Enrico, Bayerisches Geoinstitut, Bayreuth, Germany (online): "Effect of water on lattice thermal conductivity of ringwoodite and its implications for the thermal evolution of descending slabs", 09.07.2020

MEIER, Thomas, Bayerisches Geoinstitut, Bayreuth, Germany: "Think Megabars: 10 years of development and applications of high pressure NMR in diamond anvil cells", 06.10.2020

NISHIHARA, Yu, Ehime University, Geodynamics Research Center, Matsuyama, Japan (online): "Pressure effect on temperature measurements using thermocouples and its geophysical impact", 10.08.2020

SOLOMATOVA, Natalia: ENS Lyon, Laboratoire de Géologie de Lyon: Terre, Planète, Environnement, Lyon, France: "The fate of carbon after the moon-forming impact", 16.01.2020

SYVERSON, Drew, Yale University, Department of Earth and Planetary Sciences, New Haven, USA (online): "Metal cycling at mid-ocean ridge hydrothermal systems", 18.06.2020

TSUBOKAWA, Yumiko, Ehime University, Geodynamics Research Center, Matsuyama, Japan: "Dislocation creep of dry orthoenstatite aggregates under high P-T conditions: implications for the variety in strength of oceanic plates", 27.02.2020

WANG, Shui-Jiong, China University of Geosciences, Beijing, P.R. China (online): "Nickel isotopic evidence for late-stage accretion of Mercury-like differentiated planetary embryos", 12.11.2020

WILSON, Alfred: University College London, Department of Earth Sciences, London, U.K.: "Calculating entropy of silicate liquids from first principles: Thermodynamic properties of a terrestrial magma ocean", 23.01.2020

XIE, Longjian, Bayerisches Geoinstitut, Bayreuth, Germany (online): "Understanding the Earth's evolution by measurements on physicochemical properties of melts", 05.11.2020

5.5 Conference organization

20.-21.01.2020, Softskill-course for women: "Discrimination – hostility – conflict: Strategies to recognise and to fight them", speaker: Dr. Meike Lauggas, Akademische Supervisorin, Coach und Organisationsberaterin (T. BOFFA BALLARAN)

04.-08.05.2020, European Geosciences Union General Assembly 2020, online: "Evolutionary pathways of terrestrial planets: Interior/exterior coupling, feedbacks and interaction" (G. GOLABEK)

04.-08.05.2020, European Geosciences Union General Assembly 2020, online: "Quantitative structural geology" (B. GRASEMANN, M. DABROWSKI, S.M. SCHMALHOLZ, M. THIELMANN)

04.-08.05.2020, European Geosciences Union General Assembly 2020, online: "Exploring the diversity of mineralogy" (J. INGRIN, C. MCCAMMON, L. BINDI, J. MAJZLAN)

12.-16.07.2020, JpGU – AGU Joint Meeting 2020, virtual meeting, Session S-IT31: "Planetary cores: Structure, formation, and evolution" (H. TERASAKI, G. STEINLE-NEUMANN, E. OHTANI, W. MCDONOUGH)

09.-14.08.2020, Member of Scientific Program Committee for the 83rd Annual Meeting of Meteoritical Society in Glasgow, Scotland, UK, Postponed to 2022 (A. BOUVIER)

03.09.2020, Harro Schmeling Symposium, Frankfurt/M., Germany (G. GOLABEK)

17.-18.09.2020, International Workshop on 'Development of multi-anvil technology, and its applications to lower-mantel research and material sciences', Bayerisches Geoinstitut, Bayreuth, Germany, virtual (T. KATSURA)

21.09.-09.10.2020, Europlanet Science Congress 2020, virtual meeting: "Multi-disciplinary perspective on coupled planet formation and evolution: from accretion to the present-day, from core to crust" (G. GOLABEK)

20.-23.10.2020, 732. WE-Heraeus-Seminar on 'Matter under Extreme Conditions', virtual (R. REDMER, G. STEINLE-NEUMANN, Z. KONÔPKOVÁ)

01.-17.12.2020, AGU Fall Meeting 2020, online: "Mantle evolution, dynamics, chemistry, and the role of the Transition Zone" (D. LOURENÇO, K. CHOTALIA, C. MCCAMMON, L. WASZEK)

6. Visiting Scientists

6.1 Visiting scientists funded by the Bayerisches Geoinstitut

DI GENOVA, Danilo, Technische Universität Clausthal, Institut für Nichtmetallische Werkstoffe, Clausthal-Zellerfeld, Germany: 16.-18.01.2020

DOLEJŠ, David, Universität Freiberg, Institut für Geo- und Umweltnaturwissenschaften, Freiberg, Germany: 17.-19.02.2020

GEISE, Tobias, Universität Göttingen, Germany: 24.-25.02.2020

MASOTTA, Matteo, Università di Pisa, Dipartimento di Scienze della Terra, Pisa, Italy: 17.-21.02.2020

ROGMANN, Elena, Ruhr-Universität Bochum, Germany: 04.-06.08.2020

SOLOMATOVA, Natalia: ENS Lyon, Laboratoire de Géologie de Lyon: Terre, Planète, Environnement, Lyon, France: 15.-18.01.2020

WALTE, Nico, TU München, Forschungs-Neutronenquelle Heinz Maier-Leibnitz (FRM II), Garching, Germany: 17.-21.02.2020

WILSON, Alfred: University College London, Department of Earth Sciences, London, U.K.: 22.-24.01.2020

6.2 Visiting scientists supported by other externally funded BGI projects

ARMSTRONG, Katherine, University of California, Davis, USA: 09.-14.02.2020 (IRTG^{*A})

BUCHEN, Johannes, California Institute of Technology, Seismological Laboratory, Pasadena, USA: 09.-15.02.2020 (IRTG^{*A})

DRĄŻKOWSKA, Joanna, Ludwig-Maximilians-Universität, University Observatory, München, Germany: 27.-29.01.2020 (IRTG^{*A})

LICHTENBERG, Tim, University of Oxford, department of Atmospheric, Oceanic and Planetary Physics, U.K.: 28.-30.01.2020 (IRTG^{*A})

WIEDENBECK, Michael, Helmholtz-Zentrum Potsdam, Anorganische und Isotopen-geochemie, Potsdam, Germany: 03.03.2020 (ERC^{*B})

$^{*A)}$ IRTG: International Research Training Group "Deep Earth Volatile Cycles" (DFG)

$^{*B)}$ ERC: European Research Council

6.3 Visitors (externally funded)

ARAYA, Naoki, Tohoku University, Department of Earth Science, Sendai, Japan: 10.-18.02.2020

BÉJINA, Frédéric, IRAP Toulouse, France: 02.-07.03.2020

BEYER, Christopher, Ruhr-Universität Bochum, Institut für Geologie, Mineralogie und Geophysik, Bochum, Germany: 30.09.-02.10.2020

BYSTRICKY, Micha, IRAP Toulouse, France: 02.-06.03.2020

GEORGATOU, Ariadni, Université de Genève, Department of Earth Sciences, Genève, Switzerland: 02.-05.03.2020

HIRANO, Naoto, Tohoku University, Center for Northeast Asian Studies, Sendai, Japan: 12.-19.03.2020

HUANG, Yongsheng, Tohoku University, Department of Earth and Planetary Materials Science, Sendai, Japan: 06.02.-14.03.2020

IKEDA, Osamu, Tohoku University, Department of Earth Science, Sendai, Japan: 10.-22.02.2020

KERN, Deborah, Universität Hamburg, Institut für Experimentalphysik, Hamburg, Germany: 03.-05.03.2020

LIBON, Léila, Universität Potsdam, Institut für Geowissenschaften, Potsdam, Germany: 22.-29.07.2020

MUNSCH, Pascal, IRAP Toulouse, France: 04.-07.03.2020

NAKAMURA, Michihiko, Tohoku University, Department of Earth Science, Sendai, Japan: 09.-13.02.2020

NOVELLA, Davide, Università degli Studi di Pavia, Dipartimento di Scienze della Terra e dell'Ambiente, Pavia, Italy: 27.-31.01.2020

OHASHI, Tomonori, Tohoku University, Department of Earth Science, Sendai, Japan: 10.02.-16.03.2020

OHTANI, Eiji, Tohoku University, Earth and Planetary Material Physics Research Group, Sendai, Japan: 10.-13.02.2020

PAMATO, Martha, Università di Padova, Dipartimento di Geoscienze, Padua, Italy: 27.-31.01.2020

PAUSCH, Tristan, Universität Innsbruck, Institut für Mineralogie und Petrographie, Austria: 31.08.-19.09.2020

RIDOLFI, Filippo, Università degli Studi di Urbino "Carlo Bo", Department of Earth, Life and Environmental Sciences DISTEVA, Urbino, Italy: 01.-14.06.2020

SIERSCH, Nicki, Sorbonne Université, Institut de minéralogie, de physique des matériaux et de cosmochimie (IMPMC), Paris, France: 31.08.-05.09.2020

SUZUKI, Akio, Tohoku University, Earth and Planetary Material Physics Research Group, Sendai, Japan: 09.-16.02.2020, 20.-22.02.2020, 15.-19.03.2020

TAKAHASHI, Naoko, Tohoku University, Department of Earth Science, Sendai, Japan: 10.-22.02.2020

TSUBOKAWA, Yumiko, Ehime University, Geodynamics Research Center, Matsuyama, Japan: 16.-29.02.2020

XU, Fang, Sorbonne Université, Institut de minéralogie, de physique des matériaux et de cosmochimie (IMPMC), Paris, France: 01.-05.01.2020

YUTANI, Taku, Tohoku University, Center for Northeast Asian Studies, Sendai, Japan: 13.02.-19.03.2020

7. Additional Scientific Activities

7.1 Habilitation/Theses

Habilitation

OVSYANNIKOV, Sergey: From metals to insulators.

Ph.D. theses

EBERHARD, Lisa: Serpentinite phase relations – An experimental study on redox conditions and fluid migration in subduction zones.
EICHHEIMER, Philipp: Fluid flow in porous media: A combined numerical and experimental approach.
HUANG, Rong: Bridgmanite crystal chemistry and iron content in the Earth's lower mantle.
RUSTIONI, Greta: Trace element mobility in aqueous fluids and the cause of melting in subduction zones.
SATTA, Niccolò: High pressure minerals in the Earth and Moon: Understanding the Lunar impact history and Earth's deep water cycle.
TRYBEL, Florian: Structural, electronic and dynamical properties of H-bonded systems at high pressure.

M.Sc. theses

MA, Ning: Tafassites, a new group of meteorites?
SILVA-SOUZA, Danielle: Equations of state of crystalline and glassy materials from optical measurements in DACs.
SZLACHTA, Victoria: Halogens and organic compounds in subduction zone fluids.

7.2 Honours and awards

AUDÉTAT, Andreas	Brian Skinner Award for best paper in Economic Geology in 2019
FROST, Dan	Fellow of the Royal Society
KEPPLER, Hans	Heisenberg Medal, Alexander von Humboldt Foundation
XIE, Longjian	SPRUC2020 Young Scientist Award

7.3 Editorship of scientific journals

AUDÉTAT, Andreas	Editor "Journal of Petrology" Editor "Economic Geology
BOUVIER, Audrey	Associate Editor "Geochimica et Cosmochimica Acta" Guest Editor " Progress in Earth and Planetary Sciences", Special Issue for Prof. Ahmed El Goresy
DI GENOVA, Danilo	Editorial Board Member "Journal of Volcanology and Geothermal Research"
DUBROVINSKY, Leonid	Member, Editorial Board of the Journal of "High Pressure Research" Member, Advisory Board, Minerals
KEPPLER, Hans	Editorial Board "Contributions to Mineralogy and Petrology" Editorial Board "ACS Earth and Space Chemistry"
MCCAMMON, Catherine	Chief Editor and Managing Editor "Physics and Chemistry of Minerals"
MIYAJIMA, Nobuyoshi	Associate Editor "European Journal of Mineralogy"

7.4 Membership of scientific advisory bodies

BOFFA BALLARAN, Tiziana	Member, "Premio Fiorenzo Mazzi" Committee, Società Italiana di Mineralogia e Petrografia
BOUVIER, Audrey	Member, V. M. Goldschmidt Award Committee, Geochemical Society Member, International Lunar Research Team, European Space Agency Chair, Evaluation committee "CE 49, Planétologie, structure et histoire de la Terre", Agence Nationale de la Recherche Member, Scientific committee of the ATTAREK Foundation Chair, Nomenclature Committee of the Meteoritical Society Member, chemistry team, Ryugu initial analysis, Hayabusa 2 mission, Japan Aerospace Exploration Agency

DUBROVINSKY, Leonid	Member, Review Panel of Canadian Light Source Chair Subcomission on Spectroscopy, Diffraction, and new Instrumentations in Mineral Physics of the International Mineralogical Association Member Review Panel of PETRA III Member Review Panel of Research Council of Lithuania
FROST, Dan	Chair of the organizing committee for Goldschmidt 2021 Member of the Bavarian Academy of Sciences Member, German National Academy of Sciences (Leopoldina) Member of the Selection committee for Alexander von Humboldt Professorships Member of the Royal Society
KEPPLER, Hans	Member, German National Academy of Sciences (Leopoldina) Member, Bavarian Academy of Sciences Member, Alexander von Humboldt Foundation Selection Panel for Humboldt Awardees Member, Advisory Board, Dachverband Geowissenschaften
MCCAMMON, Catherine	Chair, Starting Grant Panel PE10, European Research Council Member, Advanced Grant Shadow Panel PE10, European Research Council Member, Project Review Panel P01, PETRA III Member, Council, International Mineralogical Association Member, Board of Directors, American Geophysical Union Member, Fellows Committee, VGP section, American Geophysical Union Member, Scientific Committee EMPG XVII Member, Award Committee of the International Board on the Applications of Mössbauer Spectroscopy Chair, Sub-committee "Earth's Deep Interior" of the Commission of the Physics of Minerals, International Mineralogical Association

8. Scientific and Technical Personnel

Name		Position	Duration in 2020	Funding source
ABEYKOON, Sumith	M.Sc.	Wiss. Mitarbeiter		IRTG
ASLANDUKOVA, Alena	M.Sc.	Wiss. Mitarbeiterin	from 17.08.	DFG
AUDÉTAT, Andreas	Dr.	Akad. Oberrat		BGI
BAUER, Gerald	Dipl.-Ing. (FH)	Techn. Angestellter		BGI
BOFFA BALLARAN, Tiziana	Dr.	Akad. Oberrätin		BGI
BONDAR, Dmitry	M.Sc.	Wiss. Mitarbeiter	to 14.12 from 15.12	IRTG DFG
BOUVIER, Audrey	Prof. Dr.	Professorin		BGI
BUCHERT, Petra		Fremdsprachen-Sekretärin		BGI
CALVO, Lucas	B.Sc.	Student. Hilfskraft	from 10.11.	DFG
CHANYSHEV, Artem	Dr.	Wiss. Mitarbeiter		BMBF
CIALDELLA, Laura	M.Sc.	Wiss. Mitarbeiterin		IRTG
CRINITI, Giacomo	M.Sc.	Wiss. Mitarbeiter		Leibniz
CZEKAY, Laura	M.Sc.	Wiss. Mitarbeiterin		DFG
DINIUS, Anna		Verwaltungsangestellte		BGI
DI GENOVA, Danilo	Dr.	Akad. Rat auf Zeit	from 01.03.	BGI
DOLINSCHI, Jonathan	M.Sc.	Wiss. Mitarbeiter	from 01.04.	DFG
DOMINIJANNI, Serena	M.Sc.	Wiss. Mitarbeiter		IRTG
DUBROVINSKY, Leonid	Apl. Prof. Dr.	Akad. Direktor		BGI
EBERHARD, Lisa	M.Sc.	Wiss. Mitarbeiterin	to 30.06. from 01.07.	IRTG Leibniz
EICHHEIMER, Philipp	M.Sc.	Wiss. Mitarbeiter	to 31.01.	IRTG
FANG, Jing	Dr.	Stipendiat		DAAD
FEI, Hongzhan	Dr.	Wiss. Mitarbeiter		BGI
FERREIRA, Filippe	M.Sc.	Wiss. Mitarbeiter	to 30.11.	DFG
FISCHER, Heinz		Mechaniker		BGI
FLANIGAN, Michaela	M.Sc.	Wiss. Mitarbeiterin		Leibniz
FROST, Daniel	Prof. Dr.	Stellvertr. Leiter		BGI
GOLABEK, Gregor	Prof. Dr.	Professor		BGI
HEIDELBACH, Florian	Dr.	Wiss. Mitarbeiter		BGI
HOWARD, Christopher	Dr.	Wiss. Mitarbeiter		BMBF
HUANG, Rong	Dr.	Wiss. Mitarbeiterin		Leibniz
ISHII, Takayuki	Dr.	Wiss. Mitarbeiter		DFG
KATSURA, Tomoo	Prof. Dr.	Professor		BGI

KEPPLER, Hans	Prof. Dr.	Leiter		BGI
KHANDARKHAEVA, Saiana	M.Sc.	Wiss. Mitarbeiterin	to 30.04.	DFG
KIM, Eun Jeong	Dr.	Wiss. Mitarbeiterin		EU
KOEMETS, Iuliia	M.Sc.	Wiss. Mitarbeiterin		DFG
KRAUßE, Detlef	Dipl.-Inform. (FH)	Techn. Angestellter		BGI
KRIEGL, Holger		Haustechniker		BGI
KRUPP, Alena	B.Sc.	Student. Hilfskraft	to 30.09.	EU
			from 01.10.	BGI
KURNOSOV, Alexander	Dr.	Wiss. Mitarbeiter		DFG
LANGHAMMER, Dominic	M.Sc.	Wiss. Mitarbeiter	from 01.07.	DFG
LINHARDT, Sven		Elektrotechniker		BGI
MA, Ning	B.Sc.	Student. Hilfskraft	to 31.07.	DFG
			01.08.-30.09.	BGI
	M.Sc.	Wiss. Mitarbeiter	01.10.-15.11.	Leibniz
MAN, Lianjie	M.Sc.	Wiss. Mitarbeiter		Leibniz
MARZOTTO, Enrico	M.Sc.	Wiss. Mitarbeiter		IRTG
MATTHÄUS, Rebecka		Chem.-Techn. Assistentin	from 01.10.	BGI
MCCAMMON, Catherine	Privatdozentin Dr.	Akad. Direktorin		BGI
MEIER, Thomas	Dr.	Wiss. Mitarbeiter		DFG
MELAI, Caterina	M.Sc.	Wiss. Mitarbeiterin	to 14.10.	IRTG
			from 15.10.	Leibniz
MIYAJIMA, Nobuyoshi	Dr.	Akad. Oberrat		BGI
NÉRI, Adrien	Dr.	Wiss. Mitarbeiter	from 13.01.	Leibniz
NISHIDA, Keisuke	Dr.	Wiss. Mitarbeiter	to 30.09.	DFG
NJUL, Raphael		Präparator		BGI
OVSYANNIKOV, Sergey	Dr.	Wiss. Mitarbeiter		DFG
PÖPPELBAUM, Melanie	B.Sc.	Student. Hilfskraft	from 01.10.	UBT
POSNER, Esther	Dr.	Wiss. Mitarbeiterin		DFG
POTZEL, Anke		Chem.-Techn. Assistentin		BGI
POTZEL, Janina		Sekretärin		BGI
PUREVJAV, Narangoo	Dr.	Wiss. Mitarbeiterin	from 13.01.	BGI/VP
PUTAK JURIČEK, Marija	M.Sc.	Wiss. Mitarbeiterin	to 29.02.	IRTG
			01.03.-30.09.	DFG
			from 01.10.	EU
PUTRA, Rizaldi	B.Sc.	Student. Hilfskraft	to 30.09.	EU
			from 01.10.	BGI
RAMMING, Gerd		Elektroniker		BGI

RAUSCH, Oliver		Mechaniker		BGI
ROGMANN, Elena	B.Sc.	Student. Hilfskraft	from 01.10.	DFG
ROTHER, David Alexander		Präparator		BGI
RUBIE, David C.	Prof. Dr.	Professor		EU
RUSTIONI, Greta	M.Sc.	Wiss. Mitarbeiterin		DFG
SATTA, Niccolò	M.Sc.	Wiss. Mitarbeiter	to 30.11.	IRTG
SCHARFENBERG, Romina	B.Sc.	Sekretärin	to 31.10.	BGI
SCHULZE, Hubert		Präparator		EU
SILVA SOUZA, Danielle	B.Sc.	Student. Hilfskraft	to 18.08.	DFG
			19.08.-30.09.	BGI
STEINLE-NEUMANN, Gerd	Privatdozent Dr.	Akad. Oberrat		BGI
SZLACHTA, Victoria	B.Sc.	Student. Hilfskraft	to 15.08.	DFG
			16.08.-30.09.	BGI
THIELMANN, Marcel	Dr.	Wiss. Mitarbeiter		BGI/VP
TRENZ, Ulrike		Biol.-Techn. Assistentin		BGI
TRYBEL, Florian	M.Sc.	Wiss. Mitarbeiter	to 30.09.	DFG
ÜBELHACK, Stefan		Mechaniker		BGI
VLASOV, Kirill	M.Sc.	Wiss. Mitarbeiter	to 31.10.	DFG
			from 01.11.	BMBF
WANG, Biao	M.Sc.	Wiss. Mitarbeiter	to 30.09.	DFG
WANG, Lin	Dr.	Wiss. Mitarbeiter	from 15.11.	EU
WANG, Xiaoyu	B.Sc.	Student. Hilfskraft	from 04.11.	DFG
WIESNER, Dorothea		Techn. Assistentin		BGI
WITHERS, Antony	Dr.	Wiss. Mitarbeiter		BGI
XIE, Longjian	Dr.	Wiss. Mitarbeiter	to 14.11.	BGI/VP
			from 15.11.	Carnegie
YAO, Jie	M.Sc.	Wiss. Mitarbeiter		DFG
YATSO, Kassidy		Koordinatorin IRTG	20.01.-30.09.	IRTG
YUAN, Liang	Dr.	Wiss. Mitarbeiter	to 17.11.	BGI/VP
			from 18.11.	DFG
ZHAO, Ran	B.Sc.	Student. Hilfskraft	from 30.11.	DFG

Abbreviations/explanations:

BGI	Staff Position of Bayerisches Geoinstitut
BGI/VP	Visiting Scientists' Program of Bayerisches Geoinstitut
BMBF	Federal Ministry of Education and Research
DAAD	German Academic Exchange Service
DFG	German Science Foundation
EU	European Union
IRTG	International Research Training Group "Deep Earth Volatile Cycles"
Leibniz	Leibniz-Preis der Deutschen Forschungsgemeinschaft Prof. Frost
UBT	Universität Bayreuth

Index